Structural Studies on the Target of Rapamycin Complex 1

and other regulatory and metabolic Proteins

Inauguraldissertation

zur

Erlangung der Würde eines Doktors der Philosophie

vorgelegt der

Philosophisch-Naturwissenschaftlichen Fakultät

der Universität Basel

von

Stefan Imseng

aus Raron-St.German, VS

Basel, 2017

Genehmigt von der Philosophisch-Naturwissenschaftlichen Fakultät
auf Antrag von

Prof. Dr. Maier, Timm
Prof. Dr. Schirmer, Tilman

Basel, den 21.06.2016

Prof. Dr. Schibler, Jörg
Dekan

I Abstract

Proteins are the functional units executing the genetic program of living cells. Protein activity has to be modulated and adapted to environmental and intracellular conditions throughout the life cycle of every cell. In higher eukaryotes, complex multidomain proteins and multisubunit complexes have evolved to integrate large numbers of input signals to control key steps in metabolism, growth and proliferation. Structural studies of authentic eukaryotic multidomain proteins are required to understand their emergent properties resulting from interdomain and intersubunit crosstalk and conformational dynamics. However, due to problems in sample preparation and characterization, resolving the structures of large eukaryotic protein assemblies remains a considerable challenge. This thesis provides novel structural and mechanistic insights to three highly relevant eukaryotic protein systems, based on integrative multimethod approaches to tackle the inherent complexity of each case.

Mammalian target of rapamycin (mTOR) is the master regulator of growth and proliferation; it senses nutrient and growth signals and in response mediates the switch between anabolism and catabolism. Dysregulation of mTOR signaling is implicated in metabolic diseases and cancer, and mTOR is an established drug target. mTOR is comprised in two structurally and functionally distinct signaling complexes, mTORC1 and mTORC2. In Chapter 2, we determine the structure of the human mTORC1, containing the protein subunits mTOR, Raptor and mLST8, bound to FKBP12, by combining cryo-electron microscopy of the assembled complex at 5.9 Å resolution and crystallographic studies of the 149 kDa Raptor from *Chaetomium thermophilum* at 4.3 Å resolution. The core scaffold of the complex is formed by mTOR; the Raptor N-terminal conserved (RNC) domain is bound in vicinity to the mTOR catalytic site, suggesting a key role of the RNC in substrate recognition and delivery.

Polo-like kinase 4 (PLK4) is a central controller of centriole duplication. Chapter 3 identifies a mechanism for PLK4 regulation by the partner protein STIL by using biochemical mapping, kinase assays, super resolution microscopy, isothermal calorimetry in combination with structural studies of the interaction of the PLK4-polobox 3 (PB3) domain with a coiled-coil region of STIL (STIL-CC). NMR

spectroscopy provides a solution structure of the isolated PLK4-PB3 and crystallographic structure determination reveals the mode of complex formation of PLK4-PB3 and STIL-CC. Mutations in STIL-CC abrogate the interaction to PB3 and diminish centriole duplication in cells, demonstrating the relevance of the PLK4-STIL interaction for centriole duplication.

Acetyl-CoA carboxylase (ACC) catalyzes the conversion of acetyl-CoA to malonyl-CoA, providing the building blocks for fatty acid synthesis. Eukaryotic ACCs are large multidomain proteins, that comprise a unique 120 kDa regulatory central domain (CD) besides the N- and C-terminal catalytic domains biotin carboxylase (BC) and carboxyl transferase (CT). In chapter 4 we determine the structure of the human and yeast CD and provide intermediate resolution crystal structures of up to nearly full-length ACC from *Chaetomium thermophilum.* In combination with functional assays, these data reveal the structural basis for phosphorylation-dependent control of yeast ACC activity.

In summary, the results presented in this thesis provide new structural and mechanistic insights into crucial eukaryote-specific regulatory properties of large multidomain proteins and protein complexes. These studies open important routes for further dissecting functional mechanisms by targeted biochemical and biophysical approaches. In particular for mTORC1, the current results provide a basis for analyzing the interactions with signaling partner proteins. Interdomain crosstalk and regulated protein conformational dynamics in these systems are closely linked to disease. Targeting interdomain interactions may serve as a relevant strategy for therapeutic intervention, e. g. in cancer therapy. The detailed depiction of intact assemblies of ACC and mTORC1 provides the structural groundworks for such approaches.

II Table of Contents

III List of Figures

IV Abbreviations

4EBP1	Eukaryotic translation initiation factor 4E-binding protein
αKG	α-ketoglutarate
ACC	Acetyl-CoA carboxylase
AGC	Protein kinase A, protein kinase G and protein kinase C
Akt	RAC-alpha serine/threonine-protein kinase
AMPK	AMP-activated protein kinase
APC	Anaphase promoting complex
ATM	Ataxia telangiectasia mutated
ATP	Adenosine triphosphate
ATR	Ataxia telangiectasia and Rad3-related protein
BC	Biotin carboxylase
BCCP	Biotin carboxyl carrier protein
BRCA1	Breast cancer susceptibility gene 1
CAD	Carbamoyl-phosphate synthetase 2, aspartate transcarbamylase, and dihydroorotase
Cand1	Cullin-associated NEDD8-dissociated protein 1
CASTOR	Cellular arginine sensor of mTORC1
Cep152	Centrosomal protein of 152 kDa
Cep192	Centrosomal protein of 192 kDa
Cdc5	Cell division cycle 5
CPB	Cryptic polo box
CPT-I	Carnitine O-palmitoyltransferase I
CT	Carboxyl transferase
CD	Central domain
C. elegans	*Caenorhabditis elegans*
Cryo-EM	Cryo-electron microscopy
DEPTOR	DEP domain-containing mTOR interacting protein
DNA-PKcs	DNA-dependent protein kinase catalytic subunit
E. coli	*Escherichia coli*
eIF4E	Eukaryotic translation initiation factor 4E
FAS	Fatty acid synthase
FAT	FRAP, ATM and TRRAP

FKBP12	FK506-binding protein of 12 kDa
FoxO1	Forkhead box protein O1
FoxO3a	Forkhead box protein O3a
FRAP	FKBP12-rapamycin associated protein
FRB	FKBP12-rapamycin binding domain
GAP	GTPase-activating protein
GATOR	GAP activity toward Rags
GEF	Guanosine nucleotide exchange factor
GTPase	Guanosine triphosphate
GTPase	Guanosine triphosphatase
HEAT	Huntingtin, elongation factor 3, protein phosphatase 2A and yeast kinase Tor1
His	Histidine
IGF1	Insulin-like growth factor 1
kDa	Kilo dalton
KOG1	Kontroller of growth protein 1
Map205	205 kDa microtubule-associated protein
MDa	Mega dalton
MIG12	Mid1-interacting G12-like protein
mLST8	mammalian lethal with sec-13 protein 8
mSIN1	mammalian stress-activated map kinase-interacting protein 1
mTORC1/2	mammalian target of rapamycin complex ½
NRD	Negative regulatory domain
PB	Polo-box
PBD	Polo-box domain
PI3K	Phosphoinositide 3-kinase
PIK	Phosphoinositide kinase
PDK1	Phosphoinositide-dependent kinase 1
PLK	Polo-like kinase
PPIase	Peptidylprolyl isomerase
PRAS40	Proline-rich Akt substrate of 40 kDa
PKC-α	Protein kinase C-α
Raptor	regulatory-associated protein of mTOR
Rictor	rapamycin-insensitive companion of mTOR
S6K	S6 kinase

SAS-6	Spindle assembly abnormal protein 6 homolog
Ser	Serine
SGK1	Serum- and glucocorticoide-induced protein kinase 1
SREBP	Sterol regulatory element-binding protein
TBC1D7	TBC1 domain family member 7
Thr	Threonine
TOR	Target of rapamycin
TOS	TOR signaling
TRRAP	Transformation/transcription domain-associated protein
TSC1	Tuberous sclerosis 1 protein
TSC2	Tuberous sclerosis 2 protein
Tyr	Tyrosine
ULK1	UNC-51-like kinase 1

1 Introduction

1.1 Phosphorylation is a key mechanism for controlling protein function in metabolism and proliferation

Proteins are the functional units of all living cells. They carry out a tremendous diversity of tasks: Catalyzing chemical reactions, organizing trafficking within cells, sensing extracellular signals, transporting cargo or measuring electric potential across lipid membranes, maintaining the cellular integrity, activating, inhibiting, translocating or degrading other proteins and initiating the synthesis of new proteins. The activity of individual proteins is regulated on multiple levels in order to efficiently and tightly adjust their activity in response to environmental conditions. Long term control is achieved via biosynthesis of new proteins and degradation of redundant proteins. Whilst this system is well suited for the adaptation to new cellular roles and major environmental changes, it is also slow and energy demanding. Immediate regulation can be mediated by small molecules that directly bind a target protein and in turn cause its activation, inhibition or allosteric modulation. Another mode of short-term regulation is through external or internal stimulation of signaling cascades that affect protein activity by complex formation, altered localization, and most prominently post-translational modifications.

A versatile and central example of post-translational modification is the adenosine triphosphate (ATP)-dependent transfer of a phosphoryl group onto a target protein, termed phosphorylation, catalyzed by protein kinase enzymes (Figure 1.1). Kinases are classified into Ser/Thr-kinases, Tyr-kinases and His-kinases based on the type of residue of its substrate, on which the phosphoryl group is covalently attached to. A kinase target can either be activated or inhibited upon phosphorylation. This can be achieved for instance through induction of a conformational change or the modification of a binding site for another protein. Importantly, the phosphoryl group can be removed by a phosphatase as soon as a specific function is no longer needed. This oftentimes results in an equilibrium situation between a phosphorylated and non-phosphorylated form. Regulation of the activity of the kinase or the counteracting phosphatase allows fine graded control over a large dynamic range of the target protein. The human genome encodes 518 different kinases, which is 1.7 % of all

human genes[1]. Protein kinases mediate the majority of signal transduction in human cells. They also control a vast number of processes in metabolism, transcription, cell cycle regulation, differentiation.

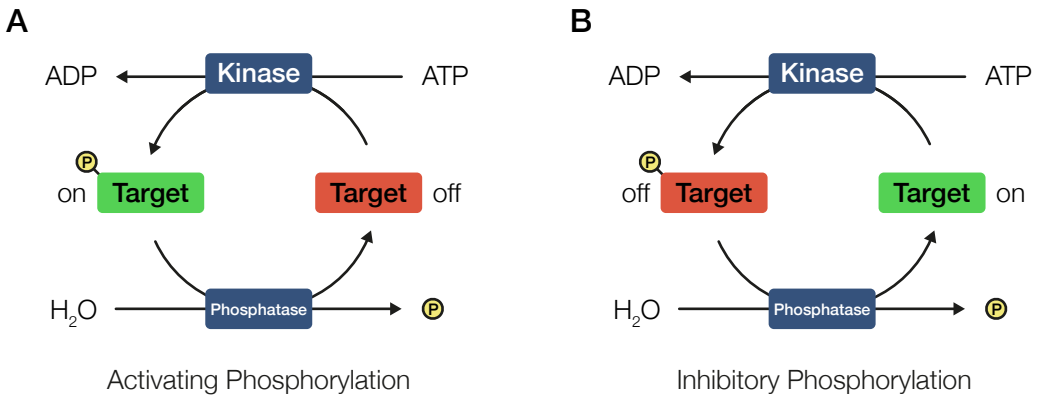

Figure 1.1 Regulation control by protein kinases.
Protein kinases transfer a phosphoryl group from ATP onto a target protein. The protein is either activated (**A**) or inhibited (**B**) upon phosphorylation. The phosphoryl group can be removed by a phosphatase.

This thesis aims to elucidate the structural basis of phosphorylation-mediated control of key regulatory processes in eukaryotic cells: Chapter 2 covers the structure determination of the mammalian target of rapamycin complex 1 (mTORC1) kinase accompanied by structural studies of the isolated subunit Raptor. mTORC1 is the master regulator of cell growth and is oftentimes deregulated in metabolic diseases and cancer. Chapter 3 explores the role of the human Polo-like kinase 4 (PLK4) in centriole duplication, a vital process during the cell cycle. Chapter 4 addresses the phosphorylation-mediated regulation of human and yeast acetyl-CoA carboxylase (ACC), a giant multi-enzyme that catalyzes the committed step in fatty acid and sterol biosynthesis.

1.2 mTOR – the master regulator of cell growth and proliferation

1.2.1 Discovery of mTOR as the cellular target of rapamycin

In 1975 a macrolide with potent antifungal activity was isolated from the soil bacterium *Streptomyces hygroscopicus* (Figure 1.2)[2]. The bacterium was cultivated from a soil sample collected on the Easter Island (called *Rapa Nui* in the local polynesian language). The macrolide was termed rapamycin, a combination of its origin and its antifungal properties[2]. Later, rapamycin was shown to also have important antiproliferative as well as immunosuppressive effects in mammals[3,4]. Rapamycin's mode of action remained unknown for over a decade after the discovery of its effects. In 1991, Heitman *et al.* identified two genes in a genetic screen in budding yeast, *TOR1* and *TOR2* (for **t**arget **o**f **r**apamycin 1 and 2), whose gene products convey the toxic effect of rapamycin[5]. In Addition, yeast strains lacking the FK506-binding protein of 12 kDa (FKBP12), a peptidylprolyl isomerase (PPIase), are completely resistant to rapamycin. This observation suggested a mechanism where rapamycin and FKBP12 form a gain of function complex, that acts on TOR1 and TOR2. Shortly after, the human ortholog mammalian TOR (mTOR) was identified[6-8]. mTOR possesses 43% and 39% sequence identity to TOR2 and TOR1, respectively, and is conserved in all eukaryotes. Whereas budding yeast and fission yeast possess two TORs, other yeast genera and eukaryotes including mammals only have a single TOR gene[9].

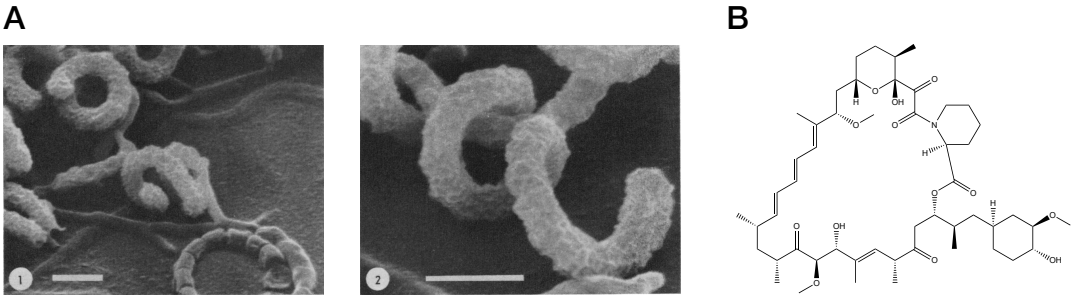

Figure 1.2 The macrolide rapamycin is produced by *Streptomyces hygroscopicus.*
A Scanning electron microscopy micrographs of *Streptomyces hygroscopicus* taken by Dietz and Mathews[10]. Individual spores are arranged in a spiral fashion. The scale bar indicates 2 µm. **B** Chemical structure of the bioactive macrolide rapamycin produced by *Streptomyces hygroscopicus.*

1.2.2 mTOR is a member of the PIKK family of kinases

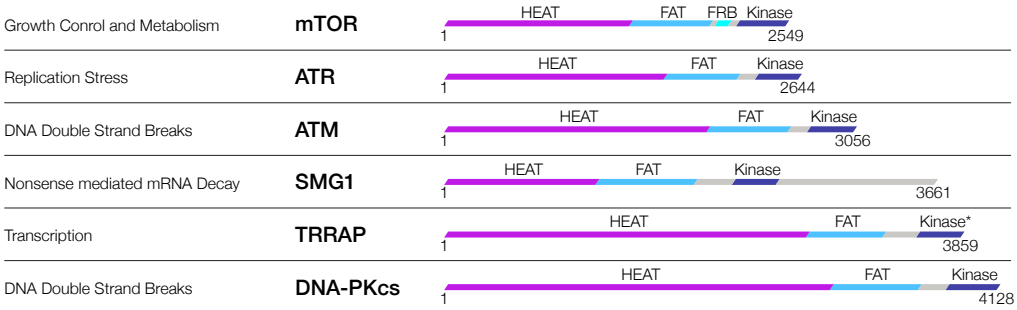

Figure 1.3 Domain organization in members of the PIKK family.
Left: Overview of the individual process each PIKK is involved. Right: PIKKs share a conserved domain architecture with a large number of α-helical repeats. The number of residues of each protein is indicated below the respective scheme. TRRAP has a non-catalytic kinase domain depicted with an asterisk.

mTOR is the founding member of the phosphatidylinositol-3 kinase related kinase (PIKK) family, that possess sequence relation to phosphatidylinositol kinases (PIK), but clearly cluster outside that family and form a distinct group[11]. There are five additional members besides mTOR: Ataxia telangiectasia mutated (ATM), Ataxia telangiectasia and Rad3-related protein (ATR), DNA-dependent protein kinase catalytic subunit (DNA-PKcs), serine/threonine-protein kinase (SMG1) and Transformation/transcription domain-associated protein (TRRAP). PIKKs are very large proteins (2549 – 4128 amino acids) with a conserved domain composition and besides mTOR typically regulate DNA damage responses (Figure 1.3)[12]. They all possess a carboxy-terminal Ser/Thr-kinase domain, whereas TRRAP lacks key catalytic residues and no kinase activity has been reported[13]. The kinase domain is related to phosphatidylinositol-3 kinases (PI3K)[14], but does not have lipid kinase activity. Adjacent to the kinase lies the FAT domain, named after the three representative proteins **F**RAP (FKBP12-rapamycin associated protein, obsolete name for mTOR), **A**TM and **T**RRAP[15]. The FAT domain spans approximately 500 residues and is predicted to comprise α-helical repeats[16]. The amino-terminal rest of the PIKKs, which makes up half of the entire protein in the case of mTOR, consists of a variable number of **H**untingtin, **e**longation factor 3, protein phosphatase 2**A** and yeast kinase **T**or1 (HEAT) repeats[17]. mTOR possesses an additional FKBP12-rapamycin binding domain (FRB), that is absent in other PIKKs and is responsible for conveying the inhibitory effect by binding rapamycin together with FKBP12[18]. However, FRB-like

insertions have been identified in SMG1, DNA-PKcs and TRRAP[19]. PIKKs are often regulated by translocation to distinct sites, where a specific activator can induce the kinase activity[12,17]. Besides, their activity can be modulated by post-translational modifications or by binding to accessory proteins.

1.2.3 mTOR functions in two distinct multi-protein complexes

Members of the PIKK family form very large multi-protein assemblies to accomplish their task. DNA-PKcs in complex with Ku70 and Ku80 is directed to DNA lesion sites and provides a scaffold for their repair[12]. ATR with its binding partner ATR-interacting protein (ATRIP) is recruited to exposed single-stranded DNA and coordinates the maintenance of DNA integrity[12]. The 289 kDa mTOR kinase exists in two distinct signaling complexes: mTOR complex 1 and 2 (mTORC1 and mTORC2, Figure 1.4). mTORC1 comprises the core components mTOR, the 149 kDa regulatory-associated protein of mammalian target of rapamycin (Raptor)[20,21] and mammalian lethal with sec-13 protein 8 (mLST8)[22]. Raptor is implicated in subcellular localization of mTORC1, recruitment of substrates and scaffolding functions[23]. mLST8 directly binds the mTOR kinase domain and modulates the kinase activity[22]. Proline-rich Akt substrate of 40 kDa (PRAS40) is a negative regulator of mTORC1 and is only bound under non-stimulating conditions[24-26].

mTORC2 comprises a core formed by mTOR, the 192 kDa rapamycin-insensitive companion of mTOR (Rictor)[27,28] together with mLST8 and mammalian stress-activated map kinase-interacting protein 1 (mSIN1)[29,30]. DEP domain-containing mTOR interacting protein (DEPTOR)[31] can both bind and inhibit mTORC1 and mTORC2. The two complexes form oligomers, most likely dimers, where each protein is present in two copies per complex[32-34].

Rapamycin inhibits mTORC1 towards some, but not all substrates, which turned out to be an extremely useful tool for many of the studies elucidating the mTOR signaling pathways described in the following two sections. mTORC2 is insensitive to acute rapamycin treatment[27,28]. However, prolonged rapamycin exposure can reduce mTORC2 signaling in certain cell lines[35].

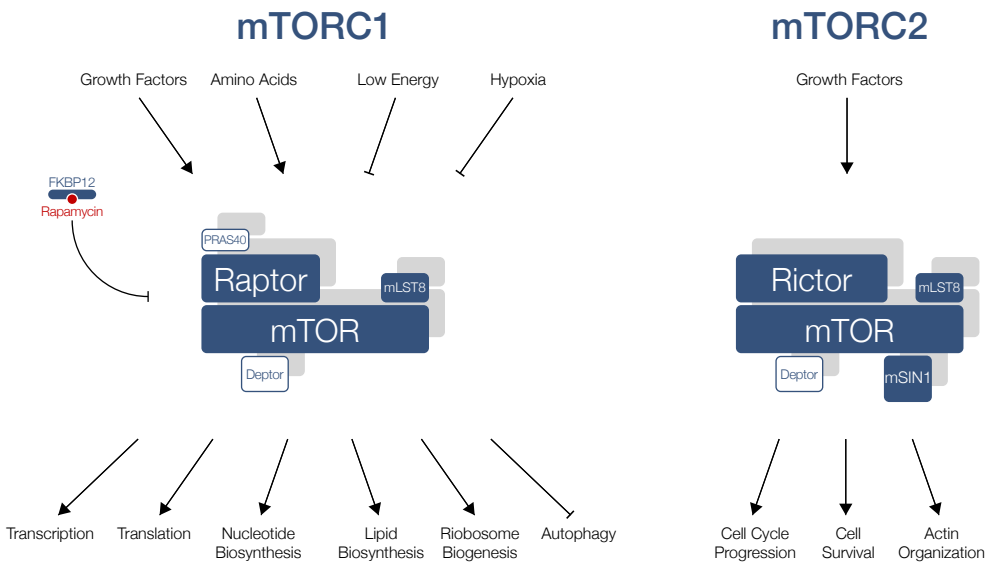

Figure 1.4 Composition and signaling of mTOR complex 1 and 2.
mTOR acts in the two structurally and functionally distinct signaling complexes mTORC1 and mTORC2. mTORC1 core components are mTOR, Raptor and mLST8. The negative regulator PRAS40 is bound to Raptor under non-stimulating conditions. mTORC2 core proteins are mTOR, Rictor, mLST8 and mSIN1. DEPTOR can bind and inhibit both complexes. The two complexes sense nutrients and growth factors and regulate a multitude of metabolic processes.

1.2.4 Upstream regulators of mTORC1 and mTORC2

The two mTOR complexes sense the extracellular and intracellular environment. mTORC1 integrates at least four major input signals: growth factors, amino acids, cellular energy status and oxygen levels. Positive mTORC1 signaling requires two prerequisites: First, mTORC1 needs to translocate to the lysosomal membrane, which is achieved by the amino acid sensing branch. And second, the lysosomal anchored Ras homolog enriched in brain (Rheb) must be in an activated, GTP-bound state induced by the growth factor sensing branch (Figure 1.5).

Growth factors

Growth factors enable mTOR signaling beyond the immediate environment of a single cell. This pathway can effectively reach entire organs and even coordinate mTOR signaling on the whole body level.

Insulin or insulin-like growth factor 1 (IGF1) stimulates mTORC1 activity via the PI3K pathway. RAC-alpha serine/threonine-protein kinase (Akt), ribosomal protein S6 kinase alpha-1(RSK1) as well as extracellular-signal-regulated kinase 1/2 (ERK1/2) are activated and in turn inactivate the tuberous sclerosis complex (TSC, comprising

TSC1, TSC2 and TBC1 domain family member 7, TBC1D7) via inhibitory phosphorylation[23,36]. TSC is the GTPase-activating protein (GAP) of Rheb, a lysosome-anchored GTP-binding protein. Rheb-GTP activates mTORC1 in an unknown manner[23]. Thus, positive growth factor sensing inactivates TSC, enabling Rheb to activate mTORC1 signaling. In Addition, Akt can stimulate mTORC1 activity in a TSC independent manner via phosphorylation of the negative regulator PRAS40, resulting in its dissociation from Raptor[24-26].

Amino acids

The availability of nutrients in the form of amino acids is a prerequisite for the synthesis of new proteins and cell growth. Thus, their sensing is crucial for proper mTORC1 signaling. Some amino acids have proven to be more potent mTORC1 activators than others[37] and different mechanisms for their sensing have been unveiled.

Amino acid sensing is integrated via a GTPase dimer composed of Ras-related GTPase (Rag) proteins. RagA or the functionally redundant RagB forms a heterodimeric complex with either RagC or its equivalent RagD, respectively. The RagA/B-RagC/D complex is tethered to the lysosomal membrane via the pentameric Ragulator complex[38,39]. The RagA/B-GTP and RagC/D-GDP state binds Raptor and brings mTORC1 to the lysosome, whereas the RagA/B-GDP and RagC/D-GTP state fails to localize mTORC1 to the lysosome[40]. The regulation of the nucleotide binding state of the Rags is complex and is only starting to be understood. A number of mechanisms have been discovered:

An important factor is the trimeric “GAP activity toward Rags” (GATOR1) complex. Active GATOR1 results in RagA/B being loaded with GDP, incompetent of mTORC1 binding[41]. GATOR1 is under negative control of the pentameric GATOR2, an integrator of leucine and arginine sensing. In the absence of leucine, Sestrin-2 is bound to GATOR2, preventing the inhibition of GATOR1[42]. During leucine stimulation, Sestrin-2 binds free leucine, dissociates from GATOR and ultimately leads to RagA/B being GTP-loaded and able to bind mTORC1. An analogous mechanism has been suggested for arginine sensing, with “cellular arginine sensor for mTORC1 1” (CASTOR1) dissociating upon arginine binding and relieving its inhibitory effect on GATOR2[43].

Glutamine is sensed indirectly via the product of glutaminolysis, α-ketoglutarate (αKG)[44]. Leucine binds and activates glutamate dehydrogenase (GDH), which

catalyzes the deamination of glutamate to αKG in glutaminolysis. αKG stimulation is sufficient to target mTORC1 to the Rags by a yet unknown mechanism.
The exact roles of the GAP of RagA/B (Folliculin) and the GEF of RagC/D (Ragulator) need to be explored. Furthermore, unraveling the integration of the different input mechanisms with previously suggested inside-out amino acid sensing mechanisms from the lysosomal lumen involving the vacuolar H^+-ATPase (v-ATPase)[45] and the protein SLC38A9[46] provide challenging tasks for future studies.

Energy status

Adenosine triphosphate (ATP) provides energy for a vast amount of cellular processes. Hence, cells need to sense the availability of ATP prior to the activation of anabolic, energy consuming pathways. The AMP-activated protein kinase (AMPK) is active under low energy levels and phosphorylates TSC2[47], feeding into the insulin sensing pathway described above. Furthermore, AMPK can directly reduce mTORC1 activity via an inhibitory phosphorylation of Raptor[48].

Hypoxia

Cells downregulate energy consuming processes under low oxygen tension. “Regulated in development and DNA damage” (REDD1) inactivates mTORC1 singling by relieving an inhibitory interaction between TSC2 and the protein 14-3-3[49].

mTORC2

Knowledge on mTORC2 signaling is sparse. mTORC2 activity is insensitive to nutrients but does respond to insulin stimulation. The mechanism involves association of the ribosome with mTORC2 in a PI3K dependent manner[50]. In Addition, the localization of mTORC2 to an endoplasmic reticulum (ER) subcompartment named mitochondria-associated ER membrane (MAM) appears to be crucial for proper mTORC2 signaling[51].

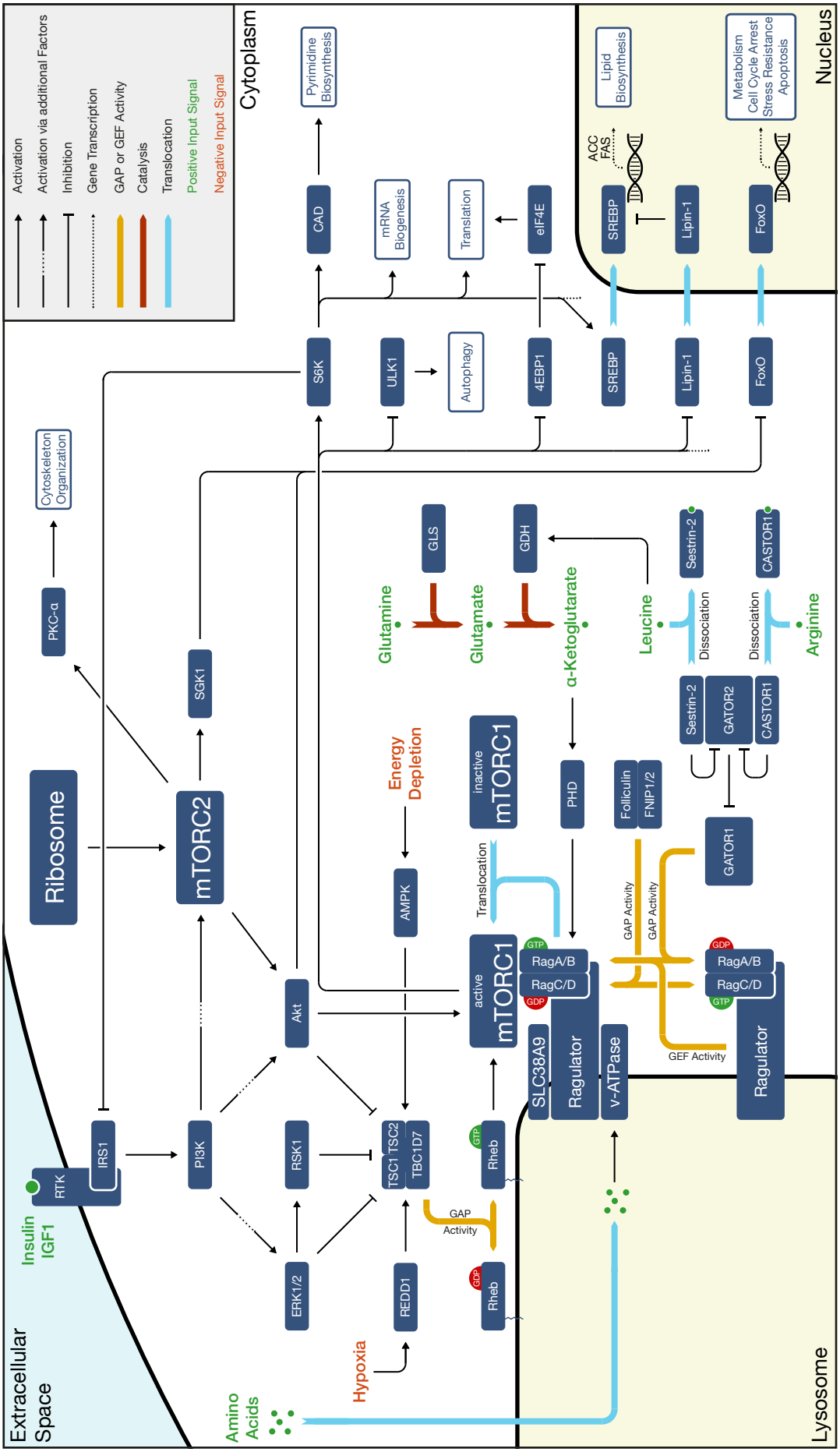
Activation
Activation via additional Factors
Inhibition
Gene Transcription
GAP or GEF Activity
Catalysis
Translocation
Positive Input Signal
Negative Input Signal
Cytoplasm
Nucleus
Extracellular Space
Lysosome
Insulin IGF1
RTK
IRS1
PI3K
Akt
mTORC2
SGK1
PKC-α
Cytoskeleton Organization
Ribosome
S6K
ULK1
Autophagy
4EBP1
eIF4E
Translation
mRNA Biogenesis
CAD
Pyrimidine Biosynthesis
SREBP
Lipin-1
FoxO
Lipid Biosynthesis
ACC
FAS
Metabolism
Cell Cycle Arrest
Stress Resistance
Apoptosis
Glutamine
GLS
Glutamate
GDH
α-Ketoglutarate
Leucine
Sestrin-2
Dissociation
CASTOR1
Arginine
Energy Depletion
AMPK
inactive mTORC1
active mTORC1
Translocation
PHD
Folliculin
FNIP1/2
GATOR2
GATOR1
GAP Activity
GEF Activity
RagA/B
RagC/D
GTP
GDP
SLC38A9
Ragulator
v-ATPase
RSK1
ERK1/2
REDD1
TSC1 TSC2
TBC1D7
Rheb
GAP Activity
Hypoxia
Amino Acids

Figure 1.5 The mTOR signaling pathways.
mTOR responds to environmental signals: Amino acids sensing pathways localize mTORC1 to the lysosomal surface through the Rag proteins, where mTORC1 is activated by Rheb under growth factor stimulation via the PI3K signaling. mTORC1 additionally senses the cellular energy status and the oxygen level, while mTORC2 solely responds to growth factor stimulation. Positive mTOR signaling affects a multitude of metabolic processes as indicated. mTORC1 substrates S6K and 4EBP1 promote protein translation. Positive mTOR signaling additionally activates pyrimidine biosynthesis, mRNA biogenesis, lipid biosynthesis and inhibits autophagy, cell cycle arrest and apoptosis.

1.2.5 Downstream effectors of mTORC1 and mTORC2

The two mTOR complexes act on a vast number of metabolic processes. In favorable growth conditions activated mTORC1 promotes key anabolic processes in order to deliver the building blocks for the generation of new biomass (Figure 1.5).

Protein translation

By far the best characterized mTORC1 effector pathway is the activation of protein translation in response to mTORC1 stimulation. S6 kinase (S6K) is a well characterized and established mTORC1 substrate. Phosphorylation at Thr389 induces a subsequent phosphorylation at Thr229 by phosphoinositide-dependent kinase 1 (PDK1), which fully activates S6K. S6K in turn activates a multitude of effectors that promote mRNA biogenesis and protein translation[52]. Moreover, S6K downregulates growth factor sensing via inhibition of IRS1, enabling negative feedback regulation of mTORC1 signaling[53].

A second well characterized mTORC1 substrate is eukaryotic translation initiation factor 4E-binding protein (4EBP1). Phosphorylated 4EBP1 is unable to bind and inhibit eukaryotic translation initiation factor 4E (eIF4E), a key factor for cap-dependent translation[54].

Pyrimidine biosynthesis

Nucleotides are the building blocks for DNA and RNA. Thus their availability is a prerequisite for the synthesis of new genetic material. mTORC1 stimulation promotes de-novo pyrimidine synthesis by S6K-mediated phosphorylation of the enzyme carbamoyl-phosphate synthetase 2, aspartate transcarbamylase, and dihydroorotase (CAD) at Ser1859[55]. CAD is 243 kDa multienzyme that comprises catalytic domains for the first three steps of pyrimidine biosynthesis. It generates a pyrimidine ring from glutamine, bicarbonate and aspartic acid.

Lipid biosynthesis

Lipids are the structural components of all biological membranes. Cell growth comes along with the increase of the membrane surface and thus demands the synthesis of new lipids. mTORC1 regulates the transcription of lipogenic genes such as fatty acid synthase (FAS) or acetyl-CoA carboxylase (ACC) via sterol regulatory element-binding protein (SREBP) transcription factors. SREBPs are either activated by S6K in an unknown manner[56] or through Lipin-1. Lipin-1 inhibits SREBP activity. Stimulated mTORC1 directly phosphorylates Lipin-1 and prevents translocation to the nucleus and hence relieves the inhibition on SREBP.

Autophagy

Autophagy regulates the degradation of cellular structures and the recycling of their components. This is especially important when the availability of nutrients is restricted. Stimulated mTORC1 signaling also promotes growth by inhibiting autophagy via UNC-51-like kinase 1 (ULK1). AMPK activates ULK1 under starvation, which in turn induces autophagosome formation. mTORC1 mediated phosphorylation of ULK1 disrupts the interaction between ULK1 and AMPK and thus directly inhibits autophagy[57].

mTORC2

mTORC2 regulates several members of the AGC (protein kinase A, protein kinase G and protein kinase C) kinase family, namely Akt, serum- and glucocorticoide-induced protein kinase 1 (SGK1) and protein kinase C-α (PKC-α). mTORC2 phosphorylation of Akt at Ser473 in combination with phosphorylation of Ser308 via the insulin sensing pathway described earlier fully activates Akt[58]. Akt and SGK1 inactivate forkhead box protein O1 (FoxO1) and FoxO3a, transcription factors for proteins involved in metabolism, stress resistance, cell cycle arrest and apoptosis[59]. Activation of PKC-α is implicated in cytoskeleton organization[27,28].

1.2.6 mTOR is a therapeutic target in immunology and oncology

Not long after the discovery of its immunosuppressive properties, rapamycin was approved by the FDA in 1999 for prevention of allograft rejection after organ transplantation and has been widely used ever since[60]. In 2002 its clinical application was extended to the prevention of restenosis after coronary stent surgery by inhibiting growth of vascular smooth muscles[61]. The fact that mTOR deregulation is also

implicated in cancer as well as the tolerability of rapamycin in patients guided efforts to expand its use to oncology. Two rapamycin derivatives (commonly referred to as rapalogues), temsirolimus and everolimus, are approved and used since 2007 and 2009, respectively, to treat advanced kidney cancer, mantle cell lymphoma and pancreatic neuroendocrine tumors[62]. However, their clinical success was well below the high expectations. Possible explanations might be the fact that rapamycin treatment only affects some but not all mTORC1 substrates and is largely ineffective towards mTORC2. Moreover, negative feedback regulation of PI3K-signaling by S6K is lost upon mTORC1 inhibition, which stimulates PI3K-Akt signaling and ultimately inhibits apoptosis via FoxO[62]. Recent attempts aim to target mTOR signaling more broadly. Specific mTOR ATP-competitors that act on both mTOR complexes as well as dual mTOR/PI3K inhibitors additionally tackling loss of negative feedback regulation are currently in clinical trials[63].

1.2.7 mTORC1 substrate recognition

The diversity of the mTOR kinase substrates requires means for their recognition in order to deliver them to the catalytic site and ensure specificity. A highly conserved TOR signaling (TOS) motif has been identified both in S6K (FDIDL, amino acids 5-9) and 4EBP1 (FEMDI, amino acids 114-118)[64,65]. An intact TOS-motif is required for binding by the mTORC1 subunit Raptor, suggesting a dedicated role of Raptor in substrate recognition and delivery to the mTOR kinase. Mutations in the TOS-motif abrogate the interaction between Raptor and the S6K / 4EBP1 and strongly reduce the phosphorylation of mTORC1-targeted sites[66,67]. The negative mTORC1 regulator PRAS40 comprises a TOS-like sequence (FVMDE, amino acids 129-133). PRAS40 binds Raptor in a TOS-dependent manner. The competition of PRAS40 with mTORC1 substrates for Raptor binding has been suggested to be the inhibitory mechanism[24]. Furthermore, 4EBP1 comprises an amino-terminal RAIP-motif (amino acids 13-16), which is required for mTOR mediated phosphorylation[68,69].

mTORC1 substrate recognition is complex and not only mediated by TOS-motif binding. First, No TOS-motifs have been identified in other mTORC1 substrates like ULK1 or Lipin-1[57,70]. And secondly, the mTORC1 specific inhibitor rapamycin completely inhibits the phosphorylation of S6K, but does only partially inhibit phosphorylation of 4EBP1[71,72]. Kinase assays on synthetic mTORC1 substrate peptides suggest that the primary sequence around the phosphorylation site

determines the sensitivity towards Rapamycin inhibition[73]. However, it is very likely that more factors, such as the accessibility of the phosphorylation site and additional recognition motifs outside the target region further modulate the substrate recognition.

1.2.8 Structural biology of the mTOR complexes

Structural knowledge on mTOR and PIKKs in general is sparse. High resolution structure determination of intact mTOR complexes was mainly hindered by the huge size of approximately 1 MDa for mTORC1 and 1.2 MDa for mTORC2 and the difficulties to produce them in sufficient amounts. However, crystal structures of some mTOR fragments in complex with specific binding partners are available. Moreover, the solution structure of the carboxy-terminal α-helix of mTOR has been determined by NMR and suggests a role for redox-dependent structural and cellular stability[74].

The crystal structure of the isolated mTOR FRB domain in complex with rapamycin and FKBP12 has been solved already in 1996 (Figure 1.6A)[18]. FKBP12 adopts a five-stranded antiparallel β-sheet preceded by a short α-helix. The FRB forms a four-helix bundle. Rapamycin is bound to both domains and forms the dimer interface. The macrolide is almost entirely buried between the two domains. The structure explains the specificity of the FKBP12-Rapamycin interaction with mTOR, but does not reveal the mechanism of mTORC1 inhibition.

Recently, a crystal structure of a carboxy-terminal mTOR fragment (amino acids 1376-2549, mTORΔN) comprising the FAT, FRB and kinase domain bound to mLST8 was determined (Figure 1.6B)[19]. The kinase domain adopts a bilobal fold similar to PI3K and canonical protein kinases. The mLST8 β-propeller is bound to the kinase C-lobe, restricting the access to the catalytic cleft. The FRB is an amino-terminal extension of the kinase N-lobe and further hinders the access to the active site. Modeling of FKBP12 onto the FRB domain restricts the catalytic cleft even more. The kinase is wrapped by the entirely α-helical FAT domain, giving the fragment a compact shape. The kinase in the mTORΔN-mLST8 fragment is in an intrinsically active conformation. Thus, the catalytic activity is likely regulated by the surroundings of the active site in the mTOR complexes. The activity is modulated by the mTOR negative regulatory domain (NRD, residues 2430-2450), whose deletion has a positive effect on kinase activity[75,76]. The NRD is not resolved in the crystal structure due to high flexibility, but it is located in close vicinity to the catalytic site and might restrict its access even more.

Altogether the mTORC1 activity is regulated via an access control mechanism, as well as specific substrate recognition mechanisms described in 1.2.7.

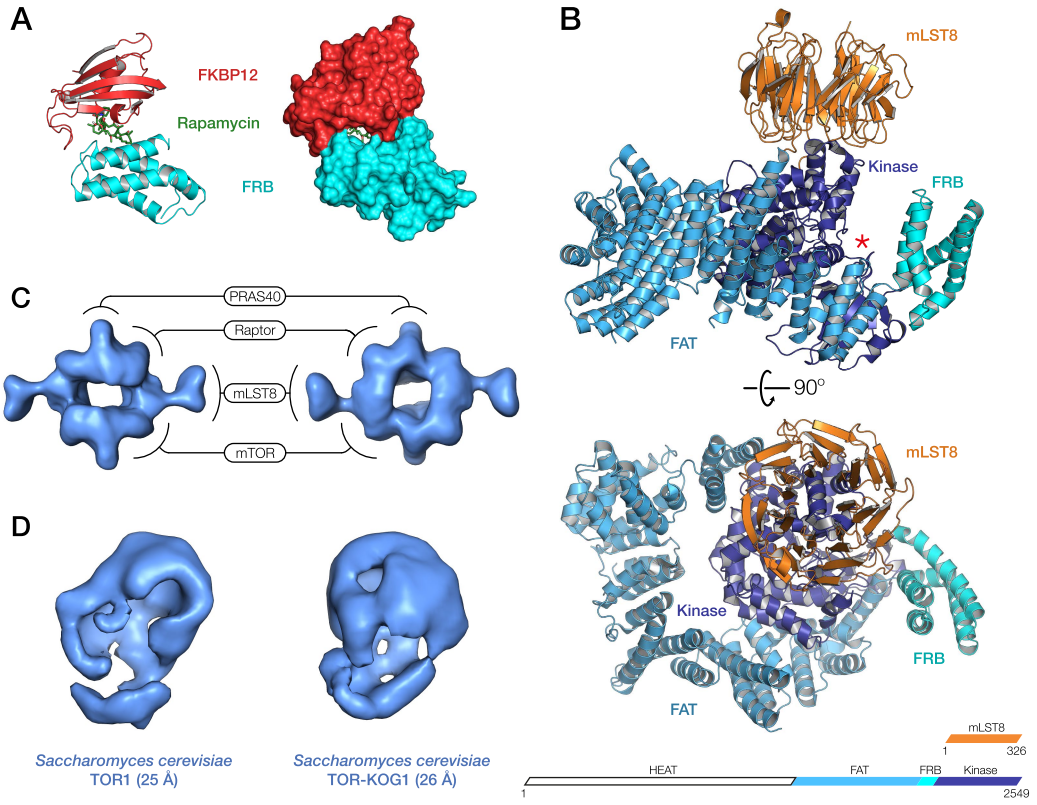

Figure 1.6 Overview of available structural information on mTOR.
A Cartoon (left) and surface (right) representation of the FRB-FKBP12-rapamycin crystal structure (PDB ID 1FAP[18]). Rapamycin forms the interface for the interaction of the FRB and FKBP12 and is almost completely buried **B** Cartoon representation of the crystal structure of mTORΔN in complex with mLST8 (PDB ID 4JSV[19]). mLST8 and the FRB limit the access to the recessed kinase active site marked with a red asterisk. **C** Single-particle cryo.EM reconstruction of human mTORC1 with substoichiometrically bound PRAS40 at 26 Å resolution (EMDB ID 5197)[77]. mTORC1 forms a dimeric rhomboid assembly with a central cavity. **D** Negative-Stain electron microscopy reconstruction of yeast TOR1 (left, EMDB ID 1360) and TOR-Kog1 (right, EMDB ID 1361) at 25 and 26 Å resolution, respectively[78].

Structural studies on TOR complexes is limited to two low resolution cryo-electron microscopy (cryo-EM) studies. An affinity purified sample comprising the mTORC1 core components mTOR, Raptor and mLST8, with substoichiometric PRAS40 was subjected to a single particle cryo-EM reconstruction[77]. The 26 Å model reveals a dimeric rhomboid mTORC1 architecture with a central cavity (Figure 1.6C). Antibody labeling experiments guided the localization of subunits mLST8 and PRAS40. In Addition, a reconstruction of isolated Raptor at 28 Å resolution was positioned into

the core, leaving the remaining density to account for mTOR. The reconstruction confirms the presumed dimeric architecture[32,34], but the insights into the assembly and interaction of individual domains are negligible due to the very low resolution. The second study subjected *Saccharomyces cerevisiae* TOR1 and a TOR-KOG1 (kontroller of growth protein 1, Raptor ortholog) complex to negative stain electron microscopy[78]. Despite the high sequence identity between TOR and mTOR (42%) as well as KOG1 and Raptor (42%) the two reconstructions largely differ from the model of human mTORC1 (Figure 1.6D) . Overall the quality of the hollowed reconstruction is poor and prohibits a meaningful interpretation.

The domain composition of Raptor and Rictor are solely based on bioinformatic studies. Homology searches of Raptor have identified a caspase-like domain in the N-terminal conserved (RNC) region, followed by three HEAT repeats and a seven bladed WD40 propeller at the carboxy-terminal end[20,21,79]. Rictor comprises several conserved regions of unknown structure or fold[27,28]. No high-resolution structure for any parts of Raptor or Rictor are available that would permit dissection of their specific functions in mTOR complex assembly and signaling.

1.3 Polo-like kinase 4 regulates centriole duplication

Living cells undergo continuous cycles of cell growth and duplication. The genetic material is duplicated in the S-phase followed by chromosome segregation and cell division in the M-Phases. These two phases are bridged by growth periods, termed G1 before and G2 after DNA replication. The cell cycle requires rigorous controll in order to spatially and temporally coordinate each individual step. Major players in cell cycle regulation of eukaryotic organisms are the Polo-like kinases (PLKs).

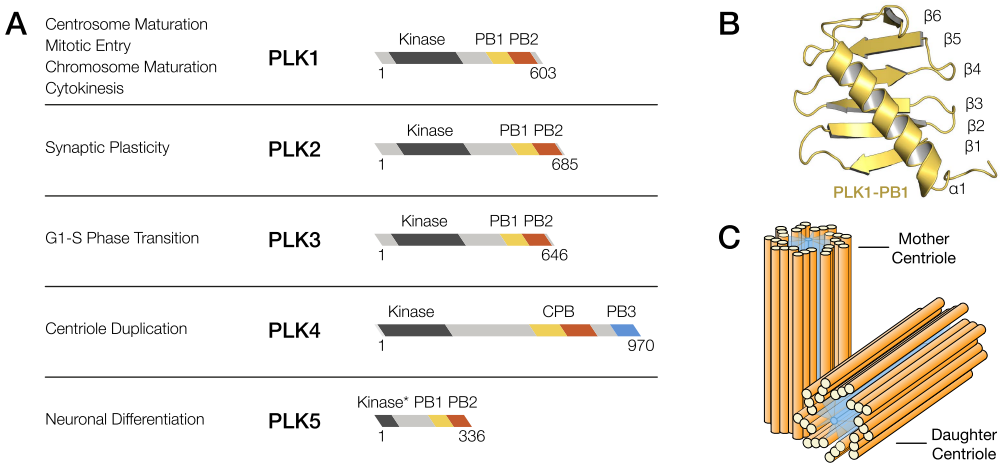

Figure 1.7 The human Polo-like kinases.
A Left: Overview of the various processes each PLK is involved. Right: Domain organization of the human Polo-like kinases. The number of residues of each protein is indicated below the respective scheme. PLK5 possesses a truncated, non-functional kinase domain depicted with an asterisk. **B** Cartoon representation of the typical β6α Polo-box fold of PLK1-PB1 (PDB ID 1UMW[80]) The Polo-box motif is a distinctive feature of all members of the Polo-like kinase family. **C** Schematic representation of a centriole pair, that makes up the core of the centrosome. Each centrosome comprises an older mother centriole and a younger daughter centriole. The centriole consists of nine microtubule-triplets generating the characteristic nine-fold symmetric assembly.

1.3.1 The Polo-like kinase family

The Polo kinase has initially been described in *Drosophila melanogaster* in the late 1980s. Mutations in *polo* cause a variety of abnormalities in mitosis of larval neuroblasts such as random orientation of the chromosomes or perturbed formation of mitotic spindels[81,82]. Polo is conserved in all eukaryotes. Cell division cycle 5 (Cdc5) in *Saccharomyces cerevisiae* and Plo1 in *Schizosaccharomyces pombe* are two well characterized Polo orthologs in yeasts[83]. Five PLK paralogs are present in humans

(Figure 1.7A). PLK1 is the ancestral member of the family and is most closely related to Polo, Cdc5 and Plo1[84]. At least three gene duplication gave rise to PLK2, PLK3, PLK4 and PLK5[84,85]. They all share a conserved amino-terminal Ser/Thr-kinase[86]. However, PLK5 has a truncated kinase that does not possess any catalytic activity[87,88]. All members additionally comprise at least two Polo-boxes (PB), the characteristic feature of the PLKs[89]. PBs possess a six-stranded antiparallel β-sheet followed by an α-helix which spans across the entire sheet (Figure 1.7B).

1.3.2 Polo-like kinase 1

PLK1, the best characterized member of the human PLKs, drives a variety of processes during cell cycle progression, including centrosome maturation, mitotic entry, chromosome maturation and cytokinesis[83,84]. Its activity is controlled through four levels of regulation: 1) PLK1 can be activated by phosphorylation of a highly conserved Threonine (Thr210) located in the activation loop[90]. 2) Binding of targets by the Polo-boxes increases the kinase activity which might together with Thr210 phosphorylation relieve an autoinhibitory interaction between the kinase domain and the Polo-boxes[80]. 3) PLK1 expression levels are tightly controlled, peaking at the G1-M phase transition[91]. 4) And lastly, PLK1 is ubiquitinated by anaphase promoting complex (APC) and targeted for proteasomal degradation. APC is most active during late M-Phase and early G1 phase, which coincides with PLK1 having its major roles during mitosis[92,93].

PLK1 has two carboxy-terminal PBs, PB1 and PB2, which together form the Polo-box domain (PBD) and typically bind phosphorylated (also referred to as “primed”) targets[80,94,95]. The target can either be primed by PLK1 itself (self-priming and binding) or by another kinase like Cyclin-dependent kinase 1 (Cdk1, non-self-priming and binding)[89]. More recent studies have revealed that the PBD can also bind non-phosphorylated targets in the case of Polo and the 205 kDa microtubule-associated protein (Map205) in *Drosophila melanogaster*[96,97]. Much less is known about the regulation of PLK2 and PLK3, but their similarity to PLK1 suggests related mechanisms of regulation[84].

1.3.3 Polo-like kinase 4

PLK4 has a specialized role in centriole duplication[98]. Overexpression of PLK4 in human cells increases centriole number, whereas PLK4 depletion reduces the number

of centrioles[99,100]. Centrioles are cylindrical microtubular structures that make up the core of the centrosome (Figure 1.7C)[101,102]. A single centrosome comprising two centrioles is present during G1-phase. The centrosome is duplicated before mitosis to later anchor the bipolar spindle during cell division. The two centrioles within the centrosome are separated and both provide the basis for the generation of a new daughter centriole. Strict control of centriole duplication is a prerequisite for proper chromosome segregation[103]. Similar to PLK1, PLK4 activity is regulated on multiple levels: 1) The abundance of PLK4 is precisely controlled through transcriptional regulators and degradation as described below. PLK4 reaches the highest levels during mitosis and is almost undetectable in the interphase[104,105]. 2) PLK4 is kept in an inactive state and is activated in S-phase. 3) Activated PLK4 trans-autophosphorylates, as monitored by phosphorylation of Ser305[106], leading to proteasomal degradation via ubiquitination. This negative feedback loop ensures that PLK4 is only active during a short time period and thus prevents the cell from over duplication of centrioles[107].

PLK4 is structurally distinct from its paralogs. In contrast to the PBD present in PLK1-3, PLK4 possesses a cryptic polo box (CPB) domain[108]. The CPB domain is composed of two Polo-boxes with minor variations to the classical Polo-box fold, which have a different relative orientation compared to PB1 and PB2 in PLK1[109,110]. Two CPB domains can interact and allow PLK4 to dimerize. The CPB binds both centrosomal protein 152 (Cep152) and centrosomal protein 192 (Cep192) in a mutually exclusive manner, which is crucial for PLK4 localization and repositioning during centriole duplication[111]. The kinase domain and the CPB are bridged by a 314 residue linker, L1. Another peculiarity of PLK4 compared to its paralogs is the presence of a third Polo-box (PB3) at the carboxy-terminal end. The crystal structure of the isolated murine PB3 reveals a domain-swapped dimer suggesting a role in PLK4 oligomerization[112]. However, the physiological relevance of this structure, crystallized under extreme conditions is doubtful.

The mode of action of PLK4 involves centriolar targeting to distinct Cep152 and Cep192 scaffolds[113]. Activated PLK4 very likely recruits spindle assembly abnormal protein 6 homolog (SAS-6), as it has been demonstrated in *Caenorhabditis. elegans*[114]. SAS-6 self-assembles into a nine-fold symmetric cartwheel and appears to provide the structural framework for the synthesis of a new centriole[115,116]. The mechanisms of PLK4 activation are largely unknown. Very likely yet unidentified protein

factors are involved. The identification of such modulators and their respective roles would allow a more complete comprehension of centriole duplication regulation.

1.4 The acetyl-CoA carboxylase

Acetyl-CoA carboxylase (ACC) is a prominent example of a proliferative metabolic enzyme that is under the control of the mTOR pathway. Mammals possess two ACCs: ACC1 and ACC2. The cytosolic ACC1 catalyzes the biotin-dependent carboxylation of acetyl-CoA to malonyl-CoA. This reaction provides the building block for fatty acid synthesis and is the rate limiting step of long-chain fatty acid biosynthesis[117]. ACC2 shares 73% sequence identity to ACC1, and possesses an amino-terminal extension that anchors it to the outer mitochondrial membrane[118]. Malonyl-CoA produced by ACC2 inhibits carnitine O-palmitoyltransferase I (CPT-I), an enzyme that induces the transport of long-chain fatty acids into the mitochondria for β-oxidation[119,120]. The central role of ACC in lipid metabolism makes it an attractive target for drug discovery against type 2 diabetes, obesity and other manifestations of the metabolic syndrome[121,122]. Moreover, elevated levels of *de novo* fatty acid synthesis are a hallmark of proliferating cancer cells due to an increased demand of membrane lipids[23]. Hence, ACC is a promising anti-cancer drug target.

1.4.1 Regulation of eukaryotic ACCs

Human ACCs are regulated on multiple levels. First, the expression levels are regulated by SREBP transcription factors under involvement of mTORC1 in response to nutrient and growth factor stimulation as described in the previous section (1.2.5.) Short-term regulation is mediated via citrate, which acts as an allosteric activator and stimulates the formation of ACC polymers of up to 8 MDa, the most active ACC form[123]. Reversible phosphorylation by AMPK and “cAMP-dependent protein kinase” (PKA) decreases the sensitivity towards citrate, and thus inactivates ACC. ACC activity is further modulated by the polymer-promoting “mid1-interacting G12-like protein” (MIG12)[124]. Breast cancer susceptibility gene 1 (BRCA1) inhibits ACC activity via binding of phosphorylated Ser1263[125-127]. Furthermore, phosphorylation at Ser80 and Ser1201 are implicated with regulation[128,129].

The highly conserved ACC from *Saccharomyces cerevisiae* (46% sequence identity to human ACC1) has not been reported to form polymers. Its activity is mainly

regulated via phosphorylation by the AMPK homolog SNF1, which has been found to greatly reduce the catalytic activity[130,131]. Several sites have been identified, namely Ser2, Ser1148, highly conserved Ser1157 and Ser1162, and are possible candidates for inhibition of ACC activity upon phosphorylation[132].

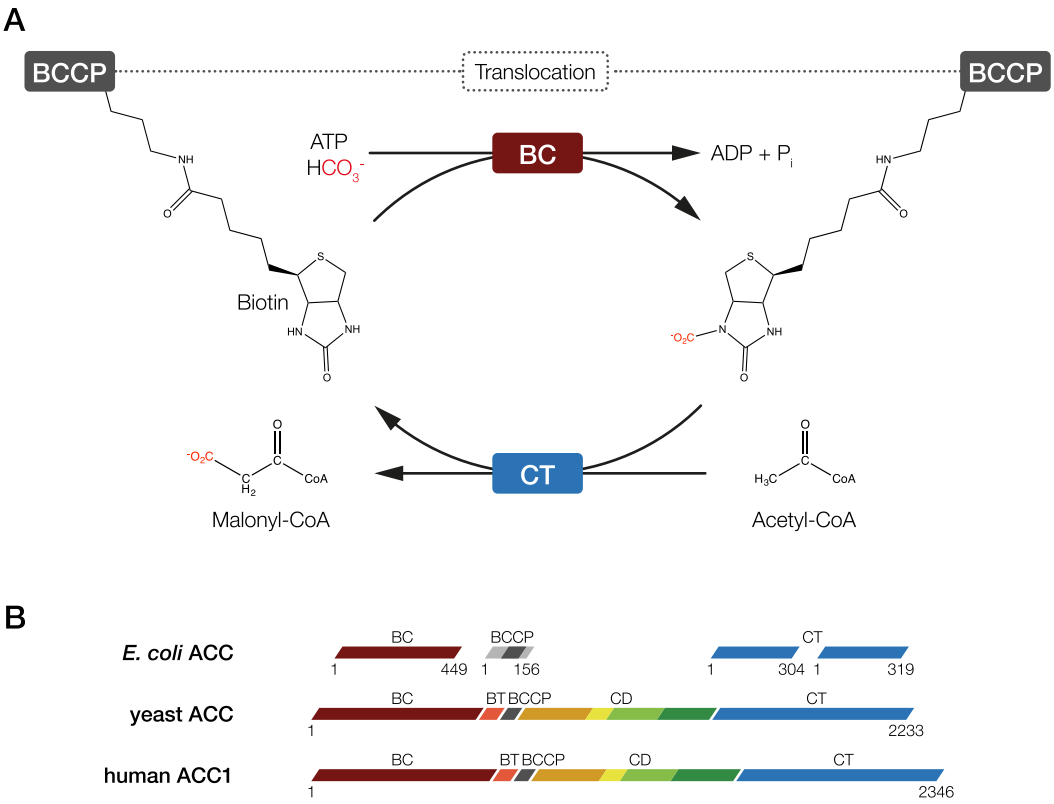

Figure 1.8 Acetyl-CoA carboxylation and domain organization of different ACCs
A Acetyl-CoA carboxylation is catalyzed by two enzymatic units. The BC transfers a CO_2 to a biotin moiety covalently attached to the BCCP and the CT catalyzes the transfer of CO_2 from biotin to acetyl-CoA. The reaction cycle involves the BCCP dependent translocation of the biotin from one active site to the other. **B** The enzymes are individual proteins in most bacteria (represented by *E. coli* ACC), whereas all the functional units are encoded on a single polypeptide chain in most eukaryotes (represented by *S. cerevisiae* ACC and human ACC1). Eukaryotic ACCs contain a unique central domain (CD).

1.4.2 Catalysis and domain organization of ACCs

Acetyl-CoA carboxylation requires two catalytic domains (Figure 1.8A): 1) The ATP-dependent biotin carboxylase (BC) transfers CO_2 from a bicarbonate source to the N1' atom of biotin. 2) The carboxyl transferase (CT) catalyzes the transfer of the CO_2 from biotin to acetyl-CoA[117]. No additional energy is required for the second reaction. The biotin is covalently attached to a lysine of the biotin carboxyl carrier protein

(BCCP), that shuttles the reaction intermediate from the first active site to the second. In the case of *Escherichia coli* (*E. coli*), ACC consists of individual proteins (Figure 1.8B), that form an unstable multi-subunit complex with the stoichiometry $(BC)_2(BCCP)_4(CT\alpha,CT\beta)_2$[118,133]. Most eukaryotic ACCs on the other hand are large (~250 kDa) multienzymes, which comprise all functional units as domains on a single poly-peptide chain[118]. In eukaryotic ACC, the carboxy-terminal CT and the amino-terminal BC are bridged by a structurally and functionally poorly characterized central domain (CD) (Figure 1.8B)[118]. Structural information on eukaryotic ACCs is limited to crystal structures of isolated BC[134], BCCP[135] and CT[136] domains. No structural information is available for the CD, that makes up one third of the entire ACC. Very likely the CD has a key role in ACC regulation reflected by the presence of several phosphorylation sites and the interaction with the inhibitory protein BRCA1. Structural studies on full-length eukaryotic ACCs are impeded by their size and by the dynamic nature of the system. It is of great relevance to structurally characterize the assembly and domain arrangement in eukaryotic ACCs, which needs to permit substrate shuttling by the BCCP . Moreover, it would allow to dissect the role of the central domain, that might mediate eukaryotic specific regulation by binding auxiliary proteins or providing a platform for regulatory phosphorylation.

1.5 Aims of the thesis

Despite their fundamental role in key metabolic processes, detailed structural information on mTOR complexes is limited to smaller fragment structures. Insights on the assembly of the individual components into large complexes are almost completely absent, mainly due to the challenges of studying such large, multi-protein complexes. This hinders the understanding of central questions in the mTOR signaling network. What is the basic mTORC1 architecture and which are the interacting domains between individual subunits? Which structures are involved in substrate recognition? Which regions may provide a platform for regulatory proteins? Therefore, the main aim of this thesis was to obtain a high-quality medium resolution model, which allows interpretation on a pseudo residue level. Of special interest was the structural analysis of the mTORC1-defining subunit Raptor, which determines the functional specificity of mTOR in mTORC1. I aimed to understand, which structural features of Raptor contribute to its three central roles, namely substrate recognition, scaffolding and Rag-targeting.

Chapter 2 presents the structure determination of ***mTORC1*** by a hybrid-method approach using cryo-electron microscopy of recombinant human mTORC1 combined with crystallographic studies of *Chaetomium thermophilum* Raptor. The structure provides major insights into the architecture of human mTOR complex 1 and implications for the substrate recognition by Raptor. Furthermore, the work sets a structural framework to address subsequent questions of mTORC1 and mTORC2 regulation. This chapter is reproduced from the publication “Architecture of human mTOR complex 1” (Aylett C.H.S.*, Sauer E.*, Imseng S.*, Boehringer D., Hall M.N., Ban N. Maier T., *Science*, 2016).

Chapter 3 covers the identification of STIL as a ***PLK4*** regulator and the implications for centriole duplication. The activating mechanisms of the Polo-like kinase 4 is poorly understood. Especially interesting was the identification of unknown protein factors and the characterization of their function in PLK4 regulation. Structure determination of the PLK4-PB3/STIL-CC complex in combination with co-immunoprecipitation experiments, cellular assays, ITC experiments and NMR studies reveal an activating role of STIL towards PLK4. The structure additionally determines a new mode for substrate binding by a Polo-box. This chapter is reproduced from the publication “STIL

binding to Polo-box 3 of PLK4 regulates Centriole Duplication" (Arquint C.*, Gabryjonzyk A*., Imseng S.*, Boehm R.*, Sauer E., Hiller S., Nigg E.A., Maier T., *eLife*, 2015).

Chapter 4 addresses the structural basis for the regulation of ***eukaryotic ACCs***. Eukaryotic acetyl-carboxylases are very large and highly dynamic multi-enzymes. Structures were only available for isolated catalytic domains, but not for the non-catalytic central domain (CD) or the overall multienzyme. The CD is implicated in regulation by phosphorylation, but its structure and function were unknown. Here, we report the crystallographic structure determination of the human and budding yeast central domain and integrate the results with intermediate and low resolution structural data on near full-length ACC from *Chaetomium thermophilum*. Altogether, our results reveal the mechanism of phosphorylation control of yeast ACC activity. This chapter is reproduced from the publication "The Dynamic Organization of Fungal Acetyl-CoA Carboxylase" (Hunkeler M.*, Stuttfeld E.*, Hagmann A., Imseng S., Maier T., *Nature Communications*, 2016).

* Authors contributed equally to this work

2 Architecture of human mTOR complex 1

Reproduced from:

Architecture of human mTOR complex 1

Christopher H. S. Aylett*, Evelyn Sauer*, **Stefan Imseng***, Daniel Boehringer, Michael N. Hall, Nenad Ban and Timm Maier

*Authors contributed equally to this work

Science 01 Jan 2016, Vol. 351, Issue 6268, pp. 48-52

DOI 10.1126/science.aaa3870

2.1 Abstract

Target of rapamycin (TOR), a conserved protein kinase and central controller of cell growth, functions in two structurally and functionally distinct complexes: TORC1 and TORC2. Dysregulation of mammalian TOR (mTOR) signaling is implicated in pathologies that include diabetes, cancer, and neurodegeneration. We resolved the architecture of human mTORC1 (mTOR with subunits Raptor and mLST8) bound to FK506 binding protein (FKBP)–rapamycin, by combining cryo–electron microscopy at 5.9 angstrom resolution with crystallographic studies of Chaetomium thermophilum Raptor at 4.3 angstrom resolution. The structure explains how FKBP-rapamycin and architectural elements of mTORC1 limit access to the recessed active site. Consistent with a role in substrate recognition and delivery, the conserved amino-terminal domain of Raptor is juxtaposed to the kinase active site.

2.2 Introduction

Since its discovery in 1991 as the target of the immunosuppressant rapamycin, TOR has emerged as a central regulator of cell growth and metabolism. TOR was identified in yeast[5,14]; the mammalian ortholog is mTOR. The serine and threonine kinase activity of TOR is tightly regulated in response to physiological conditions, and aberrant mTOR signaling occurs in multiple pathologies, including diabetes, cancer, and neurodegeneration[137,138].

TOR is the core component of two, functionally distinct signaling complexes, TOR complex 1 (TORC1) and TORC2[20,21,23,27,28,139,140]. TORC1 is sensitive to rapamycin and regulates cell growth by activating protein, lipid, and nucleotide synthesis and by inhibiting autophagy. TORC2 is less well characterized but is rapamycin insensitive and controls diverse cellular processes through phosphorylation of several targets. Mammalian TORC1 (mTORC1) contains, in addition to mTOR, Raptor (regulatory-associated protein of mTOR)[20,21], mammalian homolog of protein Lethal with Sec Thirteen (mLST8)[22,139], and possibly several noncore subunits. Whereas mTOR and mLST8 are also found in mTORC2, Raptor is absent. Instead, Rictor (rapamycin-insensitive companion of mTOR)[27,28,139] and additional subunits[29,30,141] are required for mTORC2 activity.

The regulation of mTORC1 signaling involves interactions with several binding partners and translocation of mTORC1 within the cell[23,140]. mTORC1 is activated in response to nutrients (amino acids) through the Rag guanosine triphosphatase (GTPase) signaling pathway[40,142], by growth factors through inhibition of the tuberous sclerosis complex 1 and 2 (TSC1 and TSC2) heterodimer and thereby activation of the small GTPase Rheb[143,144], and by cellular energy status through adenosine monophosphate–activated protein kinase (AMPK) phosphorylation of TSC2 and Raptor[47,48].

TOR is the founding member of the phosphatidylinositol-kinase–related kinase (PIKK) family[11], members of which share an elaborate domain organization. The kinase domain is situated at the C terminus, following long arrays of first HEAT (Huntingtin, EF3A, ATM, TOR), and then tetratricopeptide (TPR), repeats[16,145]. The crystal structure of a compact C-terminal fragment of human mTOR containing the FAT (Frap, ATM, TRRAP) domain and the kinase domain has been resolved in complex with its obligate accessory protein, mLST8[19].

Inhibition of mTOR by rapamycin is dependent on the formation of a complex with an intracellular receptor, FK506-binding protein (FKBP)[146,147], which then binds mTOR in mTORC1. FKBP interacts with mTOR through the hydrophobic rapamycin molecule, which binds pockets in each protein[5,18,148]. The N terminus of the kinase domain forms the FKBP-rapamycin complex binding (FRB) domain, which juts outward from the N-lobe[19]. Binding of the FKBP-rapamycin complex to the FRB domain has been predicted to narrow the active-site cleft[19], suggesting that rapamycin inhibition is due to steric hindrance[71]. The FRB domain also binds cognate mTOR targets, and the mutation of key residues in the FRB domain impairs phosphorylation of model substrates[19].

The catalytic activity and substrate specificity of mTORC1 are regulated by Raptor. Raptor is a multidomain protein, predicted by sequence similarity to consist of an RNC (Raptor N-terminal Conserved) domain, a central set of armadillo repeats, and a C-terminal β-propeller[20,21]. Raptor functions in substrate binding, being required for phosphorylation of many mTORC1 substrates, the best characterized of which are the translational regulators ribosomal protein S6 kinase (S6K1) and eukaryotic translation initiation factor 4E-binding protein (4EBP). Phosphorylation of these substrates is dependent on their TOR signaling (TOS) motif, which binds Raptor directly[66,67].

Biochemical investigation of the oligomeric state and composition of TORCs demonstrated that TOR and mTOR complexes are dimeric, and allowed assignment

of core components. Owing to difficulties in working with intact mTORC1, however, information on the three-dimensional arrangement of proteins and domains within the complex was limited to crystal structures of fragments[18,19], and a low-resolution (26 Å) reconstruction through cryo–electron microscopy (cryo-EM)[77] revealing twofold-symmetric, dimeric particles roughly 300 Å by 200 Å by 100 Å in size. In that study, however, the handedness of the reconstruction and the position of individual subunits could not be reliably assigned.

We resolved the structures of human mTORC1 and Chaetomium thermophilum Raptor (CtRaptor) at 5.9 and 4.3 Å resolution by cryo-EM and X-ray crystallography, respectively. We provide a description of the architecture of mTORC1 at a secondary structural level, placing the folded domains of all three mTORC1 subunits and revealing their relative arrangement within the complex.

2.3 Results and Discussion

2.3.1 Determination of the cryo-EM structure of mTORC1

We coexpressed and copurified human mTOR, Raptor, and mLST8 from insect cells, obtaining a homogeneous mTORC1 complex with a molecular size of ~1.0 MD (Supplemental Figure 2.1A,B). Purified material phosphorylated the mTORC1 substrate 4EBP1 and was inhibited by torin1 or FKBP-rapamycin, as expected for native mTORC1 (Supplemental Figure 2.1C). For structural studies, a stable mTORC1 sample was generated by expression in the presence of rapamycin followed by mild glutaraldehyde gradient fixation[149]. Single-particle analysis of cryo–electron micrographs from this mTORC1 sample yielded a reconstruction with an overall resolution of 5.9 Å (gold-standard Fourier shell correlation = 0.143 cut-off), within which only a few peripheral regions were ordered to lower resolution (Supplemental Figure 2.2, Supplemental Figure 2.3). Secondary structural elements were clearly resolved throughout most remaining regions of the complex, allowing all folded domains predicted within mTORC1 to be assigned. The reconstruction presented here is complemented by the crystal structure of C. thermophilum Raptor that fits the EM density of human mTORC1 and confirms the segregation of the Raptor and mTOR repeat regions. Both the crystal structure of the C-terminal fragment of mTOR[19] and the Raptor structure fit our density, allowing us to determine the handedness of the reconstruction (Figure 2.1 and Supplemental Figure 2.4). The overall shape of our

reconstruction agrees with that of the published reconstruction; however, it appears that the handedness of the previous reconstruction was assigned incorrectly[77].

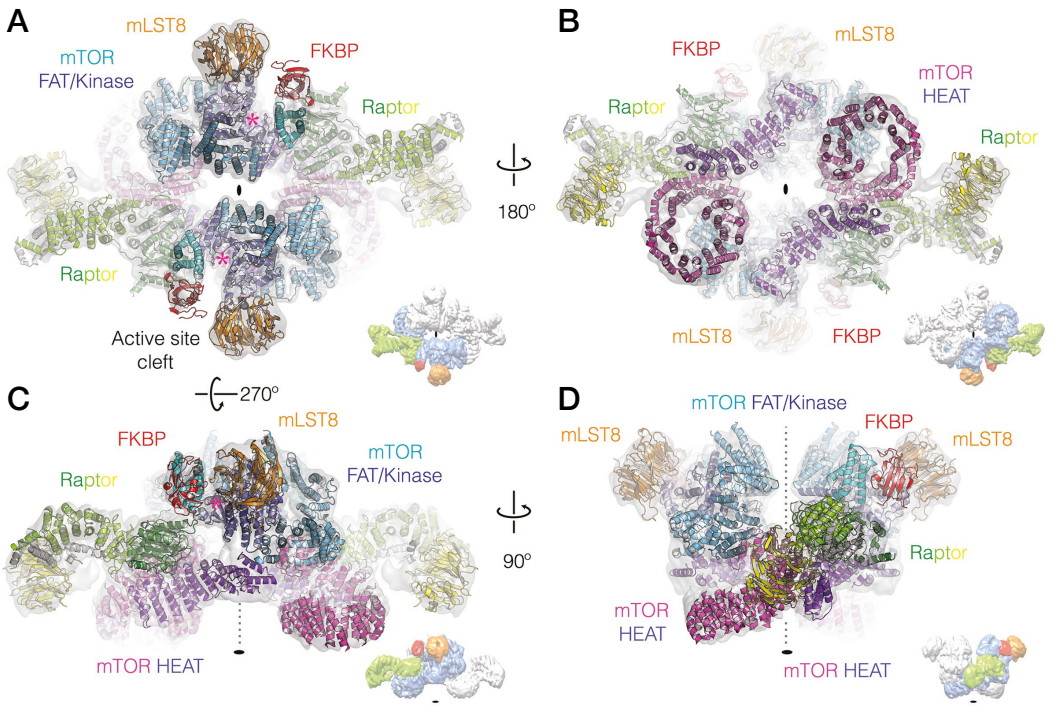

Figure 2.1 mTORC1 adopts a dimeric, lozenge-shaped architecture.
The reconstructed density obtained without masking peripheral regions, filtered to its global resolution (6.1 Å) and contoured at 3σ, is shown as a translucent surface, and the corresponding model in cartoon representation. Each successive panel (A to D) is rotated as indicated. Raptor is in shades of green, mTOR in purples (N-terminal HEAT repeats) and blues (C-terminal FAT and kinase domains), mLST8 in orange, and FKBP in red. The active site, at the base of a restrictive cleft, is indicated by a magenta asterisk. A tinted surface representation showing the surface corresponding to one of each of the subunits within the proposed model of mTORC1 is inset.

2.3.2 mTORC1 forms a hollow dimer with minimal subunit contacts

mTORC1 adopts a cage-like, dimeric architecture in which the C2 symmetry axis passes through a large cavity (>60 Å across in places), leading to its characteristic hollow lozenge shape (Figure 2.1A,B). The kinase domains of mTOR are located near the center of the assembly and come close to each other but do not make contact. Raptor and mLST8 contribute peripheral parts of the complex, making up the pinnacles of the longer and shorter axes of the lozenge, respectively. When viewed from an angle perpendicular to the symmetry axis, one face of mTORC1 is characterized by the mTOR kinase domains and mLST8 subunits, with both active-

site clefts opening outward from this side of the complex (Figure 2.1A,C). The opposite face comprises the N-terminal HEAT repeat domains of mTOR, which form superhelical α-solenoids (Figure 2.1B,D). Raptor binds within the well-ordered juncture of two HEAT repeat domains. The RNC domain abuts the FRB region of the mTOR kinase domain, and the more C-terminal armadillo repeat and β-propeller domains extend outward, becoming less well resolved (Figure 2.1B,C).

2.3.3 The mTOR HEAT repeats contain two α-helical solenoids

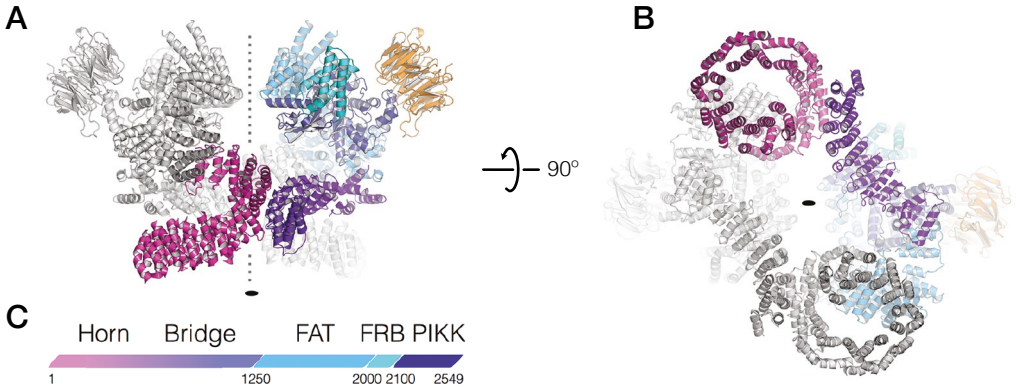

Figure 2.2 Model showing the suggested domain organization of the mTOR dimer.
A, B The C- terminal kinase and FAT domains of mTOR form a compact unit, and the N-terminal HEAT domains adopt an elongated structure with two separate a-solenoids: the "horn" and "bridge." The proposed model is shown in cartoon representation, rotated as indicated. Symmetry-related mTOR domains are shown in gray. **C** Linear representation of the domain organization of mTOR. The residue numbers indicate the domain boundaries; domain lengths are consistent in residues.

The N-terminal portion of mTOR has a bipartite structure consisting largely of α-solenoid helical repeats. The extended, N-terminal region merges directly into the more compact, C-terminal fragment, which wraps around the kinase domain. The repetitive N terminus of mTOR, a prototypical HEAT repeat[16,145], forms two α-solenoids (Figure 2.2). The larger section is a highly curved superhelix, which we have dubbed the "horn," seven repeats of which can be placed at the individual-helix level. The remaining repeats are less clearly resolved, indicating local flexibility. The smaller region adopts a relatively linear arrangement consisting of seven HEAT repeats and a helical linkage to the compact fragment, which we refer to as the "bridge" (Figure 2.2) The horn and bridge HEAT domains pack against one another. Nevertheless both sections are predominantly exposed to the environment, supporting a purported role

in binding mTOR regulators. The bridge region merges directly into the TPR repeats of the FAT domain (Figure 2.2) and the prior crystal structure of this region fits our density with only minor adjustments[19] (Figure 2.1 and Supplemental Figure 2.4).While no linkage between the two HEAT domains is visualized, their termini are in close proximity to one another. Although we cannot definitively assign sequence to regions of density at this resolution, the available evidence from studies of homologs[150] supports an interpretation in which the domains are continuous and contiguous, with the horn representing the N-terminal section and the bridge the more C-terminal part (see 2.4). This suggested topology is shown in Figure 2.2

2.3.4 mTOR HEAT repeats bridge the kinase domains

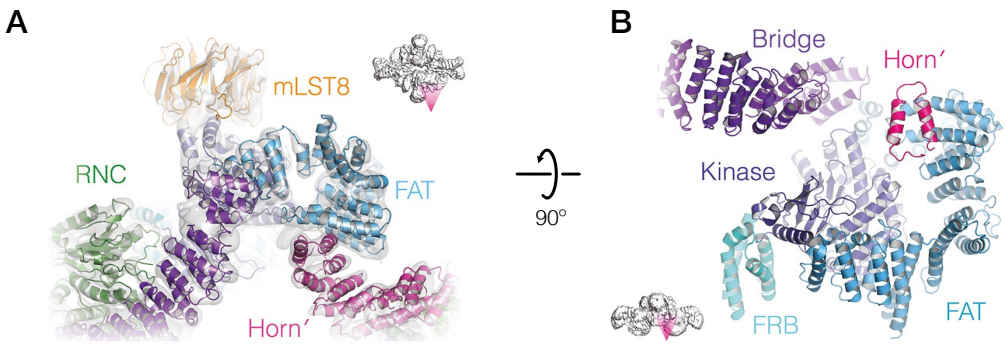

Figure 2.3 The horn and bridge of mTOR complete a full dimeric interaction, linking the two FAT-PIKK units.
A The complete interaction is shown intact, and the reconstruction, filtered to its global resolution (5.9 Å) and contoured at 6σ, is indicated as a translucent surface; the corresponding model is shown as a secondary structural cartoon. **B** The interaction surface is shown with the point of view rotated as indicated. The symmetry-related horn domain is denoted horn′.

Although Raptor is proposed to mediate mTOR dimerization by binding between the mTOR subunits[77], our structure reveals that mTOR itself forms a complete dimer (Figure 2.2). The horn and bridge HEAT domains pack against one another, and the first HEAT repeat of the mTOR horn region is buried against the base of the adjacent mTOR FAT domain, completing an interlocking interaction between the two subunits (Figure 2.3A). Dimerization changes the conformation of the FAT domain of mTOR relative to that in the monomeric crystal structure (Supplemental Figure 2.4)[19]. TPR helices 4 to 12 rotate to accommodate the interaction, presenting the interface and stacking neatly across the first repeat of the horn (Figure 2.3B). Notably, the

conformation of the kinase domain appears unaffected by dimerization. This is not unexpected, as the kinase domain can maintain an active state even in the absence of Rheb[19]. Thus regulation is probably mediated largely by controlling substrate access to the active site.

2.3.5 Structure of Raptor

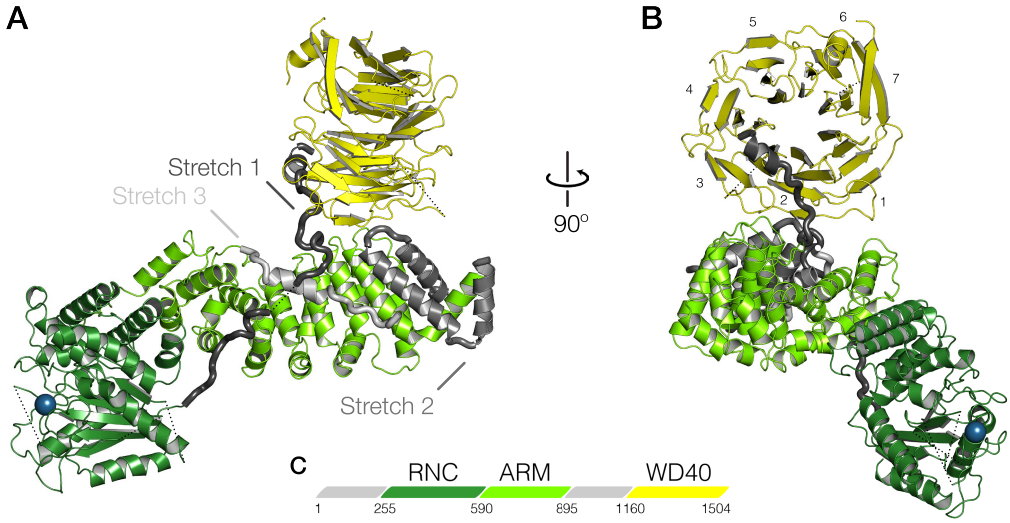

Figure 2.4 CtRaptor adopts a Z shape with the RNC domain and the β-propeller at opposing ends of the armadillo domain.
A, B CtRaptor is shown in cartoon representation, and domain borders are indicated in a sequence schematic. The putative substrate-binding site, inferred from homology to CASPases, is indicated by a blue sphere. Polypeptide linkers are shown in gray; stretch 1 (dark gray) originates from the N terminus of the RNC domain and spans the armadillo (ARM) domain to the b propeller; stretch 2 (medium gray) is associated with the C-terminal region of the armadillo domain; stretch 3 (light gray) is bound along the concave surface of the armadillo domain. **C** Linear rep- resentation of the domain organization of Raptor. The residue numbers indicate the domain bound- aries; domain lengths are consistent in residues.

Raptor determines substrate specificity of mTORC1, by mediating recruitment[40,142] and recognition[20,21]. Density corresponding to the RNC domain and the proximal part of the armadillo repeat of human Raptor is well defined in our reconstruction, whereas the distal portion of the armadillo repeat and the C-terminal β-propeller domain are flexible (Figure 2.1). To resolve the entire Raptor structure, we purified insect cell-expressed Raptor from C. thermophilum (CtRaptor), which exhibits 44% sequence identity to human Raptor (Supplemental Figure 2.5). To facilitate crystallization, CtRaptor was subjected to limited proteolysis, which removed a large N-terminal

extension absent in human Raptor (Supplemental Figure 2.6). Several smaller proteolytic fragments remained associated with the Raptor core (Supplemental Figure 2.6). Experimental phases for CtRaptor crystals were determined with a mercury derivative, and a backbone model was traced at a resolution of 4.3 Å (Supplemental Figure 2.7). CtRaptor adopts an extended Z shape with the RNC and β-propeller domains arranged at opposite ends of the armadillo domain (Figure 2.4).

The N-terminal RNC domain exhibits an α-β-α sandwich fold that is structurally related to that found in CASPases (Supplemental Figure 2.8A), consistent with conserved motifs in both families [79]. The RNC domain is connected to the armadillo domain through four helices, three of which originate from a large insertion (relative to the CASPase fold) between strand one and a shortened helix four, and the fourth from the C terminus of the RNC domain. Two of the active-site residues of CASPases are conserved in the RNC domain [79]. Our model of CtRaptor reveals that there is also structural conservation of the corresponding regions. However, the N terminus of helix 1, which contributes a key arginine residue to the CASPase active site, is displaced by more than 13 Å in CtRaptor.

The Raptor armadillo domain comprises seven helical hairpins, five of which are canonical armadillo repeats (Supplemental Figure 2.8B). The β-propeller domain of Raptor associates with the armadillo repeats through the interaction of blades two and three with repeats five, six, and seven. The interaction takes place at the rim of the b propeller, leaving the face accessible for putative interacting proteins (Figure 2.4 and Supplemental Figure 2.8B). Three additional stretches of extended CtRaptor peptide are visible in the electron density (Figure 2.4 and Supplemental Figure 2.7). Stretch 1, belonging to the N terminus, originates at the b propeller, spans the entire armadillo domain, and joins the N terminus of the RNC domain. Stretch 2 forms a V-shaped helical segment at the C terminus of the repeat domain beneath the b propeller. Stretch 3 runs along the concave face of the armadillo domain. Stretches 2 and 3 likely represent the linker region between the armadillo and β-propeller domains, corresponding to the fragments observed by mass spectrometry (Supplemental Figure 2.6). The corresponding linker region of human Raptor (residues 700 to 900) is frequently phosphorylated[151]; based on our structural data, such posttranslational modification could affect interactions with the Raptor core in vivo.

The conformation of CtRaptor in crystals is close to that of human Raptor in the mTORC1 EM reconstruction, allowing us to fit the crystal structure as a rigid body into the EM density. The projection of the β-propeller domain of Raptor away from the core

of mTORC1 is consistent with a role for this domain in the recruitment of regulatory proteins (Figure 2.1, Figure 2.4)[40,142]. The Raptor RNC domain is positioned directly at the mTOR active-site cleft, implying its involvement in Raptor-mediated substrate recognition (Figure 2.1, Figure 2.4)[66,67].

2.3.6 Raptor stabilizes the mTOR HEAT domains

Raptor is necessary for formation of the mTORC1 complex. The principal interaction between Raptor and mTOR consists of an α-solenoid stack formed between the horn and bridge domains of mTOR and the Raptor armadillo domain (Figure 2.5A). The horn and bridge domains run antiparallel to each other, forming a contact offset by half their depth (Figure 2.5B). The N-terminal helices of the Raptor armadillo repeat and the base of the RNC domain occupy this "step," making up the remaining interaction surface with the loops of the HEAT repeats within the bridge and helices of those in the horn (Figure 2.5A). Given that Raptor provides roughly two-thirds of the interaction surface stabilizing the HEAT domains, the stability of the N-terminal regions of mTOR would be weakened in its absence. The formation of the mTORC1 dimer is also dependent on the interaction between the (flexible) horn N-terminal HEAT domain of mTOR and the C-terminal FAT domain. Without stabilization of the mTOR N-terminal HEAT repeats in a single conformation, dimers could not be readily formed. Raptor binding thus may favor the dimerization of mTOR molecules without directly engaging in dimer formation [77,139].

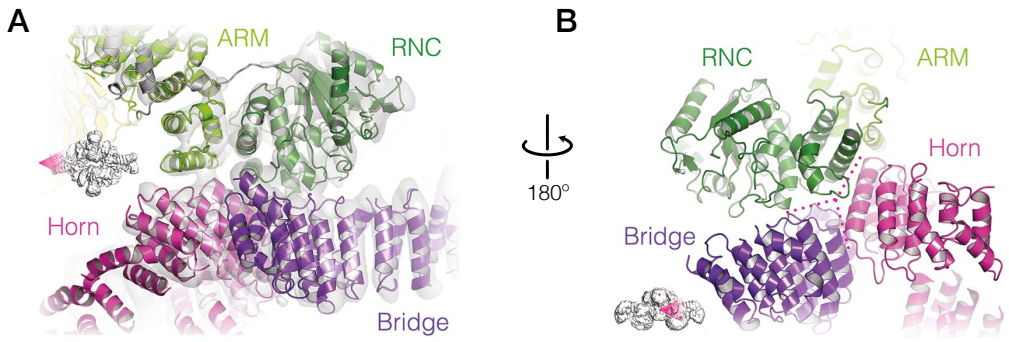

Figure 2.5 Raptor binds to and organizes the N terminus of mTOR through a horn-bridge-armadillo a-solenoid stack

A The complete interaction is shown with the reconstructed density, filtered to its global resolution (5.9 Å) and contoured at 6σ, indicated as a translucent surface; the corresponding model is shown as a secondary structural cartoon. **B** The antiparallel a-solenoid stack is shown as a secondary structural cartoon; the image generated with the point of view rotated as indicated and the threefold interaction surface are shown with dotted magenta lines.

2.3.7 Implications of mTORC1 for substrate selectivity and delivery

The structure of the C-terminal mTOR fragment revealed that the kinase domain is held in a catalytically active conformation by the surrounding FAT domain and segments inserted within the kinase domain itself[19]. The FRB domain and mLST8 limit access to the adenosine 5′-triphosphate (ATP)–binding cleft, preventing activity toward noncognate substrates, which would otherwise be problematic for a constitutively active enzyme. In our assembled complex, access to the active site is further restricted by Raptor. Whereas the FRB domain and mLST8 narrow the active-site cleft from the N- and C-lobe sites, respectively, the RNC domain additionally restricts access from the solvent-exposed surface below the FRB domain. This results in the enclosure of the active-site cleft from all directions, reducing its width to ~20 Å (Figure 2.6).

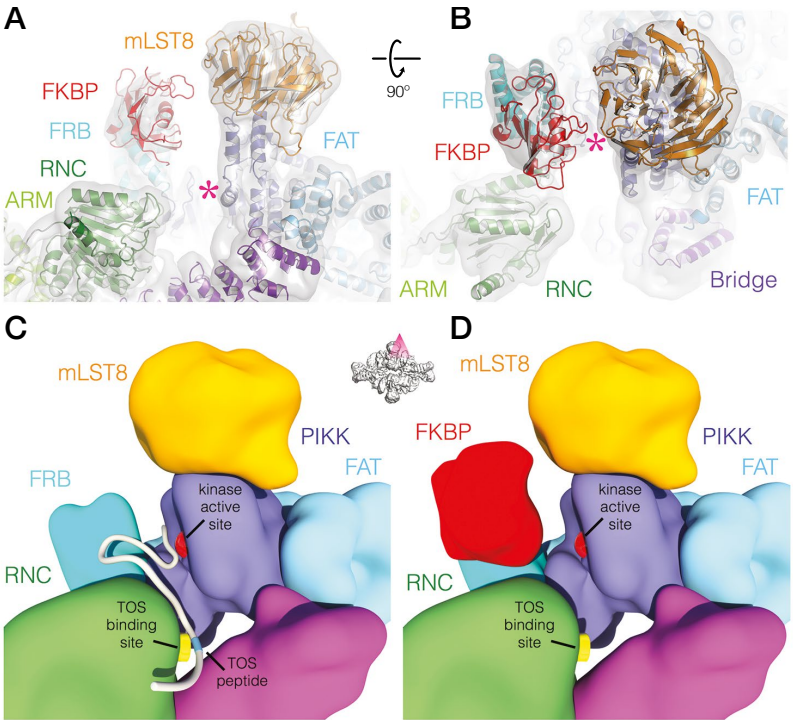

Figure 2.6 The RNC domain of Raptor is positioned adjacent to the FRB domain of mTOR, complementing the active-site cleft of the kinase domain
A,B View into the active-site cleft of one half of an mTORC1 dimer. The reconstructed density, filtered to its global resolution (5.9 Å) and contoured at 3σ, is indicated as a translucent surface, and the corresponding model is shown in cartoon representation. The active site is indicated with a magenta asterisk. Panel (B) is shown with the perspective rotated, as indicated. **C,D** Schematic illustrating the proposed mode of substrate (gray) binding and delivery to the mTOR active site.

Raptor directly interacts with substrate proteins through their TOS motifs, FDIDL in S6K[66] and FEMDI in 4EBP1[64], which include a conserved aspartate at position four. Given the structural similarity between the RNC domain and CASPases, which recognize four-residue sequences with an aspartate at position four, equivalent residues in CASPase and Raptor may function in substrate recognition (Figure 2.6C,D). The corresponding site is located directly within the mTORC1 active-site cleft, ~50 Å from the kinase center and optimally positioned for recruitment and delivery of subtrate to the active site (Figure 2.6). Considering that the peripheral Raptor b propeller has been proposed to bind proteins involved in regulating mTORC1, it is possible that this regulation occurs via the peptide stretch connecting the b propeller to the RNC domain of Raptor.

Our cryo-EM maps of mTORC1 reveal additional density next to the FRB domain (Figure 2.6). This density represents a copurified complex of Spodoptera frugiperda FKBP (SfFKBP) and rapamycin, which was used to enhance mTORC1 expression. SfFKBP shares 78% identity to human FKBP12, and its presence in purified mTORC1 was confirmed by mass spectrometry. The FKBP-rapamycin density further reduces the active-site cleft to ~10 Å. It also lies between the RNC domain and the active site, supporting steric hindrance as the mechanism by which rapamycin may inhibit mTOR toward certain substrates, but not others[71] (Figure 2.6B). Although it has been proposed that FKBP-rapamycin binding compromises mTORC1 stability, possibly by displacing Raptor[77], we do not observe this effect. Furthermore, the FRB domain that binds FKBP-rapamycin[18,148] is not near the dimerization interface; nor does it contact the RNC domain, making it unlikely that the binding of FKBP-rapamycin would destabilize mTORC1 by steric hindrance (Figure 2.6B).

2.3.8 Implications for mTORC2 and other kinases

The architecture of mTORC1 provides a structural basis for studying mTORC1 function. Given the similar overall appearance of our structure and that of TORC2[150,152], we anticipate that the architecture of mTORC1 might be conserved in parts of mTORC2. In particular, we anticipate that the mode of dimerization, in which a complete dimer is formed through mTOR-mTOR contacts alone, will be conserved. An interaction of Rictor in mTORC2 with the bridge and horn HEAT domains, similar to that of Raptor in mTORC1, could stabilize the N terminus of mTOR and facilitate mTORC2 dimerization. Raptor forms this interaction through its armadillo repeat

domain; a large domain of Rictor is also predicted to form an α-helical solenoid. Other members of the PIKK kinase family, including ATM, require accessory proteins that interact with HEAT repeats and are thought to dimerize in vivo. Although the N-terminal HEAT-repeat domains of the family are their least conserved parts, it appears possible, given the residual sequence similarity, that PIKK family members may have common modes of interaction[11].

2.4 Experimental Procedures

2.4.1 Laboratory materials

Unless otherwise stipulated, chromatography equipment was provided by GE Healthcare (Schenectady, USA), chemicals were provided by Sigma Aldrich (St. Louis, USA), electron microscopy consumables were provided by Agar Scientific (Stansted, UK), and molecular graphics were generated using Chimera [153] and PyMol (Schrödinger LLC, New York, USA).

2.4.2 Expression and purification of mTORC1

Human mTORC1 was produced using the "MultiBac" baculovirus expression system (Geneva Biotech, Geneva, Switzerland) according to the protocol of Fitzgerald and colleagues[154], using strains and media procured from "Expression Systems" (Davis, USA) and "Lonza" (Basel, Switzerland), respectively. Briefly, a fusion vector containing mTORC1 (pAB2G-mTOR, pIDK-His10-myc-flag-Raptor, pIDC-mLST8) was generated in vitro using Cre recombinase and then recombined, within EmBacY cells, with a bacmid containing the baculovirus genome. The presence of each mTORC1 subunit within the purified bacmid was verified by PCR, and baculovirus virions expressing mTORC1 were generated for large-scale infection of Sf21 cells in serum-free medium supplemented with glutamine and 2.5 μM rapamycin. mTORC1 was expressed for 120 hours prior to sonication of the cells in lysis buffer (250 mM NaCl, 50 mM NaBicine pH 8.0, 5 mM MgCl2). The lysate was cleared by centrifugation at 142 500 g and then incubated overnight with anti-flag agarose beads (GenScript, Piscataway, USA). After washing with lysis buffer, mTORC1 was eluted with flag-peptide (0.1 mg/mL), concentrated to 0.5 mL and applied to a tandem Superose 6 "Increase" gel filtration column equilibrated into 150 mM NaCl, 10 mM NaBicine, 1 mM TCEP (Supplemental Figure 2.1).

2.4.3 Multi-angle laser light scattering (MALLS)

Determination of the absolute molecular weight of mTORC1 was performed using MALLS. Purified mTORC1 was fractionated in the indicated buffer (Supplemental Figure 2.1B) using an analytical Superose 6 10/300 GL size exclusion column (0.2 mL/min) coupled directly to a miniDAWN Treos instrument (Wyatt Technologies, Goleta, USA). Protein concentration in the eluting peaks was determined in-line through measurements of the refractive index (ΔRI optiLab REX - Wyatt Technologies, Goleta, USA).

2.4.4 Kinase activity assay

In vitro kinase activity assays were performed in 50 mM KCl, 25 mM K-HEPES pH 7.4, 5 mM MgCl2 and 5 mM MnCl2 using 4EPB1 (Stratagene, La Jolla, USA) as a substrate (Supplemental Figure 2.1C). Purified mTORC1 (0.4 µg/µL, final concentrations are indicated throughout) was mixed with 4EBP1 (0.08 µg/µL) in a 50 µL reaction. Reactions were initiated by the addition of ATP (50 µM), incubated for 30 min at 37 °C, terminated through the addition of 12.5 µL 5x SDS-PAGE sample buffer and analysed by Western blot using antibodies to 4EBP (1:1000 dilution #9 452, Cell Signaling Technologies, Beverly, USA) and phospho-4EBP (1:1000 dilution #2 855, Cell Signaling Technologies, Beverly, USA). When assays were performed in the presence of Torin1 (20 µM) or rapamycin/FKBP12 (20 µM), mTORC1 was pre-incubated with the respective inhibitor for 5 min on ice prior to the addition of 4EBP1 and ATP.

2.4.5 Generation of an initial reference EM density

A sample of mTORC1 was crosslinked in 0.1% (v/v) glutaraldehyde at 0.07 mg/ml in 150 mM NaCl, 10 mM NaBicine, 1 mM TCEP for 15 min on ice. The crosslinked sample was applied to a carbon coated holey carbon grid and stained with 2% (w/v) uranyl acetate. The grid was imaged in an FEI F20 electron microscope (FEI Company, Hillsboro, USA) with 82 000 magnification at 200 kV acceleration voltage. Micrographs were acquired with a total dose of 20 e/A2 and at an applied defocus of between -0.9 and -1.7 µm. From 16 micrographs 2 544 single particle images were selected semi-automatically using BOXER [155] after manually marking representative particles in each

micrograph. The CTF was determined with CTFFIND3[156], images were binned four-fold, and extracted using RELION[157]. The images were classified into 50 classes in two dimensions using RELION and eight well-defined classes (53%) selected for initial three-dimensional reconstruction. Initial models were created using the e2initialmodel.py function in EMAN 2.1 applying C2 symmetry[155]. A 3D model, which showed a good agreement with the 2D class images, was filtered to 60 Å and used as an initial reference in a RELION reconstruction. The resulting initial model (resolution 31 Å, semi-independent half set FSC) was used for further cryo-EM refinement.

2.4.6 Cryo-EM sample preparation and cross-linking

Purified mTORC1 was applied to a 5 – 30 % (w/w) sucrose gradient in 100 mM NaCl, 50 mM NaBicine pH 8.0, 1 mM TCEP, the higher sucrose concentration buffer of which had been supplemented with 0.125 % glutaraldehyde (Grade I). Samples were subjected to ultracentrifugation for 14 hours at 100 000 · g in an SW32 rotor, and recovered by gradient fractionation. The recovered peak was quenched through the addition of NH4Cl to a final concentration of 50 mM, and then concentrated to 100 nM in 100 kDa cutoff Vivaspin concentrators. The buffer was further exchanged three times with 100 mM NaCl, 10 mM NaBicine pH 8.0, 1 mM TCEP in order to minimise the amount of residual sucrose in the final sample.

2.4.7 Cryo-EM data collection

Samples of mTORC1 (4 µL) were applied to holey carbon copper grids (R 2/2 – Quantifoil) bearing an additional fine film of carbon. Grids were blotted for three seconds and then plunged directly into a mixture of liquid ethane (33%) and propane (67%) mixture using a vitrobot mark 1 (FEI Company, Hillsboro, USA) at 6 ºC and 100% humidity. Data were then recorded semi-automatically using EPU on a Titan Krios transmission electron microscope equipped with a Falcon II direct electron detector (FEI Company, Hillsboro, USA) at 300 kV, 100 719-fold magnification and at an applied defocus of between -2.0 and -4.0 µm, resulting in 6 299 images of 4 096 by 4 096 pixels with a pixel size of 1.39 Å on the object scale. Each image was recorded as seven separate frames, comprising a total exposure of 25 electrons/Å2, which were subsequently aligned and summed using DOSEFGPUDRIFTCORR [158] to obtain a final image.

2.4.8 Cryo-EM data processing and refinement

Poor quality micrographs were rejected by eye, based on the extent and regularity of the Thon rings observed in the contrast transfer function (Supplemental Figure 2.3A,B). Estimation of the contrast transfer function was carried out for each image using CTFFIND3[156], particles were selected using boxer[155], and refinement thereafter performed using RELION[157]. Two-dimensional reference-free alignment of 569 086 boxed particles into 100 classes was performed initially using images binned four-fold; particles that did not yield high-resolution class averages were excluded from further refinement. Three-dimensional classification into 8 classes was then performed with RELION using the 50 Å low-pass filtered initial reference, yielding 309 792 high-quality mTORC1 particles after a single class with reduced Raptor occupancy had been excluded. These particles were then refined using full-sized images in a "gold-standard" refinement resulting in a density map with an estimated resolution of 6.1 Å without masking away more weakly resolved regions. Further refinement within a tight mask of the core regions with a Gaussian falloff, generated by thresholding the density at 6 σ, yielded a reconstruction with an estimated resolution of 5.9 Å at a Fourier shell correlation of 0.143[157].

2.4.9 Cloning, expression and purification of CtRaptor

CtRaptor (accession number: G0S1S2) was cloned from genomic DNA into pAceBac2 with a N-terminal His10-tag and TEV protease cleavage site. Baculovirus was generated in Sf9 cells (VWR, Radnor, USA) using the MultiBac expression system (Geneva Biotech, Geneva, Switzerland) according to manufacturer's protocols. Expression cultures were infected with a virus dilution of 1:100 (v/v) and typically harvested after 68 hours. The protein was purified using High Affinity Nickel Charged Resin (Genscript, Piscataway, USA). The N-terminal tag was removed by incubation with tobacco etch virus protease and rebinding to High Affinity Nickel Charged Resin. The protein was then applied to a size-exclusion chromatography column (HiLoad 16/600 Superdex 200 pg). Peak fractions were concentrated to 10 mg mL-1 for crystallisation.

2.4.10 Crystallization and structure determination of CtRaptor

Full-length CtRaptor was set for crystallisation using the sitting-drop vapour diffusion method. Extensive screening did not yield any crystal hits. The protein was therefore

proteolytically digested by incubating 1 µg Thermolysin (Proti-Ace 2, Hampton Research) per mg of CtRaptor in 50 mM HEPES pH 8.0, 150 mM NaCl, 1 mM CaCl2 and 2 mM TCEP prior the size-exclusion chromatography. Initial crystals grew in drops containing precipitant solution (0.1 M Bis-Tris pH 5.5, 3 M NaCl) in 1:1 (v/v) ratio at 19 °C. After several rounds of optimization, 3-dimensional crystals were grown in drops containing precipitant solution (0.1 M Bis-Tris pH 5.2-5.3, 2.6 M NaCl) in 1:1 (v/v) ratio at 30 °C. In order to obtain phase information, crystals were derivatised with 5 mM of ethylmercury-donating Thimerosal for 3 minutes, back- soaked, cryoprotected by addition of ethylene glycol to 25% (v/v) and directly flash- frozen in liquid nitrogen. X-Ray diffraction data were collected at beamlines X06SA (PXI) and X06DA (PXIII) with a PILATUS 6M and PILATUS 2M detector, respectively, and raw data were processed using XDS[159]. Initial crystals belonged to space group P41212 with unit cell parameters of a=b=195 Å, c=291 Å, and diffracted to approximately 6 Å resolution. Eleven to thirteen mercury positions were located in a mercury derivative dataset to 5.8 Å resolution using SHELXC/D[160] via the HKL2MAP interface[161]. Density modification led to an electron density map that allowed building an initial model by rigid-body docking of helical repeats and a template β-propeller. MR-SAD phasing using PHASER[162] employing the initial model resulted in a figure of merit of 0.586 for 19 Hg sites. Post-crystallization treatment using high concentrations of malonate resulted in crystal dehydration and led to crystals that still belonged to space group P41212, but with unit cell parameters of a=b=184 Å, c=273 Å, diffracting to better than 4.5 Å resolution. Multi-crystal and NCS-averaging between the original 5.8 Å resolution Hg-derivative set and a 4.3 Å resolution native dataset in the dehydrated crystal form, each containing two molecules per asymmetric unit, lead to excellent electron density maps with clearly recognizable secondary structure elements and mostly connected peptide backbone. This experimentally phased electron density map was interpreted by tracing with poly-alanine guided by predicted secondary and domain structure in O and Coot[163]. Assignment of the blades of the β-propeller was obtained by comparing the location of anomalous mercury sites with the location of cysteine residues, the preferentially derivatised sites, in a homology model. The limited resolution precludes modeling of side chains and side chain-based register assignment. Using an MLHL target to incorporate phase information and hydrogen bond restraints in addition to Ramachandran restraints to stabilise main-chain conformation, our final poly-alanine model refines against experimental data at 4.3 Å to Rwork/Rfree of 0.37/0.39. This value is in the expected range for a correct model lacking side chain atoms beyond

the β-carbon position. The number of Ramachandran outliers increases from 0.2% to 2.8% when no Ramachandran restraints are applied, which is still in a reasonable range

2.4.11 Docking and modeling into the cryo-EM map

Given the availability of a high-quality crystal structure of mTOR/mLST8 (PDB ID 4JSN: chains B and D), which fitted very cleanly into the correct hand of the density (Supplemental Figure 2.3), we docked this component first; mLST8 and residues 1 442 to 1 609 of mTOR exhibited slightly different conformations from those resolved in the crystal structure and their fit was therefore optimised separately. The crystal structure of CtRaptor was docked similarly with minimal adjustment. Consensus homology models were then prepared with PHYRE[164] for mTOR residues 1 to 1 375, which have been pruned of loops and deposited as UNK residues. Initial rigid-body fitting of all models was carried out using UCSF Chimera[153], and the models then readjusted to the observed secondary structure using COOT[163]. To correct the geometry of the final models and to remove steric clashes, the model was subjected to 300 iterations of geometry and B-factor minimisation using PHENIX.refine[165], during which secondary structural and Ramachandran restraints were applied. After minimisation, the cross-resolution between the reconstruction and the model was 7.1 Å (Fourier shell correlation cut-off = 0.5).

2.4.12 Assignment of proposed mTOR HEAT repeat topology

Two sources of prior primary information on PIKK HEAT repeat topology are available. The density making up the bridge region directly joins the FAT domain, while the known structure of DNA-PKcs[166] exhibits a very similar topology within the corresponding bridge (denoted forehead in the study[166]) adjacent the FAT domain, implying that the FAT-HEAT linkage is conserved. A cross-linking mass spectrometry study of TORC2[33] identified “intra-links” between N-terminal residues of the HEAT repeat domain and the parts of the FAT and PIKK domains adjacent the horn. If one assumes that the N-terminus of the horn represents the N-terminus of mTOR, further “intra-links” to the FAT domain from the HEAT repeat domain could also be satisfied. There are sufficient residues (~30) within many HEAT-repeat loops to bridge a large distance (>100 Å if completely extended), however loops do not typically cover such large distances, and therefore smaller distances are considered more parsimonious.

The terminus of the bridge region is within ~40 Å of that of the disordered end of the horn density through clear space, but ~70 Å from the end abutting the adjacent mTOR FAT domain through two regions of density, and over 100 Å from any other plausible terminus. In the absence of large insertions within the two HEAT-repeat domains, we conclude that other topologies are highly unlikely, but cannot be formally excluded without higher resolution data.

2.4.13 Accession numbers

The cryo-EM density maps representing mTORC1 have been deposited in the EM Databank as EMD-3212 and EMD-3213 and the corresponding model in the Protein Data Bank as PDB ID 5FLC. The crystal structure of CtRaptor has been deposited in the Protein Data Bank as PDB ID 5EF5.

2.4.14 Acknowledgements

We thank the ETH Zürich Scientific Center for Optical and Electron Microscopy (ScopeM) for access to EM facilities, P. Tittmann for technical support, T. Sharpe for size exclusion chromatography multi-angle laser light scattering analysis, the Biozentrum Proteomics Core Facility for mass spectrometric protein identification, the beamline staff at Swiss Light Source beamlines X06SA and X06DA for crystallographic support, and H. S. T. Bukhari for 3D modelling in Maya. C.H.S.A. was supported by an ETH Zürich postdoctoral fellowship and a European Molecular Biology Organization long-term fellowship. E.S. was supported by a fellowship from the People Program (Marie Curie Actions; REA grant agreement number 328159). This work was supported by the European Research Council funding to M.N.H. and N.B., and by the Swiss National Science Foundation via the National Centre of Excellence in RNA and Disease, project funding 138262 and R'Equip 145023.

2.4.15 Author contributions

SI and ES cloned constructs and purified proteins. CHSA, DB and ES prepared samples and grids, collected electron micrographs and calculated reconstructions. SI and TM collected diffraction data and solved crystal structures. CHSA, NB, MNH, SI, TM and ES interpreted structures and wrote the manuscript.

2.5 Supplemental information

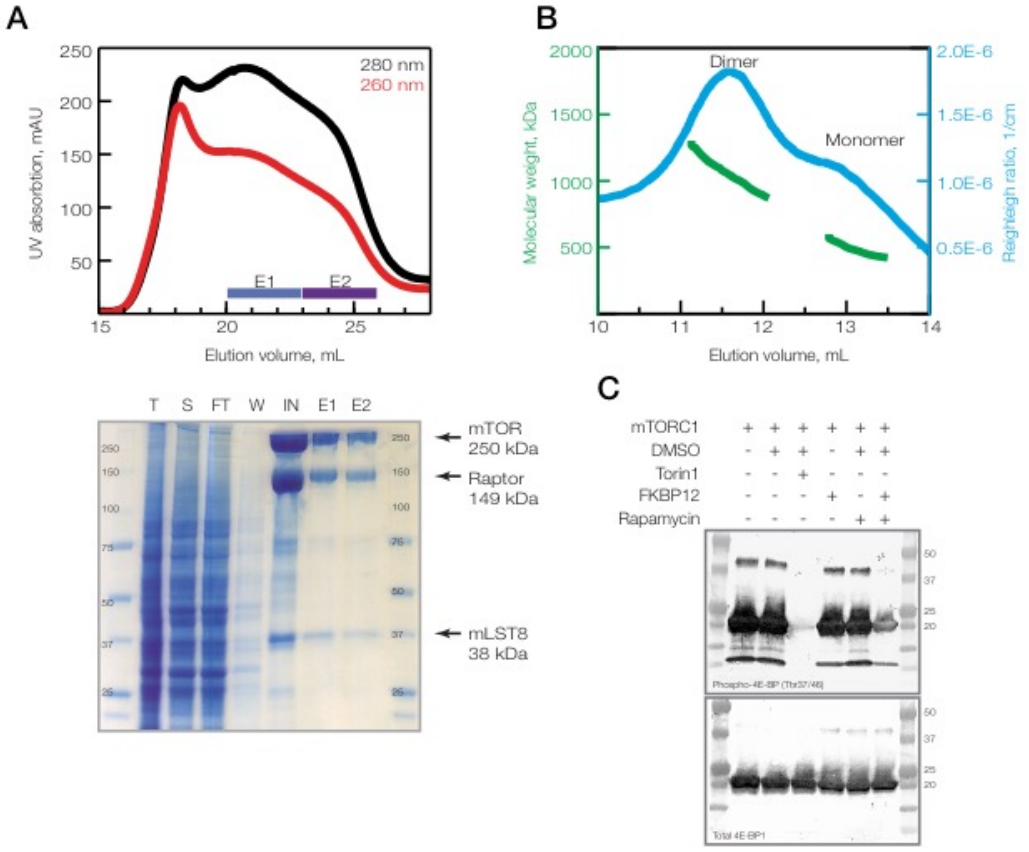

Supplemental Figure 2.1 Purification and biophysical characterisation of mTORC1.

A Size exclusion chromatography (SEC) elution profile of mTORC1 from a tandem-Superose 6 Increase 10/300 GL column at 0.1 mL/min. The lower panel shows an SDS-polyacrylamide gel of the purification process: T, total fraction; S, soluble fraction; W, wash fraction; IN, SEC input. Elution fractions E1 and E2 contained mTORC1 and were used for subsequent experiments. **B** Molecular weight determination by multi-angle laser light scattering (MALLS, Superose 6 10/300 GL, 0.2 mL/min). The elution profile shows the molecular weight (left axis) and the scattering intensity (Rayleigh ratio) at the 90° detector (right axis). mTORC1 elution peaks are visible corresponding to both dimeric (1047 kDa ± 5%) and monomeric (483 kDa ± 5%) species. **C** Kinase activity assay of purified mTORC1 (expressed in the absence of rapamycin) using 4EBP1 as a substrate. Western blots (top panel: anti-phospho-4EBP, bottom panel: anti-total-4EBP) show the phosphorylation state of 4EBP1 after incubation with mTORC1 in presence of the indicated mTORC1 inhibitors.

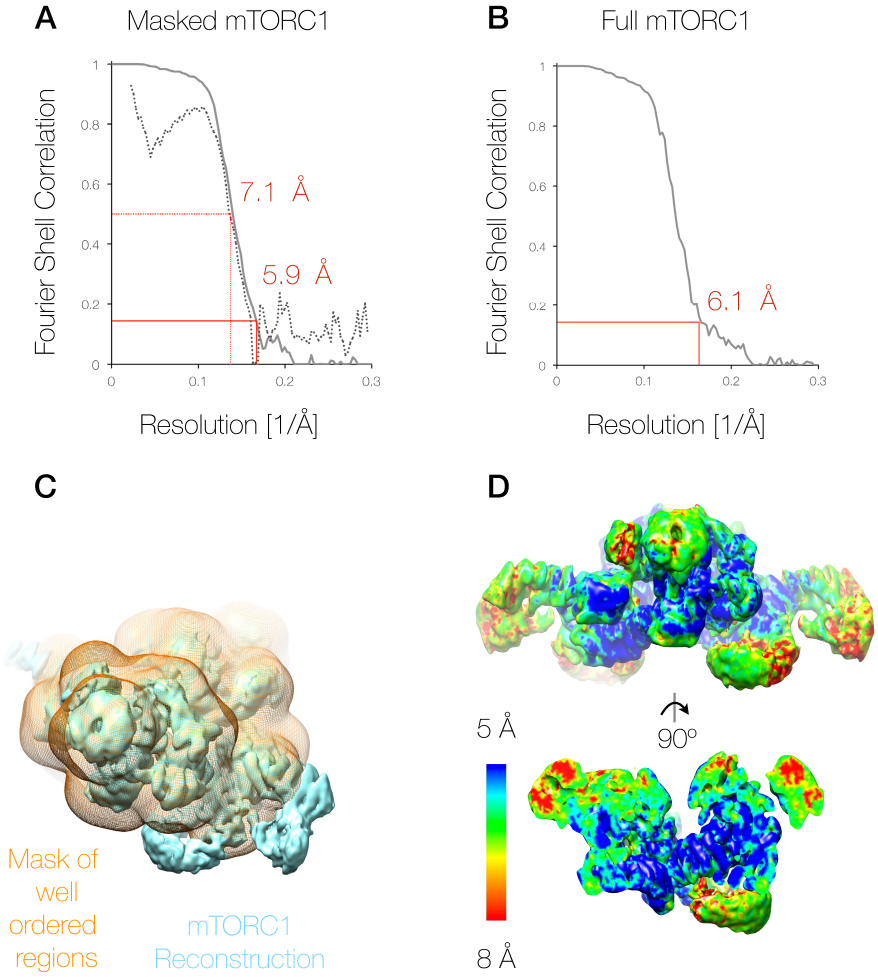

Supplemental Figure 2.2 Local and global resolution statistics for mTORC1.
A, B Fourier shell correlation for tightly masked and full mTORC1 reconstruction calculated between two independently refined half sets; resolution cut-off indicated by the red line. The "gold-standard" Fourier shell correlation was determined, and resolution estimated, according to the method of S. Scheres[157]. The cross- Fourier shell correlation between the proposed mTORC1 model and the map is shown with dotted lines in A. **C** The mask of the mTORC1 well- ordered core regions is shown superimposed on the density corresponding to the full mTORC1 reconstruction. **D** The surface and a 90o rotated internal slice through the mTORC1 density, low-pass filtered to the global resolution (5.9 Å) and contoured at 3 σ, are shown coloured according to local resolution (5 Å in blue through to 8 Å in red). Local resolution was estimated using the methodology of Kucukelbir and colleagues: ResMap[167].

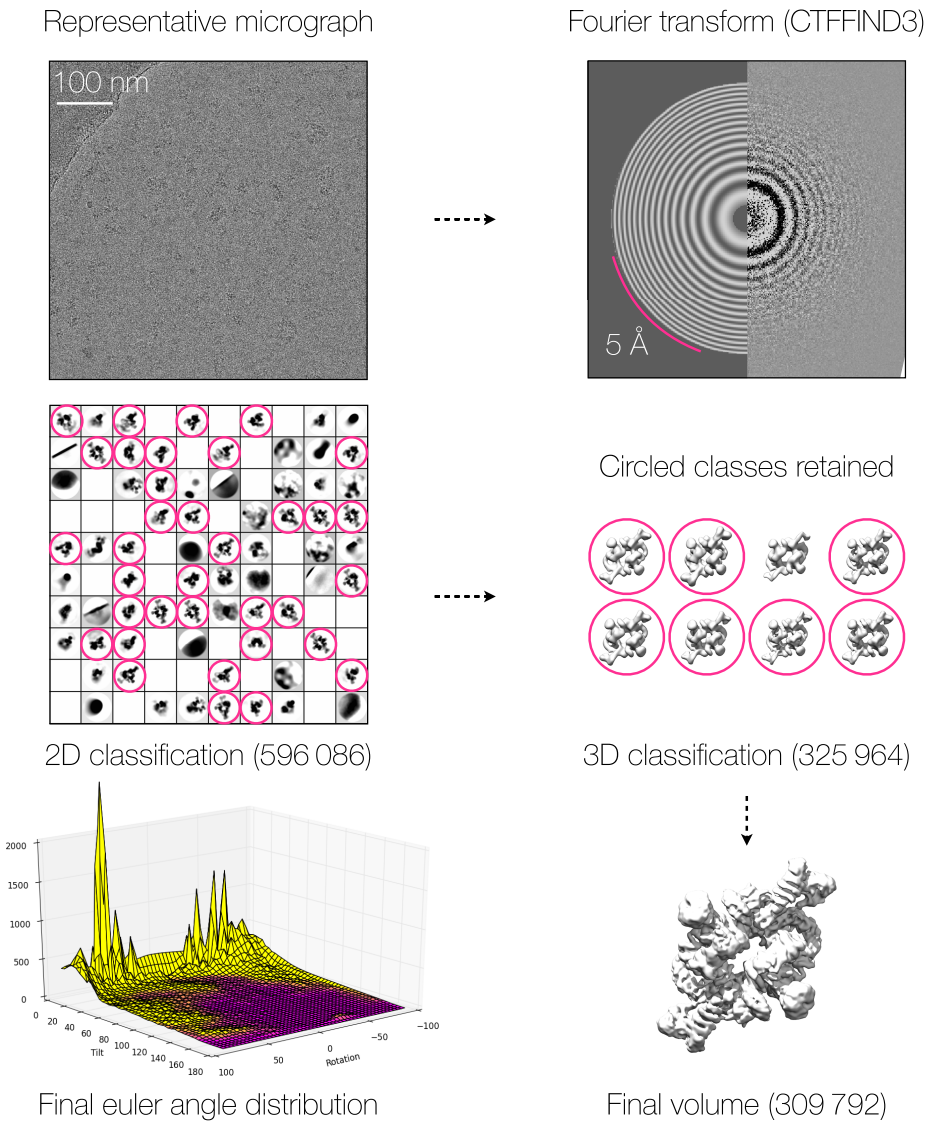

Supplemental Figure 2.3 Cryo-EM studies of mTORC1.
A sample micrograph and matched Fourier transform, the two or three-dimensional reconstructions output from each round of classification, the number of particles involved in each classification and the flow of particles between stages of the classification are shown. Magenta circles indicate the classes from which particles were retained for further classification at each stage. A three-dimensional plot of the final calculated Euler angles for all particles is shown alongside the final volume, purple indicates areas with low signal, whereas yellow indicates areas with more than 50 particles per orientation, which therefore contribute substantially to the structure. Preferential orientation is clearly visible as several large peaks near to the origin, however the spread is sufficient for three-dimensional information to be gleaned.

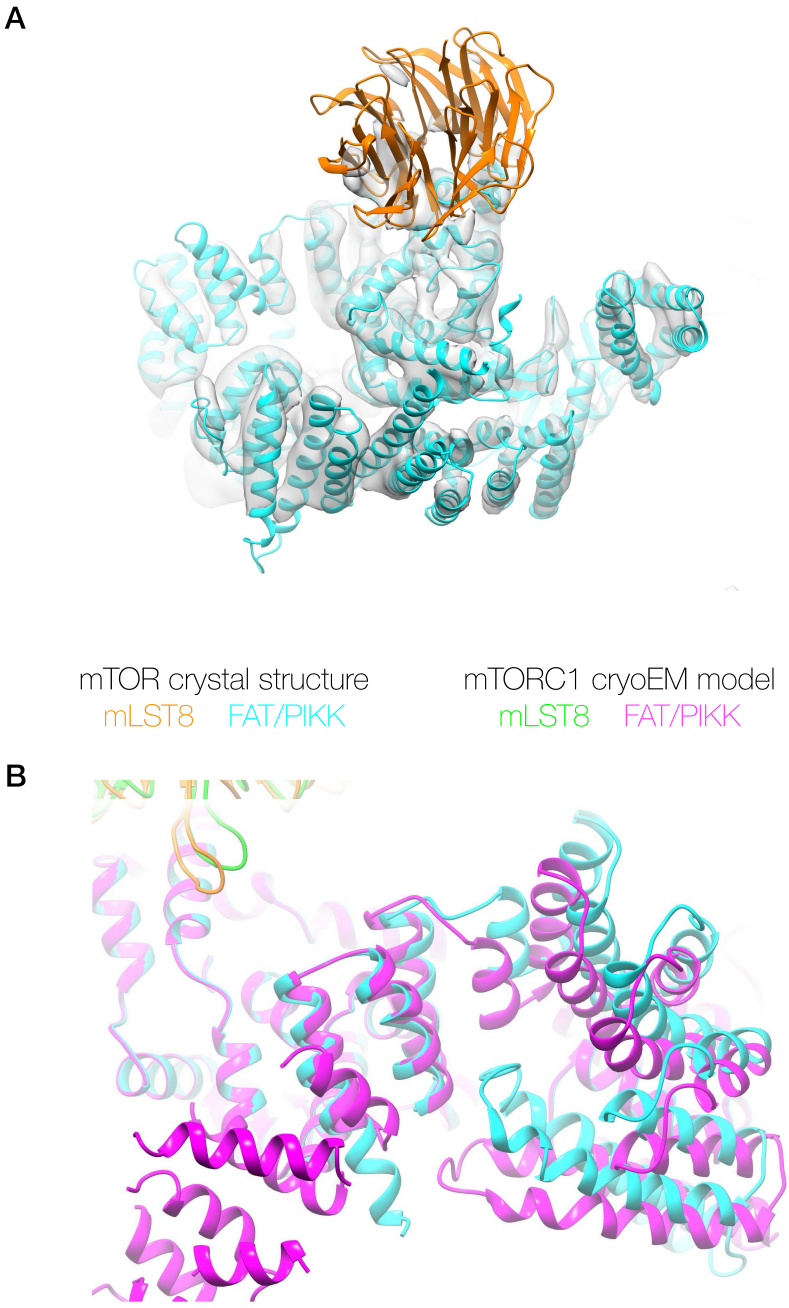

Supplemental Figure 2.4 Confirmation of the handedness of the final reconstruction. **A** The fit of the crystal structure of a C-terminal fragment of mTOR (PDB ID 4JSN chains B and D) into the reconstructed mTORC1 density is shown without adjustments, confirming the handedness of the complex. **B** The initial fit from panel B is shown compared to that of the final, refitted, model – highlighting the movement of the FAT domain on dimerisation.

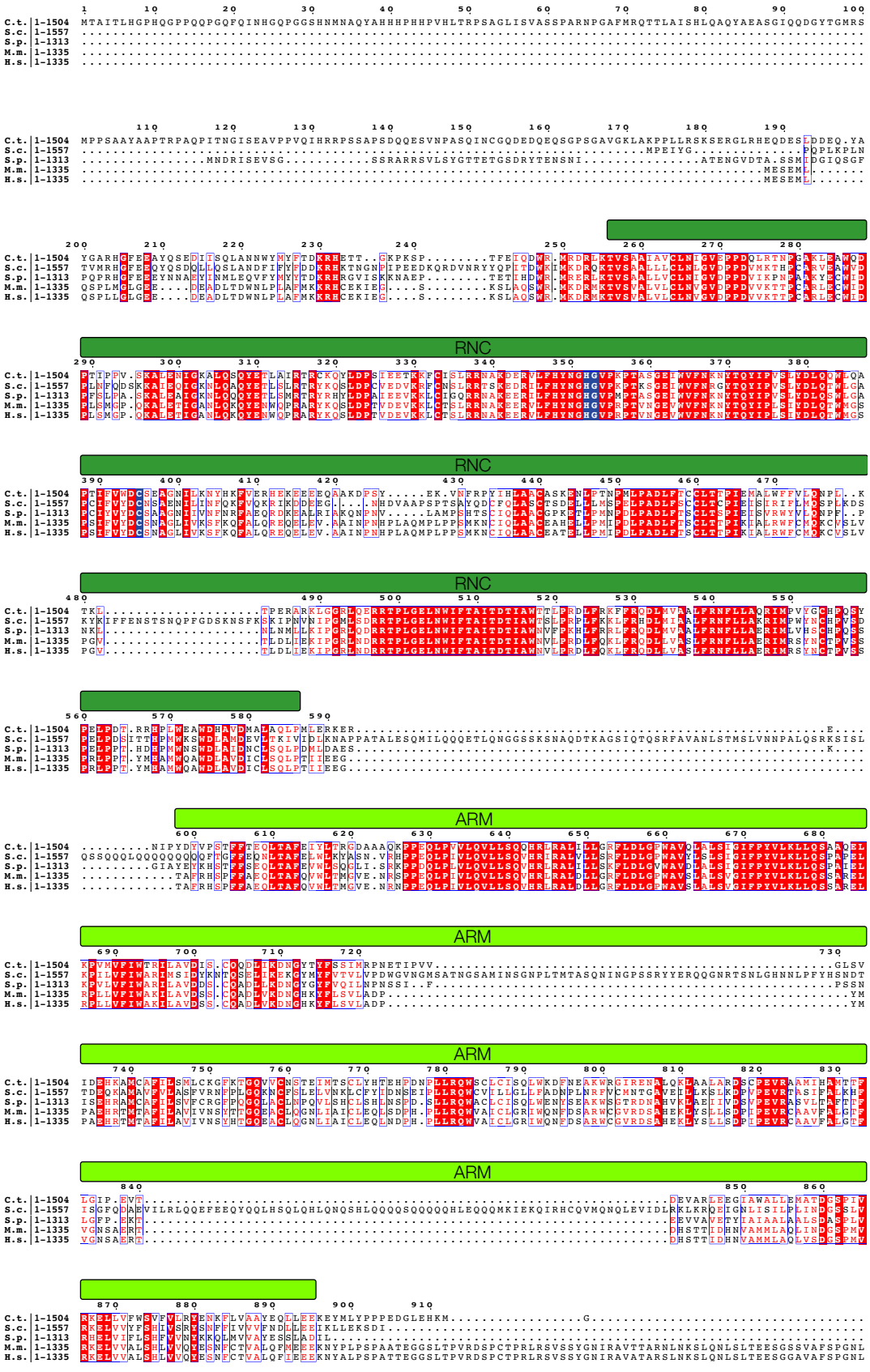
RNC
RNC
RNC
ARM
ARM
ARM
ARM

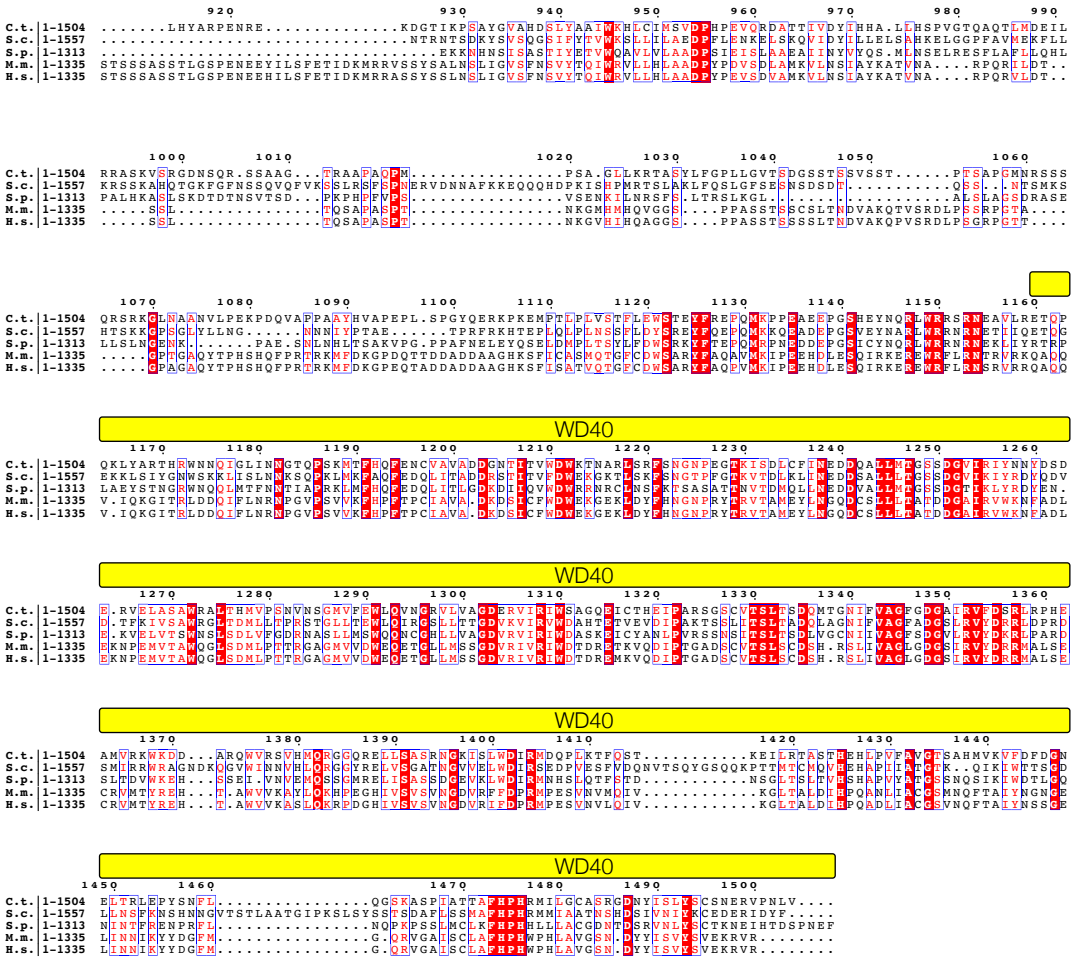

Supplemental Figure 2.5 Sequence conservation of Raptor.
Multiple sequence alignment of Raptor from selected species. Invariant residues are shown in red boxes and highly conserved residues (> 70%) in red font. Residues conserved between the Raptor family and the active site of CASPases are highlighted in blue boxes. Sequences were retrieved from the UniProt database: C.t., *Chaetomium thermophilum* (G0S1S2); S.c., *Saccharomyces cerevisiae* (P38873); S.p., *Schizosaccharomyces pombe* (P87141); M.m. *Mus musculus* (Q8K4Q0); H.s., *Homo sapiens* (Q8N122). Alignments were generated using Clustal-Omega and are represented with ESPript 3.0.

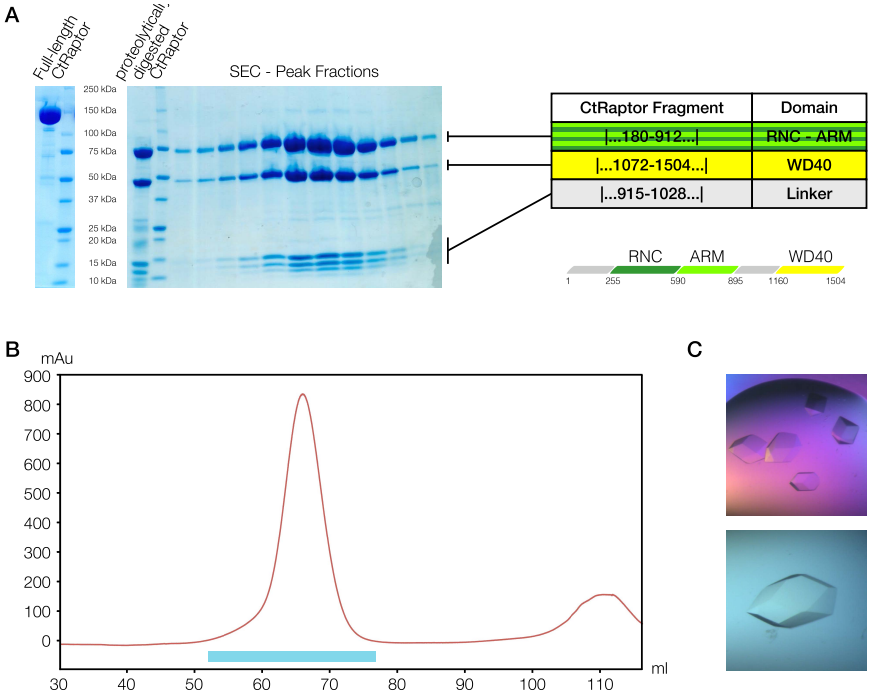

Supplemental Figure 2.6 Purification and crystallisation of CtRaptor.
A SDS poly-acrylamide gel electrophoresis of purified full-length CtRaptor (left). Input and peak fractions from size-exclusion chromatography (SEC) of proteolytically digested CtRaptor (right). Several smaller fragments are retained and co-elute with the major CtRaptor fragments in SEC. The minimal fragment sizes as determined by mass spectrometric peptide mapping and the domain assignments of fragments are listed in the table. No peptides from the non- conserved N-terminal 180 residues were identified, indicating that those fragments do not stably associate with the CtRaptor core. **B** Elution profile of proteolytically digested CtRaptor on SEC. Multiple cleaved protein fragments elute as a single, monodisperse peak with a retention volume of 66 mL, corresponding to an estimated molecular weight of 150 kDa. **C** Crystals of CtRaptor grown to 150-250 µm in size.

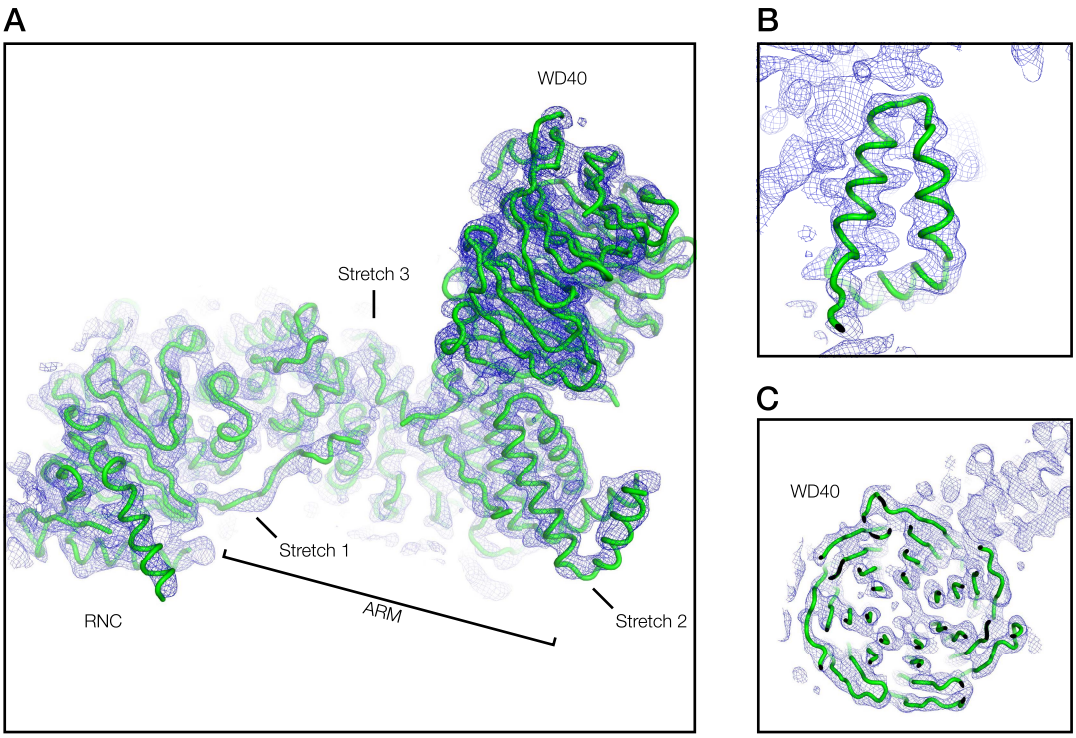

Supplemental Figure 2.7 Crystallographic maps of CtRaptor are of high quality. Electron density maps were obtained by multi-crystal and non-crystallographic symmetry averaging based on experimental mercury-derivative phasing as described in the methods section. **A** Overview of a complete Raptor chain. **B** Expanded view of an ARM repeat region of Raptor. **C** Slice through the density of the β-propeller region. All maps are contoured at 1.0 sigma level. In B and C only partial models are shown for clarity.

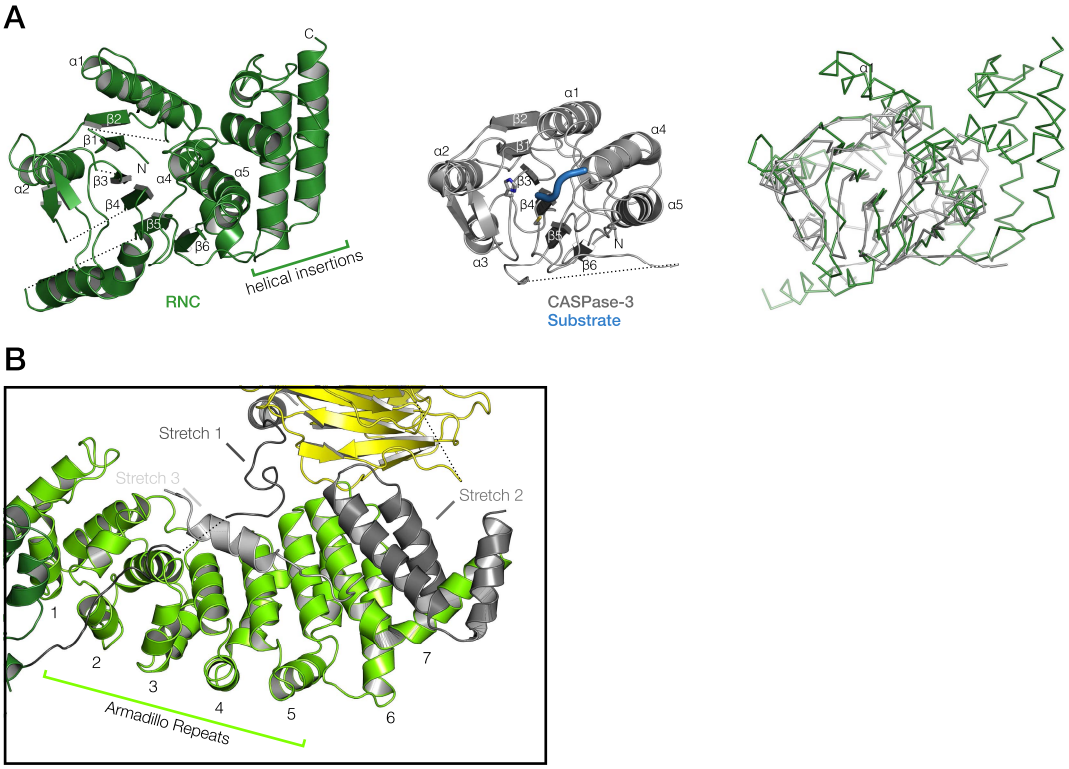

Supplemental Figure 2.8 Structural analysis of the CtRaptor RNC and armadillo domains.

A The RNC domain of CtRaptor is structurally homologous to members of the CASPase family (CASPase-3, PDB ID 1CP3, r.m.s.d. = 2.2 Å, 126 Cα; CASPase-6, PDB ID 3K7E, r.m.s.d. = 2.8 Å, 119 Cα; CASPase-7, PDB ID 1F1J, r.m.s.d. = 2.3 Å, 127 Cα; CASPase-9, PDB ID 2AR9, r.m.s.d. = 2.4 Å, 128 Cα). Left: Cartoon representation of the CtRaptor RNC domain (green). Middle: Cartoon representation of CASPase-3 (grey) in an identical orientation. Catalytic residues C163 and H121 are shown as sticks and a substrate peptide in blue. Right: structural superposition of the two domains in ribbon representation. **B** Assignment of armadillo repeat domains in CtRaptor.

Supplemental Table 2.1 Crystallographic statistics for CtRaptor structure determination.

	Hg-derivative	**Native**
Data Collection		
Space group	$P4_12_12$	$P4_12_12$
Unit cell axes a, c (Å)	194.6, 291.1	183.8, 272.1
Wavelength (Å)	1.00003	0.99188
Resolution range (Å)	48.4-5.8 (5.90-5.80)	50.0-4.3 (4.37-4.30)
Unique reflections	29272 (1423)* †	32407 (1601)
Completeness (%)	99.2 (97.3)	99.6 (99.7)
Redundancy	3.9 (3.8)* †	5.7 (5.8)
Mosaicity (º)	0.123	0.366
R_{merge} (%)	6.5 (146.7)* †	15.1 (127.1)
R_{pim} (%)	3.7 (84.7)* †	6.8 (57.3)
I/σI	14.8 (1.0)*	9.1 (1.5)
CC1/2 (%)	100 (31.3)*	99.7 (61.2)
Phasing		
Anomalous Correlation (%)	42%	
Number of Hg-sites	19	
Figure-of-merit (MR-SAD phasing)	0.59	
Refinement (poly-alanine model)		
Number of alanine residues		2033
Resolution range (Å)		49.0-4.3
R_{work}/R_{free}		0.37/0.39#
Average atomic B-Factor		78.7
Rms deviations:		
bonds (Å)		1.07
angles (°)		0.005
Ramachandran plot:		
favored (%)		94.9§
allowed (%)		4.9§
disallowed (%)		0.2§

*The values recorded in parentheses are those for the highest resolution shell

†Friedel mates treated separately

#The values are in the expected range for a correct model lacking side chain atoms beyond the β-carbon position

§After refinement with PHENIX.refine using Ramachandran restraints. The number of Ramachandran outliers increases from 0.2% to 2.8% when no Ramachandran restraints are applied.

3 STIL binding to Polo-box 3 of PLK4 regulates centriole duplication

Reproduced from:

STIL binding to Polo-box 3 of PLK4 regulates centriole duplication

Christian Arquint*, Anna-Maria Gabryjonzyk*, **Stefan Imseng***, Raphael Böhm*, Evelyn Sauer, Sebastian Hiller, Erich A. Nigg and Timm Maier

*Authors contributed equally to this work

eLife 2015; 4:e07888
DOI 10.7554/eLife.07888

3.1 Abstract

Polo-like kinases (PLK) are eukaryotic regulators of cell cycle progression, mitosis and cytokinesis; PLK4 is a master regulator of centriole duplication. Here, we demonstrate that the SCL/TAL1 interrupting locus (STIL) protein interacts via its coiled-coil region (STIL-CC) with PLK4 *in vivo*. STIL-CC is the first identified interaction partner of Polo-box 3 (PB3) of PLK4 and also uses a secondary interaction site in the PLK4 L1 region. Structure determination of free PLK4-PB3 and its STIL-CC complex via NMR and crystallography reveals a novel mode of Polo-box-peptide interaction mimicking coiled-coil formation. *In vivo* analysis of structure-guided STIL mutants reveals distinct binding modes to PLK4-PB3 and L1, as well as interplay of STIL oligomerization with PLK4 binding. We suggest that the STIL-CC/PLK4 interaction mediates PLK4 activation as well as stabilization of centriolar PLK4 and plays a key role in centriole duplication.

3.2 Introduction

Centrosomes are the major organizing centers for the microtubule network in animal cells and facilitate many microtubule-dependent cellular processes throughout the cell cycle[168-170]. During interphase, centrosomes contribute to cell shape, motility and polarity; in mitosis, they form the poles of the mitotic spindle and direct chromosome segregation. The core components of centrosomes, the centrioles, also function as basal bodies for the assembly of cilia and flagella. Mutations of centrosomal proteins have been associated with a variety of human diseases, notably ciliopathies, microcephalies and dwarfisms[171,172]. Furthermore, numerical and/or structural centrosome abnormalities have been implicated in carcinogenesis[172-175].

Centrosomes duplicate during S-phase by formation of a procentriole, the daughter centriole, orthogonally arranged to each pre-existing mother centriole[176,177]. The duplication process relies on a set of proteins conserved from *Caenorhabditis elegans* and *Drosophila melanogaster* to humans. The human core components are: the serine/threonine Polo-like kinase PLK4 (ZYG-1 in *C. elegans*), the centrosomal protein Cep192 (SPD-2 in *C. elegans*), the spindle assembly 6 homolog (*C. elegans*) protein SAS-6, the SCL/TAL1 interrupting locus protein STIL (SAS-5 in *C. elegans*) and the centrosome protein CPAP (SAS-4 in *C. elegans*) [170,178-182]. Overexpression of either,

PLK4, SAS-6 or STIL, causes formation of multiple daughter centrioles around a single mother centriole[99,183-187], while depletion of any one of these proteins blocks centriole formation[99,100,183,186-188]. Thus, PLK4, SAS-6 and STIL constitute key centriole duplication factors, the activity and levels of which need to be tightly controlled to maintain the correct centriole number[107,185,189,190]. In addition to these core components, other proteins are also essential for centriole duplication in human cells, this includes notably Cep152[191-193], which cooperates with Cep192 in PLK4 recruitment[111,113,194].

The early phase of centriole biogenesis is marked by the assembly of the cartwheel structure that serves as a scaffold for deposition of centriolar microtubules and confers the characteristic nine-fold symmetry to the centriole[170,195-197]. SAS-6 has been shown to self-assemble into cartwheel-like structures *in vitro,* indicating that it is a central component of the cartwheel[115,116,198,199]. In human cells, SAS-6, STIL and PLK4 localize to the cartwheel region, suggesting a functional interaction of these proteins in cartwheel assembly[183,185,200,201]. Such an interaction is supported by recent evidence demonstrating that PLK4 regulates complex formation between STIL and SAS-6 via phosphorylation of STIL[202-204]. This process depends on two highly conserved regions of STIL: a short coiled-coil motif (STIL-CC, residues 720-751) and the STAN (STIL/Ana2) domain (residues 1061-1147)[202,205]. This recent progress focuses attention on a detailed mechanistic understanding of the interaction between STIL and PLK4, and this in turn requires definitive structural information.

PLK4 belongs to the PLK family, which in vertebrates comprises four functional paralogues, PLK1-4. PLKs are characterized by an N-terminal Ser/Thr- kinase domain followed by a C-terminal region containing two or three Polo-box folds (PB), which regulate substrate binding, kinase activity, and localization[83,84,206]. Among the PLKs, PLK1 is the best studied; it comprises two Polo-boxes, PB1 and PB2, that form a Polo-box domain (PBD), through intramolecular heterodimerization. The PLK1-PBD generally binds to target proteins after their phosphorylation on Ser/Thr- sites within a PBD-docking motif[80,94,95,97,207]; however, in the context of the *Drosophila* microtubule-associated protein Map205 phospho-independent binding has also been described[96]. PLK4 is unique among the PLKs as it contains three -rather than two- Polo-boxes (PB1-3)[109]. The first two Polo-boxes of PLK4, PB1 and PB2 (formerly referred to as cryptic Polo-box, CPB), are sufficient for centriole localization of PLK4[99,109]. Isolated PLK4-PB3 can also localize to centrioles, but with less efficiency[109,112]. In contrast to PLK1-PBD, PLK4-PB1/2 as well as PB3 have been described to form intermolecular

homodimers and to bind their targets in a different, phospho-independent manner[109-113]. Recent work has established a crucial role for the binding of acidic regions in Cep192 and Cep152 to basic residues in PLK4-PB1/2[111,113,194]. However, no interactions of PLK4-PB3 with binding partners have been resolved so far. Moreover, the relevance of the reported domain-swapped structure of murine PB3[112] for *in vivo* interactions remains unclear.

Here, we identify STIL as a direct interaction partner and substrate of PLK4 and confirm that the STIL-CC region is essential for STIL function in centriole duplication. Most importantly, we determined the solution structure of the human PLK4-PB3 and a crystal structure of the PLK4-PB3/STIL-CC complex and use structure-based mutagenesis of STIL to demonstrate an essential role of STIL-CC for PLK4 binding and the regulation of centriole biogenesis *in vivo*. Specifically, we show that STIL-CC interacts with two regions within PLK4: it targets not only the L1 region but also is the first identified binding partner of the unique PLK4-PB3. We further show that STIL-CC binding is implicated in the stabilization of centriolar PLK4 and its concomitant activation. Collectively, our results contribute to a detailed structural and mechanistic understanding of a crucial initial step of centriole biogenesis.

3.3 Results

3.3.1 PLK4 and STIL interact *in vivo* to regulate centriole duplication

To identify centrosomal binding partners of the PLK4 Polo-box motifs, we performed an S-peptide pulldown experiment coupled to mass spectrometry analysis. We generated a U2OS Flp-In T-REx cell line that allowed for inducible expression of an S-peptide-EGFP-tagged PLK4 fragment (residues 570-970) comprising the three Polo-boxes PB1-3. We identified a set of centrosomal proteins including the two well-known PLK4-PB1/2 binding partners Cep152 and Cep192 (sixteen and four identified peptides, respectively)[113,191-194]. In addition, the key centriole duplication factor STIL co-purified with the PLK4 fragment (one identified peptide)[208]. This prompted us to further analyze the functional and structural interaction between PLK4 and STIL.

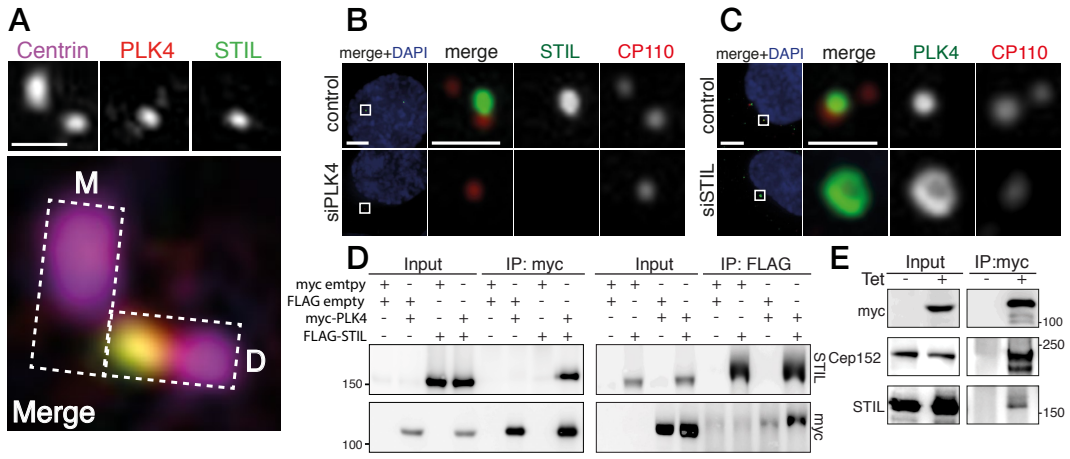

Figure 3.1 STIL is an interaction partner of PLK4.
A U2OS cells were fixed and stained with the indicated antibodies for 3D-SIM imaging. A representative 3D-SIM image is shown, demonstrating the co-localization of PLK4 and STIL at the daughter centriole. Top panel: Centrin (purple), PLK4 (red), STIL (green). Scale bar: 0.5 µm. Bottom panel: Magnified view of the centrosome (overlay image). The rectangles illustrate the orientation of the mother (M) and daughter (D) centrioles. **B** Immunostaining of STIL localization in U2OS cells depleted of endogenous PLK4. Cells were transfected for 72 hours with control or PLK4 siRNA oligonucleotides and stained with the indicated antibodies. DAPI is shown in blue. Scale bars: 1 µm. **C** Immunostaining of PLK4 localization in U2OS cells depleted of endogenous STIL (control and siSTIL). Experimental procedures as in (B). In (B) and (C), only prophase cells harboring 1-2 centrioles were analyzed (indicative of successful PLK4 or STIL depletion, respectively). **D** Western blots showing the interaction of myc-tagged PLK4 and FLAG-tagged STIL in HEK293T cells. Cells were transfected with the indicated plasmids for 36 hours, followed by lysis and immunoprecipitation using anti-myc or anti-FLAG antibodies. Antibodies used for Western blot detection are indicated. **E** Western blot showing the interaction of myc-PLK4 with endogenous STIL. Myc-PLK4 expression was induced by addition of tetracycline to U2OS T-REx cells stably harboring the myc-PLK4 transgene (-/+ Tet, 24 hours). Cells were processed for anti-myc co-immunoprecipitations and Western blot analysis using the indicated antibodies.

As 3D-SIM imaging of U2OS cells revealed extensive co-localization of STIL and PLK4 at the proximal end of daughter centrioles (Figure 3.1A), we asked whether the two proteins depend on each other for recruitment to this site. Upon depletion of PLK4, localization of STIL to centrioles was drastically reduced (1.7 ± 2.3% residual intensity compared to untreated cells, Figure 3.1B), suggesting that PLK4 is essential for STIL centriolar targeting and/or maintenance. On the other hand, PLK4 localization to centrioles was not abrogated in STIL depleted cells. On the contrary, centriolar PLK4 levels were strongly elevated and PLK4 localized in a ring-, rather than a spot-like pattern to the outer wall of centrioles[203] (Figure 3.1C). Western blot analysis confirmed significant elevation of PLK4 levels in STIL depleted cells (A-D). This increase in PLK4 levels was comparable to that observed after depletion of βTrCP, which is known to

interfere with PLK4 degradation[104,105,107,190] (Supplemental Figure 3.1). These data suggest that PLK4 degradation is strongly reduced in the absence of STIL, which then results in its accumulation around centrioles. In further support of a functional interaction between PLK4 and STIL, we also observed that STIL was phosphorylated by a recombinant GST-PLK4$_{1-430}$ fusion protein *in vitro* and *in vivo*[202-204] (Supplemental Figure 3.2A).

To confirm the interaction of STIL with PLK4, we transfected HEK293T cells with myc- and FLAG-tagged versions of both proteins and performed co-immunoprecipitation experiments. As expected, we found STIL and PLK4 to be present in the immunoprecipitates of the respective interaction partner (Figure 3.1D). Moreover, we detected endogenous STIL along with Cep152 in an immunoprecipitate of myc-PLK4, which had been isolated from a U2OS T-REx cell line (Figure 3.1E). Thus, STIL and PLK4 form a stable complex *in vivo*.

3.3.2 The STIL-CC motif is necessary for PLK4 binding and centriole duplication

To map the region of STIL required for binding to PLK4, we cloned truncated versions of the STIL protein: an N-terminal (STIL N-ter., residues 1-440), middle (STIL-MD, residues 441-880) and C-terminal (STIL C-ter., residues 881-1287) part, and subjected these fragments to co-immunoprecipitation experiments with myc-tagged PLK4-ND (Figure 3.2A-B). The PLK4-ND point mutant exhibits enhanced stabilization[107] and thus facilitates the visualization of STIL binding (Supplemental Figure 3.2B). We found that the N- and C-terminus of STIL did not bind PLK4-ND, whereas the middle part displayed efficient PLK4 binding. Accordingly, two STIL truncations containing the middle part but lacking either the N- or C-terminus (STIL-ΔN, residues 441-1287; STIL-ΔC, residues 1-880), strongly bound to PLK4-ND (Figure 3.2A-B).

The middle region of STIL contains a predicted coiled-coil (CC) motif (residues 720-751)[205]. To test the involvement of STIL-CC in PLK4 binding, we further truncated the STIL-MD and analyzed the interaction with PLK4-ND (Figure 3.2A,C). As long as the CC motif was intact, immunoprecipitation of PLK4-ND was not affected. However, truncating or removing the CC motif severely disrupted PLK4 binding, indicating that PLK4 interacts with the STIL-CC region. This finding was further confirmed by the observation that an EGFP-tagged version of STIL-CC efficiently pulled down PLK4

(Figure 3.2D), suggesting that STIL-CC alone is sufficient to bind PLK4. Accordingly, a mutant of STIL lacking the CC motif (STIL-ΔCC) did not interact with PLK4, whereas removal of another conserved region in STIL, the STAN domain (STIL-ΔSTAN), had no impact on the interaction with the kinase (Figure 3.2A, E). Therefore, the CC domain is both necessary and sufficient for STIL binding to PLK4.

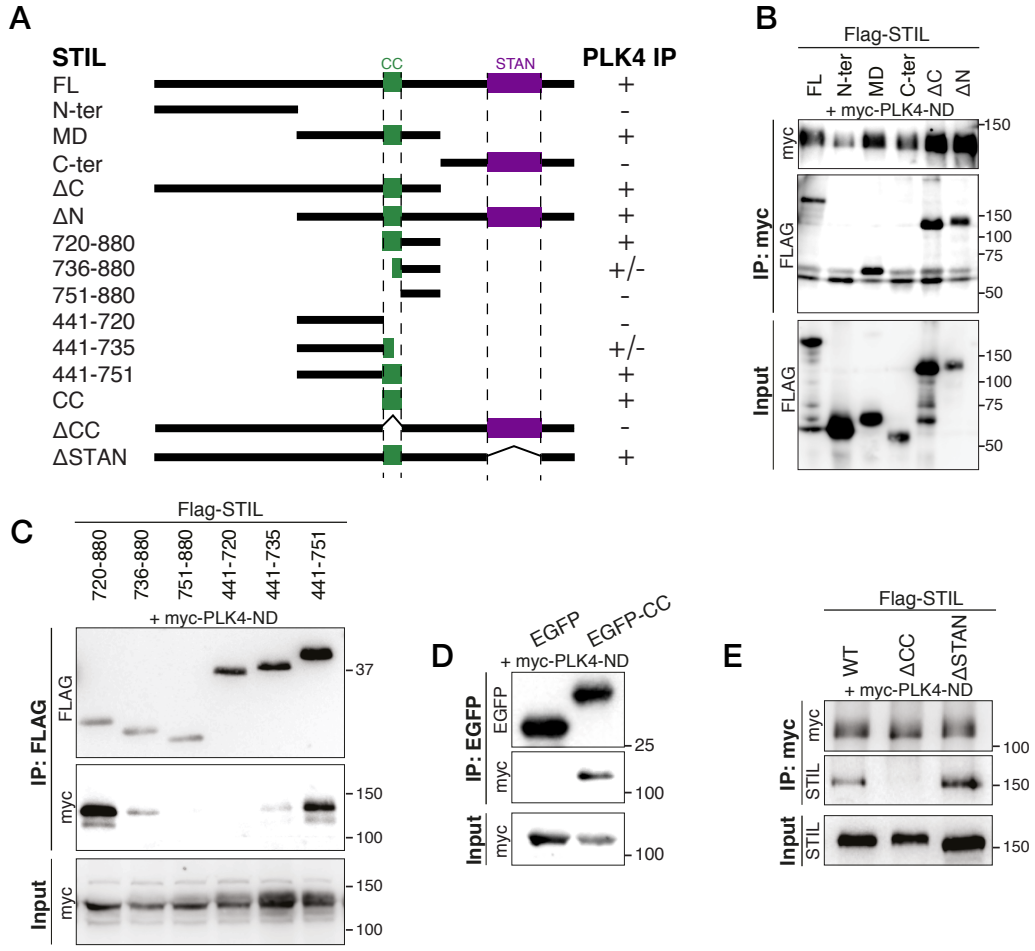

Figure 3.2 The STIL-CC motif binds to PLK4.

A Schematic illustration of STIL constructs used to map the PLK4-binding region in STIL. On the right, the relative strengths of the interactions as determined by co-immunoprecipitation experiments are indicated (+, strong; +/-, weak; -, not detected). **B** - **E** Western blot analysis of co-immunoprecipitation experiments from HEK293T cells co-expressing STIL fragments or STIL-ΔCC/ΔSTAN mutants and myc-PLK4-ND. Cells were transfected for 36 hours with the indicated plasmids and whole cell lysates were used for co-immunoprecipitation experiments with anti-myc, anti-FLAG or anti-EGFP antibodies. Antibodies for Western blot detection are indicated.

Having established the importance of the CC motif for the PLK4/STIL interaction, we next tested the requirement of this motif for STIL functionality in centriole reduplication. Therefore, we transiently overexpressed STIL-ΔCC in U2OS cells and monitored centriole numbers using immunofluorescence microscopy (Figure 3.3A-B). Overexpression of wild-type STIL (STIL-WT) caused centriole amplification in 45% of transfected cells, and roughly 20% of cells displayed 'flower-like' staining, the near-simultaneous formation of several daughter centrioles around one mother centriole (Figure 3.3A-B). In cells overexpressing STIL-ΔCC only background levels of centriole amplification could be detected (Figure 3.3B). Moreover, we observed a similar reduction in centriole amplification with the STIL-ΔSTAN mutant, in line with the requirement for the STAN domain in centriole duplication [187]. Importantly, deletion of the STAN domain had only little impact on centriolar association of STIL, whereas removal of the CC motif strongly impaired the localization of STIL to centrioles [203] (Figure 3.3C). Thus, together with the observation that PLK4 depletion leads to loss of STIL from centrioles (Figure 3.1B), these results indicate that PLK4 directly recruits STIL to the site of centriole formation. We next asked whether STIL overexpression has an impact on the localization of PLK4 to centrioles (Figure 3.1C). To this end, we overexpressed EGFP tagged STIL in U2OS cells and stained for endogenous PLK4 (Figure 3.3D-G). Under these conditions, STIL-WT triggered the near-simultaneous formation of several daughter centrioles and PLK4 formed a ring around preexisting centrioles, suggesting that STIL stabilizes centriolar PLK4 (Figure 3.3D). Overexpression of STIL-ΔCC had no effect on either centriole amplification or PLK4 localization (Figure 3.3E) and, most importantly, overexpression of STIL-ΔSTAN stabilized PLK4 at centrioles, even though this mutant did not cause formation of extra centrioles (Figure 3.3F). Therefore, we conclude that STIL can stabilize PLK4 at centrioles in a manner that is independent of centriole formation.

As STIL has been shown to self-associate[186], we also tested a possible involvement of the STIL CC motif in self-interaction. We found that STIL-MD, and, more precisely, the CC motif, is indeed strictly required for STIL self-association, whereas the STAN domain is not (Supplemental Figure 3.3). We conclude that the CC motif is critical for the function of STIL in centriole duplication through its role in PLK4 binding, STIL self-interaction, and STIL centriolar recruitment.

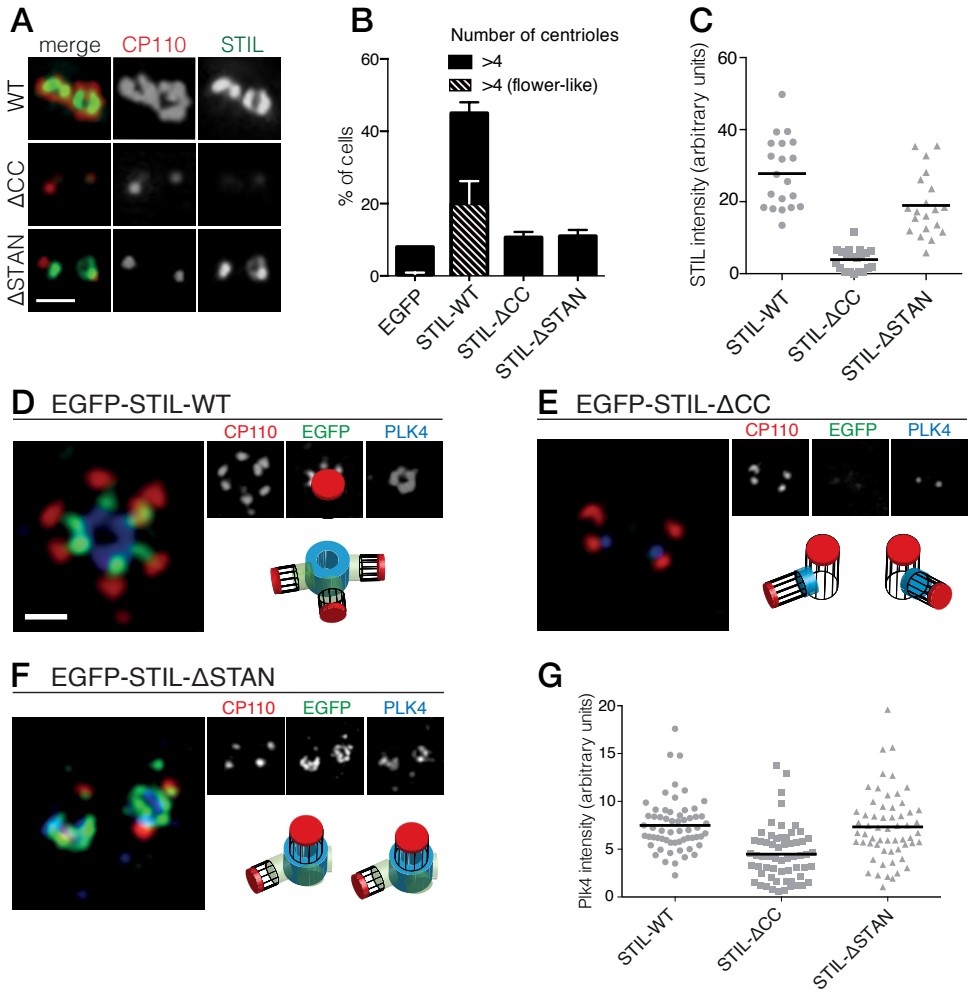

Figure 3.3 The STIL-CC motif is essential for centriole duplication.
A Immunofluorescence microscopy of U2OS cells transfected with STIL-WT, STIL-ΔCC or STIL-ΔSTAN for 48 hours. Cells were fixed and stained with the indicated antibodies. Scale bar denotes 1 µm. **B** Quantification of centriole numbers in U2OS cells after overexpression of the indicated STIL plasmids (3 experiments, a total of 300 cells were analyzed for each condition). Error bars denote SD. **C** Scatter plot to illustrate STIL signal intensity at centrosomes, after overexpression of STIL-WT, STIL-ΔCC or STIL-ΔSTAN (20 centrosomes were analyzed for each condition). **D** - **F** 3D-SIM images of U2OS cells that have been transfected with EGFP-tagged STIL-WT, STIL-ΔCC and STIL-ΔSTAN and stained with the indicated antibodies. **G** Scatter plot to illustrate measured PLK4 signal intensities at centrosomes, after overexpression of STIL-WT/ΔCC or ΔSTAN (60 centrosomes were analyzed for each condition). Scale bar denotes 1 µm.

3.3.3 STIL-CC directly binds PLK4-PB3 with nanomolar affinity

To determine which regions of PLK4 are involved in STIL binding, we generated a series of EGFP- and FLAG-tagged PLK4 fragments comprising either the N-terminal PLK4 part (residues 1-570), including the kinase domain (1-271) and the linker region L1 (265-570), or the C-terminal region containing the Polo-boxes (PB1/2 and PB3,

residues 570-970; PB1/2, residues 570-820; L2-PB3, residues 814-970; PB3, residues 880-970) (Figure 3.4A). Co-expression of the EGFP-tagged PLK4 fragments with FLAG-tagged full-length STIL, followed by anti-EGFP co-immunoprecipitation, revealed that both, the N-terminal PLK4 fragment spanning 1-570 or all C-terminal fragments harboring PB3 were sufficient for the interaction with full-length STIL (Figure 3.4B). Moreover, the STIL-CC motif alone was sufficient to bind both the N-terminus (residues 1-570) and PB3 (residues 880-970) of PLK4 (Figure 3.4C). Within the N-terminal PLK4 part, the linker region (265-570) participated in the interaction, whereas the kinase domain itself (1-271) did not (Figure 3.4D). Attempts to further narrow down the interaction region in L1 were unsuccessful, indicating a non-linear folded binding region. To quantify the PLK4-PB3/STIL-CC interaction we determined the binding affinity of PLK4-PB3 and STIL-CC using isothermal titration calorimetry. For this purpose, PB3 (residues 884-970) was recombinantly expressed in *E.coli* and purified, and a synthetic peptide corresponding to STIL-CC was subsequently titrated into a solution of PLK4-PB3. The integrated raw data are well fitted by a one-site binding model demonstrating a direct interaction between PB3 and STIL-CC with a dissociation constant K_d of 280 ± 60 nM and an equimolar stoichiometry (Figure 3.4E). In summary, we find that the STIL-CC motif directly interacts with PLK4-PB3 and that binding occurs with nanomolar affinity. Moreover, we show that STIL-CC additionally interacts with the N-terminus of PLK4, but not the PB1/2 domain. Importantly, our findings thus identify a novel binding mode for PLK4, since the previously known PLK4 binding partners Cep152 and Cep192 interact exclusively with the PB1/2 domain[113,191-194]. As STIL is the first protein known to bind PLK4-PB3, we next characterized the structural basis of the PLK4-PB3/STIL-CC interaction.

3.3.4 Structure determination and dynamics of PLK4-PB3 and its STIL-CC complex

NMR diffusion experiments confirmed that both free and STIL-bound PLK4-PB3 are monomeric in solution (Supplemental Table 3.1). The structure of human PLK4-PB3 (residues 884–970) was determined by solution NMR spectroscopy (
Figure 3.5A, Table 3.1). No crystals diffracting to high resolution were obtained for this construct, despite extensive screening of conditions. In contrast, plate-like crystals of the PLK4-PB3/STIL-CC complex diffracting to 2.6 Å resolution were obtained using seeding. The structure was solved by molecular replacement, and refined to $R_{work/free}$

of 0.22/0.25, respectively (Table 3.1) with one monomeric PLK4-PB3/STIL-CC per asymmetric unit (Figure 3.5B). The NMR structure of PLK4-PB3 in solution and the crystal structure of its STIL-CC complex display a conserved overall fold (Figure 3.5C) comprising a six-stranded antiparallel β-sheet (β1–β6) and a C-terminal α-helix (α1), which packs against the β-sheet and contacts residues from all six strands. The α-helical STIL-CC is bound in a hydrophobic cleft formed by both the β-sheet and the α1 helix of PLK4-PB3.

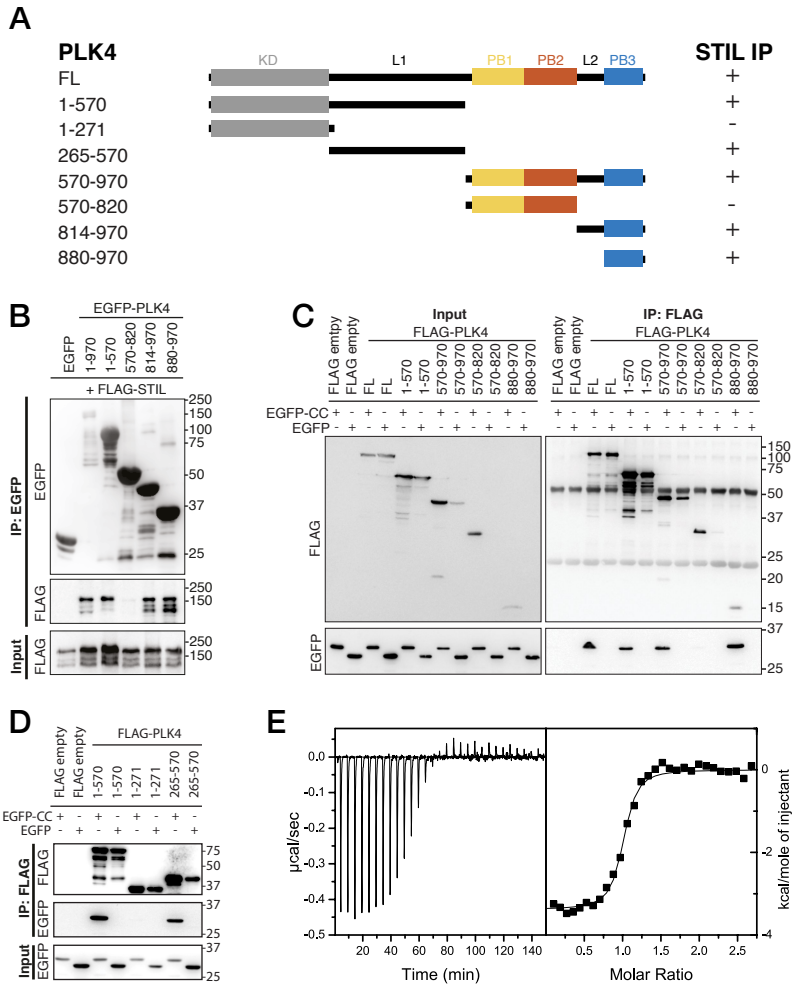

Figure 3.4 PB3 of PLK4 directly interacts with STIL-CC.
A Schematic illustration of PLK4 fragments used to map the STIL-CC binding site. Kinase domain (KD), grey; PB1, yellow; PB2, orange; PB3, blue. The relative strengths of the interactions are indicated (+, strong; -, not detected). **B** - **D** Western blots of co-immunoprecipitation experiments using HEK293T cells co-transfected with plasmids expressing PLK4 fragments and FLAG-STIL (B) or EGFP-STIL-CC (C and D). Antibodies used for Western blot detection are indicated. **E** Isothermal titration calorimetry of STIL-CC into a solution of PLK4-PB3. Left panel: Direct measurement of the Gibbs energy associated with STIL-CC binding to PLK4-PB3. Right panel: Integrated and fitted raw data using a one-site binding model.

Table 3.1 NMR and X-ray data collection and refinement statistics.

	PLK4-PB3
NMR constraints	
Distance constraints	
Total NOE	399
Intra-residue	49
Inter-residue	350
Sequential ($\|i-j\|=1$)	109
Medium-range ($\|i-j\|<4$)	100
Long-range ($\|i-j\|>5$)	141
Hydrogen bonds	16
Total dihedral angle restraints	122
ϕ	61
ψ	61

	PLK4-PB3/STIL-CC
X-ray data collection	
Space group	$C222_1$
Cell dimensions	
a, *b*, *c* (Å)	86.6, 136.3, 33.4
α, β, γ (°)	90.0, 90.0, 90.0
Resolution (Å)	68.1 – 2.60 (2.60 – 2.76)
R_{merge}	0.15 (2.37)
$CC_{1/2}$ outer shell	0.63
I / σI	10.3 (0.9)
Completeness (%)	99.7 (99)
Redundancy	6.4 (6.6)

Structure statistics	
Violations (mean and s.d.)	
Distance constraints (Å)	0.0158±0.0028
Dihedral angle constraints (°)	1.686±0.147
Max. dihedral angle violation (°)	8.40
Max. distance constraint violation (Å)	0.278
Deviations from idealized geometry	
Bond lengths (Å)	0.004±0.000
Bond angles (°)	0.483±0.017
Impropers (°)	1.391±0.102
Average pairwise r.m.s.d.[a] (Å)	
Heavy[b]	1.60±0.21
Backbone[b]	1.09±0.25

Refinement	
Resolution (Å)	20.80 – 2.60
No. reflections	6409
R_{work} / R_{free}	0.22 / 0.25
No. atoms	
Protein	1829
Water	15
B-factors	
Protein	89.7
Water	78.6
R.m.s. deviations	
Bond lengths (Å)	0.01
Bond angles (°)	1.15

[a]Pairwise r.m.s. deviation was calculated among 20 refined structures.
[b]Statistics applied for ordered regions (residues 890-961).

To further characterize differences in structure and dynamics of PLK4-PB3 seen upon STIL-CC binding in aqueous solution, free and STIL-CC-bound PLK4-PB3 were subjected to 2D [^{15}N,^{1}H]-TROSY experiments to reveal chemical shift perturbations and to ^{15}N-{1H}NOE measurements to characterize backbone dynamics on the ps- to ns-timescale (Supplemental Figure 3.4 and Supplemental Figure 3.5). Chemical shift perturbations are observed throughout most of the PB3 backbone and comprise direct STIL-CC interactions and perpetuated structural changes throughout PLK4-PB3. The most significant changes locate however around residues C954 and L955 on helix α1, where a slight kink is formed in apo PLK4-PB3. Notably, the secondary chemical shifts of these residues are substantially increased upon binding STIL-CC, suggesting a stabilization of helical conformation (Supplemental Figure 3.6). STIL-CC binding leads to an increase in averaged heteronuclear NOEs for β-strands and the α1 helix, suggesting a general reduction of fast backbone motions of PLK4-PB3 upon STIL-CC binding. Overall, the structural data reveal two core differences in PLK4-PB3 induced by STIL-CC binding: First, strand β1 is N-terminally extended by three

residues to the range 888–893, resulting in a shortening of the unstructured N-terminal region in the STIL-CC complex. Second, helix α1 slightly changes its orientation and is stabilized by STIL-CC binding (Figure 3.5C)

3.3.5 PLK4-PB3 adopts a canonical Polo-box fold

The structure of the human PLK4-PB3 resembles the canonical structures of related Polo-boxes (Supplemental Figure 3.7A). It aligns structurally well with both Polo-boxes of the PLK1-PBD[80,94]. PLK1-PB2 is a close structural homologue (1.3 Å rmsd, 79 Cα), with minor differences only in the linker to the α-helix. PLK1-PB1 is slightly more divergent, in that the C-terminal end of the α1-helix is bent towards the region, where STIL-CC is bound in PLK4-PB3. PLK4-PB3 also aligns with its two companion Polo-boxes of the PLK4-PB1/PB2 domain[109,111]. Structural divergence to PLK4-PB1 occurs in the β-hairpin region between β3-β4, which gives PLK4-PB1 its unique winged structure, as well as in the linker between β5-β6. A major distinction between PLK4-PB3 and PLK4-PB2 is the length of helix α1, which extends beyond the β-sheet in PLK4-PB2.

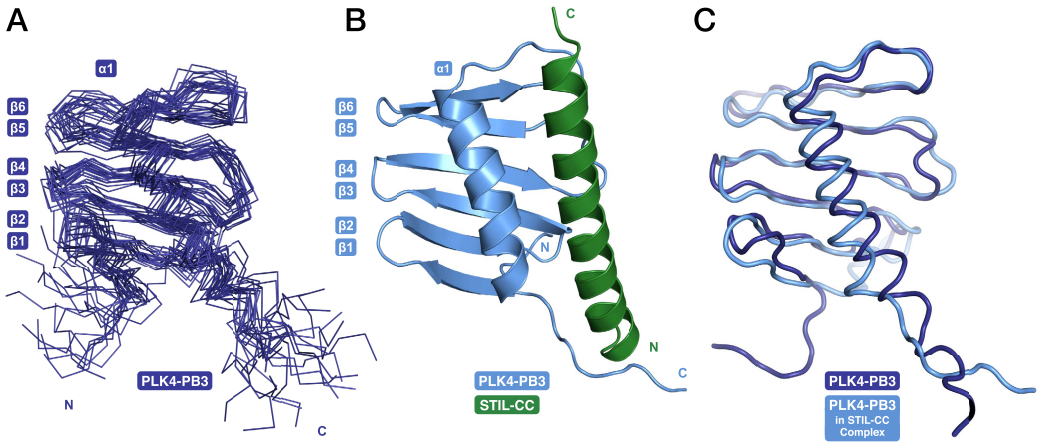

Figure 3.5 PB3 adopts a canonical Polo-box fold.
A Ensemble of 20 NMR conformers with the lowest target function of free PLK4-PB3 (dark blue) **B** the X-ray structure of the PLK4-PB3/STIL-CC complex (light blue/green) and **C** comparison of the free PLK4-PB3 (dark blue) to the PLK4-PB3 (light blue) in complex with STIL-CC by structural superposition (STIL-CC not shown for clarity).

PB3 of human PLK4 is closely related to those of its murine ortholog SAK (97% sequence identity[209]). Based on the high degree of sequence identity one would expect a highly similar structure for this protein. However, the structure of the human PLK4-PB3 determined here diverges drastically from the structure of murine SAK-PB3, that was crystallized as a domain swapped dimer[112] (Supplemental Figure 3.7B).

In SAK-PB3, the β-sheet is formed by strands β2, β3 and β4 from one monomer and strands β5 and β6 from the second (numbering according to human PLK4-PB3) and the α1 helix is shortened compared to human PLK4-PB3. The sequence region corresponding to the C-terminal half of this helix is swapped between monomers in SAK-PB3 and transformed into a β-strand, which occupies the position of strand β1 in human PLK4-PB3. The best explanation for this divergence might be the existence of an equilibrium between a monomeric and a domain-swapped form of SAK-PB3, the latter of which may be a lowly populated species that is not occurring in the full-length protein *in vivo*. Either the chemical conditions of crystallization shifted this equilibrium towards the non-native domain-swapped form or crystallization occurred selectively for the domain-swapped state. Nevertheless, our consistent results from solution and crystal structure determination strongly indicate that the canonical Polo-box fold is a relevant physiological state of the PLK4 PB3 domain.[183]

3.3.6 STIL-CC binding to PLK4-PB3 mimics coiled-coil interactions

PLK4-PB3 and STIL-CC interact along the entire STIL-helix and form a substantial interface of 934 Å^2 buried surface area[210]. Two regions on PLK4-PB3 contribute to the predominantly hydrophobic binding interface: First, the surface of the PLK4-PB3 β-sheet around residues V907, L917, V919, I926 and Y928 (Supplemental Figure 3.8), and second the α1 helix (I948, L952, L955 and L959) and the linker (L944) leading into it (Figure 3.6A). Key interacting residues on STIL-CC are leucine and isoleucine residues (L733, L736, I740, L743, L744) pointing towards the hydrophobic surface of PLK4-PB3. Additional interactions are provided by backbone-backbone hydrogen bonds between $PB3_{G922}$-$STIL_{Q739}$ and $PB3_{K943}$-$STIL_{M750}$ (Supplemental Figure 3.8), respectively. The orientation of the two helices and their hydrophobic interactions is mainly mediated by leucine residues and resembles a leucine zipper interaction, consistent with the predicted coiled-coil propensity of STIL-CC[205].

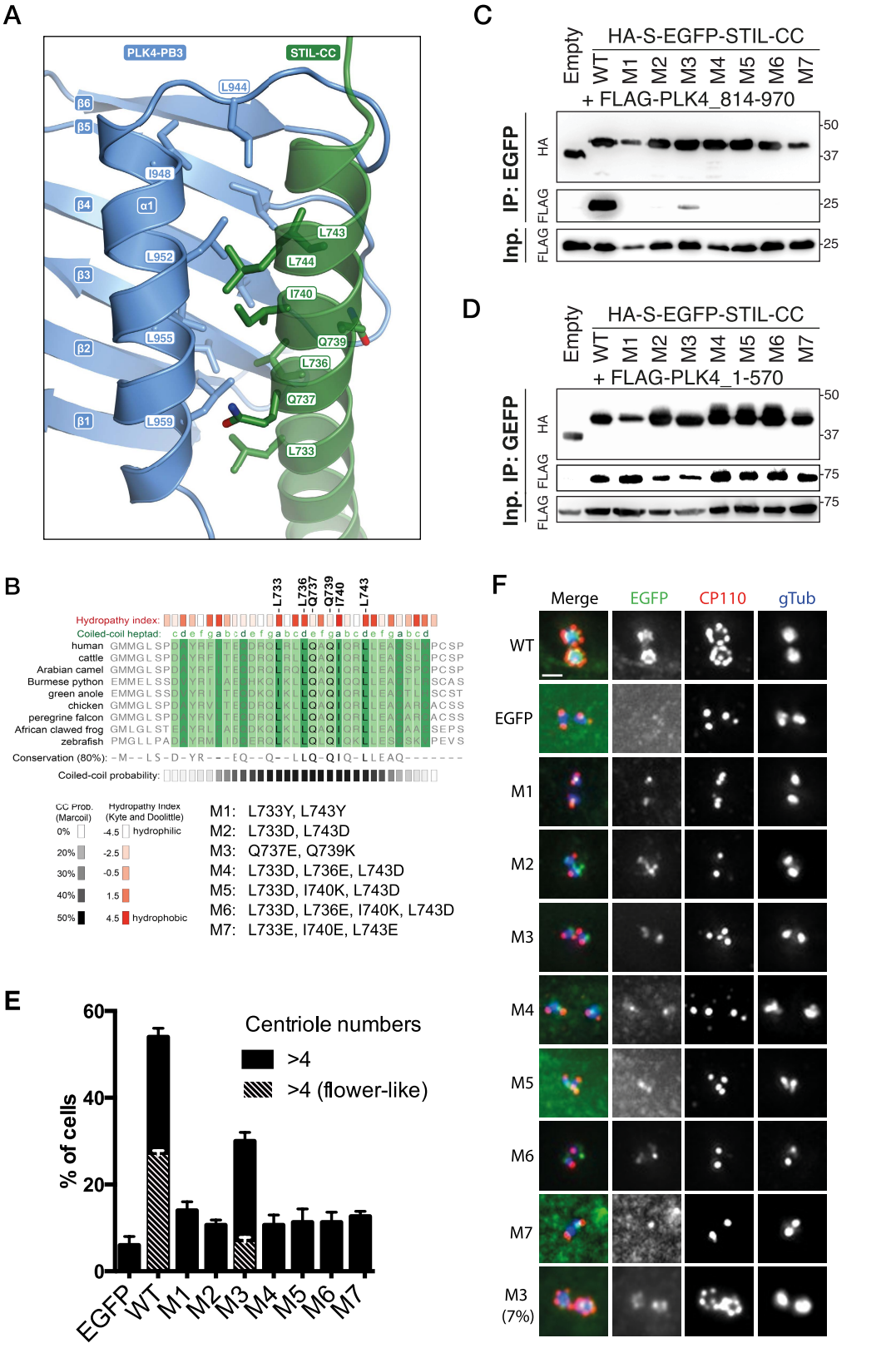

Figure 3.6 Analysis of structure-based STIL-CC mutants.

A Close-up view of the STIL-CC/PLK4-PB3 binding interface. Key contributing residues to the hydrophobic interaction between the PLK4-PB3 (light blue) α-helix and the STIL-CC (green) α-helix are indicated. **B** Multiple sequence alignment (ClustalW) of the STIL CC domain. Residues that directly participate in the PLK4-PB3 interaction are marked on top. Hydropathy index

values (according to Kyte-Doolittle) for each amino are depicted in red. CC probability values (according to MARCOIL prediction) for each amino acid are depicted in black below the alignment. The position of each amino acid in the predicted heptad repeat (labelled a-g, whereas a and d are hydrophobic positions) is shown in green on top of the alignment. **C** - **D** Control, WT or mutant versions (M1-7) of HA-S-EGFP-tagged STIL-CC were co-transfected with either PLK4-L2-PB3 (814-970) (C) or N-terminal PLK4 (1-570) (D) in HEK293T cells. EGFP-immunoprecipitations were performed and analysed by Western blotting with the indicated antibodies. **E** - **F** To assess centriole amplification, EGFP-tagged WT and mutants of full-length STIL (M1-7) were overexpressed in U2OS cells (48 hours). EGFP was used as control. E) Quantification of transfected cells with more than 4 centrioles (n=3, 50 cells each). F) Immunofluorescence images of U2OS cells after overexpression of EGFP-tagged STIL-WT or mutants M1-7 (48 hours). Centrioles were visualized by staining with antibodies against CP110 and γ-Tubulin (gTub) was used as marker for centrosomes. Scale bar: 1 µm.

Polo-box domains are crucial mediators of the interaction of Polo-like kinases with their targets and have been demonstrated to interact with irregular substrate peptides and phosphopeptides. PLK1, for example, binds phosphopeptides containing a consensus Ser-[pSer/pThr]-[Pro/X] motif[95] through a cleft within its PBD (comprising PB1 and PB2)[80,94,211] and a neighboring binding site on PB1 is used for phospho-independent recognition of a Map205 peptide[97] (Supplemental Figure 3.9A). The PLK4-PB1/2 domain has recently been shown to bind either two Cep192- or one Cep152-derived peptide in a mutually exclusive manner using large interaction interfaces extending along PB1 and PB2[111]. PLK4-PB3 reveals a novel binding mode by interacting with the helical STIL-CC region in a leucine-zipper-style via the α1 helix with further hydrophobic contacts to the central β-sheet. Remarkably, this external target interaction of PLK4-PB3 closely resembles an intramolecular interaction observed in PLK1: there, the internal Polo-cap (Pc), an N-terminal extension of PLK1-PB1 which comprises an α-helix and a linker to PB1, directly binds to PLK1-PB2 and thereby determines the relative orientation of PB1 and PB2[80]. The 17-residue α-helix of the Pc is shorter compared to the 31-residue STIL-CC, but forms a leucine-zipper with the α1-helix of PLK1-PB2, very much like STIL-CC with the α1-helix of PB3 in PLK4 (Supplemental Figure 3.9B).

3.3.7 Mutations demonstrate the relevance of PLK4/STIL-CC interactions *in vivo*

Guided by the structure of the PLK4-PB3/STIL-CC complex, we designed seven mutants of STIL to functionally evaluate the role of the PLK4-PB3 interaction with STIL

(mutants M1 to M7): In the first mutant (M1) L733 and L743 were replaced by two large residues (L733Y, L743Y). In the second mutant (M2) as well as in the mutants M4-7 we replaced hydrophobic residues (at positions a and d of the coiled-coil heptads) with charged amino acids. In mutant M3 we exchanged Q737E and Q739K in order to interfere with hydrogen bond formation ($STIL_{Q739}$-$PB3_{K943}$) (Figure 3.6B). To test the impact of these mutations on the binding affinity to PLK4, we co-transfected HA-S-EGFP-tagged mutants of STIL-CC with either FLAG-tagged PLK4-L2-PB3 (residues 814-970) or N-terminal PLK4 (residues 1-570). The corresponding EGFP-immunoprecipitation experiments revealed that all mutants except for M3 completely lost binding to PB3 (Figure 3.6C). Thus, the hydrophobic residues L733 and L743 as well as L736 and I740 are indeed essential for the interaction. Disruption of a hydrogen bond at position Q739 in M3 severely diminished the interaction with PB3 but still allowed for residual binding. Interestingly, all mutants maintained binding to the N-terminal PLK4 fragment spanning residues 1-570 (Figure 3.6D). This indicates that STIL-CC binds to the two PLK4 regions in different ways and hence may associate with the two regions simultaneously.

In parallel to the above binding studies, we also analysed the ability of the STIL mutants to cause centriole amplification. We overexpressed EGFP-tagged full-length WT or mutant STIL proteins in U2OS cells and scored for cells with more than four centrioles. STIL-WT produced centriole amplification in 54% of cells, half of them displaying a flower-like centriole arrangement. In contrast, the mutants M1-2 and M4-7 caused centriole amplification in only 11-14% of cells, comparable to centriole amplification in EGFP-transfected control cells (Figure 3.6E-F). Interestingly, in the case of M3, 30% of cells produced amplified centrioles (7% with a flower-like centriole arrangement) (Figure 3.6E-F), in line with the observed residual binding capacity to PB3 (Figure 3.6C).

3.4 Discussion

Polo-like kinases are a family of kinases with key regulatory roles in cell cycle progression, mitosis, cytokinesis and centriole duplication, with all human genes thought to have arisen by gene duplication from an ancestral PLK1-like gene[84]. PLK4, the master regulator of centriole duplication, is the most distant member of the family. It is distinguished from all other PLKs by the presence of a third C-terminally located Polo-box, PB3, in addition to the two central and closely linked Polo-boxes PB1 and

PB2[84]. PB1 and PB2 provide a dimerization platform to regulate PLK4 *trans*-autophosphorylation[212] and mediate recognition of crucial interaction partners[84,109,111]. However, no interaction partner of PLK4-PB3 had previously been identified.

Here, we demonstrate that monomeric PB3 of human PLK4 adopts a canonical Polo-box-fold and directly interacts with nanomolar affinity with the central STIL coiled-coil region, STIL-CC. The binding mode of the PLK4-PB3/STIL-CC interaction is completely different from all previously described target interactions of Polo-boxes, but resembles an intramolecular interaction of PB2 with the Pc-helix in PLK1.

We show that the interaction of STIL with PLK4 *in vivo* regulates centriole biogenesis, confirming and extending recent reports that PLK4-mediated STIL phosphorylation is crucial for SAS-6 recruitment and for triggering centriole duplication[202-204]. We further demonstrate that the STIL-CC region is necessary and sufficient to mediate the STIL-PLK4 interaction and map the binding of STIL-CC on PLK4 to two distinct domains, first to PB3, and second, to the L1 linker between the kinase and PB1/2 domain. Previous studies indicated that either the N-terminal kinase and L1[204] or, alternatively, the PB1/2 domain[203] of PLK4 are required for STIL interaction, but had failed to reveal an involvement of PB3. However, our *in vivo*, quantitative biophysical and structural data firmly establish a PLK4-PB3/STIL-CC interaction.

The binding of STIL-CC to PB3 resembles a zipper-type coiled-coil interaction based on an amphiphilic helix in PB3. However, the L1 linker region is predicted to not contain any Polo-box folds or other regions favouring coiled-coil interactions. This suggests different interaction modes between STIL-CC and PB3 or L1, respectively, and raises the exciting prospect that STIL-CC could regulate internal interactions between PB3 and the L1 linker region. As further discussed below, this may constitute an important mechanism for regulating PLK4 activity. Furthermore, our data clearly demonstrate a dual role for the STIL-CC region: first, it is an interaction partner for PLK4-PB3 in its monomeric form, and, second, it is involved in STIL-self interactions, presumably via tetramerization[213]. Mutations in the CC motif clearly abolish the interaction with PLK4-PB3. However, the same hydrophobic residues of STIL-CC are also predicted to be essential for STIL self-interaction and it is thus likely that these two processes are coupled. Therefore, the inability of STIL-CC mutations to support centriole amplification can be due to either compromised PLK4-PB3 binding, lack of STIL self association or due to failure in both processes. Furthermore, PB3-binding to STIL-CC is expected to affect the self-association of STIL with potential consequence for protein-protein interactions downstream of STIL.

Recent studies have revealed a regulatory role for PB3 in the activation of SAK/PLK4 in *Drosophila*[212]. Specifically, it was suggested that PB3, autophosphorylation of L1, and potentially further yet unidentified protein partners are important for relief of kinase auto-inhibition after SAK/PLK4 homodimerization. Our data on human PLK4 suggest to attribute a key role in such regulatory mechanism to STIL: first, STIL is the only identified interaction partner of PB3 with a direct influence on PB3 structure and dynamics; second, through its CC domain STIL is also able to interact with purported regulatory regions within L1 of human PLK4. These features make STIL a prime candidate for the role of an external factor regulating relief of PLK4 auto-inhibition in time and space (Figure 3.7, upper panel).

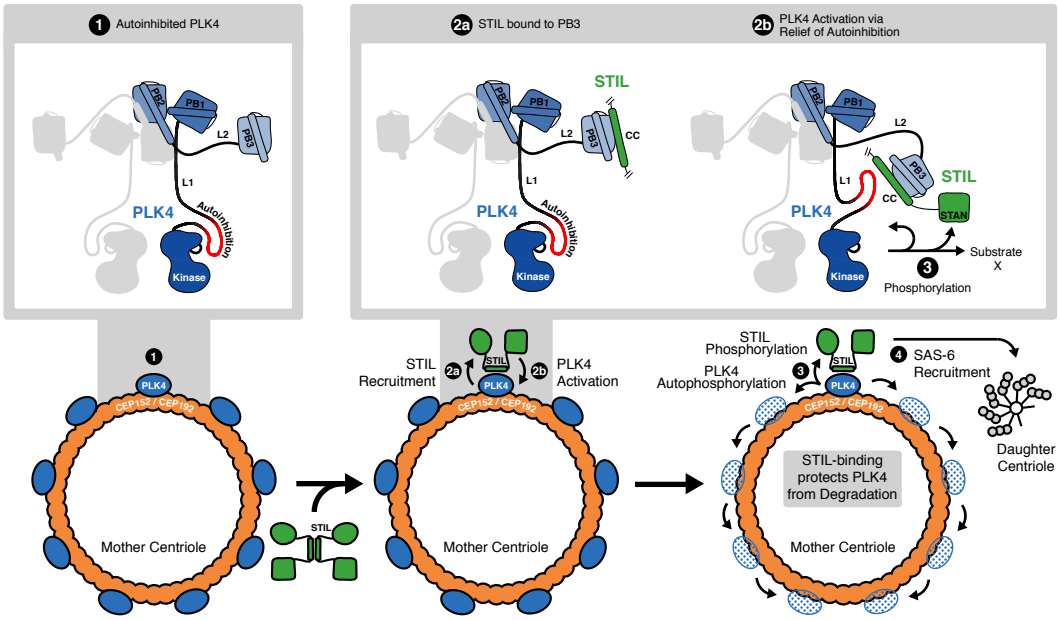

Figure 3.7 STIL binding to PLK4 regulates centriole duplication.
Hypothetical mechanism for STIL-mediated PLK4 activation: (**1**) PLK4 is bound to the mother centriole. It is intrinsically inactive, likely due to an autoinhibition by linker L1. (**2a**) STIL binds to PLK4 that has been recruited to centrioles through interactions with CEP192 and/or Cep152. (**2b**) STIL binding relieves the autoinhibition of PLK4, thus activating PLK4. (**3**) Activated PLK4 phosphorylates STIL in the STAN motif, which induces SAS-6 recruitment and daughter centriole biogenesis (**4**). Activated PLK4 also phosphorylates neighboring PLK4s in the degradation motif, triggering their degradation. At the site of cartwheel formation, the STIL-bound PLK4 is protected against degradation.

Although some mechanistic aspects of centriole biogenesis are likely to differ between species[214] it is interesting to consider our structural data on the interaction between PLK4 and STIL-CC in light of recent insights into the first steps of centriole formation.

Specifically, our data supports a model where STIL binds to PLK4 that has been recruited to centrioles through interactions with CEP192 and/or Cep152 (Figure 3.7, lower panel), either around the centriolar ring or in a localized dot-like pattern. Additional contributions to stable localization of STIL to centrioles may arise from its STAN-motif or C-terminal region, as a STIL C-terminal truncation (amino acids 1-1060) that contains the CC domain, interfered with correct localization to the centrioles[187,189]. Similarly, the isolated CC domain of Ana2 is not sufficient for centriolar targeting in Drosophila embryos[213]. Therefore, further interactions, presumably between the STAN-motif or the C-terminal region of STIL and SAS6, are likely required to stably integrate STIL into the centriolar cartwheel structure.

Once in a complex with PLK4, STIL is phosphorylated, triggering the recruitment of SAS-6 in preparation for cartwheel formation[202,203,215]. In parallel, phosphorylation may affect STIL oligomerization and association with the walls of centrioles. In view of most recent studies on PLK4 activation, our data additionally indicate that STIL-CC relieves the auto-inhibition of PLK4[212,215]. The resulting PLK4 *trans*-autophosphorylation is predicted to cause recruitment of βTrCP-SCF, followed by ubiquitin-dependent proteasomal degradation of activated PLK4[107,190]. In line with this idea, depletion of STIL leads to remarkable increase of PLK4 levels (Figure 3.1C and Supplemental Figure 3.1), suggesting that PLK4 is accumulating in an inactive and hence stabilized conformation in the absence of STIL. Our data also indicate that STIL protects activated PLK4 from degradation (Figure 3.3D-G and Ohta *et al*.[203]), possibly through binding to the PLK4-L1 linker region, which might shield the phosphorylated degradation motif (DSGHAT, residues 284-289) from recognition by βTrCP-SCF. Overall, these mechanisms provide a possible explanation for the concentration of PLK4 at the site of centriole formation (Figure 3.7, lower panel).

In summary, we have identified and structurally characterized an interaction between STIL and PLK4, two key centriole duplication factors. We show that the interaction is mediated via the STIL-CC domain and is crucial for centriole biogenesis. Importantly, STIL-CC is the first *bona fide* interaction partner of PLK4-PB3. The interaction of STIL-CC with PLK4-PB3 and a second region within the PLK4 L1 linker likely results in PLK4 activation and STIL phosphorylation by PLK4. These novel insights into the interaction and crosstalk of two key factors in centriole biogenesis provide a new perspective for further work on the critical step of condensing a PLK4 ring to a spot in localizing the initial position of daughter centriole growth.

3.5 Experimental Procedures

3.5.1 Antibodies

Antibodies against Cep152 (rabbit)[201], Centrin-3 (rabbit)[216] CP110 (rabbit)[217], CP110 (mouse)[189], myc (9E10, mouse)[218], PLK4 (mouse)[107], SAS-6 (mouse)[184], and STIL (rabbit)[183] were described previously. Monoclonal anti-FLAG M2 (Sigma-Aldrich), rabbit polyclonal anti-GFP (Abcam), monoclonal anti-γ-Tubulin TU-30 (Abcam), polyclonal anti-STIL (Abcam) and monoclonal anti-PLK4 MABC544, clone 6H5 (Merck Millipore) were purchased from the respective manufacturers. Alexa-555-, Alexa-488-, Alexa-647-labeled secondary anti-mouse and anti-rabbit antibodies were purchased from Invitrogen (Carlsbad, CA, USA). Whenever appropriate, antibodies were directly labeled with Alexa-555, Alexa-488 and Alexa-647 fluorophores, using the corresponding Antibody Labeling Kits (Invitrogen).

3.5.2 Plasmids

Cloning of myc-PLK4 full-length WT[99], myc-PLK4 full-length ND (S285A/T289A)[107] and FLAG-STIL[183] was described previously. pgLAP1 was a gift from Peter Jackson (Addgene plasmid #19702). All other plasmids were generated via the Gateway technology (Invitrogen) using the pENTR/D-TOPO entry vector (Invitrogen) and pcDNA3.1-based destination vectors containing the appropriate N-terminal tags. Mutations in STIL were generated with the QuikChange II XL Site-Directed Mutagenesis Kit (Agilent) according to the manufacturer's instructions.

3.5.3 Kinase assays

In vitro kinase assays using recombinant GST-PLK4 1-430 WT/D154A (cloned into pGEX-5X-2 (Thesis J. Westendorf)) were carried out at 30°C in kinase buffer (50 mM HEPES pH 7.0, 100 mM NaCl, 10 mM MgCl2, 5% glycerol, 1 mM DTT). Reactions were stopped after 30 minutes by addition of Laemmli sample buffer. Samples were then analyzed by autoradiography and Western blotting.

3.5.4 Cell culture and transfections

U2OS and HEK293T cells were grown at 37 °C and 5% CO2 in Dulbecco's modified Eagle's medium (DMEM), supplemented with 10% heat-inactivated fetal calf serum

(FCS, PAN Biotech, Aidenbach, Germany) and penicillin-streptomycin (100 µg/ml, Gibco-BRL, Karlsruhe, Germany). The U2OS cell line harboring the tetracycline-inducible myc-PLK4 transgene has been described[184]. The T-REx U2OS Flp-IN cell line harboring the tetracycline-inducible S-peptide-EGFP-tagged PLK4 fragment (residues 570-970) has been generated as described previously[189]. Transgene expression was induced by the addition of 1 µg/ml tetracycline. PLK4, STIL and βTrCP were depleted using siRNA oligonucleotides described previously[99,183,219]. Transfections of siRNA oligonucleotides or plasmids were performed using the transfection reagents Oligofectamin (Invitrogen) or TransIT-LT1 (Mirus Bio), respectively, according to the manufacturer's instructions.

3.5.5 Cell extracts, immunoprecipitation, Western blots and mass spectrometry

Cell lysis was performed as described previously[107] using Tris lysis buffer (50 mM Tris-HCl, pH 7.4, 150 mM NaCl, 0.5% IgePal) supplemented with protease and phosphatase inhibitors. For immunoprecipitation experiments, cell extracts (2-5 mg total protein) were incubated for 2 hours at 4 °C with appropriate beads [Anti-FLAG M2 Affinity Gel (Sigma-Aldrich), GFP-Trap agarose (ChromoTek), Affi-Prep protein A matrix (Bio-Rad Laboratories) crosslinked with 9E10 anti-myc antibodies or S-protein Agarose beads (Novagen)]. Immunocomplexes were washed 4-6 times with wash buffer (50 mM Tris-HCl pH 7.4, 150-500 mM NaCl, 0.5-1% IgePal), eluted with Laemmli buffer and analyzed by Western blotting. For mass spectrometry analysis of proteins copurifying with the S-peptide-EGFP-PLK4 fragment (residues 570-970), transgene expression was induced for 24 hours with Tetracycline (1 µg/ml). Cell extracts were subjected to S-protein immunoprecipitations and the samples were processed for mass spectrometry as described previously[220].

3.5.6 Immunofluorescence microscopy

Cells were fixed in methanol (5 minutes at -20 °C) and processed for immunofluorescence microscopy as described previously[221]. Stainings were analyzed using a DeltaVision microscope on a Nikon TE200 base (Applied Precision), equipped with a Plan Apochromat 60x 1.42 and an APOPLAN 100x 1.4 N.A. oil-immersion objective (Olympus), and a CoolSNAP HQ2 camera (Photometrics). Serial optical sections acquired 0.2 µm apart along the z-axis were processed and projected into

one image using Softworx (Applied Precision). For quantifications of STIL and PLK4 levels, intensities were measured with ImageJ and background signal intensity was subtracted. Identical image acquisition and image processing settings were used whenever measurements were compared. 3D-SIM was performed on a DeltaVision OMX-Blaze microscope system as described previously[194].

3.5.7 Expression and purification of PLK4-PB3 for structural studies

The human PLK4-PB3 (884-970) was cloned into pETG-30A (EMBL) with a N-terminal thioredoxin and hexashistidine tag, followed by tobacco etch virus (TEV) protease cleavage site (Gateway Cloning, life technologies). The vector was transformed into BL21 DE3 cells. The expression culture was induced with 0.5 mM IPTG at an OD_{600nm} of 0.5 and then grown for 18 hours at 20 °C. The protein was purified using High Affinity Nickel Charged Resin (Genscript). The N-terminal tag was removed by incubation with tobacco etch virus protease and rebinding to High Affinity Nickel Charged Resin. The PLK4-PB3 was further purified by size exclusion chromatography using a Hiload 16/60 Superdex75 column (GE). Based on this procedure, the following isotope-labeled samples were prepared for NMR experiments: [*U*-99%-^{2}H, ^{15}N]-PLK4-PB3, [*U*-99%-^{2}H, ^{15}N, ^{13}C]-PLK4-PB3, [*U*-99%-^{2}H, ^{15}N; 99%-$^{1}H^{\delta}$,$^{13}C^{\delta}$-IL;99%-$^{1}H^{\gamma}$,$^{13}C^{\gamma}$-V]-PLK4-PB3, and [*U*-99%-^{2}H, ^{15}N,^{13}C; 99%-$^{1}H^{\delta}$-IL;99%-$^{1}H^{\gamma}$,$^{13}C^{\gamma}$-V]-PLK4-PB3. All isotope-labeled reagents were purchased from Sigma-Aldrich.

3.5.8 Isothermal titration calorimetry

Isothermal titration calorimetry measurement employed a VP-ITC Instrument (Microcal). Recombinant PB3 (35.5 µM) and synthetic STIL-CC Peptide (414 µM) were dialyzed against 50 mM Hepes pH 8.0, 150 mM NaCl and 1 mM TCEP. The experiment was conducted at 25 °C. Titrations employed 30 STIL-CC injections (10 µl) each followed by a 300 s delay. The experimental data was fit with a one-site binding model.

3.5.9 NMR spectroscopy and structure determination of PLK4-PB3

All protein samples were prepared in 20 mM MOPS pH 7, 30 mM NaCl and 2 mM TCEP in 5%/95% D_2O/H_2O with a protein concentration between 0.6 and 1.2 mM. All NMR spectra were recorded at 20°C on Bruker Avance spectrometers equipped with cryogenic triple-resonance probes (field strengths 700, 800 and 900 MHz). For the

sequence-specific backbone resonance assignment of [*U*-^{2}H, ^{15}N, ^{13}C]-labeled PLK4-PB3 with and without bound STIL, the following NMR experiments were recorded: 2D [^{15}N-^{1}H]-TROSY-HSQC[222], 3D TROSY-HNCA, 3D TROSY-HNCACB, 3D TROSY-HNCO and 3D TROSY-HNCACO[223]. Chemical shift perturbations ($\Delta\delta$(HN)) of amide moieties were calculated as: $\Delta\delta(HN) = [((\delta H_{ref}-\delta H)^2+((\delta N_{ref}-\delta N)/5)^2)/2]^{0.5}$. For the sequence-specific side chain resonance assignment of [*U*-^{2}H, ^{15}N, ^{13}C-methyl-ILV]-labeled PB3, the following experiments were recorded: 3D (H)C(CC)-TOCSY-(CO)-^{15}N-HSQC and 3D H(C)(CC)-TOCSY-(CO)-^{15}N-HSQC with a TOCSY mixing time of 26.6 ns[224]. The NOE distance restraints for structural calculation were derived from 3D [^{1}H,^{1}H]-NOESY-^{15}N-TROSY[225,226] and 3D [^{1}H,^{1}H]-NOESY-^{13}C-HMQC[226] with a NOE mixing time of 100 ms. For determination of the dynamic properties of [*U*-^{2}H, ^{15}N]-PLK4-PB3 with and without bound STIL, ^{15}N{^{1}H}-NOE experiments were measured[227]. ^{15}N-filtered BPP-LED-diffusion experiments were recorded to measure the lateral diffusion of [*U*-^{2}H, ^{15}N]-PLK4-PB3, [*U*-^{2}H, ^{15}N]-PLK4-PB3/STIL-CC and [*U*-^{2}H, ^{15}N]-GB1 as a control[228].

Data were processed using Prosa[229] and analyzed with CARA[230]. The backbone assignment was done manually using CARA. Structure calculations were performed using CYANA 3.96[231], based on NOE restraints and dihedral angle restraints calculated by Talos+[232]. Hydrogen bonding restraints were added for residues in secondary structural elements that were unambiguously predicted by Talos+, and that showed the characteristic backbone NOE pattern for these secondary structural elements. A total of 100 structures were calculated by CYANA and the 20 conformers with the lowest target function were selected. A final water-refinement step of 15 ns was performed with CNS[233] Ramachandran statistics were 90.7 % in most favored regions, 7.2 % in additionally allowed regions, 1.7 % in generously allowed regions and 0.4 % in disallowed regions. Structures were analyzed using Molmol[234].

3.5.10 Crystallization and structure determination of PB3/STIL-CC

Synthetic STIL-CC peptide was incubated with recombinant PLK4-PB3 on ice for 1 hour in 20 mM HEPES-KOH pH 8.0, 150 mM NaCl and 2 mM TCEP in a 1.2-fold molar excess. The complex was concentrated to 16 mg ml^{-1} and set up for crystallization using the sitting-drop vapour diffusion method with a 1:1 (v/v) ratio of the complex and precipitant solutions. Thin needles grew in precipitant solution containing 100 mM Hepes, pH 7.0, 20 mM $MgCl_2$ and 22% Poly(acrylic acid sodium

salt) 5100. After extensive optimization and seeding plate-like crystals were grown in a drop consisting of 50% PLK4-PB3/STIL-CC complex solution, 33.3% precipitant solution (100 mM phosphate/citrate pH 4.2, 40% (v/v) Ethanol, 5% (w/v) PEG 1000) and 16.7% of seed stock solution. Crystals were flash frozen in liquid nitrogen using Perfluoropolyether (Hampton Research) as cryoprotectant.

X-ray diffraction data was collected at the beamline X06DA (PXIII) at the Swiss Light Source (Paul Scherrer Institute, Switzerland) using a PILATUS 2M detector. Crystals in the space group $C222_1$ diffracted to 2.6 Å resolution. The X-ray diffraction data was processed using XDS[159]. The structure was solved by molecular replacement with Phaser[162] using PLK1-PB1 (3P34, residues 147-331) as an initial search model. The asymmetric unit comprises one monomeric PLK4-PB3/STIL-CC complex. Model building and refinement was performed with Coot[235] and PHENIX[236] to $R_{work/free}$ of 0.22/0.25, respectively

3.6 Accession numbers

Atomic coordinates for PLK4-PB3 have been deposited in the Protein Data Bank with accession code 2n19. Sequence-specific resonance assignments have been submitted to the Biological Magnetic Resonance Data Bank under the following codes: PLK4-PB3, 25552 and holo PLK4-PB3 with bound STIL-CC, 26547. Atomic coordinates and structure factors for PLK4-PB3/STIL-CC have been deposited in the Protein Data Bank with accession code 4YYP.

3.7 Acknowledgements

Crystallographic experiments were performed on beamline x06da at the Swiss Light Source, Paul Scherrer Institut, Villigen, Switzerland. This work was supported by the Swiss National Science Foundation grant 310030B_149641 to EAN and by R'Equip 145023. C.A. was funded by a PhD fellowship from the Werner Siemens-Foundation (Zug, Switzerland). We thank Stephen C. Blacklow (Harvard Medical School), Jeff Parvin (Ohio State University Medical Center), Peter Jackson (Genentech) and Ingrid Hoffmann (Deutsches Krebsforschungszentrum) for sharing cell lines and reagents. We further acknowledge outstanding technical assistance by Elena Nigg and support by the Imaging, Biophysics and Proteomics Core Facilities of the Biozentrum.

3.8 Competing interests

None

3.9 Author contributions

C.A. and A-M.G. conducted the biochemical *in vivo* and *in vitro* characterization of STIL/PLK4 interaction. S.I. conducted ITC experiments, produced samples for NMR and X-ray crystallography and determined the structure of PLK4-PB3-STIL-CC. R.B. conducted NMR analysis. E.N, S.H. and T.M. designed experiments and supervised the work, all authors analyzed data and contributed to manuscript preparation.

3.10 Supplemental information

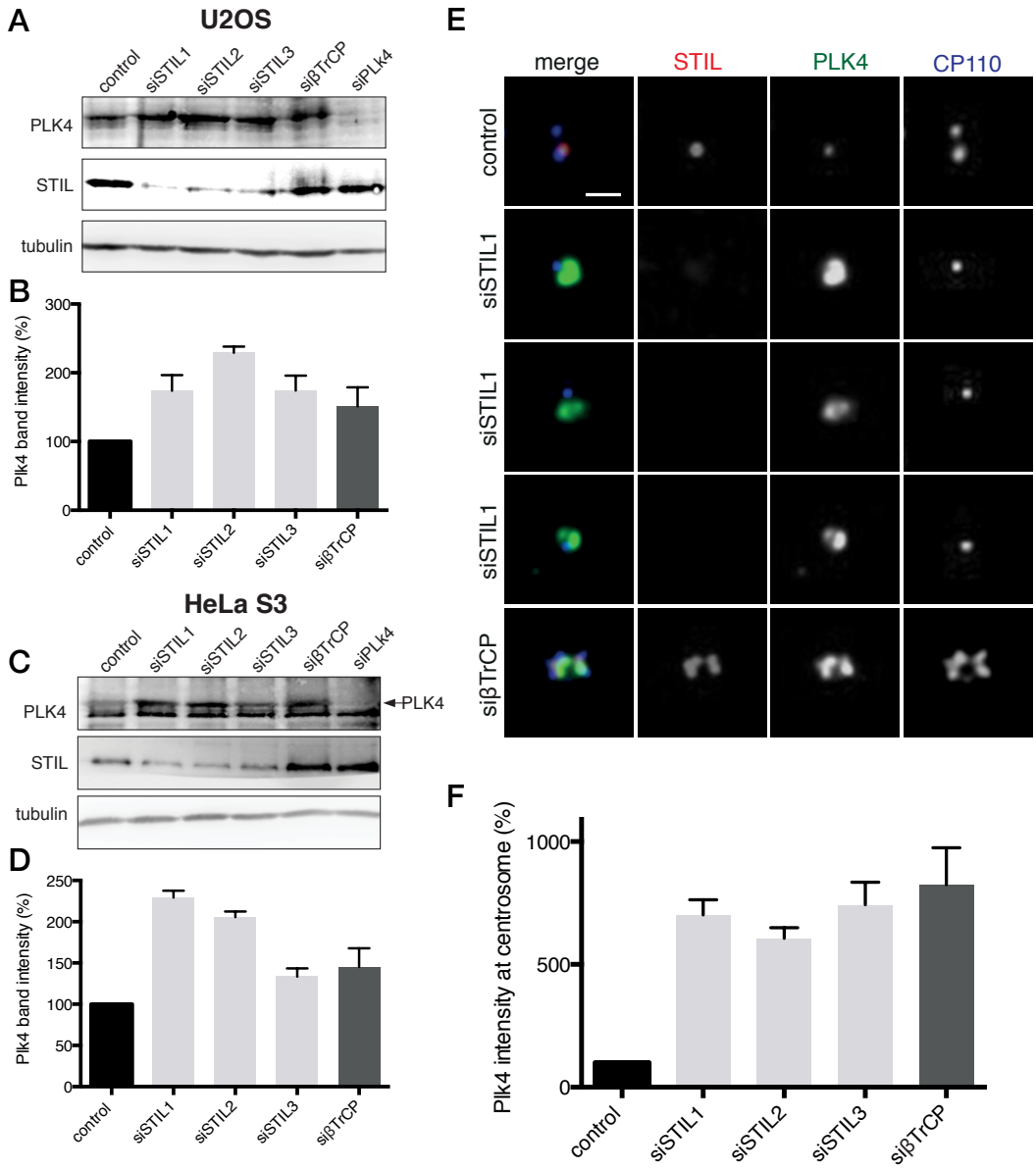

Supplemental Figure 3.1 Plk4 levels are elevated in STIL depleted cells.
A U2OS cells were transfected with control (siGL2), three different STIL (siSTIL1-3), βTrCP and Plk4 siRNA oligonucleotides for 72 hours, lysed and subjected to Western blot analysis using the indicated antibodies. **B** Graph representing Plk4 band intensities measured in Western blots from two independent experiments as described in (a). Error bars represent SEM. **C** HeLa S3 cells were transfected with control (siGL2), three different STIL (siSTIL1-3), βTrCP and Plk4 siRNA oligonucleotides for 72 hours, lysed and subjected to Western blot analysis using the indicated antibodies. **D** Graph representing Plk4 band intensities measured in Western blots from two independent experiments as described in (C). Error bars represent SEM. **E** U2OS cells were transfected with control (siGL2), three different STIL (siSTIL1-3), βTrCP and Plk4 siRNA oligonucleotides for 72 hours, fixed, stained with indicated antibodies and analysed in immunofluorescence microscopy. Representative images are shown. Scale bar: 1 µm. **F** Graph representing Plk4 levels measured in the centrosomal region of images as described in (E). 15 cells were measured for each condition in three independent experiments, error bars denote SEM.

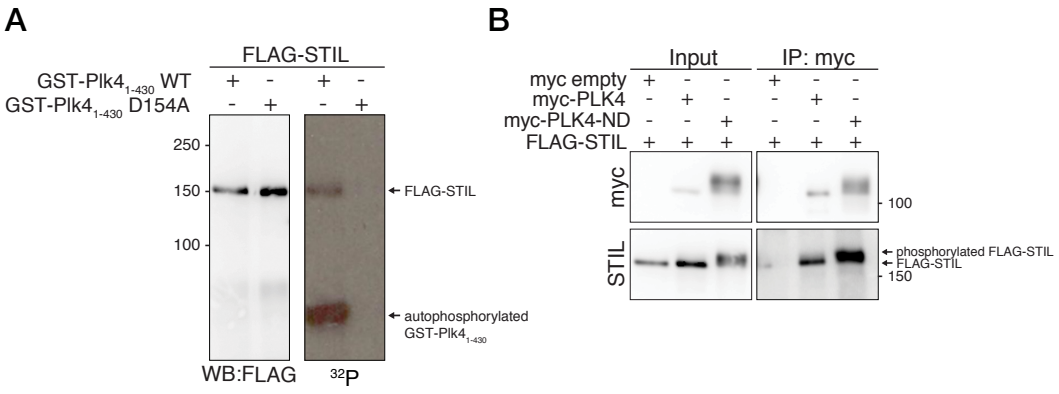

Supplemental Figure 3.2 STIL is a phosphorylation target of PLK4 and PLK4-ND.
A FLAG-STIL is phosphorylated by GST-PLK4$_{1-430}$ *in vitro.* HEK293T cells were transfected with FLAG-STIL for 48 hours. After cell lysis, FLAG-STIL was purified using anti-FLAG antibodies and subjected to an *in vitro* kinase assay with recombinant GST-PLK4$_{1-430}$ or, as a control, with a kinase-inactive version of GST-PLK4$_{1-430}$ (D154A). On the left, the Western blot probed with anti-FLAG antibody shows the amounts of FLAG-STIL used for the reactions. The autoradiograph (right side) shows the phosphorylation of FLAG-STIL by GST-PLK4$_{1-430}$ (upper band) as well as the autophosphorylation of GST-PLK4$_{1-430}$ (lower band). **B** HEK293T cells were transfected with the indicated plasmids and cell extracts were subjected to anti-myc co-immunoprecipitations followed by Western blot analysis. PLK4-ND – the non-degradable PLK4 mutant used throughout this study (S285A and T289A[107]) – exhibits enhanced stabilization and thus facilitates visualization of STIL binding (higher amounts of FLAG-STIL were detected in the precipitate of myc-PLK4-ND compared to wild-type myc-PLK4). Note the upshift of the STIL band upon co-expression with PLK4-ND, indicating that FLAG-STIL is phosphorylated by myc-PLK4-ND.[54]

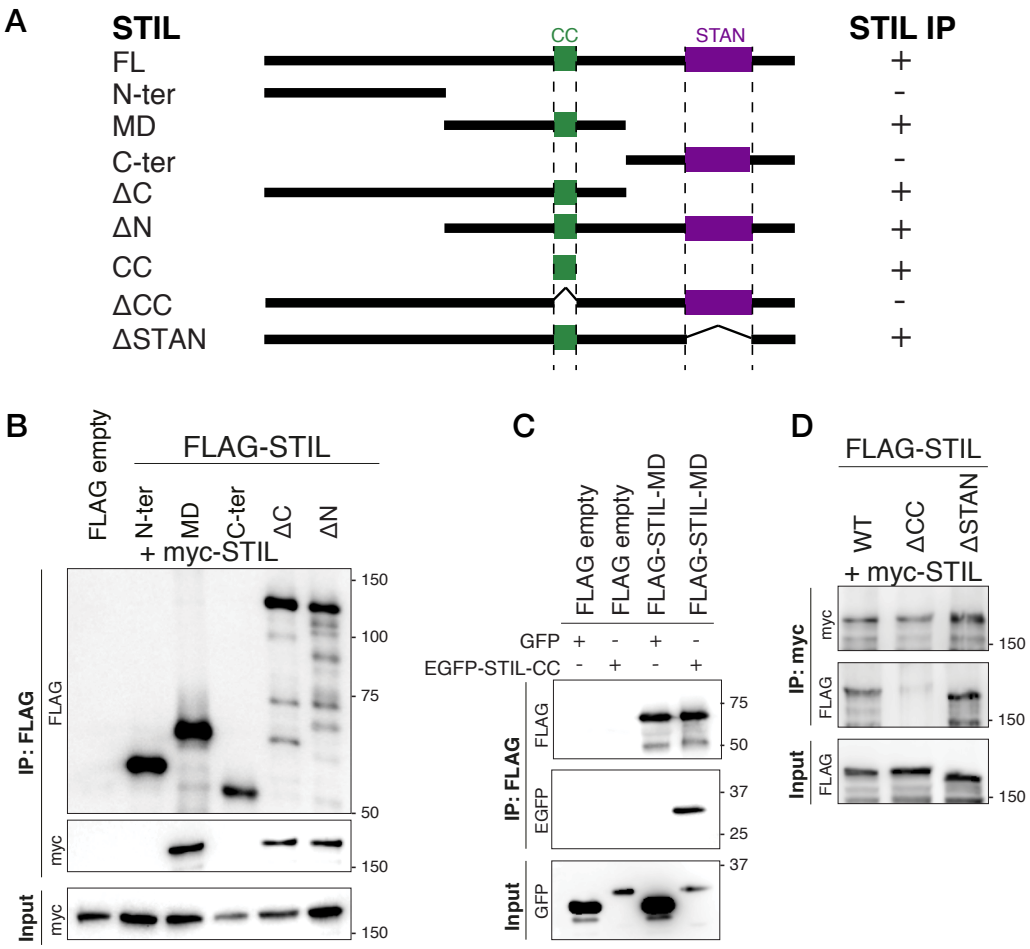

Supplemental Figure 3.3 The STIL-CC domain is essential for STIL oligomerization.
A Schematic illustration of STIL constructs used for the co-immunoprecipitation experiments shown in (B-D). On the right, the relative strengths of the interactions are indicated (+, strong; +/-, weak; -, not detected). **B-D** Western blot analysis of co-immunoprecipitation experiments to map the region required for STIL self-association. HEK293T cells were transfected with the indicated plasmids to co-express the corresponding STIL constructs for 24-36 hours. Subsequently, cells were lysed and co-immunoprecipitations were performed with anti-myc or anti-FLAG antibodies.

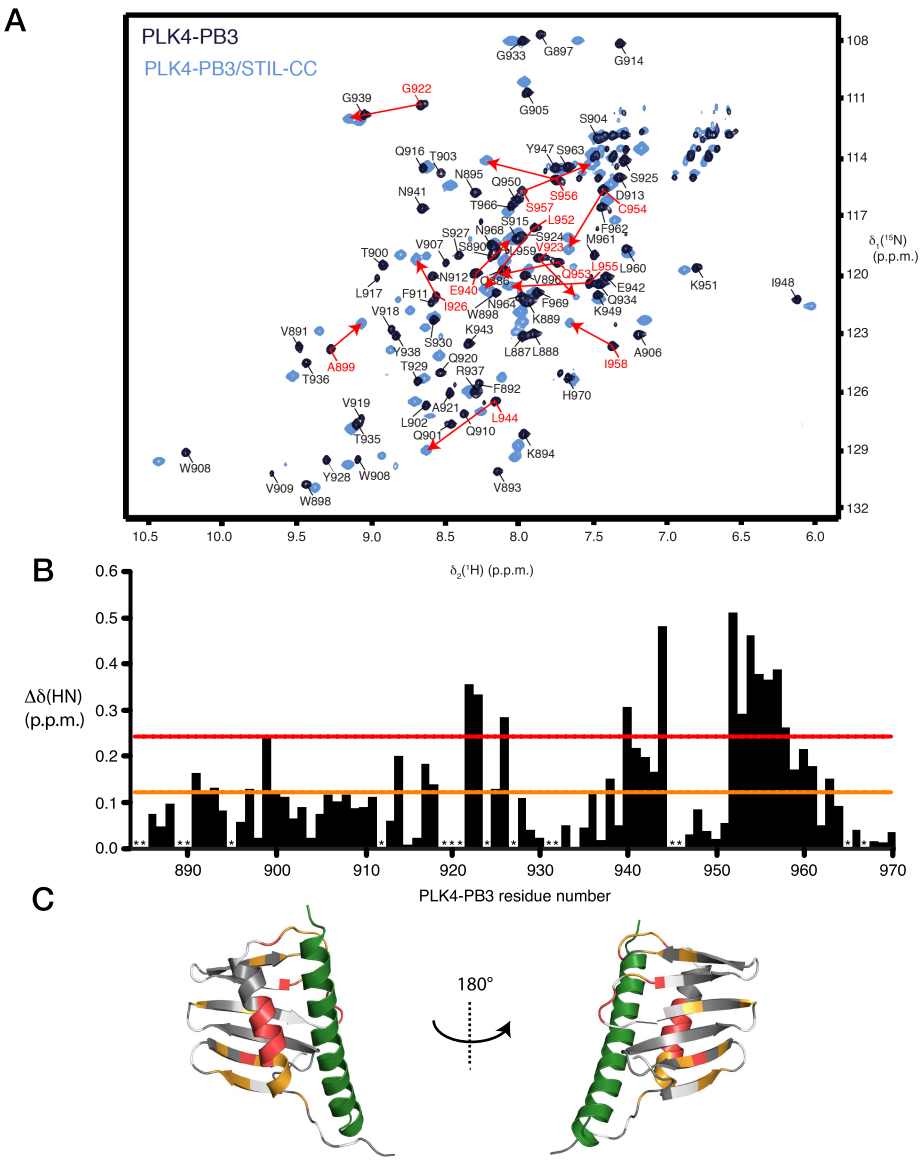

Supplemental Figure 3.4 Binding of STIL-CC to PLK4-PB3.
A Overlay of 2D [^{15}N,^{1}H]-TROSY spectra of 0.8 mM [*U*-^{15}N]-PLK4-PB3 (dark blue) and 0.6 mM [*U*-^{15}N]-PLK4-PB3 in complex with unlabeled STIL-CC (light blue) recorded at 20 °C. The sequence-specific resonance assignments for PLK4-PB3 are indicated. The assignments for PLK4-PB3 in complex with STIL-CC are not shown for clarity. Corresponding backbone amide resonances with chemical shift difference larger than two s.d. (see below) between apo and holo PLK4-PB3 are connected by red arrows. **B** Chemical shift perturbation of PLK4-PB3 amide moieties upon STIL-CC binding. The magnitude of one s.d. (0.12 p.p.m.) is indicated by an orange line and the magnitude of two s.d. (0.24 p.p.m.) is indicated by a red line. Asterisks indicate residues that are not assigned in both forms. **C** Chemical shift perturbation of PLK4-PB3 upon STIL binding, as mapped on the crystal structure of PLK4-PB3/STIL-CC in ribbon representation. Residues with (Δδ(HN) < 0.12 p.p.m.), (0.12 p.p.m. < Δδ(HN) < 0.24 ppm), and (0.24 p.p.m. < Δδ(HN)) are shown in grey, orange and red, respectively. Unassigned residues are shaded in light grey. The STIL helix is shown green.

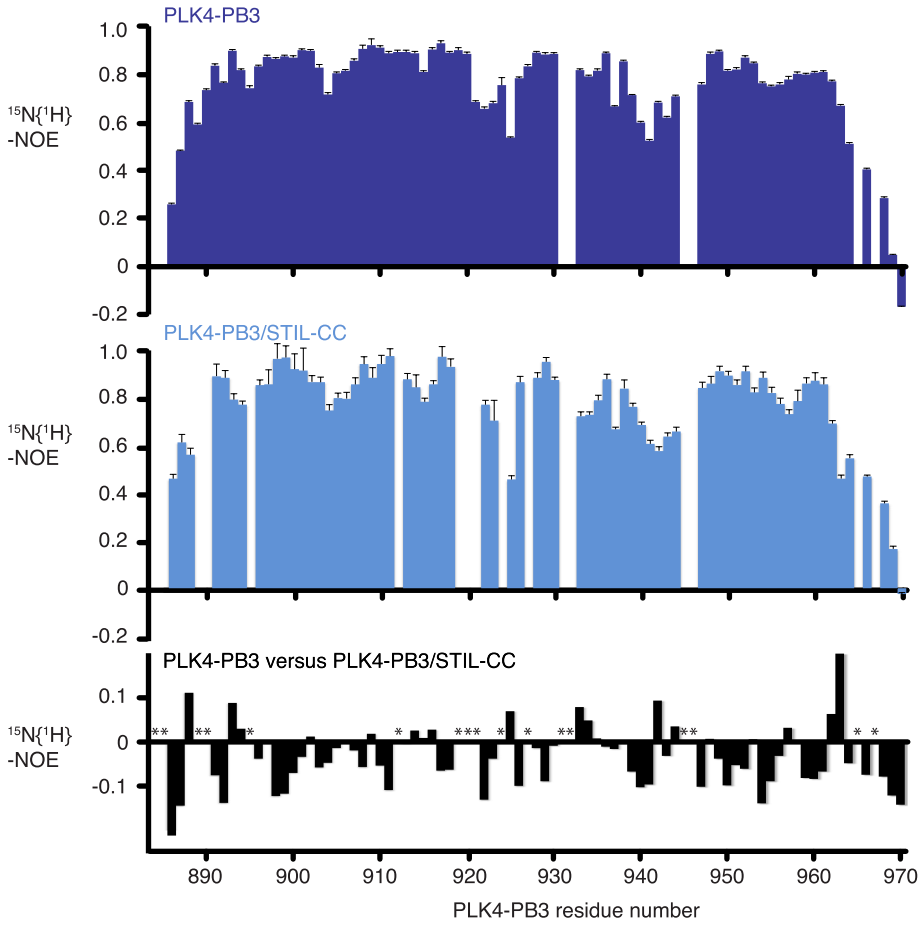

Supplemental Figure 3.5 Backbone dynamics of PLK4-PB3.
Measurements of the $^{15}N\{^{1}H\}$-NOE, which is sensitive to local dynamics on the ps–ns time scale. Backbone dynamics of PLK4-PB3 (dark blue, top) and PLK4-PB3 as part of the PLK4-PB3/STIL-CC complex (light blue, center) and their difference (black, bottom). Asterisks indicate residues that are unassigned in both forms.

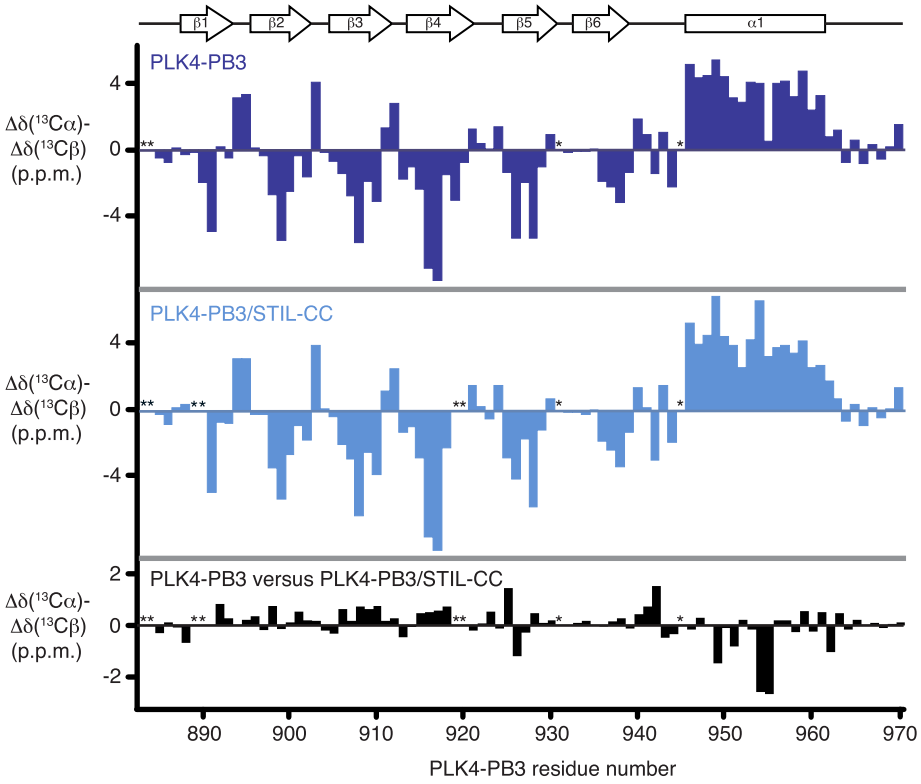

Supplemental Figure 3.6 Secondary structure elements of PLK4 in solution.
Secondary backbone ^{13}C-chemical shifts of PLK4-PB3 (dark blue) and PLK4-PB3 as part of the PLK4-PB3/STIL-CC complex (light blue) and their differences (black), plotted against the amino acid residue number of PLK4-PB3. Asterisks indicate unassigned residues. Secondary structural elements as identified in the PLK4-PB3/STIL-CC crystal structure are shown at the top. STIL-CC binding increases the helicity at residues 954 and 955 in helix α1, as indicated by an increase of secondary ^{13}C chemical shifts.

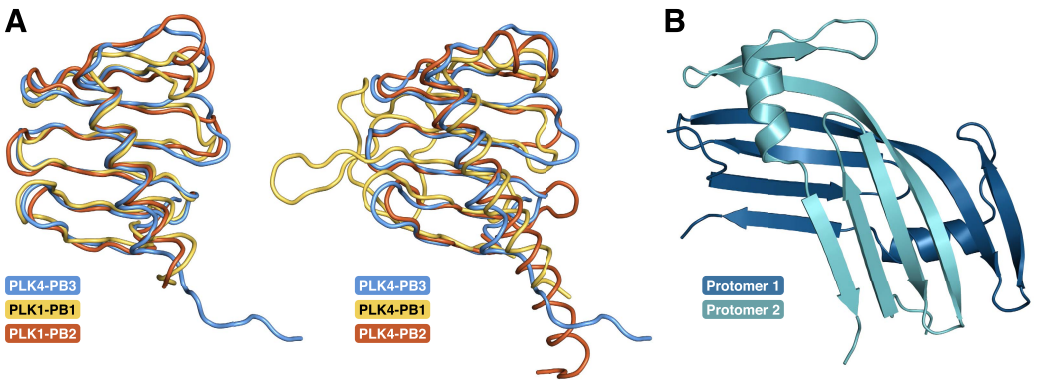

Supplemental Figure 3.7 PB3 adopts a canonical Polo-box fold

A Comparison of the fold of PLK4-PB3 (lightblue) to the folds of PB1 (1.7 Å rmsd, 72 Cα) and PB2 (1.3 Å rmsd, 79 Cα) of PLK1 (PDB accession code: 1Q4O, left)[94] and of PB1 (2.5 Å rmsd, 66 Cα) and PB2 (1.4 Å rmsd, 68 Cα) of PLK4 (PDB accession code: 4N9J, right[111] by structural superposition[237]. For the alignments the crystal structure of PLK4-PB3 was used. **B** Crystal structure of the domain-swapped dimer of the PLK4-PB3 murine ortholog SAK in cartoon representation[112].

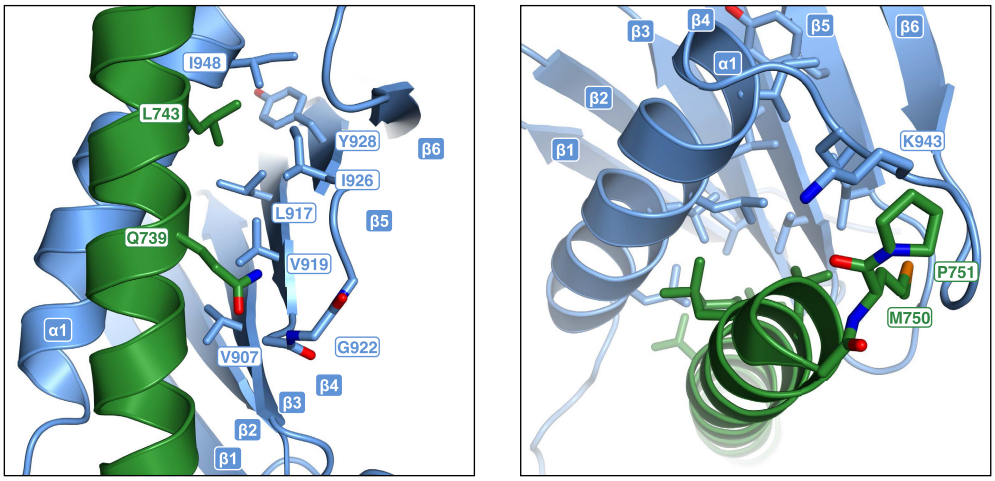

Supplemental Figure 3.8 STIL-CC binding to PLK4-PB3 mimics coiled-coil interactions

Close-up views of the STIL-CC/PLK4-PB3 binding interface. Key contributing residues to the interaction between PLK4-PB3 (light blue) and STIL-CC (green) are indicated.

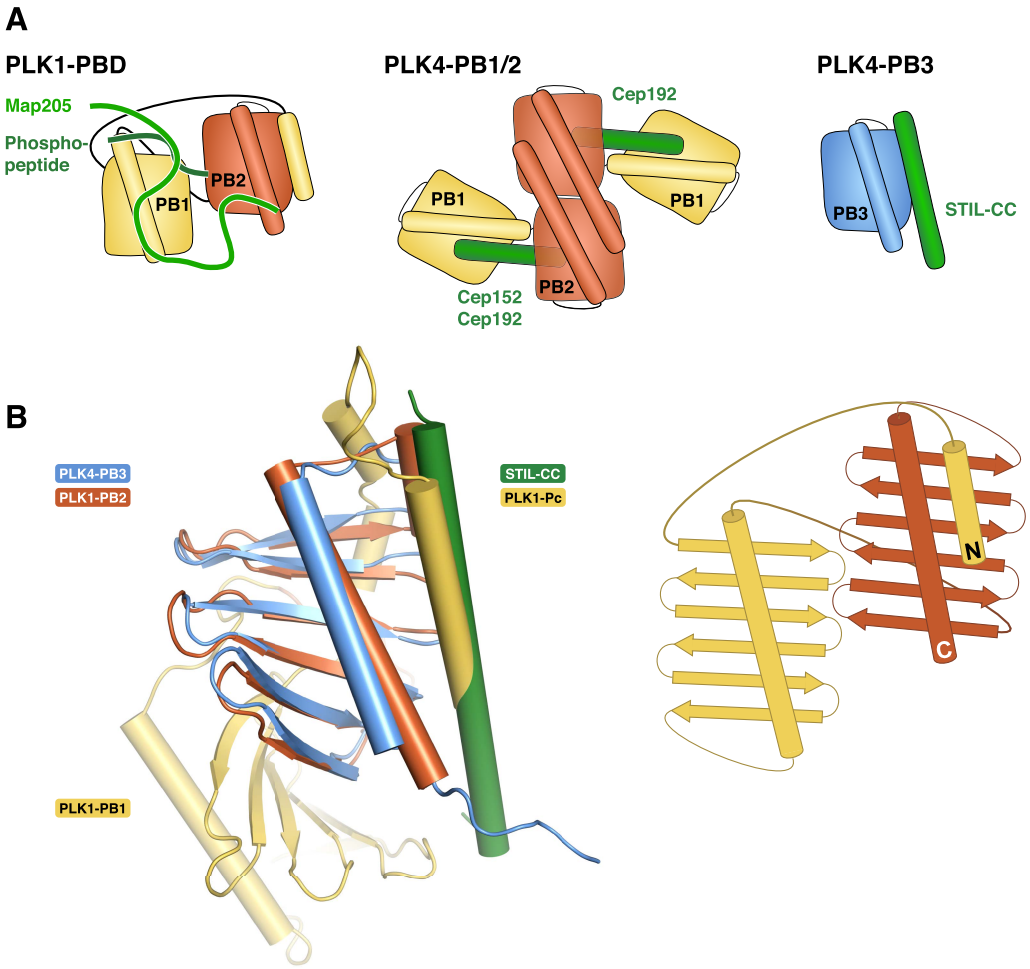

Supplemental Figure 3.9 STIL-CC binding to PLK4-PB3 resembles an intramolecular interaction of PB2 and Pc in PLK1

A Schematic representation of previously observed substrate peptide binding modes in Polo-boxes[80,94,97,111]. **B** Left: Structural superposition of PLK4-PB3 (light blue) onto PB2 (orange) in the intact PLK1-PB1/2 structure[80]. The bound STIL-CC peptide (green) occupies the same position on PLK4-PB3 as the Polo-cap helix (PLK1-Pc, yellow), which binds intramolecularly in the PLK1-PB1/2 structure. Right: Schematic representation of the relative orientation of PLK1-PB1 and PLK1-PB2 and the position of the PLK1-Pc.

Supplemental Table 3.1 Molecular mass determination by lateral diffusion measurements.

Protein molecule	Theoretical molecular mass[a]	Diffusion coefficient[b]	Experimental molecular mass[c]
PLK4-PB3	9.6 kDa	$1.13 \cdot 10^{-10}$ D [$m^2 s^{-1}$]	9.6 kDa
PLK4-PB3/STIL-CC	13.4 kDa	$9.64 \cdot 10^{-11}$ D [$m^2 s^{-1}$]	15.3 kDa
GB1[d]	6.2 kDa	$1.22 \cdot 10^{-10}$ D [$m^2 s^{-1}$]	7.6 kDa

[1]Calculated from the amino acid sequence for a protein monomer

[b]Determined by BPP-LED NMR experiments

[c]Calculated from the diffusion coefficient assuming spherical, rigid molecules

[d]Control protein: Immunoglobulin binding domain of streptococcal protein G[238]

4 The dynamic organization of fungal acetyl-CoA carboxylase

Reproduced from:

The Dynamic Organization of Fungal Acetyl-CoA Carboxylase

Moritz Hunkeler*, Edward Stuttfeld*, Anna Hagmann, **Stefan Imseng** and Timm Maier

*Authors contributed equally to this work

Nature Communications 7, Article Number: 11196

DOI 10.1038/ncomms11196

4.1 Abstract

Acetyl-CoA carboxylases (ACCs) catalyze the committed step in fatty acid biosynthesis, the ATP-dependent carboxylation of acetyl-CoA to malonyl-CoA. They are important regulatory hubs for metabolic control and relevant drug targets for the treatment of the metabolic syndrome and cancer. Eukaryotic ACCs are single-chain multienzymes characterized by a large, non-catalytic central domain (CD), whose role in ACC regulation remains poorly characterized. Here we report the crystal structure of the yeast ACC CD, revealing a unique four-domain organization. A regulatory loop, which is phosphorylated at the key functional phosphorylation site of fungal ACC, wedges into a crevice between two domains of CD. Combining the yeast CD structure with intermediate and low-resolution data of larger fragments up to intact ACCs provides a comprehensive characterization of the dynamic fungal ACC architecture. In contrast to related carboxylases, large-scale conformational changes are required for substrate turnover, and are mediated by the CD under phosphorylation control.

4.2 Introduction

Biotin-dependent acetyl-CoA carboxylases (ACCs) are essential enzymes that catalyze the ATP-dependent carboxylation of acetyl-CoA to malonyl-CoA. This reaction provides the committed activated substrate for the biosynthesis of fatty acids via fatty acid synthase[239,240]. By catalyzing this rate-limiting step in fatty acid biosynthesis, ACC plays a key role in anabolic metabolism. ACC inhibition and knock-out studies show the potential of targeting ACC for treatment of the metabolic syndrome[241-243]. Furthermore, elevated ACC activity is observed in malignant tumors[244,245]. A direct link between ACC and cancer is provided by cancer-associated mutations in the breast cancer susceptibility gene 1 (BRCA1), which relieve inhibitory interactions of BRCA1 with ACC[125,126]. Thus, ACC is a relevant drug target for type 2 diabetes and cancer[117,246,247]. Microbial ACCs are also the principal target of antifungal and antibiotic compounds, such as Soraphen A[134,248].

The principal functional protein components of ACCs have been described already in the late 1960's for *Escherichia coli* (*E. coli*) ACC[249,250]: Biotin carboxylase (BC) catalyzes the ATP-dependent carboxylation of a biotin moiety, which is covalently linked to the biotin carboxyl carrier protein (BCCP). Carboxyltransferase (CT) transfers

the activated carboxyl group from carboxy-biotin to acetyl-CoA to yield malonyl-CoA. Prokaryotic ACCs are transient assemblies of individual BC, CT and BCCP subunits[133]. Eukaryotic ACCs, instead, are multienzymes, which integrate all functional components into a single polypeptide chain of Here we report the crystal structure of the yeast ACC CD, revealing a unique four-domain organization ~2300 amino acids[240]. Human ACC occurs in two closely related isoforms, ACC1 and 2, located in the cytosol and at the outer mitochondrial membrane, respectively[251,252]. In addition to the canonical ACC components, eukaryotic ACCs contain two non-catalytic regions, the large central domain (CD) and the BC-CT interaction domain (BT). The CD comprises one third of the protein and is a unique feature of eukaryotic ACCs without homologs in other proteins. The function of this domain remains poorly characterized, although phosphorylation of several serine residues in the CD regulates ACC activity[253-255]. The BT domain has been visualized in bacterial carboxylases, where it mediates contacts between α- and β-subunits[256,257].

Structural studies on the functional architecture of intact ACCs have been hindered by their huge size and pronounced dynamics, as well as the transient assembly mode of bacterial ACCs. However, crystal structures of individual components or domains from prokaryotic and eukaryotic ACCs, respectively, have been solved[118,135,136,258,259]. The structure determination of the holoenzymes of bacterial biotin-dependent carboxylases, which lack the characteristic CD, such as the pyruvate carboxylase (PC)[260], propionyl-CoA carboxylase (PCC)[256], 3-methyl-crotonyl-CoA carboxylase (MCC)[257] and a long-chain acyl-CoA carboxylase (LCC)[261] revealed strikingly divergent architectures despite a general conservation of all functional components. In these structures, the BC and CT active sites are at distances between 40 and 80 Å, such that substrate transfer could be mediated solely by the mobility of the flexibly tethered BCCP.

Human ACC1 is regulated allosterically, via specific protein-protein interactions and by reversible phosphorylation. Dynamic polymerization of human ACC1 is linked to increased activity and is regulated allosterically by the activator citrate and the inhibitor palmitate[123,253] or by binding of the small protein MIG12[124]. Human ACC1 is further regulated by specific phosphorylation-dependent binding of BRCA1 to Ser1263 in the CD. BRCA1 binds only to the phosphorylated form of ACC1 and prevents ACC activation by phosphatase-mediated dephosphorylation[125,127]. Furthermore, phosphorylation by AMP-activated protein kinase (AMPK) and cAMP-dependent protein kinase (PKA) leads to a decrease in ACC1 activity. AMPK phosphorylates

ACC1 *in vitro* at Ser80, Ser1201 and Ser1216 and PKA at Ser78 and Ser1201. However, regulatory effects on ACC1 activity are mainly mediated by phosphorylation of Ser80 and Ser1201[128,129]. Phosphorylated Ser80, which is highly conserved only in higher eukaryotes, presumably binds into the Soraphen A-binding pocket[262]. The regulatory Ser1201 shows only moderate conservation across higher eukaryotes, while the phosphorylated Ser1216 is highly conserved across all eukaryotes. However, no effect of Ser1216 phosphorylation on ACC activity has been reported in higher eukaryotes.

For fungal ACC, neither spontaneous nor inducible polymerization has been detected despite considerable sequence conservation to human ACC1. The BRCA1-interacting phosphoserine position is not conserved in fungal ACC, and no other phospho-dependent protein-protein interactions of fungal ACC have been described. In yeast ACC, phosphorylation sites have been identified at Ser2, Ser735, Ser1148, Ser1157 and Ser1162. Of these, only Ser1157 is highly conserved in fungal ACC and aligns to Ser1216 in human ACC1. Its phosphorylation by the AMPK homologue SNF1 results in strongly reduced ACC activity[130,132,255].

Despite the outstanding relevance of ACC in primary metabolism and disease, the dynamic organization and regulation of the giant eukaryotic, and in particular fungal ACC, remain poorly characterized. Here we provide the structure of Saccharomyces cerevisiae (Sce) ACC CD, intermediate- and low-resolution structures of human (Hsa) ACC CD and larger fragments of fungal ACC from Chaetomium thermophilum (Cth; Figure 4.1A). Integrating these data with small-angle X-ray scattering (SAXS) and electron microscopy (EM) observations yield a comprehensive representation of the dynamic structure and regulation of fungal ACC.

4.3 Results

4.3.1 The organization of the yeast ACC CD

First, we focused on structure determination of the 82 kDa CD. The crystal structure of the CD of *Sce*ACC (*Sce*CD) was determined at 3.0 Å resolution by experimental phasing and refined to R_{work}/R_{free}= 0.20/0.25 (Table 4.1). The overall extent of the *Sce*CD is 70 by 75 Å (Figure 4.1B, Supplemental Figure 4.1A,B) and the attachment points of the N-terminal 26-residue linker to the BCCP and the C-terminal CT are separated by 46 Å (termini are indicated with spheres in Figure 4.1B). *Sce*CD comprises four distinct domains, an N-terminal α-helical domain (CD_N), and a central

four-helix bundle linker domain (CD_L) followed by two α-β-fold C-terminal domains (CD_{C1}/CD_{C2}). CD_N adopts a letter C shape, where one of the ends is a regular four-helix bundle (Nα3-6), the other end is a helical hairpin (Nα8,9) and the bridging region comprises six helices (Nα1,2,7,10-12). CD_L is composed of a small, irregular four-helix bundle (Lα1-4) and tightly interacts with the open face of CD_{C1} via an interface of 1300 $Å^2$ involving helices Lα3 and Lα4. CD_L does not interact with CD_N apart from the covalent linkage and forms only a small contact to CD_{C2} via a loop between Lα2/α3 and the N-terminal end of Lα1 with an interface area of 400 $Å^2$. CD_{C1}/CD_{C2} share a common fold; they are composed of six-stranded β-sheets flanked on one side by two long, bent helices inserted between strands β3/β4 and β4/β5. CD_{C2} is extended at its C-terminus by an additional β-strand and an irregular β-hairpin. On the basis of root mean square deviation of main chain atom positions of 2.2 Å, CD_{C1}/CD_{C2} are structurally more closely related to each other than to any other protein (Figure 4.1C); they may thus have evolved by duplication. Close structural homologs could not be found for the CD_N or the CD_C domains.

4.3.2 A regulatory loop mediates interdomain interactions

To define the functional state of insect-cell expressed ACC variants, we employed mass spectrometry (MS) for phosphorylation site detection. In insect-cell expressed full-length *Sce*ACC, the highly conserved Ser1157 is the only fully occupied phosphorylation site with functional relevance in *S. cerevisiae*. Additional phosphorylation was detected for Ser2101 and Tyr2179, however these sites are neither conserved across fungal ACC nor natively phosphorylated in yeast. MS analysis of dissolved crystals confirmed the phosphorylated state of Ser1157 also in *Sce*CD crystals. The *Sce*CD structure thus authentically represents the state of *Sce*ACC, where the enzyme is inhibited by SNF1-dependent phosphorylation.

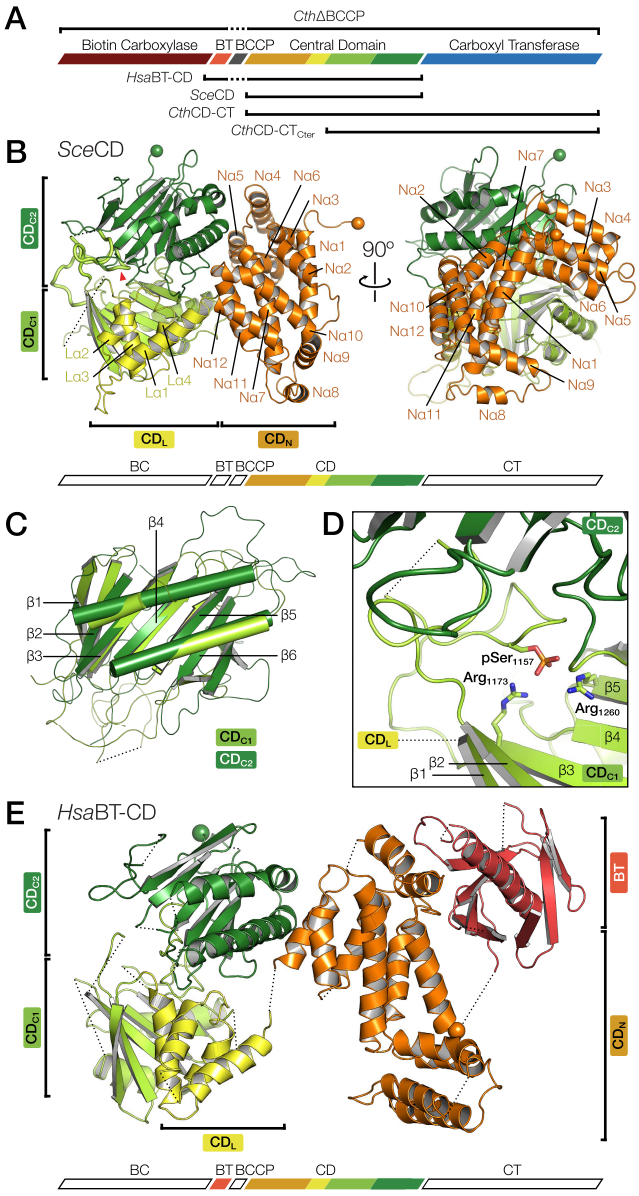

Figure 4.1 The phosphorylated central domain of yeast ACC.
A Schematic overview of the domain organization of eukaryotic ACCs. Crystallized constructs are indicated. **B** Cartoon representation of the SceCD crystal structure. CD_N is linked by a four-helix bundle (CD_L) to two a–b-fold domains (CD_{C1} and CD_{C2}). The regulatory loop is shown as bold cartoon, and the phosphorylated Ser1157 is marked by a red triangle. The N- and C termini are indicated by spheres. **C** Superposition of CD_{C1} and CD_{C2} reveals highly conserved folds. **D** The regulatory loop with the phosphorylated Ser1157 is bound into a crevice between CD_{C1} and CD_{C2}, the conserved residues Arg1173 and Arg1260 coordinate the phosphoryl-group. **E** Structural overview of *Hsa*BT-CD. The attachment points to the N-terminal BCCP domain and the C-terminal CT domain are indicated with spheres. All colourings are according to scheme A.

Table 4.1 Crystallographic data collection and refinement statistics.

*Resolution cutoffs determined based on internal correlation significant at the 0.1% level as calculated by XDS.

[w]Highest-resolution shell is shown in parentheses.

[z]Modelled only as poly-alanine.

	***Sce*CD**	***Sce*CD Thimerosal**	***Sce*CD Eu**	***Hsa*BT-CD**	***Hsa*BT-CD Cd^{+2}**	***Cth*CD-CT_{Cter1}**	***Cth*CD-CT_{Cter2}**	***Cth*CD-CT**	***Cth*ΔBCCP**
Data Collection									
Space Group	P4$_2$2$_1$2	P4$_2$2$_1$2	P4$_2$2$_1$2	I422	I422	P222	P222	P3$_2$2$_1$	P6$_2$2$_2$
Cell dimensions (Å)									
a	110.86	111.22	108.65	267.27	267.67	97.66,	100.17,	295.02,	462.20
b	110.86	111.22	108.65	267.27	267.67	165.34,	153.45,	295.02	462.20,
c	131.12	131.49	127.36	210.61	210.46	219.23	249,24	189.52	204.64
α, β, γ (°)	90, 90, 90	90, 90, 90	90, 90, 90	90, 90, 90	90, 90, 90	90, 90, 90	90, 90, 90	90, 90, 120	90, 90, 120
Resolution[w]	3.0	3.4	4.0	3.7	4.1	3.6	4.5	7.2	8.4
R_{sym}*	18.2 (389.6)	20.5 (306.1)	40.6 (327.0)	7.5 (400.9)	15 (730.5)	14.5 (384.5)	27.4 (225.6)	5.6 (302.6)	29.4 (381.7)
CC ½*	100 (58.3)	99.9 (42.6)	99.9 (48.5)	100 (59.4)	99.8 (73.2)	99.9 (50.9)	99.5 (46.7)	100 (33.3)	99.7 (35)
I / σI*	24.68 (1.46)	7.99 (0.89)	17.92 (1.85)	21.24 (1.07)	16.53 (1.41)	10.61 (0.97)	6.35 (1.00)	18.95 (0.92)	9.05 (0.9)
Completeness*	99.9 (99.9)	99.6 (100)	99.7 (96.8)	99.8 (99.1)	99.8 (99.7)	99.7 (99.9)	99.4 (98.6)	99.6 (100)	99.1 (99.9)
Redundancy*	39.1 (39.8)	12.1 (14.3)	81.6 (65.2)	13.7 (13.7)	20.9 (19.1)	12.7 (13.5)	6.1 (6.5)	9.9 (10.4)	18.5 (18.2)
Refinement									
Resolution	3.0			3.7		3.6	4.5	7.2	8.4
Total Reflections*	662713 (49004)	383712 (64731)	1018078 (58962)	1061661 (78722)	1238529 (84313)	529104 (41183)	142751 (27042)	139139 (10777)	224630 (15976)
Unique Reflections*	16929 (1232)	31675 (4521)	12473 (905)	77629 (5730)	59386 (4406)	41802 (3046)	23225 (4148)	14050 (1040)	12113 (880)
R_{cryst}/R_{free}	0.20/0.25	-	-	0.38/0.41	-	0.20/0.25	0.26/0.30	0.26/0.28	0.31/0.34
Number of Atoms									
...Protein	5543			6843		16330	16330	22582	22582
Waters	76	-	-	-	-	-	-	-	-
Ligand/ion	7	-	-	-	-	-	-	-	-
B-factors									
...Protein	129			84		221	268	276	261
Waters	84	-	-	-	-	-	-	-	-
Ligand/ion	93	-	-	-	-	-	-	-	-
R.m.s. deviations									
RMS (angles, °)	1.07	-	-	1.56	-	1.23	1.15	1.14	1.03
RMS (bonds, Å)	0.01	-	-	0.01	-	0.01	0.01	0.01	0.01

In the *Sce*CD crystal structure, the phosphorylated Ser1157 resides in a regulatory 36-amino acid loop between strands β2 and β3 of CD_{C1} (Figure 4.1B,D), which contains two additional less conserved phosphorylation sites (Ser1148, Ser1162) confirmed in yeast[263], but not occupied here. This regulatory loop wedges between the CD_{C1} and CD_{C2} domains and provides the largest contribution to the interdomain interface. The N-terminal region of the regulatory loop also directly contacts the C-terminal region of CD_{C2} leading into CT. Phosphoserine 1157 is tightly bound by two highly conserved arginines (Arg1173, Arg1260) of CD_{C1} (Figure 4.1D). Already the binding of phosphorylated Ser1157 apparently stabilizes the regulatory loop conformation, the accessory phosphorylation sites Ser1148 and Ser1162 in the same loop may further modulate the strength of interaction between the regulatory loop and the CD_{C1} and CD_{C2} domains. Phosphorylation of the regulatory loop thus determines interdomain interactions of CD_{C1} and CD_{C2} suggesting that it may exert its regulatory function by modifying the overall structure and dynamics of the CD.

The functional role of Ser1157 was confirmed by an activity assay based on the incorporation of radioactive carbonate into acid non-volatile material[264]. Phosphorylated *Sce*ACC shows only residual activity (k_{cat} = 0.4 ± 0.2 s^{-1}), which increases 16-fold (k_{cat} = 6.5 ± 0.3 s^{-1}) after dephosphorylation with λ protein phosphatase. The values obtained for dephosphorylated *Sce*ACC are comparable to earlier measurements of non-phosphorylated yeast ACC expressed in *E. coli*[265].

4.3.3 The variable CD is conserved between yeast and human

To compare the organization of fungal and human ACC CD, we determined the structure of a human ACC1 fragment that comprises the BT and CD domains (*Hsa*BT-CD), but lacks the mobile BCCP in between (Figure 4.1A). An experimentally-phased map was obtained at 3.7 Å resolution for a cadmium-derivatized crystal and was interpreted by a poly-alanine model (Figure 4.1E, Table 4.1). Each of the four CD domains in *Hsa*BT-CD individually resembles the corresponding *Sce*CD domain; however, human and yeast CDs exhibit distinct overall structures. In agreement with their tight interaction in *Sce*CD, the relative spatial arrangement of CD_{C1} and CD_L is preserved in *Hsa*BT-CD, but the human CD_L/CD_{C1} didomain is tilted by 30° based on a superposition of human and yeast CD_{C2} (Supplemental Figure 4.1C). As a result, the N-terminus of CD_L at helix Lα1, which connects to CD_N, is shifted by 12 Å. Remarkably, CD_N of *Hsa*BT-CD adopts a completely different orientation compared

to *Sce*CD. With CD_L/CD_{C1} superposed, CD_N in *Hsa*BT-CD is rotated by 160° around a hinge at the connection of CD_N/CD_L (Supplemental Figure 4.1D). This rotation displaces the N-terminus of CD_N in *Hsa*BT-CD by 51 Å compared to *Sce*CD resulting in a separation of the attachment points of the N-terminal linker to the BCCP domain and the C-terminal CT domain by 67 Å (the attachment points are indicated with spheres in Figure 4.1E). The BT domain of *Hsa*BT-CD consists of a helix that is surrounded at its N-terminus by an anti-parallel eight-stranded β-barrel. It resembles the BT of PCC[256], only the four C-terminal strands of the β-barrel are slightly tilted.

On the basis of MS analysis of insect-cell expressed human full-length ACC Ser80 shows the highest degree of phosphorylation (90%). Ser29 and Ser1263, implicated in insulin-dependent phosphorylation and BRCA1 binding, respectively, are phosphorylated at intermediate levels (40%). The highly conserved Ser1216 (corresponding to *S. cerevisiae* Ser1157), as well as Ser1201, both in the regulatory loop discussed above, are not phosphorylated. However, residual phosphorylation levels were detected for Ser1204 (7%) and Ser1218 (7%) in the same loop. MS analysis of the *Hsa*BT-CD crystallization sample reveals partial proteolytic digestion of the regulatory loop. Accordingly, most of this loop is not represented in the *Hsa*BT-CD crystal structure. The absence of the regulatory loop might be linked to the less restrained interface of CD_{C2} and CD_L/CD_{C1} and altered relative orientations of these domains. Besides the regulatory loop, also the phosphopeptide target region for BRCA1 interaction is not resolved presumably because of pronounced flexibility.

At the level of isolated yeast and human CD, the structural analysis indicates the presence of at least two hinges, one with large-scale flexibility at the CD_N/CD_L connection, and one with tunable plasticity between CD_{C2} and CD_L/CD_{C1}, plausibly affected by phosphorylation in the regulatory loop region.

4.3.4 The integration of CD into the fungal ACC multienzyme

To further obtain insights into the functional architecture of fungal ACC, we characterized larger multidomain fragments up to the intact enzymes. Using molecular replacement based on fungal ACC BC, CD and CT models, we obtained structures of a variant comprising *Cth*CT and CD_{C1}/CD_{C2} in two crystal forms at resolutions of 3.6 Å and 4.5 Å (*Cth*CD-$CT_{Cter1/2}$), respectively, as well as of a *Cth*CT linked to the entire CD at 7.2 Å resolution (*Cth*CD-CT) (Figure 4.1A, Figure 4.2, Table 4.1). No crystals diffracting to sufficient resolution were obtained for larger BC-containing

fragments, or for full-length *Cth* or *Sce*ACC. To improve crystallizibility, we generated ΔBCCP variants of full-length ACC, which based on SAXS analysis preserve properties of intact ACC (Supplemental Figure 4.2A-C). For *Cth*ΔBCCP, crystals diffracting to 8.4 Å resolution were obtained. However, molecular replacement did not reveal a unique positioning of the BC domain. Owing to the limited resolution the discussion of structures of *Cth*CD-CT and *Cth*ΔBCCP is restricted to the analysis of domain localization. Still, these structures contribute considerably to the visualization of an intrinsically dynamic fungal ACC.

In all these crystal structures, the CT domains build a canonical head-to-tail dimer[118], with active sites formed by contributions from both protomers (Figure 4.2, Supplemental Figure 4.3A). The connection of CD and CT is provided by a 10-residue peptide stretch, which links the N-terminus of CT to the irregular β-hairpin/β-strand extension of CD_{C2} (Supplemental Figure 4.3B). The connecting region is remarkably similar in isolated CD and *Cth*CD-CT_{Cter} structures, indicating inherent conformational stability. CD/CT contacts are only formed in direct vicinity of the covalent linkage and involve the β-hairpin extension of CD_{C2} as well as the loop between strands β2/β3 of the CT N-lobe, which contains a conserved RxxGxN motif. The neighboring loop on the CT side (between CT β1/β2) is displaced by 2.5 Å compared to isolated CT structures (Supplemental Figure 4.3C). On the basis of an interface area of ~600 $Å^2$ and its edge-to-edge connection characteristics, the interface between CT and CD might be classified as conformationally variable. Indeed, the comparison of the positioning of eight instances of the C-terminal part of CD relative to CT in crystal structures determined here reveals flexible interdomain linking (Figure 4.3A): The CD_{C2}/CT interface acts as a true hinge with observed rotation up to 16°, which results in a translocation of the distal end of CD_{C2} by 8 Å.

The interface between CD_{C2} and CD_L/CD_{C1}, which is mediated by the phosphorylated regulatory loop in the *Sce*CD structure, is less variable than the CD-CT junction, and permits only limited rotation and tilting (Figure 4.3B). Analysis of the impact of phosphorylation on the interface between CD_{C2} and CD_L/CD_{C1} in *Cth*ACC variant structures is precluded by the limited crystallographic resolution. However, MS analysis of *Cth*CD-CT and CthΔBCCP constructs revealed between 60 and 70% phosphorylation of Ser1170 (corresponding to *Sce*ACC Ser1157).

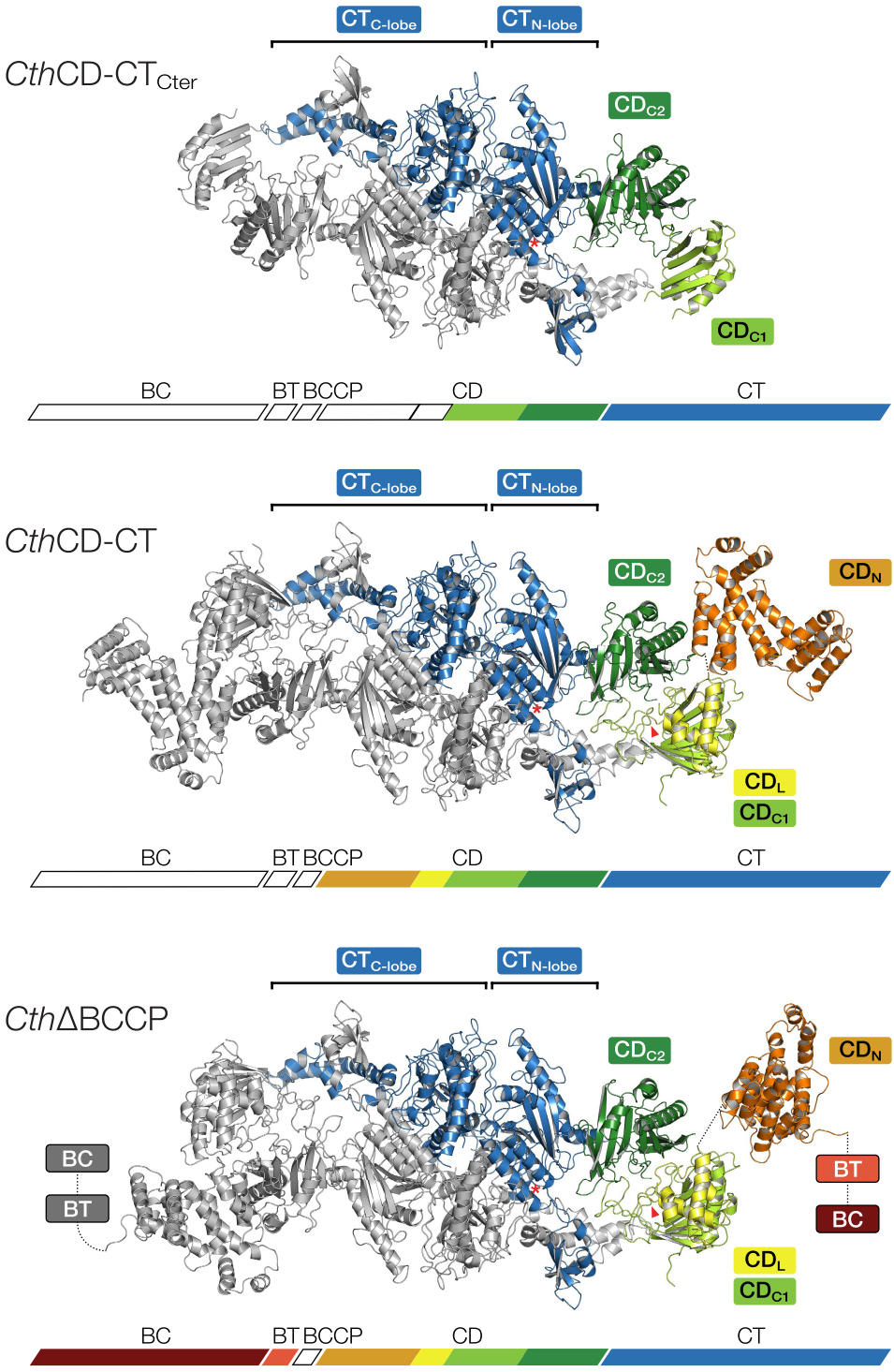

Figure 4.2 Architecture of the CD–CT core of fungal ACC.
Cartoon representation of crystal structures of multidomain constructs of *Cth*ACC. One protomer is shown in colour and one in grey. Individual domains are labelled; the active site of CT and the position of the conserved regulatory phosphoserine site based on *Sce*CD are indicated by an asterisk and a triangle, respectively.

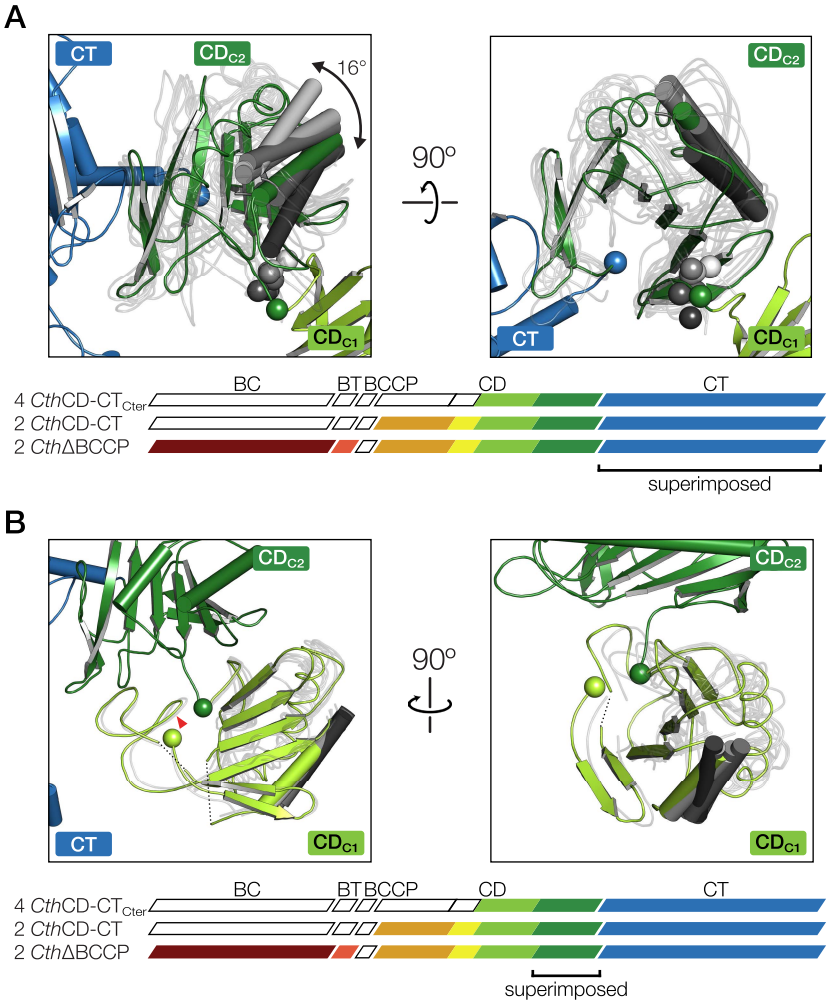

Figure 4.3 Variability of the connections of CD_{C2} to CT and CDC1 in fungal ACC
A Hinge properties of the CD_{C2}–CT connection analysed by a CT-based superposition of eight instances of the CD_{C2}-CT segment. For clarity, only one protomer of CthCD-CTCter1 is shown in full colour as reference. For other instances, CD_{C2} domains are shown in transparent tube representation with only one helix each highlighted. The range of hinge bending is indicated and the connection points between CD_{C2} and CT (blue) as well as between CD_{C1} and CD_{C2} (green and grey) are marked as spheres. **B** The interdomain interface of CD_{C1} and CD_{C2} exhibits only limited plasticity. Representation as in a, but the CD_{C1} and CD_{C2} are superposed based on CD_{C2}. One protomer of CthDBCCP is shown in colour, the CD_L domains are omitted for clarity and the position of the phosphorylated serine based on SceCD is indicated with a red triangle. The connection points from CDC1 to CDC2 and to CDL are represented by green spheres.

The CD_N domain positioning relative to CD_L/CD_{C1} is highly variable with three main orientations observed in the structures of *Sce*CD and the larger *Cth*ACC fragments: CD_N tilts, resulting in a displacement of its N-terminus by 23 Å (Figure 4.4A, observed in both protomers of *Cth*CD-CT and one protomer of *Cth*ΔBCCP). In addition, CD_N can rotate around hinges in the connection between CD_N/CD_L by 70° (Figure 4.4B),

observed in the second protomer of *Cth*ΔBCCP) and 160° (Figure 4.4C, observed in *Sce*CD) leading to displacement of the anchor site for the BCCP linker by up to 33 and 40 Å, respectively.

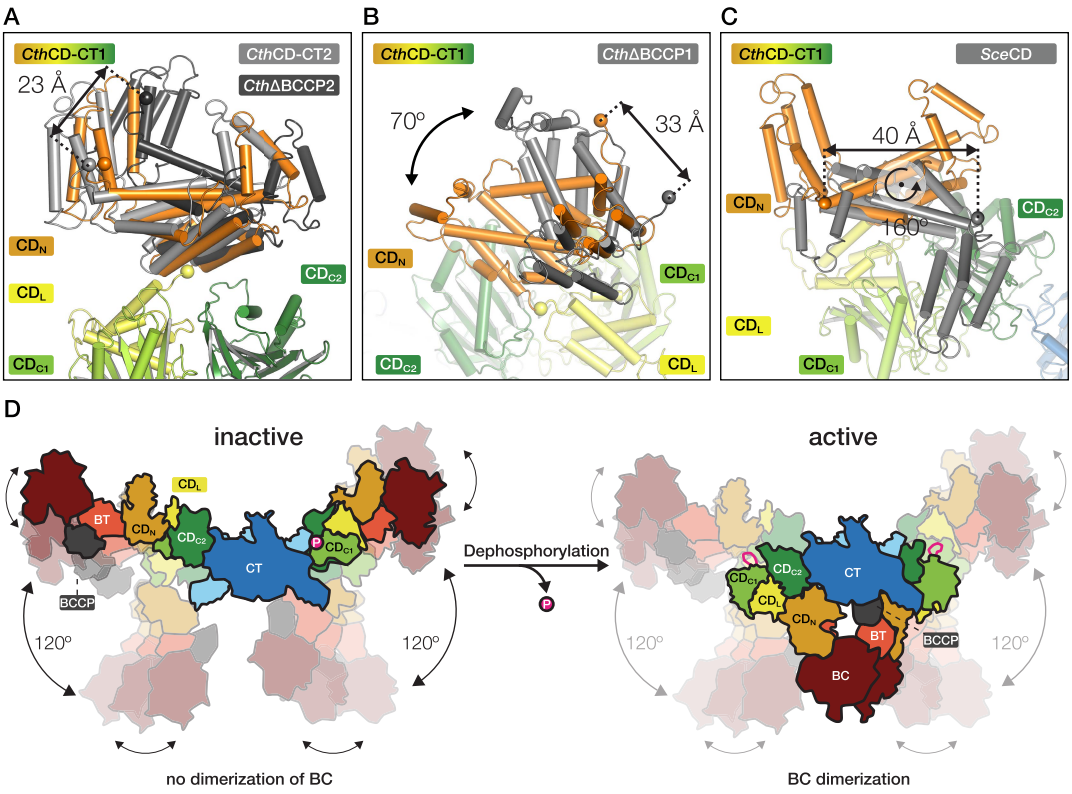

Figure 4.4 The conformational dynamics of fungal ACC.
A-C Large-scale conformational variability of the CD_N domain relative to the CD_L/CD_{C1} domain. CthCD-CT1 (in colour) serves as reference, the compared structures (as indicated, numbers after construct name differentiate between individual protomers) are shown in grey. Domains other than CD_N and CD_L/CD_{C1} are omitted for clarity. The domains are labelled and the distances between the N termini of CD_N (spheres) in the compared structures are indicated. **D** Schematic model of fungal ACC showing the intrinsic, regulated flexibility of CD in the phosphorylated inhibited or the non-phosphorylated activated state. Flexibility of the CD_{C2}/CT and CD_N/CD_L hinges is illustrated by arrows. The Ser1157 phosphorylation site and the regulatory loop are schematically indicated in magenta.

Conformational variability in the CD thus contributes considerably to variations in the spacing between the BC and CT domains, and may extend to distance variations beyond the mobility range of the flexibly tethered BCCP. On the basis of the occurrence of related conformational changes between fungal and human ACC fragments, the observed set of conformations may well represent general states present in all eukaryotic ACCs.

4.3.5 Large-scale conformational variability of fungal ACC

To obtain a comprehensive view of fungal ACC dynamics in solution, we employed SAXS and EM. SAXS analysis of *Cth*ACC agrees with a dimeric state and an elongated shape with a maximum extent of 350 Å (Supplemental Table 4.1). The smooth appearance of scattering curves and derived distance distributions might indicate substantial interdomain flexibility [266] (Supplemental Figure 4.2A-C). Direct observation of individual full- length CthACC particles, according to MS results predominantly in a phosphorylated low-activity state, in negative stain EM reveals a large set of conformations from rod-like extended to U-shaped particles. Class averages, obtained by maximum-likelihood-based 2D classification, are focused on the dimeric CT domain and the full BC-BCCP-CD domain of only one protomer, due to the non-coordinated motions of the lateral BC/CD regions relative to the CT dimer. They identify the connections between CD_N/CD_L and between CD_{C2}/CT as major contributors to conformational heterogeneity (Supplemental Figure 4.4A,B). The flexibility in the CD_{C2}/CT hinge appears substantially larger than the variations observed in the set of crystal structures. The BC domain is not completely disordered, but laterally attached to BT/CD_N in a generally conserved position, albeit with increased flexibility. Surprisingly, in both the linear and U-shaped conformations, the approximate distances between the BC and CT active sites would remain larger than 110 Å. These observed distances are considerably larger than in static structures of any other related biotin-dependent carboxylase. Furthermore, based on an average length of the BCCP-CD linker in fungal ACC of 26 amino acids, mobility of the BCCP alone would not be sufficient to bridge the active sites of BC and CT. Consequently, increased flexibility or additional modes of conformational changes may be required for productive catalysis. The most relevant candidate site for mediating such additional flexibility and permitting an extended set of conformations is the CD_{C1}/CD_{C2} interface, which is rigidified by the Ser1157-phosphorylated regulatory loop as depicted in the *Sce*CD crystal structure.

4.4 Discussion

Altogether, the architecture of fungal ACC is based on the central dimeric CT domain (Figure 4.4D). The CD consists of four distinct subdomains and acts as a tether from the CT to the mobile BCCP and an oriented BC domain. The CD has no direct role in

substrate recognition or catalysis but contributes to the regulation of all eukaryotic ACCs. In higher eukaryotic ACCs, regulation via phosphorylation is achieved by combining the effects of phosphorylation at Ser80, Ser1201 and Ser1263. In fungal ACC however, Ser1157 in the regulatory loop of the CD is the only phosphorylation site that has been demonstrated to be both phosphorylated *in vivo* and involved in the regulation of ACC activity. In its phosphorylated state, the regulatory loop containing Ser1157 wedges between CD_{C1}/CD_{C2} and presumably limits the conformational freedom at this interdomain interface. However, flexibility at this hinge may be required for full ACC activity, as the distances between the BCCP anchor points and the active sites of BC and CT observed here are such large, that mobility of the BCCP alone is not sufficient for substrate transfer. The current data thus suggest that regulation of fungal ACC is mediated by controlling the dynamics of the unique CD, rather than directly affecting catalytic turnover at the active sites of BC and CT. A comparison between fungal and human ACC will help to further discriminate mechanistic differences that contribute to the extended control and polymerization of human ACC. Most recently, a crystal structure of near full-length non-phosphorylated ACC from *S. cerevisae* (lacking only 21 N-terminal amino acids, here denoted as flACC) was published by Wei and Tong[265]. In flACC, the ACC dimer obeys two-fold symmetry and assembles in a triangular architecture with dimeric BC domains (Supplemental Figure 4.5). In their study, mutational data indicate a requirement for BC dimerization for catalytic activity. The transition from the elongated open shape, observed in our experiments, towards a compact triangular shape is based on an intricate interplay of several hinge-bending motions in the CD (Figure 4.4D). Comparison of flACC with our *Cth*ΔBCCP structure reveals the CD_{C2}/CT hinge as a major contributor to conformational flexibility (Supplemental Figure 4.5B,C). In flACC, CD_{C2} rotates ~120° with respect to the CT domain. A second hinge can be identified between CD_{C1}/CD_{C2}. On the basis of a superposition of CD_{C2}, CD_{C1} of the phosphorylated *Sce*CD is rotated by 30° relative to CD_{C1} of the non-phosphorylated flACC (Supplemental Figure 4.5D), similar to what we have observed for the non-phosphorylated *Hsa*BT-CD (Supplemental Figure 4.1D). When inspecting all individual protomer and fragment structures in their study, Wei & Tong also identify the CD_N/CD_{C1} connection as a highly flexible hinge, in agreement with our observations.

The only bona-fide regulatory phophorylation site of fungal ACC in the regulatory loop is directly participating in CD_{C1}/CD_{C2} domain interactions and thus stabilizes the hinge conformation. In flACC, the regulatory loop is mostly disordered, illustrating the

increased flexibility due to the absence of the phosphoryl-group. Only in three out of eight observed protomers a short peptide stretch (including Ser1157) was modeled. In those instances the Ser1157 residue is located at a distance of 14 – 20 Å away from the location of the phosphorylated serine observed here, based on superposition of either CD_{C1} or CD_{C2}. Applying the conformation of the CD_{C1}/CD_{C2} hinge observed in *Sce*CD on flACC leads to CD_N sterically clashing with CD_{C2} and BT/CD_N clashing with CT (Supplemental Figure 4.6A,B). Thus, in accordance with the results presented here, phosphorylation of Ser1157 in *Sce*ACC most likely limits flexibility in the CD_{C1}/CD_{C2} hinge such that activation through BC dimerization is not possible (Figure 4.4D), which however does not exclude intermolecular dimerization. In addition, EM micrographs of phosphorylated and dephosphorylated *Sce*ACC display for both samples mainly elongated and U-shaped conformations and reveal no apparent differences in particle shape distributions, (Supplemental Figure 4.7). This implicates that the triangular shape with dimeric BC domains has a low population also in the active form, even though a biasing influence of grid preparation cannot be excluded completely.

Large-scale conformational variability has also been observed in most other carrier-protein based multienzymes, including polyketide[267] and fatty acid synthases (with the exception of fungal-type fatty acid synthases)[268,269], non-ribosomal peptide synthetases[270] and the pyruvate dehydrogenase complexes[271], although based on completely different architectures. Together, this structural information suggests that variable carrier protein tethering is not sufficient for efficient substrate transfer and catalysis in any of these systems. The determination of a set of crystal structures of *Sce*ACC in two states, unphosphorylated[265] and phosphorylated at the major regulatory site Ser1157, provides a unique depiction of multienzyme regulation by post-translational modification (Figure 4.4D). The phosphorylated regulatory loop binds to an allosteric site at the interface of two non-catalytic domains and restricts conformational freedom at several hinges in the dynamic ACC. It disfavors the adoption of a rare, compact conformation, in which intramolecular dimerization of the BC domains[265] results in catalytic turnover. The regulation of activity thus results from restrained large-scale conformational dynamics rather than a direct or indirect influence on active site structure. To our best knowledge, ACC is the first multienzyme for which such phosphorylation-dependent mechanical control mechanism has been visualized. However, the example of ACC now demonstrates the possibility of regulating activity by controlled dynamics of non-enzymatic linker regions also in other

families of carrier-dependent multienzymes. Understanding such structural and dynamic constraints imposed by scaffolding and linking in carrier-protein based multienzyme systems is a critical prerequisite for engineering of efficient biosynthetic assembly lines.

4.5 Experimental Procedures

4.5.1 Protein expression & purification

All proteins were expressed in the Baculovirus Expression Vector System. The MultiBac™ insect cell expression plasmid pACEBACI (Geneva Biotech) was modified to host a GATEWAY® (LifeTechnologies) cassette with an N-terminal 10xHis-tag, named pAB1GW-NH10 hereafter. Full-length *Hsa*ACC (Genebank accession #U19822), *Sce*ACC (#NC_001146), *Cth*ACC (#XM_006692575) were cloned into pAB1GW-NH10 using GATEWAY® according to manufacturers manual. Truncated variants were constructed by PCR amplification, digestion of the template DNA with DpnI, phosphorylation of the PCR-product and religation of the linear fragment to a circular plasmid. The following constructs were used for this study: *Sce*ACC (1-2233), *Cth*ACC (1-2297), *Cth*ΔBCCP (1-2297, Δ700-765), *Cth*CD-CT (788-2297), *Cth*CD-CT_{Cter} (1114-2297), *Sce*CD (768-1494), *Hsa*BT-CD (622-1584, Δ753-818). Bacmid and virus production was carried out according to MultiBac™ instructions[154]. Baculovirus generation and amplification as well as protein expression were performed in Sf21 cells (Expression Systems) in Insect-Xpress medium (Lonza). The cells were harvested between 68-96h post infection by centrifugation and stored at -80 °C until being processed.

Cells were lysed by sonication and the lysate was cleared by ultracentrifugation. Soluble protein was purified using Ni-NTA (Genscript) and size exclusion chromatography (Superose 6, GE Healthcare). The affinity tag was removed by TEV-cleavage overnight at 4°C. TEV-protease and uncleaved protein were removed by orthogonal Ni-NTA purification prior to size exclusion chromatography. *Sce*ACC, *Cth*ACC and *Cth*ΔBCCP were further purified by high-resolution anion exchange chromatography prior to size exclusion chromatography. Purified *Sce*CD, *Cth*CD-CT_{Cter}, *Cth*CD-CT, *Cth*ΔBCCP, *Sce*ACC were concentrated to 10 mg ml^{-1} in 30 mM MOPS pH 7, 200 mM ammonium sulfate, 5% glycerol and 10 mM dithiothreitol and purified *Hsa*BT-CD was concentrated to 20 mg ml^{-1} in 20 mM bicine pH 8.0, 200 mM

NaCl, 5% glycerol, and 5 mM TCEP. Proteins were used directly or were stored at -80°C after flash-freezing in liquid nitrogen.

4.5.2 Protein crystallization

All crystallization experiments were conducted using sitting drop vapour diffusion. *Sce*CD crystals were grown at 19 °C by mixing protein and reservoir solution (0.1 M BisTrisPropane pH 6.5, 0.05 – 0.2 M di-sodium malonate, 20 – 30% polyethylene glycol (PEG) 3350, 10 mM trimethylamine or 2% benzamidine) in a 1:1 or 2:1 ratio. Crystals appeared after several days and continued to grow for 20 to 200 days. Crystals were cryo-protected by short incubation in mother liquor supplemented with 22% ethylene glycol and flash-cooled in liquid nitrogen. For heavy metal derivatization the crystals were incubated in stabilization solution supplemented with 1 mM Thimerosal or 10 mM $EuCl_2$, respectively, and then backsoaked for 15 seconds in stabilization solution without heavy metal.

Initial crystals of *Hsa*BT-CD grew in 0.1 M Tris pH 8.5, 0.35 M tri-potassium citrate and 2 – 3.5% PEG10000 at 19 °C. After several rounds of optimization good quality diffraction crystals were obtained at 20°C in 0.1M MES pH 6, 0.25 – 0.35 M tri-potassium citrate, 2 – 5% PEG10000, 0.01 – 0.04 M cadmium chloride. The protein drop contained a 1:1 ratio of protein and reservoir solution. Crystals grew immediately and stopped growing after 3 days. They were dehydrated and cryoprotected in several steps in artificial mother liquor containing incrementally increasing concentrations of tri-potassium citrate, PEG10000 and ethylene glycol and then flash-cooled in liquid nitrogen. The final solution was composed of 0.1 M MES pH6, 0.5 M tri-potassium citrate, 6.75% PEG10000, 0.01 M cadmium chloride.

*Cth*CD-CT_{Cter} crystals were grown at 19°C by mixing protein and reservoir solution (0.1 M Hepes pH 7.5, 2 – 7% Tacsimate pH 7, 7.5 – 15% PEGMME5000) in a 1:1 ratio. Crystals appeared after several days and continued to grow for up to two weeks. Crystals were cryo-protected by short incubation in mother liquor supplemented with 22% ethylene glycol.

*Cth*CD-CT ACC crystals were grown at 19 °C by mixing protein and reservoir solution (0.1 M Bicine pH 8.5 – 9.5, 4 – 8% PEG8000) in a 1:1 or 1:2 ratio. Crystals grew 8 to 10 days and were cryo-protected by short incubation in mother liquor supplemented with 22% ethylene glycol before flash-cooling in liquid nitrogen.

*Cth*ΔBCCP ACC crystals were grown at 19 °C by mixing protein and reservoir solution (0.1 M morpheus buffer 3, 7 – 12% Morpheus ethylene glycols mix, 8 – 12% PEG4000, 17 – 23% glycerol) in a 1:1 or 1:2 ratio. Crystals grew up to three weeks and were cryo-protected in reservoir solution before flash cooling in liquid nitrogen.

4.5.3 Structure determination and analysis of phosphorylation

All X-ray diffraction data were collected at beamlines X06SA (PXI) and X06DA (PXIII) at the Swiss Light Source (SLS, Paul Scherrer Institute, Villigen, Switzerland) equipped with PILATUS detectors, respectively. The wavelength of data collection was 1.000 Å for native crystals, and 1.527 Å and 1.907 Å for crystals derivatized with europium and cadmium, respectively. Raw data were processed using XDS[159]. Molecular replacement was carried out using Phaser 2.5.7 and 2.6.0, density modification was done using Parrot[272,273] and resolve, multi crystal averaging[165] was carried out using phenix. All model building was conducted using Coot[163] and figures were prepared using PyMOL (Schrödinger LLC).

Diffraction of initial *Sce*CD crystals in space group $P4_32_12$ with unit cell dimensions of a = b = 110.3 Å and c = 131.7 Å was limited to 3.5 Å. The resolution was improved to 3 Å by addition of trimethylamine or benzamidine to the reservoir solution without significant changes in unit cell dimensions. Crystals derivatized with thimerosal and europium were used for initial SAD phase determination using the SHELXC/D package[160]. Two mercury and four europium sites were located and an initial model was placed in the resulting maps. Since crystals derivatized with europium were slightly non-isomorphous with a c-axis length of 127 Å, multi crystal averaging was used for density modification and provided directly interpretable maps. Iterative cycles of model building and refinement in Buster (version 2.10.2; Global Phasing Ltd.) converged at R_{work}/R_{free} of 0.20/0.25. The final model lacks the disordered N-terminus (amino acids 768 – 789), an extended loop in the CD_{C1} domain (1204 – 1215) and a short stretch (1147 – 1152) preceding the regulatory loop. Based on temperature factor analysis, the start and end of the regulatory loop show higher disorder than the region around the interacting phosphoserine 1157. MS analysis of dissolved crystals detected quantitative phosphorylation of the regulatory Ser1157, as also found for full length *Sce*ACC, and additionally albeit with much lower occurrence, phosphorylation of Ser790, Ser1137, Ser1148 and Ser1159. A modeled phosphoryl-position for Ser1159 could overlap with the one of Ser1157, and might be represented in the

crystal. For all other phosphorylation sites no difference density could be observed, probably due to very low occupancy. PDBeFold [237] was used to search for structural homologues. The thresholds for lowest acceptable percentage of matched secondary structure elements were 70% for the search query and 20% for the result.

Initial *Hsa*BT-CD crystals were obtained in space group $I4_122$ with a = b = 240.1 Å and c = 768.9 Å and diffracted to only 7.5 Å. Optimized and dehydrated crystals also belonged to space group $I4_122$ but with unit cell parameters a = b = 267.3 Å and c = 210.6 Å and diffracted up to a resolution of 3.7 Å. Phase information was obtained from SAD based on bound cadmium ions from the crystallization condition. Six cadmium positions were located in a 4.0 Å resolution dataset at 1.9 Å wavelength using SHELXC/D [274] via the HKL2MAP interface [161]. Density modification and phasing based on this anomalous dataset, a 3.7 Å resolution data set at 1.0 Å wavelength, and additional non-isomorphous lower resolution datasets led to a high-quality electron density map. At the intermediate resolution obtained, the map was interpreted by a poly-alanine model, which was guided by predicted secondary structure as well as sequence and structural alignment with *Sce*CD. The final model refines against experimental data with with R_{work}/R_{free} of 0.38/0.41, as expected for a poly-alanine model[165]. Two *Hsa*BT-CD monomers are packed in the asymmetric unit via the CD_N and BT domains. Density on top of the β-barrel of one BT most likely representing parts of the BT-CD linker guided the assignment of this BT to its linked CD partner domain. This BT-to-CD assignment was further supported by the analysis of an additional lower resolution crystal form. Cadmium ions were found to participate in crystal packing.

In *Hsa*ACC phosphorylation at regulatory sites was detected as provided in the main text. No phosphorylation was detected for other phosphosites previously identified in large-scale phosphoproteomics studies, namely serines 5, 23, 25, 48, 53, 78, 488, 786, 1273[275-277].

Two different crystal forms were obtained for *Cth*CD-CT_{Cter}, diffracting to 3.6 Å and 4.5 Å, respectively. Both forms packed in space group $P2_12_12_1$ with unit cell constants of a = 97.7 Å, b = 165.3 Å and c = 219.2 Å or a = 100.2 Å, b = 153.5 Å and c = 249.2 Å, respectively. Phases were determined by molecular replacement using a homology model based on *Sce*CT (pdb 1od2) as search model in Phaser[162,273,278], multi crystal averaging was applied in density modification. The CT domain was rebuilt and an initial homology model based on the *Sce*CD structure was fitted into difference density for *Cth*CD-CT_{Cter1}. Iterative cycles of rebuilding and refinement in Buster converged at

R_{work}/R_{free} of 0.20/0.25. The refined CD fragment served as a starting model for rebuilding *Cth*CD-CT_{Cter2} at lower resolution. Coordinate refinement in Buster was additionally guided by reference model restraints and converged at R_{work}/R_{free} of 0.26/0.30. Residues 1114 – 1188, 1213 – 1252, 1380 – 1385 and 2188 – 2195 were disordered in both crystal forms and are not included in the models. Conservation was mapped onto the *Cth*CD-CT_{Cter1} crystal structure using al2co[279] based on a sequence alignment of 367 fungal ACC sequences calculated by Clustal Omega[209]. MS analysis of purified protein detected 7% phosphorylation at Ser1170 (corresponding to Ser1157 in SceCD).

*Cth*CD-CT crystallized in $P3_12_12$ with unit cell constants of a = b = 195.0 Å and c = 189.5 Å and crystals diffracted to a resolution of 7.2 Å. The structure was solved by molecular replacement using a model composed of *Cth*CT and CD_{C2} as search model in Phaser. CD_{C1} and CD_N were placed manually into the resulting maps and the model was refined using rigid-body, domain-wise TLS and B-factor refinement and NCS- and reference model restrained coordinate refinement in Buster to R_{work}/R_{free} of 0.26/0.28. Residues 1033 – 1035, 1134 – 1152, 1214 – 1252, 2188 – 2195 and 2260 – 2297 were not included in the models. Conservation was mapped onto the *Cth*CD-CT crystal structure as for *Cth*CD-CT_{Cter}. MS analysis of purified protein detected 60% phosphorylation at Ser1170 (corresponding to Ser1157 in SceCD).

*Cth*ΔBCCP ACC crystallized in $P6_422$ with unit cell constants of a = b = 462.2 Å and c = 204.6 Å, resolution was limited to 8.4 Å. Structure determination and refinement was performed as for *Cth*CD-CT. Final R_{work}/R_{free} were 0.31/0.34. Although substantial difference density is observed, in accordance with the lack of the BT and BC domains in the model, no defined positioning of these domains could be derived. In Addition, residues 1033 – 1035, 1134 – 1152, 1214 – 1252, 2188 – 2195 and 2260 – 2297 were not included in the models. MS analysis of purified protein detected 70% phosphorylation at Ser1170 (corresponding to Ser1157 in SceCD).

4.5.4 Small-angle x-ray scattering

Proteins were thawed on ice and dialyzed overnight against 30 mM MOPS pH 7, 200 mM ammonium sulfate, 5% glycerol and 10 mM dithiothreitol. Raw scattering data were measured at SAXS beamline B21 at Diamond Light Source. The samples were measured at concentrations of 2.5, 5 and 10 mg ml^{-1}. Data were processed using the ATSAS package [280] according to standard procedures[281,282]. A slight increase in

scattering in the very low-resolution range was observed with increasing protein concentrations, which may be due to interparticle attraction or minor aggregation. Scattering intensities were thus extrapolated to zero concentration using point-wise extrapolation implemented in Primus[283]. Direct comparison of raw scattering curves demonstrates the similarity of *Cth*ACC and *Cth*ΔBCCP, and the derived values such as Rg and Porod Volume match within expected error margins. Molecular mass estimations based on the SAXS-MOW method[284] derive values of 534.7 kDa and 534.0 kDa for *Cth*ACC and *Cth*ΔBCCP, respectively. The relative discrepancies to the theoretical weights of 516.8 kDa (*Cth*ACC) and 503.0 kDa (*Cth*ΔBCCP) are 3.5% and 6.2%, which is in a typical range for this method[284].

4.5.5 Electron microscopy

Full-length *Cth*ACC was diluted to 0.01 mg ml^{-1} in 30 mM MOPS pH 7.0, 200 mM ammonium sulphate, 5% glycerol, and 10 mM dithiothreitol. Protein sample was adsorbed to a 200 µm copper grid and stained with 2% uranyl acetate. Grids of *Cth*ACC were imaged on a CM-200 microscope (Philips) equipped with a TVIPS F416 4k CMOS camera (Tietz Video and Image Processing Systems). The voltage used was 200 kV; and a magnification of 50000 x results in a pixel size of 2.14 Å. Initial image processing and particle picking was carried out using Xmipp[285,286]. 22309 particles were picked semi-automatically from 236 micrographs with a box size of 300x300 pixels. After extraction, particles with a z-score of >3 were discarded and 22257 particles were aligned and classified into 48 2D class averages using maximum-likelihood target function in Fourier space (MLF2D). After 72 iterations, 4226 additional particles were discarded and the remaining 18031 particles were re-aligned and classified into 36 classes using MLF2D with a high-resolution cutoff of 30 Å. After 44 iterations the alignment converged and class averages were extracted.

4.5.6 *In vitro* biotinylation and activity assay

To ensure full functionality, *Sce*ACC was biotinylated *in vitro* using the *E. coli* biotin ligase BirA. The reaction mixture contained 10 µM ACC, 3.7 µM BirA, 50 mM Tris-HCl, pH 8, 5.5 mM $MgCl_2$, 0.5 mM biotin, 60 mM NaCl, 3 mM ATP, 10% glycerol and the reaction was allowed to proceed for 7 h at 30 °C.

The catalytic activity of phosphorylated and dephosphorylated *Sce*ACC was measured following the incorporation of radioactive ^{14}C into acid-stable non-volatile

material[264]. Dephosphorylated ACC was prepared by over-night treatment with λ protein phosphatase (New England Biolabs) of partially purified ACC before the final gel filtration step. The removal of the phosphoryl group from Ser1157 was confirmed by MS. The reaction mixture contained 0.5 µg recombinant ACC in 100 mM potassium phosphate, pH 8, 3 mM ATP, 5 mM $MgCl_2$, 50 mM $NaH^{14}CO_3$ (specific activity 7.4 MBq $mmol^{-1}$) and 1 mM acetyl-CoA in a total reation volume of 100 µl. The reaction mixture was incubated for 15 min at 30 °C, stopped by addition of 200 µl 6 M HCl and subsequently evaporated to dryness at 85 °C. The non-volatile residue was redissolved in 100 µl of water, 1 ml Ultima Gold™ XR scintillation medium (Perkin Elmer) was added and the ^{14}C radioactivity was measured in a Packard Tricarb 2000CA liquid scintillation analyzer. Measurements were carried out in five replicates and catalytic activities were calculated using a standard curve derived from measurements of varying concentrations of $NaH^{14}CO_3$ in reaction buffer.

4.6 Accession numbers

Atomic coordinates and structure factors have been deposited in the Protein Data Bank with accession codes 5I6E (*Sce*CD), 5I87 (*Hsa*BT-CD), 5I6F/5I6G (*Cth*CD-$CT_{Cter1/2}$), 5I6H *Cth*CD-CT), and 5I6I (*Cth*ΔBCCP).

4.7 Acknowledgements

We thank the staff of beamlines X06DA and X06SA at Paul Scherrer Institute, Villigen, Switzerland, for support with crystallographic data collection and the beamline scientists of B21 at Diamond Light Source, Oxfordshire, U.K., for support with SAXS measurements. We thank K. Goldie and H. Stahlberg (C-CINA, Basel, Switzerland) for their support with electron microscopy, the Biophysics facility of the Biozentrum for protein characterization and the Proteomics core facility for mass spectrometry and identification of post-translational modifications. Moritz Hunkeler acknowledges generous support by a Novartis Excellence Fellowship. Anna Hagmann is supported by a “Fellowship for Excellence” of the Biozentrum Basel International PhD Program. This work was supported by Swiss National Science Foundation grants 138262, 159696 and 145023.

4.8 Competing interests

The authors declare no competing interests.

4.9 Author contributions

MH cloned, expressed, purified and crystallized fungal ACC constructs, determined their structure, and carried out SAXS analysis. ES cloned, expressed and crystallized human ACC CD and determined its structure. EM analysis was carried out by ES, MH and AH. SI contributed to structural analysis and figure preparation. TM designed and supervised work and analyzed crystallographic data, all authors contributed to manuscript preparation.

4.10 Supplemental information

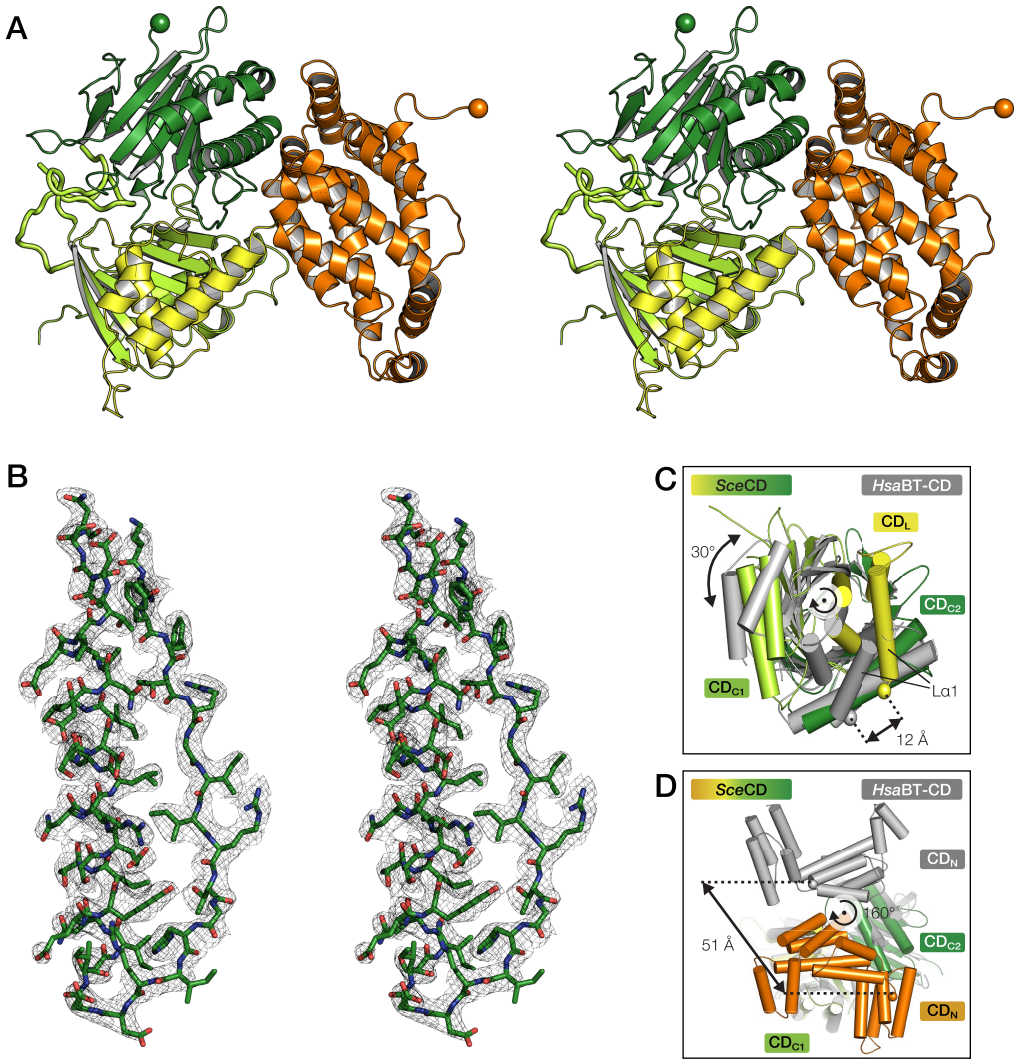

Supplemental Figure 4.1 Structure of SceCD and comparison to HsaBT-CD.
A Stereo view of *Sce*CD accompanying Fig 1b. **B** Stereo view of a representative part of the electron density in CD_{C2} of *Sce*CD. Shown is a 2Fo-Fc map contoured at 1 σ. **B** 30° rotation of CD_{C1} between structures of *Sce*CD and *Hsa*BT-CD visualized based on CD_{C2} superposition. *Sce*CD is shown in color and *Hsa*BT-CD is shown in gray. Both CD_N domains and the *Hsa*BT domain were omitted for clarity. The α-helix Lα1 of both structures, the domain rotation and the distance between N-termini (shown as spheres) is indicated. **D** A 160° rotation relates CD_N in *Sce*CD to *Hsa*BT-CD based on a superposition of CD_L/CD_{C1}. *Hsa*BT domain was removed for clarity. Spheres indicate the N-termini and the coloring is as in (c).

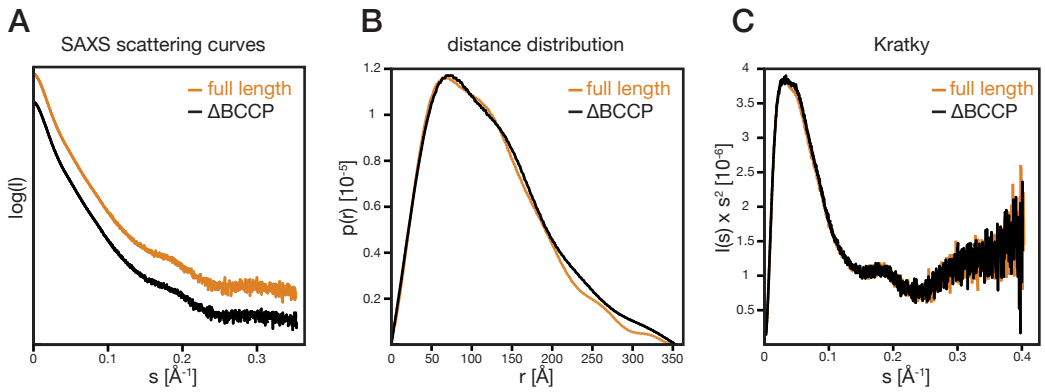

Supplemental Figure 4.2 SAXS analysis of fungal ACC.
Scattering curves **A**, distance distribution **B** and Kratky plots **C** of full-length *Cth*ACC (orange) and *Cth*ΔBCCP (black) demonstrating that BCCP-deletion has no impact on the overall solution structure. For clarity, scattering curves are shown with a y-axis offset.

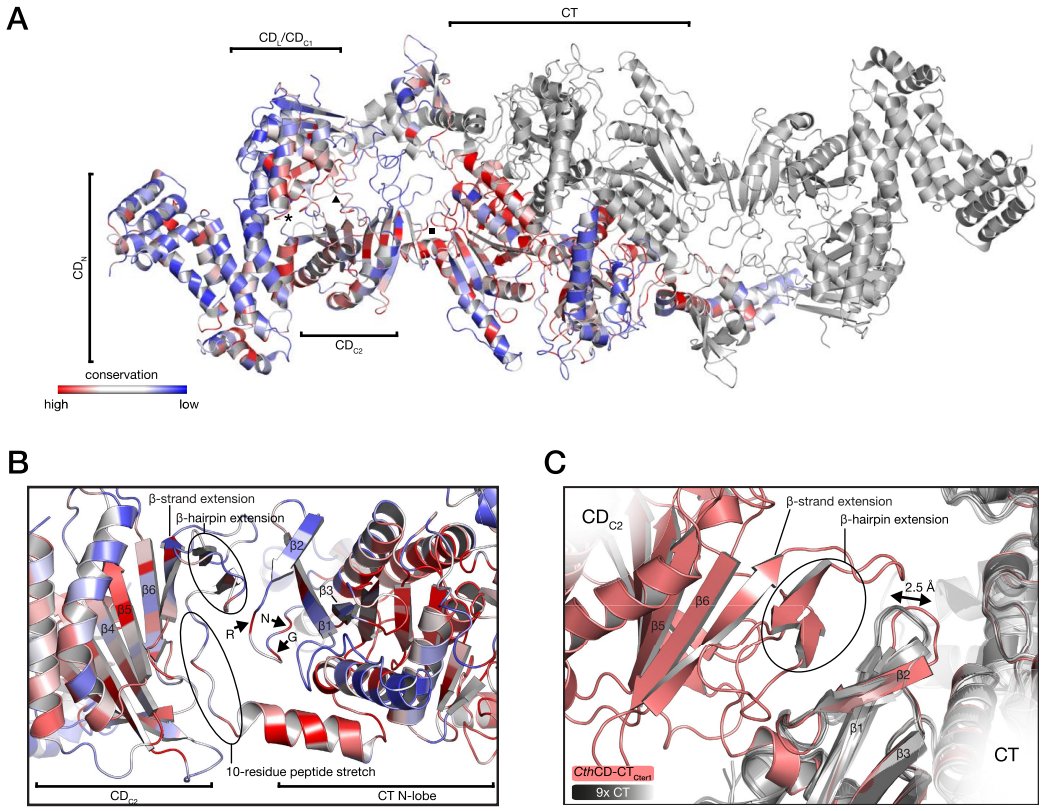

Supplemental Figure 4.3 Conservation analysis of *Cth*ACC.

A Cartoon representation of *Cth*CD-CT with one protomer colored according to conservation in a gradient from high (red) to low (blue). The second protomer is colored in gray. Contact regions of CD_N and CD_L/CD_{C1} (asterisk), CD_{C1} and CD_{C2} (triangle) and CD_{C2} and CT (square) are surrounded by regions of higher conservation. **B** Close-up on the edge- like hinge between CD_{C2} and CT. Highly conserved residues of the RxxGxN motif are indicated as well as important strands of CD_{C2} and CT. The second CT protomer is omitted for clarity. **C** Superposition of nine isolated CT crystal structures (gray) onto the CT domain of *Cth*CD-CT_{Cter1} (red). The loop preceding the conserved RxxGxN motif is displaced in the CD-CT contact by 2.5 Å compared to isolated crystal structures. PDB accession codes of structures used for superposition: 1od2, 1uys, 1uyt, 1w2x, 3h0j, 3h0q, 3k8x, 3pgq, 2tv5.

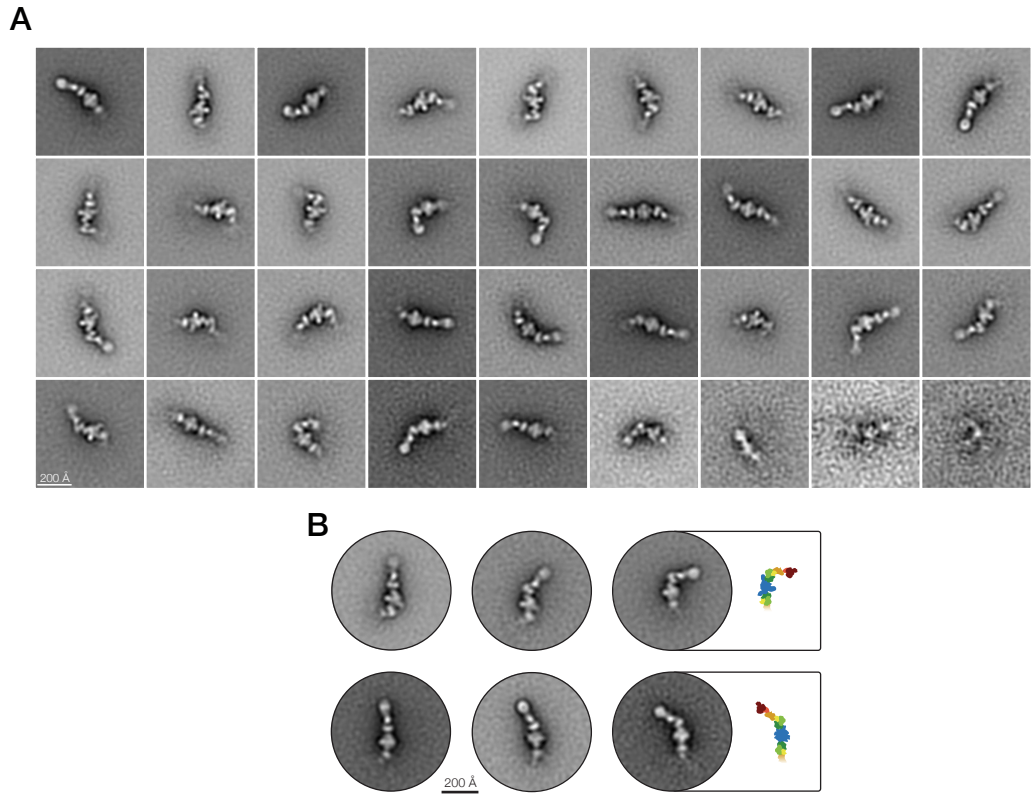

Supplemental Figure 4.4 Negative stain electron microscopy class averages of CthACC illustrating its flexibility.

A 18031 particles were 2D-classified into 36 classes using the MLF2D method. Classes are sorted by number of particles per class, with the highest number at the top left and the lowest number at the bottom right. Scale bar 200 Å. **B** 2D-class averages from negative stain EM analysis depict the ensemble of solution conformations of the intrinsic flexibility of *Cth*ACC. Scale bar 200 Å.

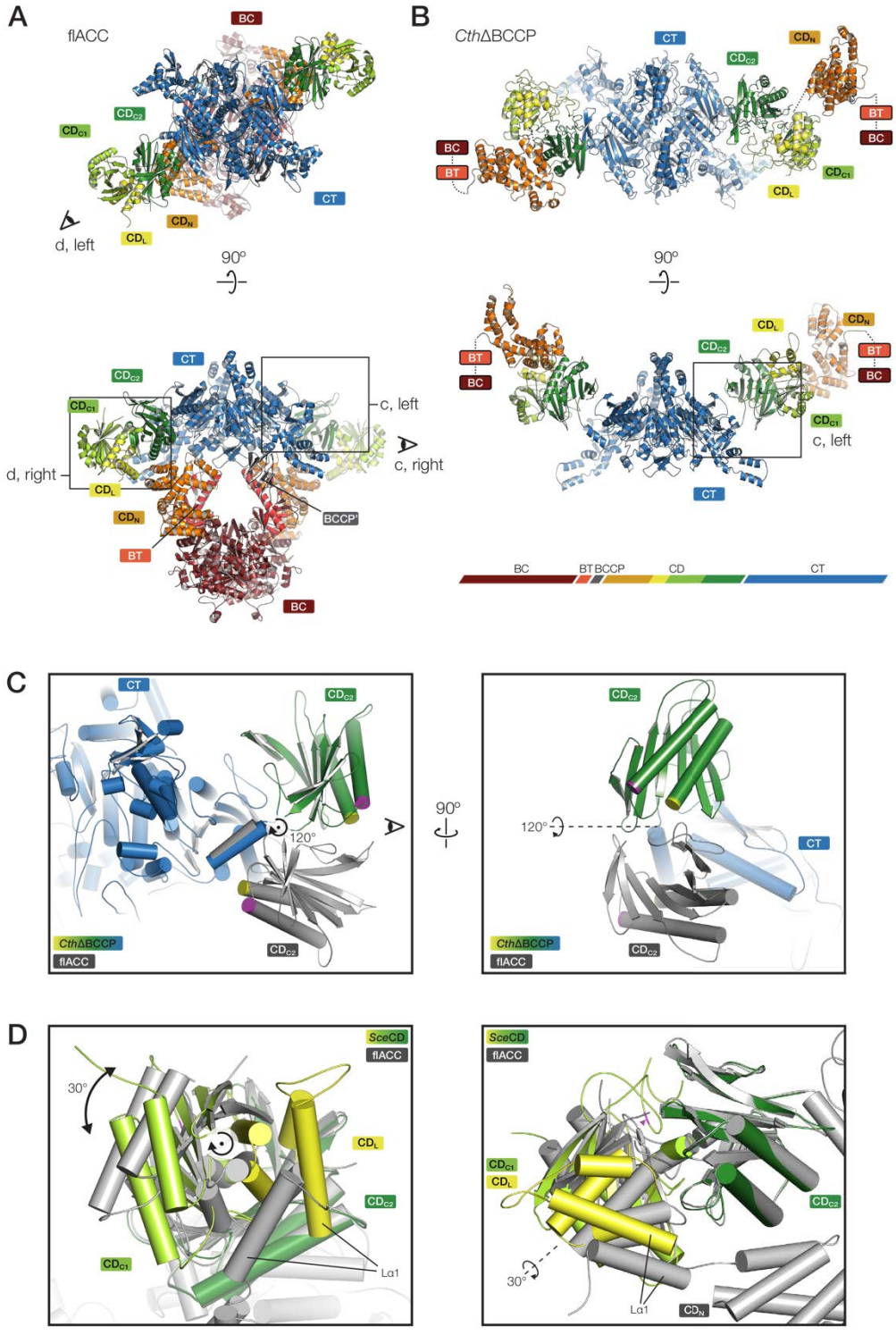
A
flACC
BC
CD$_{C2}$
CD$_{C1}$
CT
CD$_N$
CD$_L$
d, left
90°
CT
CD$_{C2}$
CD$_{C1}$
c, left
d, right
c, right
CD$_L$
CD$_N$
BCCP
BT
BC
B
CthΔBCCP
CT
CD$_{C2}$
CD$_N$
BT
BC
BC
BT
CD$_{C1}$
CD$_L$
90°
CD$_L$
CD$_N$
CD$_{C2}$
BT
BC
BT
BC
CD$_{C1}$
c, left
CT
BC
BT BCCP
CD
CT
C
CT
CD$_{C2}$
120°
CthΔBCCP
flACC
CD$_{C2}$
90°
CD$_{C2}$
120°
CT
CthΔBCCP
flACC
CD$_{C2}$
D
SceCD
flACC
30°
CD$_L$
CD$_{C2}$
CD$_{C1}$
La1
SceCD
flACC
CD$_{C1}$
CD$_L$
CD$_{C2}$
30°
La1
CD$_N$

Supplemental Figure 4.5 Conformational variability in fungal ACC.
A Cartoon representation of triangular flACC (PDB accession code: 5csl). In (a) and (b) domains are colored according to the linear sequence scheme in (b). **B** Cartoon representation of *Cth*ΔBCCP. The orientations of (a) and (b) are based on a superposition of the CT domains. Fields of view for panels (c) and (d) are indicated with boxes and eyes. **C** Left: Detailed view of the CD_{C2}/CT 120° hinge motion viewed along the rotation axis. *Cth*ΔBCCP is colored and flACC is shown in gray for clarity. Corresponding ends of CD_{C2}-helices are colored in yellow and magenta. The rotation axis is indicated and the view for the right subpanel is indicated with an eye. Right: View onto the rotation axis. **D** Conformational states of the CD_{C1}-CD_{C2} hinge in the non-phosphorylated flACC and in the phosphorylated *Sce*CD crystal structures when superimposed on CD_{C2} domains. Lα1, the first N-terminal helix of the CD_L domain, is labeled to illustrate the conformational differences. The left panel shows the view along the rotation axis, the right panel corresponds to a view onto the axis. The position of the phosphorylated Ser1157 in the regulatory loop is indicated by a magenta triangle.

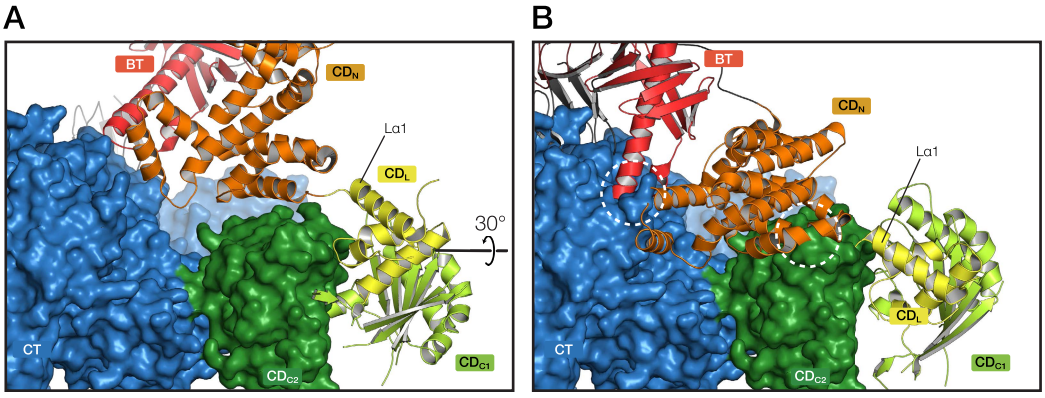

Supplemental Figure 4.6 Conformation of phosphorylated CDC1-CDC2 hinge is incompatible with BT/CDN conformation in flACC.

A Detailed view on flACC (PDB accession code: 5csl) with CT and CD_{C2} domains shown as surface and BT, BCCP, CD_N, CD_L and CD_{C1} domains shown as cartoon **B** flACC model with the CD_{C1}-CD_{C2} hinge conformation as observed in the *Sce*CD crystal structure. Clashes of BT/CD_N with CT and CD_N with CD_{C2}, that are caused by the 30° rotation of CD_{C1} relative to CD_{C2} (rotation axis shown in (a)), are indicated with white circles. For orientation, the first helix of CD_L is labeled in both panels.

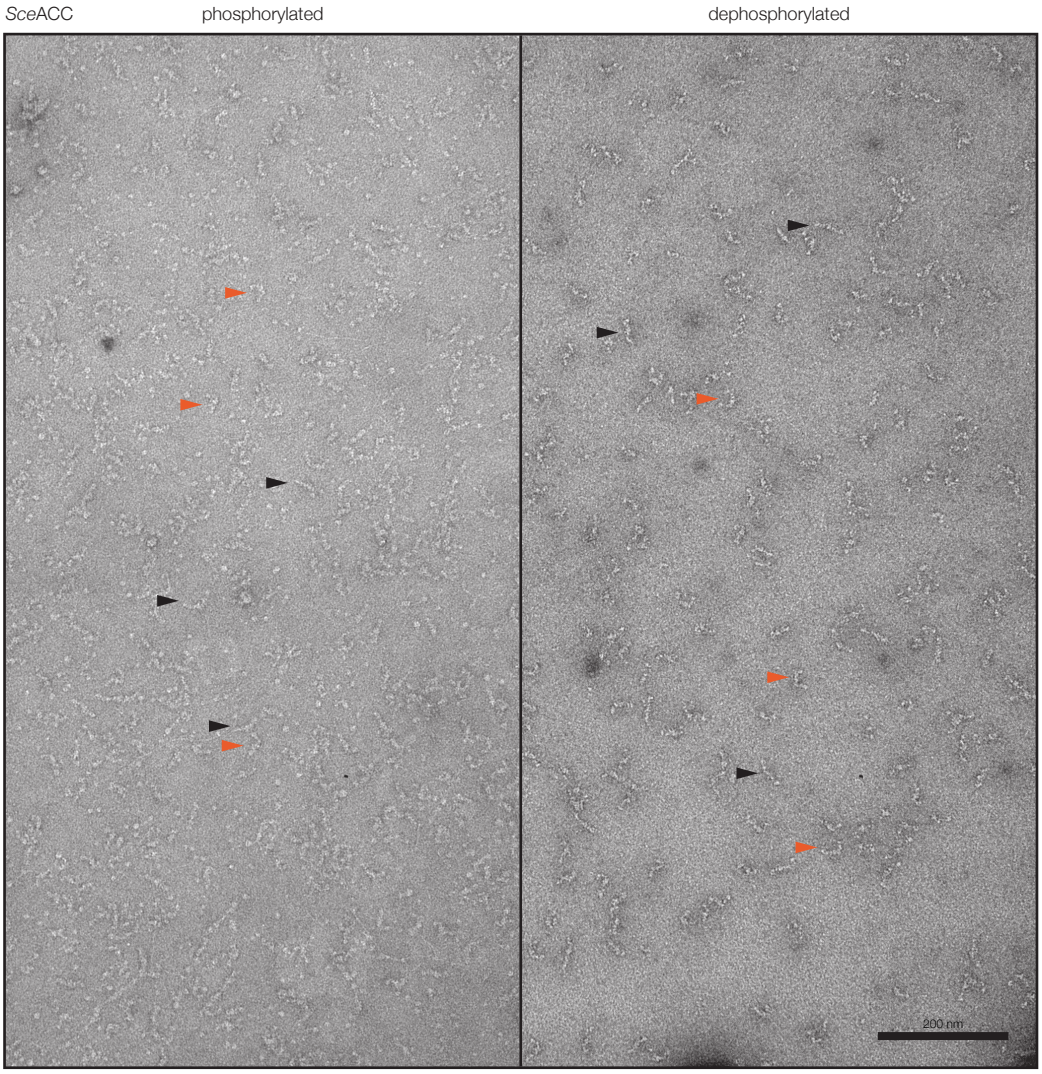

Supplemental Figure 4.7 Negative stain electron microscopy of phosphorylated and dephosphorylated *SceACC* shows similar degree of conformational flexibility.
Micrographs of phosphorylated (left) and dephosphorylated *Sce*ACC (right) are shown side by side. Selected particles representing elongated and U-shaped molecules are indicated with black and orange arrows, respectively. The scale bar is 200 nm.

Supplemental Table 4.1 Small angle x-ray scattering data collection and processing.

	full length *Cth*ACC	***Cth*ΔBCCP**
Instrument	B21 at Diamond Light Source	B21 at Diamond Light Source
Beam size (mm)	1 x 5	1 x 5
Wavelength (Å)	1	1
q range ($Å^{-1}$)	0.005 - 0.4	0.005 - 0.4
Detector distance (m)	3.92	3.92
Temperature (K)	293	293
Protein concentration (mg/ml)	3, 6, 10	3, 6, 10
Scan repeats	30	30
Total exposure time (s)	300	300
Capillary diameter (mm)	1.6	1.6
I(0) ($Å^{-1}$) [from P(r)]	0.023	0.024
Rg (Å) [from P(r)]	94	97
Rg (Å) (from Guinier)	89 ± 2	92 ± 3
Porod volume estimate ($Å^3$)	1176290	1174390
Dmax (Å)	350	350

5 Discussion and Outlook

5.1 The organization of mTOR complex 1

The structure determination of the human mTORC1 by cryo-electron microscopy revealed a truly unique architecture. Both, the previously solved crystal structure of the mTORΔN-mLST8 fragment reported by Yang et al.[19], as well as the structure of isolated Raptor from *Chaetomium thermophilum* are unambiguously placed in the EM-map. Furthermore, the high quality of the EM map allowed *de novo* interpretation of the mTOR HEAT domain region by placement of α-helical repeats without assigned register or directionality, providing a first complete model of the entire mTOR complex 1 at pseudo-residue resolution. mTORC1 adopts a dimeric, lozenge shaped structure with the two catalytic clefts facing outwards. Access to the active site is not only recessed by mLST8 and the FRB domain as reported earlier[19], but also by the highly conserved Raptor RNC domain. The structure of isolated CtRaptor reveals a Z-shaped domain arrangement with central ARM repeats flanked by the amino-terminal RNC and a carboxy-terminal WD40 propeller on opposite sides.

Very recently, Baretic *et al.* reported the structure of a Tor-Lst8 complex from the thermotolerant yeast *Kluyveromyces marxianus*.[287] In this study, Lst8 and a ZZ-tagged Tor were stably integrated into the *K. marxianus* genome under a galactose inducible promoter. Galactose induced expression followed by antibody purification yielded a monodisperse Tor-Lst8 sample, which was subjected to single particle analysis by cryo-electron microscopy. Despite the absence of the *Kluyveromyces marxianus* ortholog of Raptor, the organization of Tor-Lst8 closely resembles those of the corresponding regions in the human mTORC1 reconstruction (Figure 5.1A,B). The structural core comprising the bridge, FAT and kinase domain is significantly better resolved than the horn region and Lst8, again similar to human mTORC1 (Supplemental Figure 2.2).

Baretic *et al.* observed weak density of the negative regulatory domain (NRD), whose deletion increases mTORC1 activity[75,76]. The NRD is an integral part of the kinase domain, but could not be modeled in the crystal structure due to high flexibility[19]. It blocks the catalytic cleft from the opposite side as Raptor does in our reconstruction

of the mTORC1. The NRD could act as another gatekeeper that regulates access to the active site.

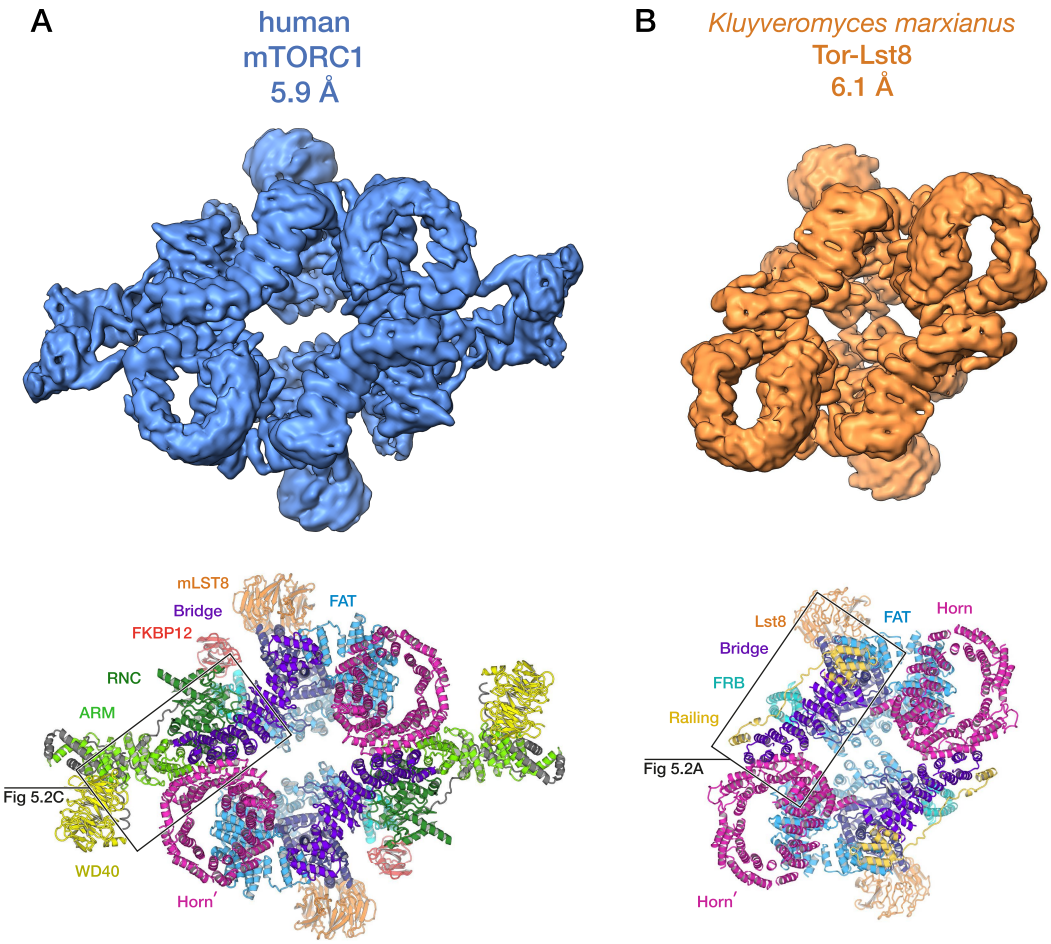

Figure 5.1 mTOR-mLST8 core architecture is conserved in *Kluyveromyces marxianus*.
Cryo-EM reconstruction of human mTORC1 (**A**) and *K. marxianus* Tor-Lst8 (**B**, EMDB ID 3329) with cartoon representation of the derived structures below. The architecture of the TOR-LST8 core is highly conserved between species.

Interestingly, Baretic *et al.* observe additional density on the concave side of the bridge in the Tor1-Lst8 structure. In order to determine the connectivity within the HEAT domain, which could not be resolved in the reconstruction of human mTORC1, they inserted tandem red fluorescent proteins (RFP) at three different positions between the α-helical repeats. Guided by the position of the RFPs in the EM-density, they could unambiguously determine the connection topology of the horn, bridge and a newly identified stretch termed 'railing' (Figure 5.2A). This topology differs from the one initially proposed in chapter 2. The direction of both the horn and the bridge is inverted

(Figure 5.2B). The horn directly connects to the bridge at the side previously suggested to be the amino-terminus. The bridge then directs to the horn of the other protomer (Horn' in Figure 5.2A) and leads to the railing. The railing runs back on the concave side of the bridge and connects via the helical 'cap' to the FAT domain.

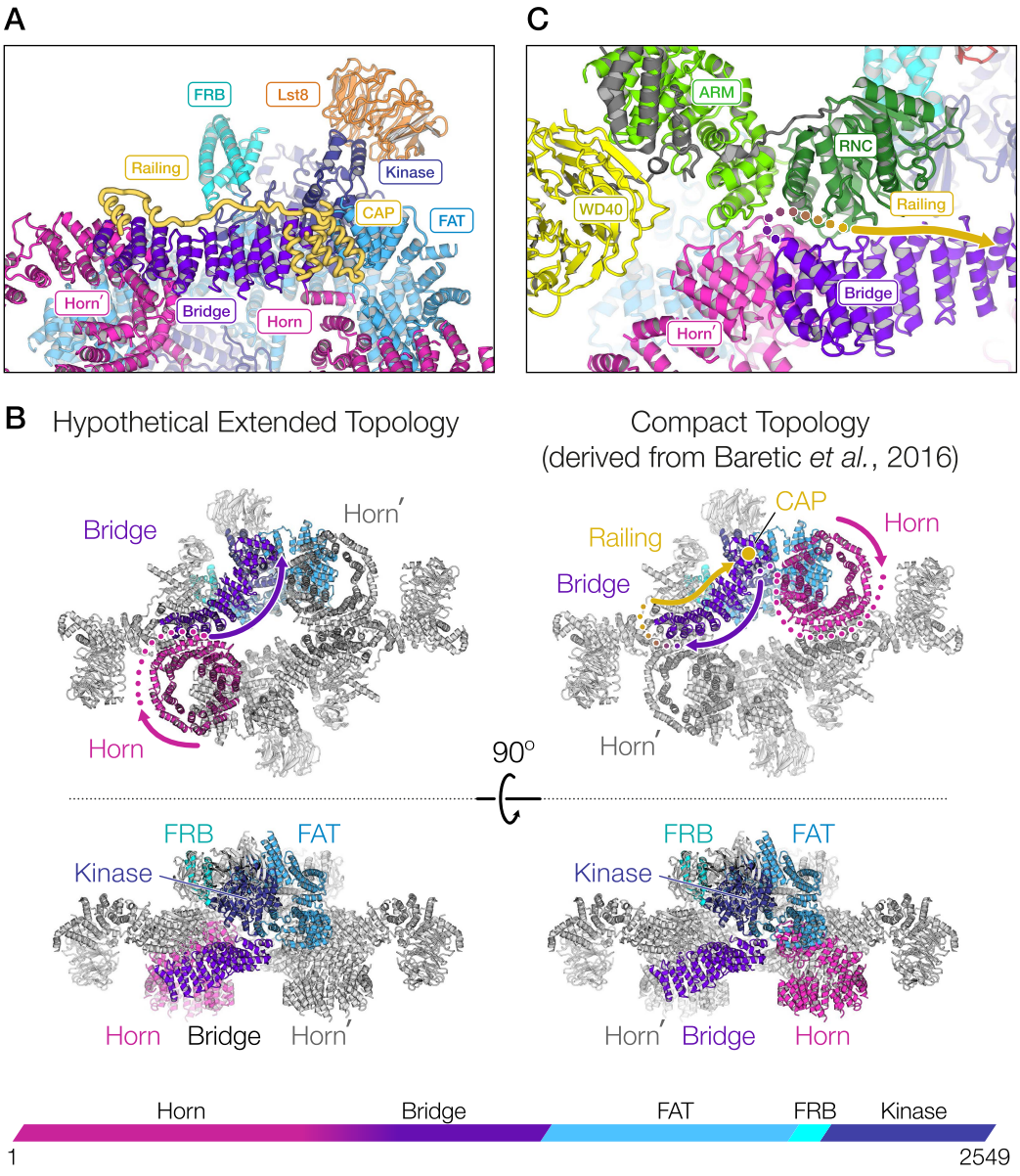

Figure 5.2 mTOR domain connectivity and implications for the dimer interface. **A** Close-up view of the 'railing' and 'cap' connection between the horn and the bridge in the structure of K. marxianus repoted by Baretic et al. B mTOR kinase topology as suggested in 2.3.3 (left) and as determined by Baretic et al. Only one mTOR protomer is colored, whereas the other protomer, Raptor, mLST8 and FKBP12 is shown in gray. The suggested connectivity within the HEAT domain is indicated with arrows and dots. The horn of the opposite mTOR protomer is indicated with a prime. **C** Close-up view of the interface formed by Raptor, the bridge from one mTOR protomer and horn (indicated with a prime) from the opposite mTOR protomer. Schematic of the mTOR domain architecture is indicated below.

The experimentally well supported topology proposed by Baretic *et al.* now provides an unambiguous assignment of the dimeric topology of mTOR, superseding the initial hypothesis formulated in chapter 2 (2.3.6): Raptor contacts both mTOR protomers (Figure 5.2C) such that the two dimerization interfaces are equivalent to those described as interfaces between Raptor and the horn and bridge of one mTOR protomer in 2.3.6.

5.2 Implications for mTORC2

The preservation of the basic core structure in the absence of a Raptor ortholog of *K. marxianus* Tor-Lst8 shows that mTOR provides the basic scaffold for mTORC1, which remains mostly unaffected by Raptor binding, although Raptor interaction may further stabilize the overall complex [287]. This hints to a preserved central mTOR scaffold also in mTORC2 with the mTORC2-specific Rictor subunit occupying the position of Raptor or other accessible sites. A recent bioinformatics search analyzed the Rictor domain arrangement and found a resemblance to Raptor[288]. The prediction algorithm identified amino-terminal and central HEAT repeats and a carboxy-terminal WD40 domain. The study further predicts a pleckstrin homology (PH) domain which mediates cellular localization and a ribosome binding domain that could mediate the reported ribosome association[50].

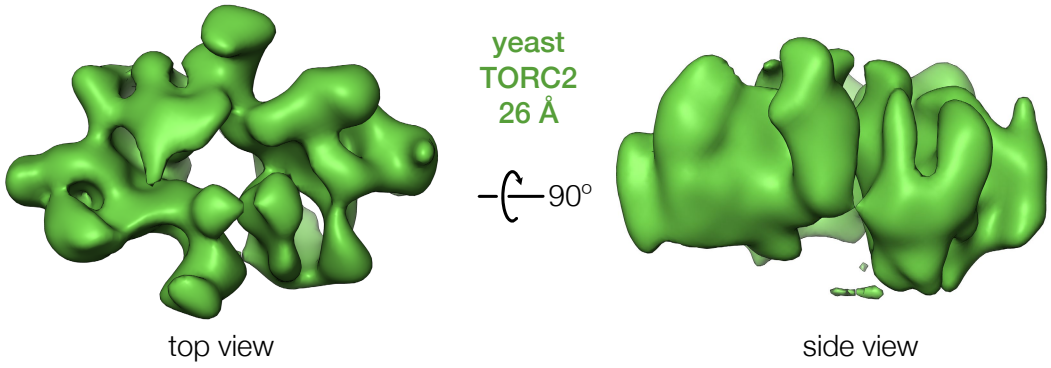

Figure 5.3 *S. cerevisiae* TORC2 negative stain EM reconstruction at 26 Å resolution. Top view (left) and side view (right) of the single particle EM reconstruction of yeast TORC2 at 26 Å[150]. Incomplete information causes blurring along the top view axis.

Recent work from Gaubitz *et al.* aimed to determine the architecture of TORC2 from budding yeast[150]. Purification via TAP-tagged AVO3, the yeast Rictor ortholog, from

Saccharomyces cerevisiae cell extracts yielded a sample that was subjected to single particle negative stain EM analysis. The low resolution reconstructions at 26 Å reveals a dimeric, rhomboid shape with a central cavity, similar to mTORC1 (Figure 5.3). However, the overall quality of the EM-map is impaired due to a preferred orientation of the particles on the EM-grid. The information for the reconstruction is hence incomplete, which causes blurring of the EM density along the top view axis (Figure 5.3, right panel). Localization of individual proteins was approached using deletion or truncation of specific subunits or insertion of bulky maltose binding protein (MBP)-fusions followed by EM-analysis. The carboxy-terminal region of AVO3 likely shields the FRB domain, as its deletion renders mTORC2 sensitive to rapamycin mediated inhibition.

The low resolution as well as the overall quality of the reconstruction hinder a meaningful interpretation of the TORC2 architecture presented by Gaubitz *et al.* However, it confirms an expected dimeric mTORC2 assembly. It is of great relevance to further elucidate the architecture of mTORC2. A similar approach as used for the mTORC1 reconstruction could be employed, by combining a single particle cryo-EM reconstruction of intact mTORC2, complemented with structure determination of the core components Rictor and Sin1. The determination of the mTORC2 structure would permit the design of targeted structural but also biochemical studies in order to dissect the divergent regulatory mechanism between mTORC1 and mTORC2. The structure could reveal domains in proximity to the catalytic site which might be involved in substrate recognition. It would further allow to elucidate the structural basis for membrane targeting of mTORC2 which could be mediated by the PH domains of Sin1, Rictor or both[289].

5.3 Implications for the regulation of the mTOR complexes

The novel insights to mTOR complex 1 organization provide a framework for an analysis of mTOR regulation. The Raptor RNC domain is positioned in close proximity to the kinase active site in mTORC1. In addition to the FRB[19] and the NRD[287], it further limits the accessibility of the mTOR active site. The RNC adopts a caspase fold, but has not been reported to have proteolytic activity. Despite the presence of a conserved Cys-His dyad[79], this is not unexpected, as caspases are activated by specific proteolytic cleavage and the functional assembly is dimeric [290]. Both the high conservation and its location within mTORC1 suggest a key role in substrate

recognition and delivery via the TOS-motif, which has been shown to directly interact with Raptor[66,67]. The resemblance between the TOS-motif and caspase target sequence with an aspartate at position four might hint to a related binding mode. Further biochemical and structural work is required to characterize the interaction between Raptor and its substrate via the TOS-motif. Structure determination of a synthetic TOS-peptide bound to Raptor would reveal its TOS-binding site. Moreover, a Raptor crystal structure at atomic resolution would allow identification of the residues involved in substrate binding. Additional biophysical techniques such as fluorescence polarization or isothermal calorimetry can be applied to determine the kinetics and thermodynamics of the binding. An established binding experiment would allow verification of identified interacting residues by comparing the binding affinities of Raptor mutants to wild-type Raptor. Moreover, it would permit to compare the binding affinities for the S6K, 4EBP1 and the negative regulator PRAS40 TOS-motifs in order to determine the relative specificity.

Importantly, substrate binding needs to be examined on the level of the entire complex using cryo-EM reconstruction of mTORC1 substrate complexes. 4EBP1 belongs to a family of intrinsically disordered proteins[291], which might hinder its visualization in such a complex. S6K is larger than 4EBP1 (S6K1, 59 kDa; 4EBP1, 12 kDa) and possesses a folded kinase domain, which facilitates its visualization by cryo-EM. The reconstruction of a S6K bound to mTORC1 would allow to dissect how Raptor and the FRB domain orchestrate its positioning during catalysis.

The mTOR complex 1 adopts a surprisingly open structure and exposes a large surface area. One side is exclusively formed by α-helical HEAT repeats (Figure 2.1). HEAT repeats are versatile mediators of protein-protein interactions[292], exemplified by the two HEAT repeat comprising proteins Importin β and Cullin-associated NEDD8-dissociated protein 1 (Cand1, Figure 5.4A,B). Importin β binds Ran-GTP and conducts its transport through the nuclear pore complex[293] and Cand1 binds and inhibits Cullin-1 (Cul1) and Roc1, which form the catalytic core of the SCF ubiquitin ligation complex[294]. In both instances HEAT repeats adopt a characteristic curved structure and bind the interaction partner in the concave surface. The mTOR HEAT domain comprising the bridge and the highly curved horn provides a large platform for mTOR interacting proteins. Tel2 stabilizes all members of the PIKK family[295] by binding to their HEAT repeat domain. The binding interface on mTOR was mapped to the residues residues 400-806 located in the horn. The crystal structure of *Saccharomyces cerevisiae* reveales two HEAT-like repeat domains (Figure 5.4), which are artificially

joined for crystallization purposes, but connected via a 40 residue linker in the wild-type protein [296]. Cul1 also comprises α-helical repeats, hence the interaction between mTOR and Tel2 might resemble the binding of Cul1 and Cand1 (Figure 5.4).

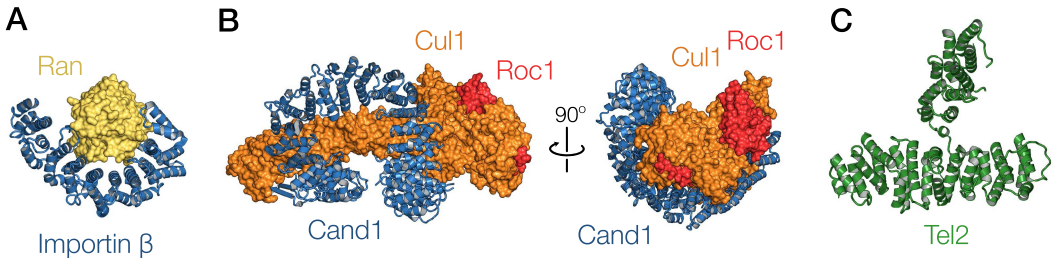

Figure 5.4 Versatility of HEAT repeat structures.
A Importin β (blue) binds Ran (yellow) on the concave surface of the curved HEAT repeats and mediates the transfer through the nuclear pore. **B** The Cul1-Roc1 complex is bound in a groove formed by the Cand1 HEAT repeats. **C** Cartoon representation of the crystal structure of *Saccharomyces cerevisae* Tel2.

Furthermore, the mTORC1 is decorated with WD40 β-propellers at four different sides (Figure 2.1). Two of them are formed by mLST8 and two are comprised in the carboxy-terminal region of Raptor. WD40 domains are mediators of protein-protein interactions[297] and occur in 1 % of all human proteins[298]. Targets are preferentially bound at the top central channel, but contacts to the side are reported as well[298]. The RagA/B-GTP and RagC/D-GDP heterodimer directly binds Raptor and tethers mTORC1 to the lysosome under amino acid stimulation[40]. The binding region of the budding yeast orthologs Gtr1 (RagA/B) and Gtr2 (RagC/D) were mapped to WD40 propeller and parts of the ARM domain of the Raptor ortholog Mip1[299]. Structural characterization of RagA/B-RagC/D in complex either with isolated Raptor or in context of the entire mTORC1 would elucidate the dual role of Raptor in lysosomal targeting and substrate recruitment.

5.4 Regulation of PLK4 activity

The results presented in chapter 3 identify STIL as a PLK4 interacting protein. The binding is mapped onto the PB3 and L1 linker region of PLK4 and the coiled-coil region of STIL. Structure determination of the PB3/STIL-CC complex, biophysical characterization of the binding, supplemented with in vivo experiments of structure guided mutations consolidate the role of STIL on PLK4 regulation. Furthermore, the structure defines a new mode of Polo-box substrate interaction.

Recently Klebba *et al.*[212] dissected the mode of PLK4 activation in *Drosophila melanogaster*. They found that the PLK4 is regulated via an autoinhibitory mechanism, related to PLK1[97] regulation. In the proposed mechanism, the L1 linker between the kinase and the first two Polo-boxes shields the activation loop from an activating phosphorylation. This model is in agreement with elevated kinase activity by mutations in the linker region, that likely impair the inhibitory interaction between L1 and the activation loop. Moreover, PLK4 was dramatically stabilized upon PB3 truncation. This suggests a role of the PB3 domain in stimulation of PLK4 kinase activity by relieving the autoinhibition, which evidently leads to autophosphorylation and subsequent proteasomal degradation[107]. The relief of the autoinhibition requires an unidentified factor, as recombinantly produced PB3 fails to stimulate kinase activity *in vitro*.

The conservation of an autoinhibitory regulation between human PLK1 and *Drosophila melanogaster* PLK4 argues that a mechanism similar to Polo regulation described above also holds true for human PLK4. The results presented in chapter 3 are in agreement with such a model. STIL-CC interacts with PLK4 both with PB3 and L1, presumably via distinct interfaces. This makes STIL a prime candidate for the unknown mediator of PB3-dependent relief of the L1-autoinhibition proposed by Klebba *et al.* Taken together with the results from chapter 3, this suggests the following mechanism (Figure 3.7): STIL is recruited to the centriole by PLK4. STIL binding relieves PLK4 autoinhibition and activates the kinase. PLK4 phosphorylates STIL, which triggers SAS-6 recruitment and cartwheel formation, the structural framework for formation of a daughter centriole. Activated PLK4 autophosphorylates and causes its proteasomal degradation.

Further studies are needed to confirm this model. Analogous experiments to the study by Klebba *et al.* should be transferred to a human system to elucidate the autoinhibitory mechanism for PLK4. In Addition, the role of STIL as a PLK4 activator can be assessed both *in vitro* and *in vivo*. Moreover, structural characterization of the STIL interaction with PLK4-L1 using linker comprising fragments for co-crystallization with STIL-CC is of great interest. However, this might be very challenging due to the linker presumably being highly flexible and unstructured. It is also of great relevance to temporally resolve the individual events in PLK4 regulation: the recruitment to the centriole, activation, phosphorylation of targets and degradation. In Addition, studies aiming to identify new players are key to further dissect the detailed mechanisms in centriole duplication in the future.

5.5 Regulation of ACC activity

Our structure determination of isolated yeast and human central domain of ACC reveals its unique domain composition. Together with studies on larger up to almost full-length variants of *Chaetomium thermophilum* ACC the work demonstrates the highly flexible nature of ACCs. Furthermore, it provides the structural basis for the inhibition of SNF1-mediated phosphorylation. The phospho-Ser1157 drastically reduces the flexibility by locking the hinge between CD_{C1} and CD_{C2} , which evidently obstructs an activated conformation with dimerizing BC domains reported by Wei and Tong[265].

Taken together, the results presented in chapter 4 deliver an experimentally well founded model of yeast ACC regulation. But the work also raises new questions regarding the mechanisms of human ACC regulation. Although the domain architecture is conserved across species, several observations suggest a divergent mode of regulation. First, AMPK mediated phosphorylation of Ser1216, the equivalent of yeast Ser1157, has not been shown to reduce the activity of human ACC. Secondly, the most active form of human ACC is polymeric. And lastly, activity depends on the two modulating proteins BRCA1 and MIG12. BRCA1 binds and inhibits phosphorylated Ser1263, a site which is not conserved in yeast, and MIG12 as well as citrate promote ACC polymerization.

Regulatory phosphorylation by AMPK occurs at Ser80 and Ser1201[129]. Ser1201 is located in the loop between CD_{C1} and CD_{C2} as Ser1157 in yeast, however not in the same position. It still might conduct an analogous function, as the two phosphoryl-coordinating arginines from yeast are conserved in humans. Mass spectrometric analysis revealed that Ser1201 was not phosphorylated to high levels in insect cell expressed human CD, which was used for crystallization and structure determination. The regulatory loop between CD_{C1} and CD_{C2} was thus flexible and could not be built at position Ser1201 in the electron density map. Structure determination of AMPK treated or a phosphomimetic S1201D mutated CD could reveal an analogous mechanism to yeast Ser1157. Ser80, however, is conserved in all higher eukaryotes, but not in yeast. Ser80 precedes the BC domain and prevents BC dimerization upon phosphorylation and might have an improrant regulatory role.

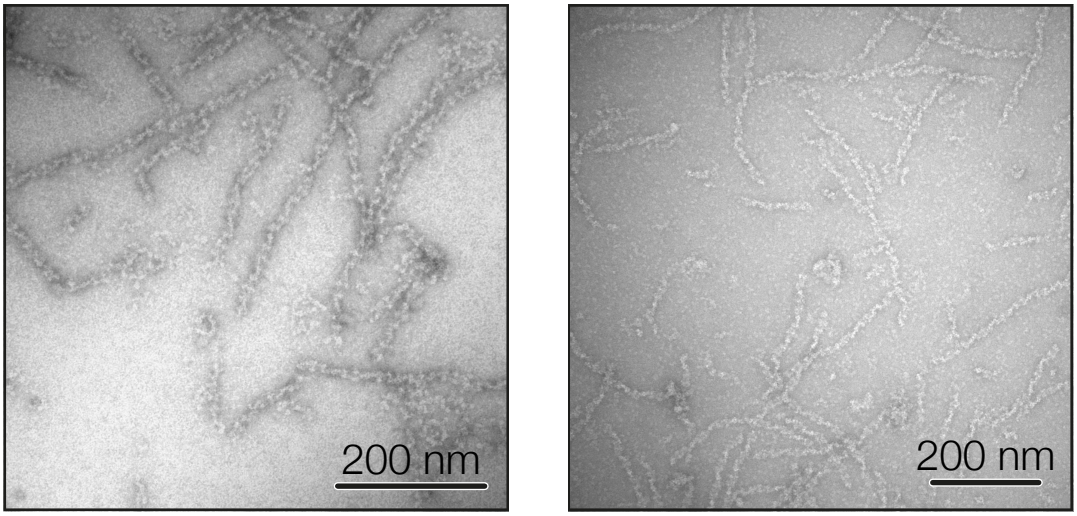

Figure 5.5 human ACC forms filamentous polymers
Negative-stain electron micrographs of human ACC1 filaments taken by Moritz Hunkeler. ACC1 is most active in the polymeric form.

A highly interesting question is the regulation of the polymeric form of the human ACC (Figure 5.5). First, the role of the promoting factors MIG12 and citrate needs to be elucidated. And secondly, the consequences of ACC polymerization on its activity have to be characterized. The work on yeast ACC has demonstrated that flexibility is crucial for activity. It is thus puzzling how ACC in a fixed, polymeric conformation can be more active. The catalytic sites of the BC and CT domains might be positioned in close proximity in the filamentous form and thus lock ACC in a highly active conformation. Structural characterization of the polymeric ACC is fundamental to address this question. Cryo-electron microscopy of filaments to at least intermediate resolution would allow docking of individual ACC dimers and provide the structural basis of ACC activation upon polymerization.

5.6 General Outlook

Proteins are the functional units of life and conduct the majority of essential regulatory and enzymatic processes. The work presented in this thesis, highlights the complex architecture of multidomain proteins and the importance of interdomain crosstalk and conformational changes for the regulation of protein function. Comparative proteomic and bioinformatic studies have revealed a particular enrichment of multidomain proteins in higher eukaryotic organisms: Only 40 % of all prokaryotic proteins but 65 % of all eukaryotic proteins comprise multiple domains; and more than 8 % of all proteins in multicellular organisms consists of domain repeats compared to only 3-4 % in archaea, bacteria and yeast[300]. Many multidomain proteins occurred late in evolution, and their development is presumably linked to processes specific for multicellular organisms, such as cell adhesion and signaling[301]. Linking of multiple domains and the duplication of domains has permitted diversification of basal evolutionary capabilities and the adoption of a new cellular tasks. PLK4, for example, originates from a gene duplication event of an earlier precursor PLK [84], which allowed uncoupling from of ancestral PLKs and diversification of the regulation of centriole duplication. The PB3 domain of PLK4 originated from either PB1 or PB2[84] and provided an additional site for interaction and regulation by STIL.

Domain duplication is commonly accompanied by recombination with additional domains[302]. In yeast ACC, the duplicated CD_1 and CD_2 are recombined with two helical subdomains, which join to form the regulatory central domain. Domain duplication has created a hinge region, which can be locked in a specific orientation by phosphorylation to restrict the conformational flexibility of the BC and CT domains and to efficiently control overall multienzyme activity. mTOR is composed of α-helical HEAT repeat units fused to a catalytic kinase domain. The mTORC1 core component Raptor is a repeat containing multi-domain protein as well. Seven WD40 repeats at the carboxy-terminal end form a β-propeller, that is connected to the proposed substrate recognition domain via α-helical armadillo repeats.

At a general perspective, the examples presented in this thesis demonstrate the necessity to study intact eukaryotic multidomain proteins because their emergent regulatory properties can't simply be extrapolated from structures of prokaryotic homologues or isolated fragments. Due to the difficulties in studying very large and dynamic systems, multidomain proteins are dramatically underrepresented in the

current set of known protein structures. The examples provided here clearly demonstrate that for comprehensive studies a multimethod approach is required to obtain both, atomic models, as well as representations of natural conformational variability.

Cryo-EM analysis of intact multidomain proteins combined with crystallographic experiments of isolated subunits permits identification and structural characterization of interdomain interactions and regulatory mechanisms. Complementary characterization by small-angle X-ray scattering and NMR resolves dynamic interdomain and interprotein properties and allows dissection of regulatory consequences upon association or dissociation. A particular challenge for structure determination of highly dynamic systems is the establishment of conformationally homogenous samples. This requires careful monitoring of the functional state of the respective proteins and may involve interventions such as alterations of posttranslational modifications by mutations or trapping of specific conformation by chemical cross-linking. Studies of even more elaborate eukaryotic protein multidomain and multisubunit complex may eventually require the development of completely novel techniques for *in vitro* or *in silico* sample purification: The human proteasome is a central cellular proteolytic machine required for protein homeostasis that is composed of 33 distinct subunits[303]. The kinetochore complex, that connects centromeric DNA to the spindle microtubules during cell division comprises over 80 subunits [304]. End the spliceosome complexes feature over 300 distinct subunits[305].

Structural and mechanistic studies of intact multidomain proteins are critically required to understand patient-specific mutations. While direct variation of conserved catalytic residues are lethal for essential proteins, disease-related variations can accumulate in accessory and regulatory regions. For example, genetic alterations e.g. SNPs of mTOR are distributed throughout the mTOR sequence and involve numerous regions outside the catalytic core[306]. Due to their relevance for regulation of protein activity, interdomain interactions in complex eukaryotic proteins should also be regarded as relevant targets for therapeutically interfering with protein function, in addition to direct targeting of active sites or of protein-protein interactions. mTOR, for example, is a relevant drug target for metabolic diseases and cancer. However, current drugs either specifically target only either the active site or or the nearby FKBP12-dependent allosteric rapamycin binding site, while the largest part of the mTORC1 surface, in particular the defining and regulatory but non-catalytic Raptor protein has not been exploited for drug discovery. Targeted impairment of substrate recognition or

association with external stimulators may thus provide novel approaches for the development of mTOR inhibitors with unique specificity and pharmacological profiles.

6 Acknowledgments

First of all, I would like to thank my Ph.D. committee for guiding me through the past years. Great thanks to Timm for accepting me in your lab and always keeping me on the right track. And thanks for being an incredibly awesome boss over the past years. Thank you Tilman for much helpful advice. Thank you Mike for great support during the past years, both scientifically and personally. It was a great pleasure to attend your seminars and discuss with you the progress of my work.
Many thanks to Evelyn for being a great member of the TOR-team. Thanks also to the extended TOR-team in Zurich, Chris, Daniel and Nenad for a very fruitful collaboration. Many thanks to Christian, Anna-Maria, Raphael, Sebastian and Erich for an inspiring collaboration on the PLK4 project.
Very special thanks to Moritz for being such a great fellow over many years now. I am wondering where destiny will guide us next. Many thanks to Roman "the walking labbook" Jakob for guiding me through the early days. Thank you Eddi for many cool and fun discussions and for a great trip to the rural eastern Germany. Thank you Anna for being a fun bench and office neighbor and for introducing me to the fascinating world of CrossFit. Thank you fabulous Fab for nightly trips to France. Thanks to Habib "the Dude" Bukhari for providing me with new series. Thank you Freddy for being an awesome lab member. Thank you Domi for organizing our legendary happy hours. Thanks to Tim Sharpe for great assistance and meaningful insights on the behavior of meerkats. Thanks to the entire third floor for being a fun floor. And thanks to the Biozentrum for an excellent working environment.

I would also like to thank my family: Norbert (†2007), Anny, Martin and Caroline.

7 References

1. Manning, G., Whyte, D.B., Martinez, R., Hunter, T. & Sudarsanam, S. The protein kinase complement of the human genome. *Science* **298**, 1912-+ (2002).
2. Vezina, C., Kudelski, A. & Sehgal, S.N. Rapamycin (Ay-22,989), a New Antifungal Antibiotic .1. Taxonomy of Producing Streptomycete and Isolation of Active Principle. *Journal of Antibiotics* **28**, 721-726 (1975).
3. Martel, R.R., Klicius, J. & Galet, S. Inhibition of Immune-Response by Rapamycin, a New Antifungal Antibiotic. *Canadian Journal of Physiology and Pharmacology* **55**, 48-51 (1977).
4. Houchens, D.P., Ovejera, A.A., Riblet, S.M. & Slagel, D.E. Human-Brain Tumor Xenografts in Nude-Mice as a Chemotherapy Model. *European Journal of Cancer & Clinical Oncology* **19**, 799-805 (1983).
5. Heitman, J., Movva, N.R. & Hall, M.N. Targets for Cell-Cycle Arrest by the Immunosuppressant Rapamycin in Yeast. *Science* **253**, 905-909 (1991).
6. Brown, E.J. et al. A Mammalian Protein Targeted by G1-Arresting Rapamycin-Receptor Complex. *Nature* **369**, 756-758 (1994).
7. Sabatini, D.M., Erdjumentbromage, H., Lui, M., Tempst, P. & Snyder, S.H. Raft1 - a Mammalian Protein That Binds to Fkbp12 in a Rapamycin-Dependent Fashion and Is Homologous to Yeast Tors. *Cell* **78**, 35-43 (1994).
8. Sabers, C.J. et al. Isolation of a Protein Target of the Fkbp12-Rapamycin Complex in Mammalian-Cells. *Journal of Biological Chemistry* **270**, 815-822 (1995).
9. Jacinto, E. & Lorberg, A. TOR regulation of AGC kinases in yeast and mammals. *Biochemical Journal* **410**, 19-37 (2008).
10. Dietz, A. & Mathews, J. Scanning Electron Microscopy of Selected Members of Streptomyces Hygroscopicus Group. *Applied Microbiology* **18**, 694-& (1969).
11. Keith, C.T. & Schreiber, S.L. Pik-Related Kinases - DNA-Repair, Recombination, and Cell-Cycle Checkpoints. *Science* **270**, 50-51 (1995).
12. Lovejoy, C.A. & Cortez, D. Common mechanisms of PIKK regulation. *DNA Repair* **8**, 1004-1008 (2009).
13. McMahon, S.B., Van Buskirk, H.A., Dugan, K.A., Copeland, T.D. & Cole, M.D. The novel ATM-related protein TRRAP is an essential cofactor for the c-Myc and E2F oncoproteins. *Cell* **94**, 363-374 (1998).
14. Kunz, J. et al. Target of Rapamycin in Yeast, Tor2, Is an Essential Phosphatidylinositol Kinase Homolog Required for G(1) Progression. *Cell* **73**, 585-596 (1993).
15. Bosotti, R., Isacchi, A. & Sonnhammer, E.L.L. FAT: a novel domain in PIK-related kinases. *Trends in Biochemical Sciences* **25**, 225-227 (2000).

16. Knutson, B.A. Insights into the domain and repeat architecture of target of rapamycin. *Journal of Structural Biology* **170**, 354-363 (2010).

17. Perry, J. & Kleckner, N. The ATRs, ATMs, and TORs are giant HEAT repeat proteins. *Cell* **112**, 151-155 (2003).

18. Choi, J.W., Chen, J., Schreiber, S.L. & Clardy, J. Structure of the FKBP12-rapamycin complex interacting with the binding domain of human FRAP. *Science* **273**, 239-242 (1996).

19. Yang, H.J. et al. mTOR kinase structure, mechanism and regulation. *Nature* **497**, 217-+ (2013).

20. Hara, K. et al. Raptor, a binding partner of target of rapamycin (TOR), mediates TOR action. *Cell* **110**, 177-189 (2002).

21. Kim, D.H. et al. MTOR interacts with Raptor to form a nutrient-sensitive complex that signals to the cell growth machinery. *Cell* **110**, 163-175 (2002).

22. Kim, D.H. et al. G beta L, a positive regulator of the rapamycin-sensitive pathway required for the nutrient-sensitive interaction between raptor and mTOR. *Molecular Cell* **11**, 895-904 (2003).

23. Laplante, M. & Sabatini, D.M. mTOR Signaling in Growth Control and Disease. *Cell* **149**, 274-293 (2012).

24. Oshiro, N. et al. The proline-rich akt substrate of 40 kDa (PRAS40) is a physiological substrate of mammalian target of rapamycin complex 1. *Journal of Biological Chemistry* **282**, 20329-20339 (2007).

25. Sancak, Y. et al. PRAS40 is an insulin-regulated inhibitor of the mTORC1 protein kinase. *Molecular Cell* **25**, 903-915 (2007).

26. Wang, L.F., Harris, T.E., Roth, R.A. & Lawrence, J.C. PRAS40 regulates mTORC1 kinase activity by functioning as a direct inhibitor of substrate binding. *Journal of Biological Chemistry* **282**, 20036-20044 (2007).

27. Jacinto, E. et al. Mammalian TOR complex 2 controls the actin cytoskeleton and is rapamycin insensitive. *Nature Cell Biology* **6**, 1122-U30 (2004).

28. Sarbassov, D.D. et al. Rictor, a novel binding partner of mTOR, defines a rapamycin-insensitive and raptor-independent pathway that regulates the cytoskeleton. *Current Biology* **14**, 1296-1302 (2004).

29. Frias, M.A. et al. mSin1 is necessary for Akt/PKB phosphorylation, and its isoforms define three distinct mTORC2s. *Current Biology* **16**, 1865-1870 (2006).

30. Jacinto, E. et al. SIN1/MIP1 maintains rictor-mTOR complex integrity and regulates Akt phosphorylation and substrate specificity. *Cell* **127**, 125-137 (2006).

31. Peterson, T.R. et al. DEPTOR Is an mTOR Inhibitor Frequently Overexpressed in Multiple Myeloma Cells and Required for Their Survival. *Cell* **137**, 873-886 (2009).

32. Wang, L.F., Rhodes, C.J. & Lawrence, J.C. Activation of mammalian target of rapamycin (mTOR) by insulin is associated with stimulation of 4EBP1 binding to dimeric mTOR complex 1. *Journal of Biological Chemistry* **281**, 24293-24303 (2006).

33. Wullschleger, S., Loewith, R. & Hall, M.N. TOR signaling in growth and metabolism. *Cell* **124**, 471-484 (2006).

34. Jain, A. et al. Stoichiometry and assembly of mTOR complexes revealed by single-molecule pulldown. *Proceedings of the National Academy of Sciences of the United States of America* **111**, 17833-17838 (2014).

35. Sarbassov, D.D. et al. Prolonged rapamycin treatment inhibits mTORC2 assembly and Akt/PKB. *Molecular Cell* **22**, 159-168 (2006).

36. Dibble, C.C. et al. TBC1D7 Is a Third Subunit of the TSC1-TSC2 Complex Upstream of mTORC1. *Molecular Cell* **47**, 535-546 (2012).

37. Hara, K. et al. Amino acid sufficiency and mTOR regulate p70 S6 kinase and eIF-4E BP1 through a common effector mechanism. *Journal of Biological Chemistry* **273**, 14484-14494 (1998).

38. Sancak, Y. et al. Ragulator-Rag Complex Targets mTORC1 to the Lysosomal Surface and Is Necessary for Its Activation by Amino Acids. *Cell* **141**, 290-303 (2010).

39. Bar-Peled, L., Schweitzer, L.D., Zoncu, R. & Sabatini, D.M. Ragulator Is a GEF for the Rag GTPases that Signal Amino Acid Levels tomTORC1. *Cell* **150**, 1196-1208 (2012).

40. Sancak, Y. et al. The Rag GTPases bind raptor and mediate amino acid signaling to mTORC1. *Science* **320**, 1496-1501 (2008).

41. Bar-Peled, L. et al. A Tumor Suppressor Complex with GAP Activity for the Rag GTPases That Signal Amino Acid Sufficiency to mTORC1. *Science* **340**, 1100-1106 (2013).

42. Wolfson, R.L. et al. Sestrin2 is a leucine sensor for the mTORC1 pathway. *Science* **351**, 43-48 (2016).

43. Chantranupong, L. et al. The CASTOR Proteins Are Arginine Sensors for the mTORC1 Pathway. *Cell* **165**, 153-164 (2016).

44. Duran, R.V. et al. Glutaminolysis Activates Rag-mTORC1 Signaling. *Molecular Cell* **47**, 349-358 (2012).

45. Zoncu, R. et al. mTORC1 Senses Lysosomal Amino Acids Through an Inside-Out Mechanism That Requires the Vacuolar H+-ATPase. *Science* **334**, 678-683 (2011).

46. Wang, S.Y. et al. Lysosomal amino acid transporter SLC38A9 signals arginine sufficiency to mTORC1. *Science* **347**, 188-194 (2015).

47. Inoki, K., Zhu, T.Q. & Guan, K.L. TSC2 mediates cellular energy response to control cell growth and survival. *Cell* **115**, 577-590 (2003).

48. Gwinn, D.M. et al. AMPK phosphorylation of raptor mediates a metabolic checkpoint. *Molecular Cell* **30**, 214-226 (2008).

49. Brugarolas, J. et al. Regulation of mTOR function in response to hypoxia by REDD1 and the TSC1/TSC2 tumor suppressor complex. *Genes & Development* **18**, 2893-2904 (2004).

50. Zinzalla, V., Stracka, D., Oppliger, W. & Hall, M.N. Activation of mTORC2 by Association with the Ribosome. *Cell* **144**, 757-768 (2011).

51. Betz, C. et al. mTOR complex 2-Akt signaling at mitochondria-associated endoplasmic reticulum membranes (MAM) regulates mitochondrial physiology. *Proceedings of the National Academy of Sciences of the United States of America* **110**, 12526-12534 (2013).

52. Ma, X.J.M. & Blenis, J. Molecular mechanisms of mTOR-mediated translational control. *Nature Reviews Molecular Cell Biology* **10**, 307-318 (2009).

53. Um, S.H. et al. Absence of S6K1 protects against age- and diet-induced obesity while enhancing insulin sensitivity. *Nature* **431**, 200-205 (2004).

54. Richter, J.D. & Sonenberg, N. Regulation of cap-dependent translation by eIF4E inhibitory proteins. *Nature* **433**, 477-480 (2005).

55. Robitaille, A.M. et al. Quantitative Phosphoproteomics Reveal mTORC1 Activates de Novo Pyrimidine Synthesis. *Science* **339**, 1320-1323 (2013).

56. Duvel, K. et al. Activation of a Metabolic Gene Regulatory Network Downstream of mTOR Complex 1. *Molecular Cell* **39**, 171-183 (2010).

57. Kim, J., Kundu, M., Viollet, B. & Guan, K.L. AMPK and mTOR regulate autophagy through direct phosphorylation of Ulk1. *Nature Cell Biology* **13**, 132-U71 (2011).

58. Sarbassov, D.D., Guertin, D.A., Ali, S.M. & Sabatini, D.M. Phosphorylation and regulation of Akt/PKB by the rictor-mTOR complex. *Science* **307**, 1098-1101 (2005).

59. Calnan, D.R. & Brunet, A. The FoxO code. *Oncogene* **27**, 2276-2288 (2008).

60. Wander, S.A., Hennessy, B.T. & Slingerland, J.M. Next-generation mTOR inhibitors in clinical oncology: how pathway complexity informs therapeutic strategy. *Journal of Clinical Investigation* **121**, 1231-1241 (2011).

61. Thompson, C.A. First drug-eluting coronary stent approved. *American Journal of Health-System Pharmacy* **60**, 1210-+ (2003).

62. Benjamin, D., Colombi, M., Moroni, C. & Hall, M.N. Rapamycin passes the torch: a new generation of mTOR inhibitors. *Nature Reviews Drug Discovery* **10**, 868-880 (2011).

63. Bhat, M. et al. Targeting the translation machinery in cancer. *Nature Reviews Drug Discovery* **14**, 261-278 (2015).

64. Schalm, S.S. & Blenis, J. Identification of a conserved motif required for mTOR signaling. *Current Biology* **12**, 632-9 (2002).

65. Wang, X.M., Li, W., Parra, J.L., Beugnet, A. & Proud, C.G. The C terminus of initiation factor 4E-binding protein 1 contains multiple regulatory features that influence its function and phosphorylation. *Molecular and Cellular Biology* **23**, 1546-1557 (2003).

66. Nojima, H. et al. The mammalian target of rapamycin (mTOR) partner, raptor, binds the mTOR substrates, p70 S6 kinase and 4E-BP1, through their TOR signaling (TOS) motif (vol 278, pg 15461, 2003). *Journal of Biological Chemistry* **278**, 26302-26302 (2003).

67. Schaim, S.S., Fingar, D.C., Sabatini, D.M. & Blenis, J. TOS motif-mediated raptor binding regulates 4E-BP1 multisite phosphorylation and function. *Current Biology* **13**, 797-806 (2003).

68. Beugnet, A., Wang, X. & Proud, C.G. Target of rapamycin (TOR)-signaling and RAIP motifs play distinct roles in the mammalian TOR-dependent phosphorylation of initiation factor 4E-binding protein 1. *Journal of Biological Chemistry* **278**, 40717-22 (2003).

69. Eguchi, S. et al. Different roles for the TOS and RAIP motifs of the translational regulator protein 4E-BP1 in the association with raptor and phosphorylation by mTOR in the regulation of cell size. *Genes to Cells* **11**, 757-766 (2006).

70. Peterson, T.R. et al. mTOR Complex 1 Regulates Lipin 1 Localization to Control the SREBP Pathway. *Cell* **146**, 408-420 (2011).

71. Choo, A.Y. & Blenis, J. Not all substrates are treated equally Implications for mTOR, rapamycin-resistance and cancer therapy. *Cell Cycle* **8**, 567-572 (2009).

72. Thoreen, C.C. & Sabatini, D.M. Rapamycin inhibits mTORC1, but not completely. *Autophagy* **5**, 725-726 (2009).

73. Kang, S.A. et al. mTORC1 Phosphorylation Sites Encode Their Sensitivity to Starvation and Rapamycin. *Science* **341**, 364-+ (2013).

74. Dames, S.A., Mulet, J.M., Rathgeb-Szabo, K., Hall, M.N. & Grzesiek, S. The solution structure of the FATC domain of the protein kinase target of rapamycin suggests a role for redox-dependent structural and cellular stability. *Journal of Biological Chemistry* **280**, 20558-20564 (2005).

75. McMahon, L.P., Choi, K.M., Lin, T.A., Abraham, R.T. & Lawrence, J.C. The rapamycin-binding domain governs substrate selectivity by the mammalian target of rapamycin. *Molecular and Cellular Biology* **22**, 7428-7438 (2002).

76. Sekulic, A. et al. A direct linkage between the phosphoinositide 3-Kinase-AKT signaling pathway and the mammalian target of rapamycin in mitogen-stimulated and transformed cells. *Cancer Research* **60**, 3504-3513 (2000).

77. Yip, C.K., Murata, K., Walz, T., Sabatini, D.M. & Kang, S.A. Structure of the Human mTOR Complex I and Its Implications for Rapamycin Inhibition. *Molecular Cell* **38**, 768-774 (2010).

78. Adami, A., Garcia-Alvarez, B., Arias-Palomo, E., Barford, D. & Llorca, O. Structure of TOR and its complex with KOG1. *Molecular Cell* **27**, 509-516 (2007).

79. Ginalski, K., Zhang, H. & Grishin, N.V. Raptor protein contains a caspase-like domain. *Trends in Biochemical Sciences* **29**, 522-524 (2004).

80. Elia, A.E.H. et al. The molecular basis for phosphodependent substrate targeting and regulation of Plks by the Polo-box domain. *Cell* **115**, 83-95 (2003).

81. Sunkel, C.E. & Glover, D.M. Polo, a Mitotic Mutant of Drosophila Displaying Abnormal Spindle Poles. *Journal of Cell Science* **89**, 25-38 (1988).

82. Llamazares, S. et al. Polo Encodes a Protein-Kinase Homolog Required for Mitosis in Drosophila. *Genes & Development* **5**, 2153-2165 (1991).

83. Archambault, V. & Glover, D.M. Polo-like kinases: conservation and divergence in their functions and regulation. *Nature Reviews Molecular Cell Biology* **10**, 265-275 (2009).

84. Zitouni, S., Nabais, C., Jana, S.C., Guerrero, A. & Bettencourt-Dias, M. Polo-like kinases: structural variations lead to multiple functions. *Nature Reviews Molecular Cell Biology* **15**, 433-452 (2014).

85. Carvalho-Santos, Z. et al. Stepwise evolution of the centriole-assembly pathway. *Journal of Cell Science* **123**, 1414-1426 (2010).

86. Kothe, M. et al. Structure of the catalytic domain of human polo-like kinase 1. *Biochemistry* **46**, 5960-5971 (2007).

87. de Carcer, G. et al. Plk5, a Polo Box Domain-Only Protein with Specific Roles in Neuron Differentiation and Glioblastoma Suppression. *Molecular and Cellular Biology* **31**, 1225-1239 (2011).

88. de Carcer, G., Manning, G. & Malumbres, M. From Plk1 to Plk5 Functional evolution of Polo-like kinases. *Cell Cycle* **10**, 2255-2262 (2011).

89. Park, J.E. et al. Polo-box domain: a versatile mediator of polo-like kinase function. *Cellular and Molecular Life Sciences* **67**, 1957-1970 (2010).

90. Jang, Y.J., Ma, S., Terada, Y. & Erikson, R.L. Phosphorylation of threonine 210 and the role of serine 137 in the regulation of mammalian polo-like kinase. *Journal of Biological Chemistry* **277**, 44115-44120 (2002).

91. Uchiumi, T., Longo, D.L. & Ferris, D.K. Cell cycle regulation of the human polo-like kinase (PLK) promoter. *Journal of Biological Chemistry* **272**, 9166-9174 (1997).

92. Ferris, D.K., Maloid, S.C. & Li, C.C.H. Ubiquitination and proteasome mediated degradation of polo-like kinase. *Biochemical and Biophysical Research Communications* **252**, 340-344 (1998).

93. Lindon, C. & Pines, J. Ordered proteolysis in anaphase inactivates Plk1 to contribute to proper mitotic exit in human cells. *Journal of Cell Biology* **164**, 233-241 (2004).

94. Cheng, K.Y., Lowe, E.D., Sinclair, J., Nigg, E.A. & Johnson, L.N. The crystal structure of the human polo-like kinase-1 polo box domain and its phospho-peptide complex. *Embo Journal* **22**, 5757-5768 (2003).

95. Elia, A.E.H., Cantley, L.C. & Yaffe, M.B. Proteomic screen finds pSer/pThr-binding domain localizing Plk1 to mitotic substrates. *Science* **299**, 1228-1231 (2003).

96. Archambault, V., D'Avino, P.P., Deery, M.J., Lilley, K.S. & Glover, D.M. Sequestration of Polo kinase to microtubules by phosphopriming-independent binding to Map205 is relieved by phosphorylation at a CDK site in mitosis. *Genes & Development* **22**, 2707-2720 (2008).

97. Xu, J., Shen, C., Wang, T. & Quan, J.M. Structural basis for the inhibition of Polo-like kinase 1. *Nature Structural & Molecular Biology* **20**, 1047-1053 (2013).

98. Sillibourne, J.E. & Bornens, M. Polo-like kinase 4: the odd one out of the family. *Cell Division* **5**(2010).

99. Habedanck, R., Stierhof, Y.D., Wilkinson, C.J. & Nigg, E.A. The Polo kinase Plk4 functions in centriole duplication. *Nature Cell Biology* **7**, 1140-1146 (2005).

100. Bettencourt-Dias, M. et al. SAK/PLK4 is required for centriole duplication and flagella development. *Current Biology* **15**, 2199-2207 (2005).

101. Paintrand, M., Moudjou, M., Delacroix, H. & Bornens, M. Centrosome Organization and Centriole Architecture - Their Sensitivity to Divalent-Cations. *Journal of Structural Biology* **108**, 107-128 (1992).

102. Chretien, D., Buendia, B., Fuller, S.D. & Karsenti, E. Reconstruction of the centrosome cycle from cryoelectron micrographs. *Journal of Structural Biology* **120**, 117-133 (1997).

103. Nigg, E.A. Centrosome duplication: of rules and licenses. *Trends in Cell Biology* **17**, 215-221 (2007).

104. Cunha-Ferreira, I. et al. The SCF/Slimb Ubiquitin Ligase Limits Centrosome Amplification through Degradation of SAK/PLK4. *Current Biology* **19**, 43-49 (2009).

105. Rogers, G.C., Rusan, N.M., Roberts, D.M., Peifer, M. & Rogers, S.L. The SCF Slimb ubiquitin ligase regulates Plk4/Sak levels to block centriole reduplication. *J. Cell Biol.* **184**, 225-39 (2009).

106. Sillibourne, J.E. et al. Autophosphorylation of Polo-like Kinase 4 and Its Role in Centriole Duplication. *Molecular Biology of the Cell* **21**, 547-561 (2010).

107. Guderian, G., Westendorf, J., Uldschmid, A. & Nigg, E.A. Plk4 trans-autophosphorylation regulates centriole number by controlling betaTrCP-mediated degradation. *J. Cell Sci.* **123**, 2163-9 (2010).

108. Swallow, C.J., Ko, M.A., Siddiqui, N.U., Hudson, J.W. & Dennis, J.W. Sak/Plk4 and mitotic fidelity. *Oncogene* **24**, 306-312 (2005).

109. Slevin, L.K. et al. The Structure of the Plk4 Cryptic Polo Box Reveals Two Tandem Polo Boxes Required for Centriole Duplication. *Structure* **20**, 1905-1917 (2012).

110. Shimanovskaya, E. et al. Structure of the C. elegans ZYG-1 Cryptic Polo Box Suggests a Conserved Mechanism for Centriolar Docking of Plk4 Kinases. *Structure* **22**, 1090-1104 (2014).

111. Park, S.Y. et al. Molecular basis for unidirectional scaffold switching of human Plk4 in centriole biogenesis. *Nature Structural & Molecular Biology* **21**, 696-703 (2014).

112. Leung, G.C. et al. The Sak polo-box comprises a structural domain sufficient for mitotic subcellular localization. *Nature Structural Biology* **9**, 719-724 (2002).

113. Kim, T.S. et al. Hierarchical recruitment of Plk4 and regulation of centriole biogenesis by two centrosomal scaffolds, Cep192 and Cep152. *Proceedings of the National Academy of Sciences of the United States of America* **110**, E4849-E4857 (2013).

114. Lettman, M.M. et al. Direct Binding of SAS-6 to ZYG-1 Recruits SAS-6 to the Mother Centriole for Cartwheel Assembly. *Developmental Cell* **25**, 284-298 (2013).

115. Kitagawa, D. et al. Structural Basis of the 9-Fold Symmetry of Centrioles. *Cell* **144**, 364-375 (2011).

116. van Breugel, M. et al. Structures of SAS-6 Suggest Its Organization in Centrioles. *Science* **331**, 1196-1199 (2011).

117. Tong, L. Acetyl-coenzyme A carboxylase: crucial metabolic enzyme and attractive target for drug discovery. *Cellular and Molecular Life Sciences* **62**, 1784-1803 (2005).

118. Tong, L. Structure and function of biotin-dependent carboxylases. *Cellular and Molecular Life Sciences* **70**, 863-891 (2013).

119. McGarry, J.D. & Brown, N.F. The mitochondrial carnitine palmitoyltransferase system - From concept to molecular analysis. *European Journal of Biochemistry* **244**, 1-14 (1997).

120. Ramsay, R.R., Gandour, R.D. & van der Leij, F.R. Molecular enzymology of carnitine transfer and transport. *Biochimica Et Biophysica Acta-Protein Structure and Molecular Enzymology* **1546**, 21-43 (2001).

121. Harwood, H.J. Treating the metabolic syndrome: acetyl-CoA carboxylase inhibition. *Expert Opinion on Therapeutic Targets* **9**, 267-281 (2005).

122. Lenhard, J.M. & Gottschalk, W.K. Preclinical developments in type 2 diabetes. *Advanced Drug Delivery Reviews* **54**, 1199-1212 (2002).

123. Munday, M.R. Regulation of mammalian acetyl-CoA carboxylase. *Biochemical Society Transactions* **30**, 1059-1064 (2002).

124. Kim, C.W. et al. Induced polymerization of mammalian acetyl-CoA carboxylase by MIG12 provides a tertiary level of regulation of fatty acid synthesis. *Proceedings of the National Academy of Sciences of the United States of America* **107**, 9626-9631 (2010).

125. Shen, Y. & Tong, L. Structural evidence for direct interactions between the BRCT domains of human BRCA1 and a phospho-peptide from human ACC1. *Biochemistry* **47**, 5767-5773 (2008).

126. Williams, R.S., Lee, M.S., Hau, D.D. & Glover, J.N.M. Structural basis of phosphopeptide recognition by the BRCT domain of BRCA1. *Nature Structural & Molecular Biology* **11**, 519-525 (2004).

127. Ray, H., Moreau, K., Dizin, E., Callebaut, I. & Dalla Venezia, N. ACCA phosphopeptide recognition by the BRCT repeats of BRCA1. *Journal of Molecular Biology* **359**, 973-982 (2006).

128. Ha, J., Daniel, S., Broyles, S.S. & Kim, K.H. Critical Phosphorylation Sites for Acetyl-Coa Carboxylase Activity. *Journal of Biological Chemistry* **269**, 22162-22168 (1994).

129. Davies, S.P., Sim, A.T. & Hardie, D.G. Location and function of three sites phosphorylated on rat acetyl-CoA carboxylase by the AMP-activated protein kinase. *European Journal of Biochemistry* **187**, 183-90 (1990).

130. Woods, A. et al. Yeast Snf1 Is Functionally Related to Mammalian Amp-Activated Protein-Kinase and Regulates Acetyl-Coa Carboxylase in-Vivo. *Journal of Biological Chemistry* **269**, 19509-19515 (1994).

131. Shi, S.B., Chen, Y., Siewers, V. & Nielsen, J. Improving Production of Malonyl Coenzyme A-Derived Metabolites by Abolishing Snf1-Dependent Regulation of Acc1. *Mbio* **5**(2014).

132. Ficarro, S.B. et al. Phosphoproteome analysis by mass spectrometry and its application to Saccharomyces cerevisiae. *Nature Biotechnology* **20**, 301-305 (2002).

133. Cronan, J.E. & Waldrop, G.L. Multi-subunit acetyl-CoA carboxylases. *Progress in Lipid Research* **41**, 407-435 (2002).

134. Shen, Y., Volrath, S.L., Weatherly, S.C., Elich, T.D. & Tong, L. A mechanism for the potent inhibition of eukaryotic acetyl-coenzyme a carboxylase by soraphen A, a macrocyclic polyketide natural product. *Molecular Cell* **16**, 881-891 (2004).

135. Athappilly, F.K. & Hendrickson, W.A. Structure of the biotinyl domain of acetyl-coenzyme A carboxylase determined by MAD phasing. *Structure* **3**, 1407-1419 (1995).

136. Zhang, H.L., Yang, Z.R., Shen, Y. & Tong, L. Crystal structure of the carboxyltransferase domain of acetyl-coenzyme a carboxylase. *Science* **299**, 2064-2067 (2003).

137. Dazert, E. & Hall, M.N. mTOR signaling in disease. *Curr Opin Cell Biol* **23**, 744-55 (2011).

138. Menon, S. & Manning, B.D. Common corruption of the mTOR signaling network in human tumors. *Oncogene* **27 Suppl 2**, S43-51 (2008).

139. Loewith, R. et al. Two TOR complexes, only one of which is rapamycin sensitive, have distinct roles in cell growth control. *Molecular Cell* **10**, 457-468 (2002).

140. Shimobayashi, M. & Hall, M.N. Making new contacts: the mTOR network in metabolism and signalling crosstalk. *Nature Reviews Molecular Cell Biology* **15**, 155-162 (2014).

141. Yang, Q., Inoki, K., Ikenoue, T. & Guan, K.L. Identification of Sin1 as an essential TORC2 component required for complex formation and kinase activity. *Genes & Development* **20**, 2820-2832 (2006).

142. Kim, E., Goraksha-Hicks, P., Li, L., Neufeld, T.P. & Guan, K.L. Regulation of TORC1 by Rag GTPases in nutrient response. *Nature Cell Biology* **10**, 935-945 (2008).

143. Inoki, K., Li, Y., Xu, T. & Guan, K.L. Rheb GTPase is a direct target of TSC2 GAP activity and regulates mTOR signaling. *Genes Dev* **17**, 1829-34 (2003).

144. Zhang, Y. et al. Rheb is a direct target of the tuberous sclerosis tumour suppressor proteins. *Nature Cell Biology* **5**, 578-581 (2003).

145. Andrade, M.A. & Bork, P. Heat Repeats in the Huntingtons-Disease Protein. *Nature Genetics* **11**, 115-116 (1995).

146. Harding, M.W., Galat, A., Uehling, D.E. & Schreiber, S.L. A Receptor for the Immunosuppressant Fk506 Is a Cis-Trans Peptidyl-Prolyl Isomerase. *Nature* **341**, 758-760 (1989).

147. Siekierka, J.J., Hung, S.H.Y., Poe, M., Lin, C.S. & Sigal, N.H. A Cytosolic Binding-Protein for the Immunosuppressant Fk506 Has Peptidyl-Prolyl Isomerase Activity but Is Distinct from Cyclophilin. *Nature* **341**, 755-757 (1989).

148. Chen, J., Zheng, X.F., Brown, E.J. & Schreiber, S.L. Identification of an 11-Kda Fkbp12-Rapamycin-Binding Domain within the 289-Kda Fkbp12-Rapamycin-Associated Protein and Characterization of a Critical Serine

Residue. *Proceedings of the National Academy of Sciences of the United States of America* **92**, 4947-4951 (1995).

149. Kastner, B. et al. GraFix: sample preparation for single-particle electron cryomicroscopy. *Nature Methods* **5**, 53-55 (2008).

150. Gaubitz, C. et al. Molecular Basis of the Rapamycin Insensitivity of Target Of Rapamycin Complex 2. *Molecular Cell* **58**, 977-988 (2015).

151. Foster, K.G. & Fingar, D.C. Mammalian Target of Rapamycin (mTOR): Conducting the Cellular Signaling Symphony. *Journal of Biological Chemistry* **285**, 14071-14077 (2010).

152. Wullschleger, S., Loewith, R., Oppliger, W. & Hall, M.N. Molecular organization of target of rapamycin complex 2. *Journal of Biological Chemistry* **280**, 30697-30704 (2005).

153. Pettersen, E.F. et al. UCSF chimera - A visualization system for exploratory research and analysis. *Journal of Computational Chemistry* **25**, 1605-1612 (2004).

154. Fitzgerald, D.J. et al. Protein complex expression by using multigene baculoviral vectors. *Nature Methods* **3**, 1021-1032 (2006).

155. Ludtke, S.J., Baldwin, P.R. & Chiu, W. EMAN: Semiautomated software for high-resolution single-particle reconstructions. *Journal of Structural Biology* **128**, 82-97 (1999).

156. Mindell, J.A. & Grigorieff, N. Accurate determination of local defocus and specimen tilt in electron microscopy. *Journal of Structural Biology* **142**, 334-347 (2003).

157. Scheres, S.H.W. RELION: Implementation of a Bayesian approach to cryo-EM structure determination. *Journal of Structural Biology* **180**, 519-530 (2012).

158. Li, X.M. et al. Electron counting and beam-induced motion correction enable near-atomic-resolution single-particle cryo-EM. *Nature Methods* **10**, 584-+ (2013).

159. Kabsch, W. Xds. *Acta Crystallographica Section D-Biological Crystallography* **66**, 125-132 (2010).

160. Sheldrick, G.M. A short history of SHELX. *Acta Crystallographica Section A* **64**, 112-122 (2008).

161. Pape, T. & Schneider, T.R. HKL2MAP: a graphical user interface for macromolecular phasing with SHELX programs. *Journal of Applied Crystallography* **37**, 843-844 (2004).

162. McCoy, A.J. et al. Phaser crystallographic software. *Journal of Applied Crystallography* **40**, 658-674 (2007).

163. Emsley, P., Lohkamp, B., Scott, W.G. & Cowtan, K. Features and development of Coot. *Acta Crystallographica Section D-Biological Crystallography* **66**, 486-501 (2010).

164. Kelley, L.A., Mezulis, S., Yates, C.M., Wass, M.N. & Sternberg, M.J.E. The Phyre2 web portal for protein modeling, prediction and analysis. *Nature Protocols* **10**, 845-858 (2015).

165. Adams, P.D. et al. PHENIX: a comprehensive Python-based system for macromolecular structure solution. *Acta Crystallographica Section D-Biological Crystallography* **66**, 213-221 (2010).

166. Sibanda, B.L., Chirgadze, D.Y. & Blundell, T.L. Crystal structure of DNA-PKcs reveals a large open-ring cradle comprised of HEAT repeats. *Nature* **463**, 118-U132 (2010).

167. Kucukelbir, A., Sigworth, F.J. & Tagare, H.D. Quantifying the local resolution of cryo-EMEM density maps. *Nature Methods* **11**, 63-+ (2014).

168. Bettencourt-Dias, M. & Glover, D.M. Centrosome biogenesis and function: centrosomics brings new understanding. *Nature Reviews Molecular Cell Biology* **8**, 451-463 (2007).

169. Bornens, M. The Centrosome in Cells and Organisms. *Science* **335**, 422-426 (2012).

170. Gonczy, P. Towards a molecular architecture of centriole assembly. *Nature Reviews Molecular Cell Biology* **13**, 425-435 (2012).

171. Chavali, P.L., Putz, M. & Gergely, F. Small organelle, big responsibility: the role of centrosomes in development and disease. *Philosophical Transactions of the Royal Society B-Biological Sciences* **369** (2014).

172. Nigg, E.A. & Raff, J.W. Centrioles, Centrosomes, and Cilia in Health and Disease. *Cell* **139**, 663-678 (2009).

173. Basto, R. et al. Centrosome amplification can initiate tumorigenesis in flies. *Cell* **133**, 1032-1042 (2008).

174. Ganem, N.J., Godinho, S.A. & Pellman, D. A mechanism linking extra centrosomes to chromosomal instability. *Nature* **460**, 278-282 (2009).

175. Nigg, E.A. Centrosome aberrations: Cause or consequence of cancer progression? *Nature Reviews Cancer* **2**, 815-825 (2002).

176. Firat-Karalar, E.N. & Stearns, T. The centriole duplication cycle. *Philosophical Transactions of the Royal Society B-Biological Sciences* **369** (2014).

177. Sluder, G. One to only two: a short history of the centrosome and its duplication. *Philosophical Transactions of the Royal Society B-Biological Sciences* **369** (2014).

178. Azimzadeh, J. & Marshall, W.F. Building the Centriole. *Current Biology* **20**, R816-R825 (2010).

179. Carvalho-Santos, Z., Azimzadeh, J., Pereira-Leal, J.B. & Bettencourt-Dias, M. Tracing the origins of centrioles, cilia, and flagella. *Journal of Cell Biology* **194**, 165-175 (2011).

180. Brito, D.A., Gouveia, S.M. & Bettencourt-Dias, M. Deconstructing the centriole: structure and number control. *Current Opinion in Cell Biology* **24**, 4-13 (2012).

181. Nigg, E.A. & Stearns, T. The centrosome cycle: Centriole biogenesis, duplication and inherent asymmetries. *Nature Cell Biology* **13**, 1154-1160 (2011).

182. Strnad, P. & Gonczy, P. Mechanisms of procentriole formation. *Trends in Cell Biology* **18**, 389-396 (2008).

183. Arquint, C., Sonnen, K.F., Stierhof, Y.D. & Nigg, E.A. Cell-cycle-regulated expression of STIL controls centriole number in human cells. *Journal of Cell Science* **125**, 1342-1352 (2012).

184. Kleylein-Sohn, J. et al. Plk4-induced centriole biogenesis in human cells. *Developmental Cell* **13**, 190-202 (2007).

185. Strnad, P. et al. Regulated HsSAS-6 levels ensure formation of a single procentriole per centriole during the centrosome duplication cycle. *Developmental Cell* **13**, 203-213 (2007).

186. Tang, C.J. et al. The human microcephaly protein STIL interacts with CPAP and is required for procentriole formation. *EMBO J.* **30**, 4790-804 (2011).

187. Vulprecht, J. et al. STIL is required for centriole duplication in human cells. *Journal of Cell Science* **125**, 1353-1362 (2012).

188. Leidel, S., Delattre, M., Cerutti, L., Baumer, K. & Gonczy, P. SAS-6 defines a protein family required for centrosome duplication in C-elegans and in human cells. *Nature Cell Biology* **7**, 115-125 (2005).

189. Arquint, C. & Nigg, E.A. STIL microcephaly mutations interfere with APC/C-mediated degradation and cause centriole amplification. *Curr. Biol.* **24**, 351-60 (2014).

190. Holland, A.J., Lan, W.J., Niessen, S., Hoover, H. & Cleveland, D.W. Polo-like kinase 4 kinase activity limits centrosome overduplication by autoregulating its own stability. *Journal of Cell Biology* **188**, 191-198 (2010).

191. Cizmecioglu, O. et al. Cep152 acts as a scaffold for recruitment of Plk4 and CPAP to the centrosome. *Journal of Cell Biology* **191**, 731-739 (2010).

192. Dzhindzhev, N.S. et al. Asterless is a scaffold for the onset of centriole assembly. *Nature* **467**, 714-718 (2010).

193. Hatch, E.M., Kulukian, A., Holland, A.J., Cleveland, D.W. & Stearns, T. Cep152 interacts with Plk4 and is required for centriole duplication. *Journal of Cell Biology* **191**, 721-729 (2010).

194. Sonnen, K.F., Gabryjonczyk, A.M., Anselm, E., Stierhof, Y.D. & Nigg, E.A. Human Cep192 and Cep152 cooperate in Plk4 recruitment and centriole duplication. *Journal of Cell Science* **126**, 3223-3233 (2013).

195. Hirono, M. Cartwheel assembly. *Philosophical Transactions of the Royal Society B-Biological Sciences* **369** (2014).

196. Nakazawa, Y., Hiraki, M., Kamiya, R. & Hirono, M. SAS-6 is a cartwheel protein that establishes the 9-fold symmetry of the centriole. *Current Biology* **17**, 2169-2174 (2007).

197. Winey, M. & O'Toole, E. Centriole structure. *Philosophical Transactions of the Royal Society B-Biological Sciences* **369** (2014).

198. Guichard, P. et al. Native Architecture of the Centriole Proximal Region Reveals Features Underlying Its 9-Fold Radial Symmetry. *Current Biology* **23**, 1620-1628 (2013).

199. van Breugel, M., Wilcken, R., McLaughlin, S.H., Rutherford, T.J. & Johnson, C.M. Structure of the SAS-6 cartwheel hub from Leishmania major. *Elife* **3**(2014).

200. Fong, C.S., Kim, M., Yang, T.T., Liao, J.C. & Tsou, M.F.B. SAS-6 Assembly Templated by the Lumen of Cartwheel-less Centrioles Precedes Centriole Duplication. *Developmental Cell* **30**, 488-488 (2014).

201. Sonnen, K.F., Schermelleh, L., Leonhardt, H. & Nigg, E.A. 3D-structured illumination microscopy provides novel insight into architecture of human centrosomes. *Biology Open* **1**, 965-976 (2012).

202. Dzhindzhev, N.S. et al. Plk4 Phosphorylates Ana2 to Trigger Sas6 Recruitment and Procentriole Formation. *Current Biology* **24**, 2526-2532 (2014).

203. Ohta, M. et al. Direct interaction of Plk4 with STIL ensures formation of a single procentriole per parental centriole. *Nat. Commun.* **5**, 5267 (2014).

204. Kratz, A.S., Barenz, F., Richter, K.T. & Hoffmann, I. Plk4-dependent phosphorylation of STIL is required for centriole duplication. *Biol. Open.* (2015).

205. Stevens, N.R., Dobbelaere, J., Brunk, K., Franz, A. & Raff, J.W. Drosophila Ana2 is a conserved centriole duplication factor. *J. Cell Biol.* **188**, 313-23 (2010).

206. Lowery, D.M., Lim, D. & Yaffe, M.B. Structure and function of Polo-like kinases. *Oncogene* **24**, 248-59 (2005).

207. Yun, S.M. et al. Structural and functional analyses of minimal phosphopeptides targeting the polo-box domain of polo-like kinase 1. *Nature Structural & Molecular Biology* **16**, 876-82 (2009).

208. Firat-Karalar, E.N., Rauniyar, N., Yates, J.R. & Stearns, T. Proximity Interactions among Centrosome Components Identify Regulators of Centriole Duplication. *Current Biology* **24**, 664-670 (2014).

209. Sievers, F. et al. Fast, scalable generation of high-quality protein multiple sequence alignments using Clustal Omega. *Molecular Systems Biology* **7** (2011).

210. Krissinel, E. & Henrick, K. Inference of macromolecular assemblies from crystalline state. *Journal of Molecular Biology* **372**, 774-797 (2007).

211. Sledz, P. et al. From crystal packing to molecular recognition: prediction and discovery of a binding site on the surface of polo-like kinase 1. *Angew Chem Int Ed Engl* **50**, 4003-6 (2011).

212. Klebba, J.E., Buster, D.W., McLamarrah, T.A., Rusan, N.M. & Rogers, G.C. Autoinhibition and relief mechanism for Polo-like kinase 4. *Proc. Natl. Acad. Sci. USA* **112**, E657-E666 (2015).

213. Cottee, M.A. et al. The homo-oligomerisation of both Sas-6 and Ana2 is required for efficient centriole assembly in flies. *Elife* **4**(2015).

214. Kim, M., Fong, C.S. & Tsou, M.F. Centriole duplication: when PLK4 meets Ana2/STIL. *Current Biology* **24**, R1046-8 (2014).

215. Moyer, T.C., Clutario, K.M., Lambrus, B.G., Daggubati, V. & Holland, A.J. Binding of STIL to Plk4 activates kinase activity to promote centriole assembly. *Journal of Cell Biology* **209**, 863-78 (2015).

216. Thein, K.H., Kleylein-Sohn, J., Nigg, E.A. & Gruneberg, U. Astrin is required for the maintenance of sister chromatid cohesion and centrosome integrity. *Journal of Cell Biology* **178**, 345-354 (2007).

217. Schmidt, T.I. et al. Control of Centriole Length by CPAP and CP110. *Current Biology* **19**, 1005-1011 (2009).

218. Evan, G.I., Lewis, G.K., Ramsay, G. & Bishop, J.M. Isolation of monoclonal antibodies specific for human c-myc proto-oncogene product. *Mol. Cell Biol.* **5**, 3610-6 (1985).

219. Guardavaccaro, D. et al. Control of meiotic and mitotic progression by the F box protein beta-Trcp1 in vivo. *Developmental Cell* **4**, 799-812 (2003).

220. Maze, A., Glatter, T. & Bumann, D. The central metabolism regulator EIIAGlc switches Salmonella from growth arrest to acute virulence through activation of virulence factor secretion. *Cell Rep* **7**, 1426-33 (2014).

221. Meraldi, P., Lukas, J., Fry, A.M., Bartek, J. & Nigg, E.A. Centrosome duplication in mammalian somatic cells requires E2F and Cdk2-cyclin A. *Nature Cell Biology* **1**, 88-93 (1999).

222. Pervushin, K., Riek, R., Wider, G. & Wuthrich, K. Attenuated T2 relaxation by mutual cancellation of dipole-dipole coupling and chemical shift anisotropy indicates an avenue to NMR structures of very large biological macromolecules in solution. *Proc. Natl. Acad. Sci. USA* **94**, 12366-71 (1997).

223. Salzmann, M., Pervushin, K., Wider, G., Senn, H. & Wuthrich, K. TROSY in triple-resonance experiments: new perspectives for sequential NMR assignment of large proteins. *Proc. Natl. Acad. Sci. USA* **95**, 13585-90 (1998).

224. Grzesiek, S. & Bax, A. Amino acid type determination in the sequential assignment procedure of uniformly 13C/15N-enriched proteins. *J. Biomol. NMR* **3**, 185-204 (1993).

225. Marion, D. et al. Overcoming the overlap problem in the assignment of 1H NMR spectra of larger proteins by use of three-dimensional heteronuclear 1H-15N Hartmann-Hahn-multiple quantum coherence and nuclear Overhauser-multiple quantum coherence spectroscopy: application to interleukin 1 beta. *Biochemistry* **28**, 6150-6 (1989).

226. Zuiderweg, E.R. & Fesik, S.W. Heteronuclear three-dimensional NMR spectroscopy of the inflammatory protein C5a. *Biochemistry* **28**, 2387-91 (1989).

227. Zhu, G., Xia, Y., Nicholson, L.K. & Sze, K.H. Protein dynamics measurements by TROSY-based NMR experiments. *J. Magn. Reson.* **143**, 423-6 (2000).

228. Chou, J.J., Baber, J.L. & Bax, A. Characterization of phospholipid mixed micelles by translational diffusion. *J. Biomol. NMR* **29**, 299-308 (2004).

229. Guntert, P., Dotsch, V., Wider, G. & Wuthrich, K. Processing of Multidimensional Nmr Data with the New Software Prosa. *J. Biomol. NMR* **2**, 619-629 (1992).

230. Keller, R. The computer aided resonance assignment tutorial. *CANTINA Verlag; Goldau* (2004).

231. Herrmann, T., Guntert, P. & Wuthrich, K. Protein NMR structure determination with automated NOE assignment using the new software CANDID and the torsion angle dynamics algorithm DYANA. *J. Mol. Biol.* **319**, 209-27 (2002).

232. Shen, Y., Delaglio, F., Cornilescu, G. & Bax, A. TALOS+: a hybrid method for predicting protein backbone torsion angles from NMR chemical shifts. *J Biomol NMR* **44**, 213-23 (2009).

233. Brunger, A.T. et al. Crystallography & NMR system: A new software suite for macromolecular structure determination. *Acta Crystallogr. D Biol. Crystallogr.* **54**, 905-21 (1998).

234. Koradi, R., Billeter, M. & Wuthrich, K. MOLMOL: a program for display and analysis of macromolecular structures. *J. Mol. Graph.* **14**, 51-5, 29-32 (1996).

235. Emsley, P. & Cowtan, K. Coot: model-building tools for molecular graphics. *Acta Crystallogr. D Biol. Crystallogr.* **60**, 2126-32 (2004).

236. Adams, P.D. et al. PHENIX: building new software for automated crystallographic structure determination. *Acta Crystallogr. D Biol. Crystallogr.* **58**, 1948-54 (2002).

237. Krissinel, E. & Henrick, K. Secondary-structure matching (SSM), a new tool for fast protein structure alignment in three dimensions. *Acta Crystallographica Section D-Biological Crystallography* **60**, 2256-2268 (2004).

238. Gronenborn, A.M. et al. A Novel, Highly Stable Fold of the Immunoglobulin Binding Domain of Streptococcal Protein-G. *Science* **253**, 657-661 (1991).

239. Wakil, S.J., Titchener, E.B. & Gibson, D.M. Evidence for the participation of biotin in the enzymic synthesis of fatty acids. *Biochim Biophys Acta* **29**, 225-6 (1958).

240. Wakil, S.J., Stoops, J.K. & Joshi, V.C. Fatty acid synthesis and its regulation. *Annu Rev Biochem* **52**, 537-79 (1983).

241. Abu-Elheiga, L., Matzuk, M.M., Abo-Hashema, K.A. & Wakil, S.J. Continuous fatty acid oxidation and reduced fat storage in mice lacking acetyl-CoA carboxylase 2. *Science* **291**, 2613-6 (2001).

242. Abu-Elheiga, L., Oh, W., Kordari, P. & Wakil, S.J. Acetyl-CoA carboxylase 2 mutant mice are protected against obesity and diabetes induced by high-fat/high-carbohydrate diets. *Proc Natl Acad Sci U S A* **100**, 10207-12 (2003).

243. Harwood, H.J., Jr. Acetyl-CoA carboxylase inhibition for the treatment of metabolic syndrome. *Curr Opin Investig Drugs* **5**, 283-9 (2004).

244. Milgraum, L.Z., Witters, L.A., Pasternack, G.R. & Kuhajda, F.P. Enzymes of the fatty acid synthesis pathway are highly expressed in in situ breast carcinoma. *Clin Cancer Res* **3**, 2115-20 (1997).

245. Swinnen, J.V., Brusselmans, K. & Verhoeven, G. Increased lipogenesis in cancer cells: new players, novel targets. *Curr Opin Clin Nutr Metab Care* **9**, 358-65 (2006).

246. Campbell, J.W. & Cronan, J.E., Jr. Bacterial fatty acid biosynthesis: targets for antibacterial drug discovery. *Annu Rev Microbiol* **55**, 305-32 (2001).

247. Wakil, S.J. & Abu-Elheiga, L.A. Fatty acid metabolism: target for metabolic syndrome. *J Lipid Res* **50 Suppl**, S138-43 (2009).

248. Weatherly, S.C., Volrath, S.L. & Elich, T.D. Expression and characterization of recombinant fungal acetyl-CoA carboxylase and isolation of a soraphen-binding domain. *Biochemical Journal* **380**, 105-10 (2004).

249. Alberts, A.W. & Vagelos, P.R. Acetyl CoA carboxylase. I. Requirement for two protein fractions. *Proc Natl Acad Sci U S A* **59**, 561-8 (1968).

250. Alberts, A.W., Nervi, A.M. & Vagelos, P.R. Acetyl CoA carboxylase, II. Deomonstration of biotin-protein and biotin carboxylase subunits. *Proc Natl Acad Sci U S A* **63**, 1319-26 (1969).

251. Bianchi, A. et al. Identification of an isozymic form of acetyl-CoA carboxylase. *Journal of Biological Chemistry* **265**, 1502-9 (1990).

252. Abu-Elheiga, L. et al. The subcellular localization of acetyl-CoA carboxylase 2. *Proc Natl Acad Sci U S A* **97**, 1444-9 (2000).

253. Brownsey, R.W., Boone, A.N., Elliott, J.E., Kulpa, J.E. & Lee, W.M. Regulation of acetyl-CoA carboxylase. *Biochem Soc Trans* **34**, 223-7 (2006).

254. Munday, M.R. Regulation of mammalian acetyl-CoA carboxylase. *Biochem Soc Trans* **30**, 1059-64 (2002).

255. Shi, S., Chen, Y., Siewers, V. & Nielsen, J. Improving production of malonyl coenzyme A-derived metabolites by abolishing Snf1-dependent regulation of Acc1. *Mbio* **5**, e01130-14 (2014).

256. Huang, C.S. et al. Crystal structure of the alpha(6)beta(6) holoenzyme of propionyl-coenzyme A carboxylase. *Nature* **466**, 1001-5 (2010).

257. Huang, C.S., Ge, P., Zhou, Z.H. & Tong, L. An unanticipated architecture of the 750-kDa alpha6beta6 holoenzyme of 3-methylcrotonyl-CoA carboxylase. *Nature* **481**, 219-23 (2012).

258. Waldrop, G.L., Rayment, I. & Holden, H.M. Three-dimensional structure of the biotin carboxylase subunit of acetyl-CoA carboxylase. *Biochemistry* **33**, 10249-56 (1994).

259. Bilder, P. et al. The structure of the carboxyltransferase component of acetyl-coA carboxylase reveals a zinc-binding motif unique to the bacterial enzyme. *Biochemistry* **45**, 1712-22 (2006).

260. St Maurice, M. et al. Domain architecture of pyruvate carboxylase, a biotin-dependent multifunctional enzyme. *Science* **317**, 1076-9 (2007).

261. Tran, T.H. et al. Structure and function of a single-chain, multi-domain long-chain acyl-CoA carboxylase. *Nature* **518**, 120-4 (2015).

262. Cho, Y.S. et al. Molecular mechanism for the regulation of human ACC2 through phosphorylation by AMPK. *Biochem Biophys Res Commun* **391**, 187-92 (2010).

263. Holt, L.J. et al. Global analysis of Cdk1 substrate phosphorylation sites provides insights into evolution. *Science* **325**, 1682-6 (2009).

264. Diacovich, L. et al. Kinetic and structural analysis of a new group of Acyl-CoA carboxylases found in Streptomyces coelicolor A3(2). *Journal of Biological Chemistry* **277**, 31228-36 (2002).

265. Wei, J. & Tong, L. Crystal structure of the 500-kDa yeast acetyl-CoA carboxylase holoenzyme dimer. *Nature* **526**, 723-727 (2015).

266. Bernado, P. Effect of interdomain dynamics on the structure determination of modular proteins by small-angle scattering. *Eur Biophys J* **39**, 769-80 (2010).

267. Smith, J.L., Skiniotis, G. & Sherman, D.H. Architecture of the polyketide synthase module: surprises from electron cryo-microscopy. *Curr Opin Struct Biol* **31**, 9-19 (2015).

268. Maier, T., Leibundgut, M. & Ban, N. The crystal structure of a mammalian fatty acid synthase. *Science* **321**, 1315-22 (2008).

269. Brignole, E.J., Smith, S. & Asturias, F.J. Conformational flexibility of metazoan fatty acid synthase enables catalysis. *Nature Structural & Molecular Biology* **16**, 190-7 (2009).

270. Strieker, M., Tanovic, A. & Marahiel, M.A. Nonribosomal peptide synthetases: structures and dynamics. *Curr Opin Struct Biol* **20**, 234-40 (2010).

271. Patel, M.S., Nemeria, N.S., Furey, W. & Jordan, F. The pyruvate dehydrogenase complexes: structure-based function and regulation. *Journal of Biological Chemistry* **289**, 16615-23 (2014).

272. Zhang, K.Y., Cowtan, K. & Main, P. Combining constraints for electron-density modification. *Methods Enzymol* **277**, 53-64 (1997).

273. Winn, M.D. et al. Overview of the CCP4 suite and current developments. *Acta Crystallogr D Biol Crystallogr* **67**, 235-42 (2011).

274. Sheldrick, G.M. A short history of SHELX. *Acta Crystallographica. Section A: Crystal Physics, Diffraction, Theoretical and General Crystallography* **64**, 112-22 (2008).

275. Olsen, J.V. et al. Quantitative phosphoproteomics reveals widespread full phosphorylation site occupancy during mitosis. *Sci Signal* **3**, ra3 (2010).

276. Bian, Y. et al. An enzyme assisted RP-RPLC approach for in-depth analysis of human liver phosphoproteome. *J Proteomics* **96**, 253-62 (2014).

277. Cantin, G.T. et al. Combining protein-based IMAC, peptide-based IMAC, and MudPIT for efficient phosphoproteomic analysis. *J Proteome Res* **7**, 1346-51 (2008).

278. Biasini, M. et al. SWISS-MODEL: modelling protein tertiary and quaternary structure using evolutionary information. *Nucleic Acids Res* **42**, W252-8 (2014).

279. Pei, J. & Grishin, N.V. AL2CO: calculation of positional conservation in a protein sequence alignment. *Bioinformatics* **17**, 700-12 (2001).

280. Petoukhov, M.V. et al. New developments in the program package for small-angle scattering data analysis. *Journal of Applied Crystallography* **45**, 342-350 (2012).

281. Skou, S., Gillilan, R.E. & Ando, N. Synchrotron-based small-angle X-ray scattering of proteins in solution. *Nature Protocols* **9**, 1727-1739 (2014).

282. Jacques, D.A. & Trewhella, J. Small-angle scattering for structural biology-Expanding the frontier while avoiding the pitfalls. *Protein Science* **19**, 642-657 (2010).

283. Konarev, P.V., Volkov, V.V., Sokolova, A.V., Koch, M.H.J. & Svergun, D.I. PRIMUS: a Windows PC-based system for small-angle scattering data analysis. *Journal of Applied Crystallography* **36**, 1277-1282 (2003).

284. Fischer, H., Neto, M.D., Napolitano, H.B., Polikarpov, I. & Craievich, A.F. Determination of the molecular weight of proteins in solution from a single small-angle X-ray scattering measurement on a relative scale. *Journal of Applied Crystallography* **43**, 101-109 (2010).

285. Scheres, S.H. A Bayesian view on cryo-EM structure determination. *Journal of Molecular Biology* **415**, 406-18 (2012).

286. Marabini, R. et al. Xmipp: An Image Processing Package for Electron Microscopy. *Journal of Structural Biology* **116**, 237-40 (1996).

287. Baretic, D., Berndt, A., Ohashi, Y., Johnson, C.M. & Williams, R.L. Tor forms a dimer through an N-terminal helical solenoid with a complex topology. *Nat. Commun.* **7**(2016).

288. Zhou, P., Zhang, N., Nussinov, R. & Ma, B.Y. Defining the Domain Arrangement of the Mammalian Target of Rapamycin Complex Component Rictor Protein. *Journal of Computational Biology* **22**, 876-886 (2015).

289. Pan, D.Q. & Matsuura, Y. Structures of the pleckstrin homology domain of Saccharomyces cerevisiae Avo1 and its human orthologue Sin1, an essential subunit of TOR complex 2. *Acta Crystallographica Section F-Structural Biology and Crystallization Communications* **68**, 386-392 (2012).

290. Donepudi, M. & Grutter, M.G. Structure and zymogen activation of caspases. *Biophysical Chemistry* **101**, 145-153 (2002).

291. Tait, S. et al. Local control of a disorder-order transition in 4E-BP1 underpins regulation of translation via eIF4E. *Proceedings of the National Academy of Sciences of the United States of America* **107**, 17627-17632 (2010).

292. Andrade, M.A., Perez-Iratxeta, C. & Ponting, C.P. Protein repeats: Structures, functions, and evolution. *Journal of Structural Biology* **134**, 117-131 (2001).

293. Vetter, I.R., Arndt, A., Kutay, U., Gorlich, D. & Wittinghofer, A. Structural view of the Ran-importin beta interaction at 2.3 angstrom resolution. *Cell* **97**, 635-646 (1999).

294. Goldenberg, S.J. et al. Structure of the Cand1-Cul1-Roc1 complex reveals regulatory mechanisms for the assembly of the multisubunit cullin-dependent ubiquitin ligases. *Cell* **119**, 517-528 (2004).

295. Takai, H., Wang, R.C., Takai, K.K., Yang, H. & de Lange, T. Tel2 regulates the stability of PI3K-related protein kinases. *Cell* **131**, 1248-59 (2007).

296. Takai, H., Xie, Y.H., de Lange, T. & Pavletich, N.P. Tel2 structure and function in the Hsp90-dependent maturation of mTOR and ATR complexes. *Genes & Development* **24**, 2019-2030 (2010).

297. Xu, C. & Min, J.R. Structure and function of WD40 domain proteins. *Protein & Cell* **2**, 202-214 (2011).

298. Stirnimann, C.U., Petsalaki, E., Russell, R.B. & Muller, C.W. WD40 proteins propel cellular networks. *Trends in Biochemical Sciences* **35**, 565-574 (2010).

299. Sekiguchi, T., Kamada, Y., Furuno, N., Funakoshi, M. & Kobayashi, H. Amino acid residues required for Gtr1p-Gtr2p complex formation and its interactions with the Ego1p-Ego3p complex and TORC1 components in yeast. *Genes to Cells* **19**, 449-463 (2014).

300. Ekman, D., Bjorklund, A.K., Frey-Skott, J. & Elofsson, A. Multi-domain proteins in the three kingdoms of life: Orphan domains and other unassigned regions. *Journal of Molecular Biology* **348**, 231-243 (2005).

301. Apic, G., Gough, J. & Teichmann, S.A. Domain combinations in archaeal, eubacterial and eukaryotic proteomes. *Journal of Molecular Biology* **310**, 311-325 (2001).

302. Vogel, C., Bashton, M., Kerrison, N.D., Chothia, C. & Teichmann, S.A. Structure, function and evolution of multidomain proteins. *Curr Opin Struct Biol* **14**, 208-16 (2004).

303. Besche, H.C., Peth, A. & Goldberg, A.L. Getting to First Base in Proteasome Assembly. *Cell* **138**, 25-28 (2009).

304. Cheeseman, I.M. & Desai, A. Molecular architecture of the kinetochore-microtubule interface. *Nat Rev Mol Cell Biol* **9**, 33-46 (2008).

305. Nilsen, T.W. The spliceosome: the most complex macromolecular machine in the cell? *Bioessays* **25**, 1147-1149 (2003).

306. Grabiner, B.C. et al. A Diverse Array of Cancer-Associated MTOR Mutations Are Hyperactivating and Can Predict Rapamycin Sensitivity. *Cancer Discovery* **4**, 554-563 (2014).